

UCLA

UCLA Electronic Theses and Dissertations

Title

Development of Semiconductor-Based Membrane Potential Nanosensors For Neuron Research

Permalink

<https://escholarship.org/uc/item/7m0013p5>

Author

Kuo, Yung

Publication Date

2019

Peer reviewed|Thesis/dissertation

UNIVERSITY OF CALIFORNIA

Los Angeles

Development of Semiconductor-Based
Membrane Potential Nanosensors
For Neuron Research

A dissertation submitted in partial satisfaction of the
requirements for the degree Doctor of Philosophy
in Chemistry

by

Yung Kuo

2019

© Copyright by

Yung Kuo

2019

ABSTRACT OF THE DISSERTATION

Development of Semiconductor-Based Membrane Potential Nanosensors For Neuron Research

by

Yung Kuo

Doctor of Philosophy in Chemistry

University of California, Los Angeles, 2019

Professor Shimon Weiss, Chair

Visualizing neural activities is an important step towards studying and understanding the human brain. Since neural signals are transmitted through modulations of their membrane potentials, a membrane potential sensor capable of translating such signals into experimental observables is essential for recording neural signals. Moreover, the capability of observing membrane potential in the functional structures of a neuron, which can be as small as femto-liters in volume, is crucial for studying important brain functions such as memory. For this reason, we developed inorganic nanosensors based on semiconductor nanorods as membrane potential sensors. These nanorods, which operate via the quantum confined Stark effect, display large voltage sensitivities by changes in fluorescence intensity, spectra and lifetime, allowing non-invasive observation of minute fluctuations in the membrane of live cells. The extreme brightness of these nanorods also allow single particle recordings, which will enable studies of membrane potentials in tiny neuronal structure such as synapses. In this thesis, we will first introduce the background, review the

existing membrane potential sensors and introduce the relevant literatures regarding solid-state membrane potential sensors. For our development, we will first describe the development of a spectrally-resolved microscope for measuring the spectra of single nanoparticles in Chapter 2. Then, the characterizations of the quantum confined Stark effect in a variety of nanoparticles will be described in Chapter 3. The temporal response, long-term stability and the capability of recording electric field modulation at 1 kHz using a single nanorod will be reported and discussed. In Chapter 4, we will demonstrate a surface functionalization approach utilizing designed alpha-helical peptides and zwitterionic ligands for facilitating insertion of the nanorods into lipid membranes. These functionalized nanorods were shown to spontaneously insert into cell membranes and report membrane potential in live cells. The detailed characterization of the functionalized nanorods in the membrane and the capability of recording the membrane potential using a single functionalized nanorod will be demonstrated in Chapter 5.

The dissertation of Yung Kuo is approved.

William M. Gelbart

David Bernard Bensimon

Joshua Trachtenberg

Shimon Weiss, Committee Chair

University of California, Los Angeles

2019

*To my husband, Stephen Sasaki,
for his love and support throughout our time
pursuing our PhDs together*

Table of Contents

| | |
|---|-----|
| Table of Contents..... | vi |
| Acknowledgements..... | vii |
| Vita | ix |
| Chapter 1 Introduction..... | 1 |
| Background..... | 2 |
| Quantum dots..... | 3 |
| Quantum confined Stark effect | 4 |
| Membrane potential probes | 5 |
| References | 10 |
| Chapter 2 Development of a single-particle spectrally-resolve microscope | 17 |
| Chapter 3 Measurements of the quantum confined Stark effect of single semiconductor nanosensors | 27 |
| Chapter 4 Functionalization of voltage sensitive nanorods for membrane insertion | 61 |
| Chapter 5 Membrane potential reporting in live cells using functionalized nanorods | 89 |

Acknowledgements

This work would not be possible without the support from my advisor, Shimon Weiss, the many collaborators who involved in scientific discussions, and the past and current members of the Weiss lab, Kyoungwon (Philip) Park, Jianqing (Jack) Li, Joonhyuck Park, Xavier Michalet and Antonino Ingargiola. Philip pioneered this project and taught me everything I need when I first joined the lab in 2013. Jack contributed to the nanoparticle synthesis and has been my biggest support for any miscellaneous questions I had inside and outside of the lab. Joonhyuck, Xavier and Antonino have directly contributed to this work through nanoparticle functionalization, time-resolved measurements, and data analysis, respectively. I would also like to thank my collaborators, Noga Meir, Alexey Chizhik, Omri Bar-Elli, Emory Chan, Dan Oron, Joerg Enderlein, Yi-Lin Huang, Evan Miller, Volodymyr Shvadchak, Peng Zou, and colleagues in UCLA, Xinghong Dai, Lawrence Hsiung, Wookyeom Kim, Z. Hong Zhou, Alex J. Levine, who contributed to this work through collaborations and discussions.

Chapter 2 is a reprint of the original article published in *Proceedings of SPIE* 10352, 103520L (2017), titled “Development of a high throughput single-particle screening for inorganic semiconductor nanorods as neural voltage sensor” by authors: Y. Kuo, K. Park, J. Li, A. Ingargiola, J. Park, V. Shvadchak, S. Weiss. DOI: 10.1117/12.2273089. Reprinted with permission from SPIE.

Chapter 3 is a reprint of the original article published in *ACS Photonics* 5 (12), 4788-4800 in October 2018, titled “Characterizing the quantum-confined Stark effect in semiconductor quantum dots and nanorods for single-molecule electrophysiology.”, by authors: Y. Kuo, J. Li, X. Michalet, A. Chizhik, N. Meir, O. Bar-Elli, E. Chan, D. Oron, J. Enderlein, S. Weiss. DOI: 10.1021/acsphotonics.8b00617. Reprinted with permission from *ACS Photonics* 5 (12), 4788-4800 (2018). Copyright 2018 American Chemical Society.

Chapter 4 is a manuscript titled “Improved surface functionalization and characterization of membrane targeted semiconductor voltage nanosensors” in preparation for publication. The

authors of this manuscript are Joonhyuck Park, Yung Kuo, Jack Li, Yi-Lin Huang, Evan Miller, and Shimon Weiss. Joonhyuck Park conducted all experiments, analyzed the data, and wrote the manuscript. I developed the assay and built the setup for modulating the membrane potential of valinomycin-treated cells by manipulating the potassium concentrations in the extracellular media. Jack Li and I synthesized ZnSe/CdS NRs using WANDA. Shimon Weiss, Joonhyuck Park, and I designed the experiments. Shimon Weiss, Evan Miller and I helped in writing and revising the manuscript. All authors have given approval for including the manuscript in this dissertation.

Chapter 5 is a reprint of the original article published in *Science Advances*, 4 (1), e1601453 in 2018, titled “Membrane insertion of—and membrane potential sensing by—semiconductor voltage nanosensors: Feasibility demonstration.”, by authors: Park, K.; Kuo, Y.; Shvadchak, V.; Ingargiola, A.; Dai, X.; Hsiung, L.; Kim, W.; Zhou, H.; Zou, P.; Levine, A. J.; Li, J.; Weiss, S. DOI: 10.1126/sciadv.1601453 © The Authors, some rights reserved; exclusive licensee American Association for the Advancement of Science. Distributed under a Creative Commons Attribution NonCommercial License 4.0 (CC BY-NC) <http://creativecommons.org/licenses/by-nc/4.0/>. Reprinted with permission from AAAS. For this work, K.P. and Y.K. performed the experiments, data analysis, and wrote the manuscript. V.S. designed the peptides and helped edit the manuscript. A.I. performed the signal analysis for the patch-clamp experiments and wrote the manuscript. X.D. and Z.H.Z. performed the vesicle imaging with cryoEM. L.H. and W.K. performed the experiments. P.Z. performed the patch-clamp experiment. J.L. synthesized the NPs for this study. A.J.L. developed the theory, performed the simulations for membrane insertion, and wrote the manuscript. S.W. conceived and managed the project and wrote the manuscript. All authors discussed the results and contributed to the writing of the manuscript.

During my graduate career, I had two amazing undergrads, Moonsun Choi and Yoojin Kim, whom I thank for technical assistance. The funding sources for the specific works are acknowledged in each chapter. Lastly, I would like to thank Prof. Ken-Tsung Wong and Ms. In-Fang Li, who inspired and always encouraged me to pursue my career as a chemist and a scientist.

Vita

YUNG KUO

EDUCATION

Sep 2010 - Jun 2012 **M.S. Chemistry**, National Taiwan University, Taipei, Taiwan (GPA: 4.0/4.0)
Sep 2006 - Jun 2010 **B.S. Chemistry**, National Taiwan University, Taipei, Taiwan

EXPERIENCES

Sep 2013 – present **Graduate Student Researcher**
Teaching Assistant
University of California, Los Angeles, Los Angeles, CA
Jul 2008 – Jul 2013 **Master’s Research Assistant**
Graduate and Undergraduate Student Researcher
Institute of Atomic and Molecular Sciences, Academia Sinica, Taipei, Taiwan
Sep 2009 - Jun 2011 **Teaching assistant**
National Taiwan University, Taipei, Taiwan

AWARDS AND HONORS

Mar 2016 **251st ACS national meeting travel award**
Sep 2013-Aug 2015 **Government Scholarship for Study Abroad**
Ministry of Education, Republic of China (\$16,000/y. Total: \$32,000)
Jun 2012 **Dean’s Award**
highest honor for Master graduates of College of Science, National Taiwan University
Dec 2012 **Graduate Dissertation Award**
80th Chinese Chemical Society annual meeting, Tainan, Taiwan
Jun 2012 **Poster Award**
Graduate student poster session, National Taiwan University
Since 2012 **Honorary member**
The Phi Tau Phi Scholastic Honor Society of the Republic of China

PUBLICATIONS

1. Characterizing the quantum-confined Stark effect in semiconductor quantum dots and nanorods for single-molecule electrophysiology.
Y. Kuo, J. Li, X. Michalet, A. Chizhik, N. Meir, O. Bar-Elli, E. Chan, D. Oron, J. Enderlein, S. Weiss.
ACS Photonics 5 (12), 4788-4800 (2018). *Featured on journal cover*
2. Membrane insertion of—and membrane potential sensing by—semiconductor voltage nanosensors: Feasibility demonstration.
K. Park, **Y. Kuo**, V. Shvadchak, A. Ingargiola, X. Dai, L. Hsiung, W. Kim, H. Zhou, P. Zou, A. J. Levine, J. Li, S. Weiss.
Science Advances, 4 (1) (2018).
3. Shot noise limited voltage sensing with single nanorods via the quantum confined Stark effect.
O. Bar-Elli, D. Steinitz, G. Yang, R. Tenne, A. Ludwig, **Y. Kuo**, A. Triller, S. Weiss, D. Oron.
ACS Photonics, 5 (7), 2860-2867 (2018).
4. Development of a high throughput single-particle screening for inorganic semiconductor nanorods as neural voltage sensor.
Y. Kuo, K. Park, J. Li, A. Ingargiola, J. Park, V. Shvadchak, S. Weiss.
Proceedings of SPIE 10352, 103520L (2017).
5. Improved surface functionalization and characterization of membrane targeted semiconductor voltage

nanosensors

- J. Park, **Y. Kuo**, J. Li, Y. Huang, E. Miller, S. Weiss
(in preparation) (2019)
6. A 512×512 SPAD image sensor with integrated gating for widefield FLIM
A. Ulku, C. Bruschini, I. Antolovic, **Y. Kuo**, R. Ankri, S. Weiss, X. Michalet, Edoardo Charbon
IEEE Journal of Selected Topics in Quantum Electronics, 25 (1), 1-12 (2019).
 7. Fluorescent nanodiamond as a probe for the intercellular transport of proteins in vivo.
Y. Kuo, T.-Y. Hsu, Y.-C. Wu, H.-C. Chang.
Biomaterials, 34, 8352 (2013).
 8. Fluorescence lifetime imaging microscopy of nanodiamonds *in vivo*.
Y. Kuo, T.-Y. Hsu, Y.-C. Wu, J.-H. Hsu, H.-C. Chang.
Proceedings of SPIE, 8635, 863503 (2013).
 9. Tracking the engraftment and regenerative capabilities of transplanted lung stem cells using fluorescent nanodiamonds.
T.-J. Wu, Y.-K. Tzeng, W.-W. Chang, C.-A. Cheng, **Y. Kuo**, C.-H. Chien, H.-C. Chang, J. Yu.
Nat. Nanotechnol., 8, 682 (2013).
 10. Superresolution Imaging of Albumin-Conjugated Fluorescent Nanodiamonds in Cells by Stimulated Emission Depletion.
Y.-K. Tzeng, O. Faklaris, B.-M. Chang, **Y. Kuo**, J.-H. Hsu, H.-C. Chang.
Angew. Chem. Int. Ed., 50, 2262 (2011).
 11. Measuring Förster resonance energy transfer between fluorescent nanodiamonds and near-infrared dyes by acceptor photobleaching.
Y.-Y. Chen, H. Shu, **Y. Kuo**, Y.-K. Tzeng, H.-C. Chang.
Diamond Relat. Mater., 20, 803 (2011).

PRESENTATIONS

- May. 17 2018 **2018 Neural Microcircuits Symposium**, Los Angeles, CA
Y. Kuo, et. al. *Voltage sensitive probes based on fluorescent semiconductor nanorods.*
- Aug. 07 2017 **SPIE Optics + Photonics 2017**, San Diego, CA, Oral presentation
Y. Kuo, K. Park, J. Li, A. Ingargiola, J. Park, V. Shvadchak, S. Weiss. *Development of a high throughput single-particle screening for inorganic semiconductor nanorods as neural voltage sensor.*
- Mar. 02 2016 **60th Biophysical Society Annual Meeting**, Los Angeles, CA. Oral presentation
K. W. Park, **Y. Kuo**, V. Shvadchak, A. Ingargiola, X. Dai, L. Hsiung, W. Kim, H. Zhou, P. Zou, A. Levine, J. Li, S. Weiss. *Sensing membrane potential by inorganic semiconductor nanorods.*
- Mar. 15 2016 **251st ACS National Meeting**, San Diego, CA. Oral presentation.
K. W. Park, **Y. Kuo**, V. Shvadchak, A. Ingargiola, X. Dai, L. Hsiung, W. Kim, H. Zhou, P. Zou, A. Levine, J. Li, S. Weiss. *Sensing membrane potential by inorganic semiconductor nanorods.*
- Mar. 14 2016 **251st ACS National Meeting**, San Diego, CA. Oral presentation.
J.J. Li, **Y. Kuo**, S. Weiss. *Semiconductor nanorods functionalization for plasma membrane insertion.*
- Oct. 19 2015 **Glenn T. Seaborg Symposium**, Los Angeles, CA. poster presentation.
K. W. Park, **Y. Kuo**, V. Shvadchak, A. Ingargiola, X. Dai, L. Hsiung, W. Kim, H. Zhou, P. Zou, A. Levine, J. Li, S. Weiss. *Sensing membrane potential by inorganic semiconductor nanorods.*

Chapter 1
Introduction

Background

Neurons, or nerve cells, are essential cells in charge of transmitting signals for receiving sensory inputs, to actuate movements and to create intelligence^{1, 2}. Neurons transmit and process both electrical and chemical signals, both of which are difficult to monitor due to the fast dynamics and the small volume where the processes happen within. The electrical signals, for example, have intricate dynamics at the sub-millisecond time scale, which will require recordings at rates faster than few kHz to resolve the signals. A sensor capable of resolving and monitoring these signals with high temporal and spatial resolutions will allow neuroscientists to visualize neural activities, study how individual neurons communicate in a neural network and decode how billions of neurons corroborate human intelligence.

In this work, we focus on developing a sensor for reporting the electrical signals. The electrical signals transmitted in neurons or other excitable cells are generated via modulations of the neurons' membrane potential, resulted from the different ion concentrations across the plasma membrane. The membrane potential is usually ~ -60 mV to -70 mV at rest, called the resting potential. This potential difference, or voltage, can rapidly change when a signal comes to open a subset of ion channels to allow fast influx and outflux of the accumulated ions, creating an upswing of the membrane potential to ~ 40 mV. The change of membrane potential then triggers other ion channels in the proximity to open, and the signal propagates across the neuron, while another subset of ion channels work to restore the resting potential. Despite the simplistic picture, the electrical impulses, called the action potentials, occur within a few milliseconds and exhibit a wide range of frequencies and waveforms in different types of neurons, in different parts of a single neuron (for example, presynaptic terminals vs soma³) or when different types and numbers of voltage-gated ion channels are expressed⁴⁻¹¹. Although early studies of the Hodgkin-Huxley model¹² successfully described the action potentials in a squid giant axon, neurons in vertebrates and invertebrates have much more complex firing behaviors^{7, 8, 13}. In order to study neurosciences beyond a simple squid, especially in mammalian brains, tools capable of resolving action

potentials at various frequencies, firing patterns, and spike shapes/ waveforms without averaging are required.

Besides tools capable of resolving action potentials with high temporal resolution, tools that allow monitor of electrical events with high spatial resolution is also desired. The uprising field of studies in, for example, the dendritic spines and synapses, of a neuron has urged the development of tools for monitoring electrical events in sub-micrometer spaces. Many important brain functions such as transmission of signals, plasticity and even memories¹⁴⁻¹⁷ are facilitated by complex electrical and chemical events in such tiny structures. However, studies in such structures are currently very challenging for several reasons. (1) There is a huge number of synapses and dendritic spines in a single neuron. For example, there are averagely 7000 synaptic connections in each neuron in the human brain¹⁸. Monitoring such large number of tiny structures requires wide-field detection with high spatial resolution. (2) Dendritic spines are extremely dynamic in shape and size¹⁹⁻²¹. (3) Although the electrical events are correlated with ionic fluxes and chemical release involved in the signaling¹⁶, other than Ca²⁺ sensitive dyes, there are not many tools available for monitoring these processes either electrically or chemically in such tiny structures. To decode information in sub-micrometer structures like the spines and synapses and to monitor hundreds to thousands of spines or synapses in a single neuron require probes that can report local electric field with single-molecule or nanometer spatial resolution and wide-field detection compatibility.

Quantum dots

Quantum dots (QDs) are fluorescent nanoparticles usually composed of semiconductor materials. Due to their small size, usually between 2 nm to 15 nm, these nanoparticles exhibit unique optical properties different from conventional fluorophores. The semiconductor material allows continuous absorption of photons with energies above the bandgap, so the QDs can be excited with a wide range of colors above the bandgap, creating excited electrons in the conduction band and leaving excited holes in the valance band. These short-lived excited electrons and holes

are called charge carriers, and they form bound excitons when attracted to each other through the Coulomb force. Due to fast thermalizations, the majority of the charge carriers recombine at the band edge, usually few nanoseconds to microseconds after photon excitations, emitting photons matching the bandgap energy and therefore creating a relatively narrow emission spectrum. Sometimes, charge carriers can release their energy through non-radiative pathways without emitting photons. When the size of a QD (or nanorod, nanowire, nanoplatelet ... etc.) is of the same order as the Bohr radius of the exciton, the exciton is quantum confined within the nanocrystal in at least one of the three dimensions, resulting in discretized energy spectra, a larger bandgap compared to the bulk material, and size-dependent optical and electrical properties due to the size-dependent confinement energy. The absorption and emission spectra of a QD shift towards higher energy when the size of the QD decreases, and QDs of the same material can and have been synthesized to create various emission wavelengths, from ultraviolet (UV) to near-infrared (NIR) by simply manipulating the nanoparticle size²². The charge carriers' wavefunctions, optical transition dipoles, and other optical and electronic properties can also be manipulated by the sizes and shapes of the nanoparticles, creating desired functions for a wide range of applications in, for example, photovoltaics, light emission, photodetectors, and nanosensors²³⁻²⁸.

Quantum confined Stark effect

The quantum confined Stark effect (QCSE) describes the effect of an electric field on the optical absorption and emission spectra of a quantum well or a QD. When an electric field is applied to a quantum well, the potential landscape of the quantum well is changed, and the electron states shift toward lower energy while the hole states shift toward higher energy. The reduced energy gap between the electron and the hole results in lower energy of the emitted photon when the charges recombine, and therefore the emission red shifts, as compared to the emission without field perturbation. Meanwhile, the electron and the hole wavefunctions are distorted under an electric field. Due to their opposite charges, the electron is pulled to one side of the quantum well, while the hole is pulled to the other side, causing reduced overlap integral

between the two wavefunctions and decreased probability of recombination. A smaller recombination probability suggests reduced radiative decay rate and elongated excited state lifetime, if the non-radiative decay rates remain unaffected under an electric field. As a result, the reduced radiative rate also reduces the quantum yield because the excited state energy is more likely to be released via competing non-radiative pathways instead of via emitting a photon. These phenomena are further enhanced when the charge carriers are quantum confined within a potential well or a QD. Unlike in bulk materials, where the Franz-Keldysh effect predicts mostly broadenings of the band-edge absorption and emission, the confined excitonic states in a quantum well under an electric field remain well-resolved. In addition, the band-edge absorption and emission of a quantum well exhibit Stark shifts that are many times larger than the zero-field electron-hole binding energy without ionization because the large potential walls confine the charge carriers within the well with little tunneling outside of the well²⁹.

Capitalizing the QCSE, many optical switches and electro-optic modulation devices have been proposed and designed using quantum wells³⁰⁻³². The QCSE has also been observed in colloidal spherical CdSe QDs and nanocrystals composed of other materials and of other shapes³³⁻³⁴. Therefore, using semiconductor nanoparticles as nanosensors for optical detection of the electric field has also been modeled and tested³⁵⁻³⁹.

Membrane potential probes

Numerous probes have been developed for monitoring the membrane potentials in live cells. These includes electrical recordings using patch clamp or microelectrode arrays, and fluorescence recordings using organic fluorescent voltage-sensitive dyes (VSD), genetically-encoded voltage indicators (GEVIs) or other nanoparticle-based voltage sensors.

Electrical recordings

In patch clamp, a micropipette is used to patch onto the cell membrane to form electrical seal with Giga-Ohm resistance, called gigaseal. Patch clamp allows monitoring of voltage and current across a membrane using electrodes placed within the micropipette and in the biological

media because the gigaseal minimizes current leakage through the biological media. The electrical recording methods have very fast recording rate due to the fast response of modern-day electronics. However, the patch clamp technique is invasive, and the bulky micropipettes prevent recordings at multiple sites in a small field-of-view due to space constraints, even with multi-pipette patch clamping⁴⁰. Similarly, the microelectrode arrays⁴¹ have the advantage of fast recording and is capable of recording at many sites within the range of the array. However, besides being very invasive, the microelectrode array has limited spatial resolution and fixed number of recording sites dictated by the number of microelectrodes in the array. The microelectrodes also do not record the signals from specific neurons but instead record events within the tissue, often at a distance from neurons. The signals are therefore from multiple sources and require post-recording analyses.

Fluorescence recordings

Fluorescent probes have been developed to circumvent the drawbacks of the electrical recording methods. These probes are designed to associate with the cell membrane and exhibit changes in fluorescence properties depending on the membrane potential. Therefore, the membrane potential changes can be monitor through a fluorescence microscope, which allows recording wherever the probes are located with no space constraint and the invasiveness is significantly reduced. The spatial resolution is then dependent on the optics and only limited by the optical diffraction limit. One other advantage these fluorescent membrane potential probes have over electrical recording methods is that a fluorescence microscope is the only instrument required, while electrical recording methods usually require voltage amplifiers, micromanipulators, and/or microscopes. The recording using fluorescent probes is therefore cheaper, simpler and less demanding in terms of training, as compared to the patch clamp technique. However, since the fluorescence signals are secondary signals in response to the electrical signals, the fluorescent probes need to be carefully calibrated in order to translate the measured photons into electrical signals. The kinetics of these fluorescent probes are also of

concern. The fluorescent probes need to have kinetic response much faster than the timescale of neural voltage activities to avoid distortion to the observed waveform of the action potentials.

In the past, fluorescent calcium indicators were utilized to record the action potential activities *in vivo* due to the lack of effective voltage imaging methods⁴²⁻⁴⁶. The fluctuation in Ca^{2+} concentration is triggered by voltage-gated calcium channels due to action potential activities and therefore is a secondary signal, which is then translated into tertiary photon signals by the fluorescent calcium indicators. The kinetics of commercial calcium indicators, tens to hundreds of milliseconds, are much slower than the timescales of action potentials, which last only few milliseconds from depolarization, repolarization, to returning to the resting potential. Therefore, the observed calcium signaling waveforms are distorted from the waveform of action potentials, and the calcium indicators struggle to resolve fast spike trains.

For voltage-sensitive fluorescent probes, the majority are embedded or partially embedded in the lipid membrane bilayers. These probes display membrane potential-dependent fluorescence via a variety of different mechanisms⁴⁷, including electrochromism, photoinduced electron transfer (PeT)⁴⁸, conformational changes of a voltage-sensitive domain in conjugation with a fluorescent protein^{49, 50}, natural electrochromism based on bacteriorhodopsin^{51, 52}, and Föster resonance energy transfer (FRET)⁵³. Regardless of the voltage-sensing mechanisms, most of these fluorescent probes display changes in the fluorescence intensity correlated to the membrane potential. Therefore, the voltage sensitivity is usually expressed as the percent change of fluorescence intensity as compared to that when the membrane is at resting potential, labeled as $\Delta F/F$ with the ΔF being the change in fluorescence intensity and the F being the fluorescence intensity at resting potential. Other fluorescent probes display changes of the fluorescence spectra or their Föster resonance energy transfer (FRET) efficiency and thus allow for ratiometric readouts, quantified as $\Delta R/R$. Mermaid2, an example for the FRET based probe, is reported to exhibit 48.5% $\Delta R/R$ per 100 mV⁵⁴. However, fluorescent probes suffer from several issues, including toxicity, low brightness, changing membrane capacitance, and/or photobleaching⁴⁷.

Fluorescent voltage-sensitive dye

The voltage sensitivities, $\Delta F/F$, of commercial VSDs are typically less than 20% (7.5% per 100 mV for di-8-ANEPPS⁵⁵, 4.13% at 560 nm and 2.12% at 620 nm per 150 mV for di-4-ANEPPS⁵⁶, 2-3 % for RH237⁵⁷ and 11.9% for JPW-6003⁵⁸), while some novel VSDs that are not yet commercialized have been reported to exhibit a $\Delta F/F$ as large as 24% per 100 mV⁴⁸.

Genetically encoded voltage indicator

GEVIs have a wide range of $\Delta F/F$, from as low as < 5% for the GEVIs based on ion channel scaffolds to ~20% per 100 mV for the rhodopsin-based GEVIs such as QuasAr2 or Archer1⁵⁹⁻⁶². However, GEVIs often have slow kinetics, and the waveforms of action potentials recorded by GEVIs fluorescence are therefore convoluted with their response function⁶².

Other voltage sensors

Many solid-state materials have been developed as membrane potential probes to overcome the drawbacks of VSDs or GEVIs. These include QDs, functionalized QDs, defect centers in diamonds and others. Although most of these fluorescent sensors are not yet sufficiently reliable for commercialization, these solid-state crystals or nanocrystals usually have higher photostability than organic fluorophores and therefore offer alternatives as future membrane potential probes.

Three mechanisms have been demonstrated for QDs to perform as membrane potential sensors, FRET, PeT and QCSE. For FRET-based sensors, it has been demonstrated using glutathione-capped QDs as the donors and dipicrylamine (DPA) as a membrane embedded acceptor, which translocate to different leaflets within the membrane depending on the membrane potential⁶³. For PeT-based sensors, it has been accomplished using QDs as the donors and fullerene as the electron acceptors. The donors and acceptors are conjugated by a short peptide, and the electron transfer efficiency can be tuned by changing the peptide lengths⁶⁴. In contrast to the two mechanisms mentioned above, QCSE-based voltage sensors do not require an additional acceptor molecule to attain the voltage sensitivity. QDs or nanrods with

heterostructures have also been proposed, modeled, and demonstrated experimentally to display large intrinsic voltage-dependent fluorescence based on the QCSE³⁴⁻³⁶. Similar to all the other sensors, these QD-based voltage sensors would require interfacing with the cell membrane in order to sense the membrane potential, which is more difficult to achieve compared to genetically-encoded sensors or small organic molecules which can be synthesized with lipophilic functional groups.

The other solid-state voltage sensor was achieved using optically detected magnetic resonance (ODMR) using the defect centers in diamonds. When an action potential passes through the axon of a neuron creating a local magnetic field, the nitrogen-vacancy (NV) color centers in the proximity display magnetic field-dependent laser-induced fluorescence, which can be detected from a photodetector⁶⁵. These defect centers could be fabricated in a single crystal diamond substrate or created in a nanodiamond^{65, 66}, and due to the remote sensing capability, this sensor does not have to be associated with the cell membrane for voltage sensing.

References

1. Azevedo, F. A. C.; Carvalho, L. R. B.; Grinberg, L. T.; Farfel, J. M.; Ferretti, R. E. L.; Leite, R. E. P.; Filho, W. J.; Lent, R.; Herculano-Houzel, S., Equal numbers of neuronal and nonneuronal cells make the human brain an isometrically scaled-up primate brain. *The Journal of Comparative Neurology* **2009**, *513* (5), 532-541.
2. Lodish, H.; Berk, A.; Zipursky, S. L.; Matsudaira, P.; Baltimore, D.; Darnell, J., *Molecular Cell Biology*. 4th ed.; W. H. Freeman: New York, 2000.
3. Geiger, J. R. P.; Jonas, P., Dynamic Control of Presynaptic Ca²⁺ Inflow by Fast-Inactivating K⁺ Channels in Hippocampal Mossy Fiber Boutons. *Neuron* **2000**, *28* (3), 927-939.
4. Bean, B. P., The action potential in mammalian central neurons. *Nat Rev Neurosci* **2007**, *8* (6), 451-465.
5. Connors, B. W.; Gutnick, M. J., Intrinsic firing patterns of diverse neocortical neurons. *Trends in Neurosciences* **1990**, *13* (3), 99-104.
6. Erisir, A.; Lau, D.; Rudy, B.; Leonard, C. S., Function of Specific K⁺ Channels in Sustained High-Frequency Firing of Fast-Spiking Neocortical Interneurons. *Journal of Neurophysiology* **1999**, *82* (5), 2476.
7. Connor, J. A., Neural repetitive firing: a comparative study of membrane properties of crustacean walking leg axons. *Journal of Neurophysiology* **1975**, *38* (4), 922.
8. Hille, B., *Ion Channels of Excitable Membranes*. 3rd ed.; Sinauer Associates, Inc.: Sunderland, Massachusetts U.S.A., 2001.
9. Tateno, T.; Harsch, A.; Robinson, H. P. C., Threshold Firing Frequency–Current Relationships of Neurons in Rat Somatosensory Cortex: Type 1 and Type 2 Dynamics. *Journal of Neurophysiology* **2004**, *92* (4), 2283.
10. Zhou, F. M.; Hablitz, J. J., Layer I neurons of rat neocortex. I. Action potential and repetitive firing properties. *Journal of Neurophysiology* **1996**, *76* (2), 651.

11. Descalzo, V. F.; Nowak, L. G.; Brumberg, J. C.; McCormick, D. A.; Sanchez-Vives, M. V., Slow Adaptation in Fast-Spiking Neurons of Visual Cortex. *Journal of Neurophysiology* **2005**, *93* (2), 1111.
12. Hodgkin, A. L.; Huxley, A. F., A quantitative description of membrane current and its application to conduction and excitation in nerve. *The Journal of Physiology* **1952**, *117* (4), 500-544.
13. Llinas, R. R., The intrinsic electrophysiological properties of mammalian neurons: insights into central nervous system function. *Science* **1988**, *242* (4886), 1654.
14. Nimchinsky, E. A.; Sabatini, B. L.; Svoboda, K., Structure and Function of Dendritic Spines. *Annual Review of Physiology* **2002**, *64* (1), 313-353.
15. Hering, H.; Sheng, M., Dendritic spines : structure, dynamics and regulation. *Nat Rev Neurosci* **2001**, *2* (12), 880-888.
16. Rochefort, N. L.; Konnerth, A., Dendritic spines: from structure to &emdash;in vivo&emdash; function. *EMBO reports* **2012**, *13* (8), 699.
17. Sala, C.; Segal, M., Dendritic Spines: The Locus of Structural and Functional Plasticity. *Physiological Reviews* **2014**, *94* (1), 141.
18. Pakkenberg, B.; Pelvig, D.; Marner, L.; Bundgaard, M. J.; Gundersen, H. J. G.; Nyengaard, J. R.; Regeur, L., Aging and the human neocortex. *Experimental Gerontology* **2003**, *38* (1), 95-99.
19. Bonhoeffer, T.; Yuste, R., Spine Motility. *Neuron* **2002**, *35* (6), 1019-1027.
20. Yoshihara, Y.; De Roo, M.; Muller, D., Dendritic spine formation and stabilization. *Current Opinion in Neurobiology* **2009**, *19* (2), 146-153.
21. Dailey, M. E.; Smith, S. J., The Dynamics of Dendritic Structure in Developing Hippocampal Slices. *The Journal of Neuroscience* **1996**, *16* (9), 2983.
22. Norris, D. J.; Bawendi, M. G., Measurement and assignment of the size-dependent optical spectrum in CdSe quantum dots. *Physical Review B* **1996**, *53* (24), 16338-16346.

23. Tang, J.; Kemp, K. W.; Hoogland, S.; Jeong, K. S.; Liu, H.; Levina, L.; Furukawa, M.; Wang, X.; Debnath, R.; Cha, D.; Chou, K. W.; Fischer, A.; Amassian, A.; Asbury, J. B.; Sargent, E. H., Colloidal-quantum-dot photovoltaics using atomic-ligand passivation. *Nature Materials* **2011**, *10*, 765.
24. Anikeeva, P. O.; Halpert, J. E.; Bawendi, M. G.; Bulović, V., Quantum Dot Light-Emitting Devices with Electroluminescence Tunable over the Entire Visible Spectrum. *Nano Letters* **2009**, *9* (7), 2532-2536.
25. Konstantatos, G.; Howard, I.; Fischer, A.; Hoogland, S.; Clifford, J.; Klem, E.; Levina, L.; Sargent, E. H., Ultrasensitive solution-cast quantum dot photodetectors. *Nature* **2006**, *442*, 180.
26. Zhang, C.-Y.; Yeh, H.-C.; Kuroki, M. T.; Wang, T.-H., Single-quantum-dot-based DNA nanosensor. *Nature Materials* **2005**, *4*, 826.
27. Orte, A.; Alvarez-Pez, J. M.; Ruedas-Rama, M. J., Fluorescence Lifetime Imaging Microscopy for the Detection of Intracellular pH with Quantum Dot Nanosensors. *ACS Nano* **2013**, *7* (7), 6387-6395.
28. Nozik, A. J., Quantum dot solar cells. *Physica E: Low-dimensional Systems and Nanostructures* **2002**, *14* (1), 115-120.
29. Miller, D. A. B.; Chemla, D. S.; Damen, T. C.; Gossard, A. C.; Wiegmann, W.; Wood, T. H.; Burrus, C. A., Band-Edge Electroabsorption in Quantum Well Structures: The Quantum-Confined Stark Effect. *Physical Review Letters* **1984**, *53* (22), 2173-2176.
30. Cavenett, B. C.; Wang, S. Y.; Prior, K. A., Semiconductor Modulators and Optical Switches. *physica status solidi (b)* **1995**, *187* (2), 347-353.
31. Fox, A. M., Optoelectronics in quantum well structures. *Contemporary Physics* **1996**, *37* (2), 111-125.

32. Kuo, Y.; Lee, Y. K.; Ge, Y.; Ren, S.; Roth, J. E.; Kamins, T. I.; Miller, D. A. B.; Harris, J. S., Quantum-Confined Stark Effect in Ge/SiGe Quantum Wells on Si for Optical Modulators. *IEEE Journal of Selected Topics in Quantum Electronics* **2006**, *12* (6), 1503-1513.
33. Empedocles, S. A.; Bawendi, M. G., Quantum-Confined Stark Effect in Single CdSe Nanocrystallite Quantum Dots. *Science* **1997**, *278* (5346), 2114.
34. Park, K.; Deutsch, Z.; Li, J. J.; Oron, D.; Weiss, S., Single Molecule Quantum-Confined Stark Effect Measurements of Semiconductor Nanoparticles at Room Temperature. *ACS Nano* **2012**, *6* (11), 10013-10023.
35. Park, K.; Weiss, S., Design Rules for Membrane-Embedded Voltage-Sensing Nanoparticles. *Biophysical Journal* **2017**, *112* (4), 703-713.
36. Marshall, J. D.; Schnitzer, M. J., Optical Strategies for Sensing Neuronal Voltage Using Quantum Dots and Other Semiconductor Nanocrystals. *ACS Nano* **2013**, *7* (5), 4601-4609.
37. Rowland, C. E.; Susumu, K.; Stewart, M. H.; Oh, E.; Mäkinen, A. J.; O'Shaughnessy, T. J.; Kushto, G.; Wolak, M. A.; Erickson, J. S.; L. Efros, A.; Huston, A. L.; Delehanty, J. B., Electric Field Modulation of Semiconductor Quantum Dot Photoluminescence: Insights Into the Design of Robust Voltage-Sensitive Cellular Imaging Probes. *Nano Letters* **2015**, *15* (10), 6848-6854.
38. Efros, A. L.; Delehanty, J. B.; Huston, A. L.; Medintz, I. L.; Barbic, M.; Harris, T. D., Evaluating the potential of using quantum dots for monitoring electrical signals in neurons. *Nature Nanotechnology* **2018**, *13* (4), 278-288.
39. Park, K.; Kuo, Y.; Shvadchak, V.; Ingargiola, A.; Dai, X.; Hsiung, L.; Kim, W.; Zhou, H.; Zou, P.; Levine, A. J.; Li, J.; Weiss, S., Membrane insertion of—and membrane potential sensing by—semiconductor voltage nanosensors: Feasibility demonstration. *Science Advances* **2018**, *4* (1), e1601453.
40. Perin, R.; Markram, H., A Computer-assisted Multi-electrode Patch-clamp System. **2013**, (80), e50630.

41. Obien, M. E. J.; Deligkaris, K.; Bullmann, T.; Bakkum, D. J.; Frey, U., Revealing neuronal function through microelectrode array recordings. *Frontiers in neuroscience* **2015**, *8*, 423-423.
42. Kerr, J. N. D.; Greenberg, D.; Helmchen, F., Imaging input and output of neocortical networks *in vivo*. *Proceedings of the National Academy of Sciences of the United States of America* **2005**, *102* (39), 14063.
43. Mao, B.-Q.; Hamzei-Sichani, F.; Aronov, D.; Froemke, R. C.; Yuste, R., Dynamics of Spontaneous Activity in Neocortical Slices. *Neuron* **2001**, *32* (5), 883-898.
44. Ohki, K.; Chung, S.; Ch'ng, Y. H.; Kara, P.; Reid, R. C., Functional imaging with cellular resolution reveals precise micro-architecture in visual cortex. *Nature* **2005**, *433*, 597.
45. Stosiek, C.; Garaschuk, O.; Holthoff, K.; Konnerth, A., *In vivo* two-photon calcium imaging of neuronal networks. *Proceedings of the National Academy of Sciences* **2003**, *100* (12), 7319.
46. Grienberger, C.; Konnerth, A., Imaging Calcium in Neurons. *Neuron* **2012**, *73* (5), 862-885.
47. Kulkarni, R. U.; Miller, E. W., Voltage Imaging: Pitfalls and Potential. *Biochemistry* **2017**.
48. Huang, Y.-L.; Walker, A. S.; Miller, E. W., A Photostable Silicon Rhodamine Platform for Optical Voltage Sensing. *Journal of the American Chemical Society* **2015**, *137* (33), 10767-10776.
49. Dimitrov, D.; He, Y.; Mutoh, H.; Baker, B.; Cohen, L.; Akemann, W.; Knöpfel, T., Engineering and Characterization of an Enhanced Fluorescent Protein Voltage Sensor. *PLoS ONE* **2007**, *2* (5), e440.
50. Jin, L.; Han, Z.; Platisa, J.; Woollorton, Julian R. A.; Cohen, Lawrence B.; Pieribone, Vincent A., Single Action Potentials and Subthreshold Electrical Events Imaged in Neurons with a Fluorescent Protein Voltage Probe. *Neuron* **2012**, *75* (5), 779-785.
51. Kralj, J. M.; Douglass, A. D.; Hochbaum, D. R.; Maclaurin, D.; Cohen, A. E., Optical recording of action potentials in mammalian neurons using a microbial rhodopsin. *Nat Meth* **2012**, *9* (1), 90-95.

52. Kralj, J. M.; Hochbaum, D. R.; Douglass, A. D.; Cohen, A. E., Electrical Spiking in *Escherichia coli* Probed with a Fluorescent Voltage-Indicating Protein. *Science* **2011**, *333* (6040), 345.
53. Gong, Y.; Wagner, M. J.; Zhong Li, J.; Schnitzer, M. J., Imaging neural spiking in brain tissue using FRET-opsin protein voltage sensors. *Nature Communications* **2014**, *5*, 3674.
54. Tsutsui, H.; Jinno, Y.; Tomita, A.; Niino, Y.; Yamada, Y.; Mikoshiba, K.; Miyawaki, A.; Okamura, Y., Improved detection of electrical activity with a voltage probe based on a voltage-sensing phosphatase. *The Journal of Physiology* **2013**, *591* (18), 4427-4437.
55. Hardy, M. E. L.; Lawrence, C. L.; Standen, N. B.; Rodrigo, G. C., Can optical recordings of membrane potential be used to screen for drug-induced action potential prolongation in single cardiac myocytes? *Journal of Pharmacological and Toxicological Methods* **2006**, *54* (2), 173-182.
56. Kao, W. Y.; Davis, C. E.; Kim, Y. I.; Beach, J. M., Fluorescence Emission Spectral Shift Measurements of Membrane Potential in Single Cells. *Biophysical Journal* **2001**, *81* (2), 1163-1170.
57. Choi, B.-R.; Salama, G., Simultaneous maps of optical action potentials and calcium transients in guinea-pig hearts: mechanisms underlying concordant alternans. *The Journal of Physiology* **2000**, *529* (Pt 1), 171-188.
58. Matiukas, A.; Mitrea, B. G.; Qin, M.; Pertsov, A. M.; Shvedko, A. G.; Warren, M. D.; Zaitsev, A. V.; Wuskell, J. P.; Wei, M.-d.; Watras, J.; Loew, L. M., Near-infrared voltage-sensitive fluorescent dyes optimized for optical mapping in blood-perfused myocardium. *Heart Rhythm* **2007**, *4* (11), 1441-1451.
59. Hochbaum, D. R.; Zhao, Y.; Farhi, S. L.; Klapoetke, N.; Werley, C. A.; Kapoor, V.; Zou, P.; Kralj, J. M.; Maclaurin, D.; Smedemark-Margulies, N.; Saulnier, J. L.; Boulting, G. L.; Straub, C.; Cho, Y. K.; Melkonian, M.; Wong, G. K.-S.; Harrison, D. J.; Murthy, V. N.; Sabatini,

- B. L.; Boyden, E. S.; Campbell, R. E.; Cohen, A. E., All-optical electrophysiology in mammalian neurons using engineered microbial rhodopsins. *Nature Methods* **2014**, *11*, 825.
60. Flytzanis, N. C.; Bedbrook, C. N.; Chiu, H.; Engqvist, M. K. M.; Xiao, C.; Chan, K. Y.; Sternberg, P. W.; Arnold, F. H.; Gradinaru, V., Archaelhodopsin variants with enhanced voltage-sensitive fluorescence in mammalian and *Caenorhabditis elegans* neurons. *Nature Communications* **2014**, *5*, 4894.
61. Bando, Y.; Sakamoto, M.; Kim, S.; Ayzenshtat, I.; Yuste, R., Comparative Evaluation of Genetically Encoded Voltage Indicators. *Cell Reports* **2019**, *26* (3), 802-813.e4.
62. Xu, Y.; Zou, P.; Cohen, A. E., Voltage imaging with genetically encoded indicators. *Current Opinion in Chemical Biology* **2017**, *39*, 1-10.
63. Chen, G.; Zhang, Y.; Peng, Z.; Huang, D.; Li, C.; Wang, Q., Glutathione-capped quantum dots for plasma membrane labeling and membrane potential imaging. *Nano Research* **2019**.
64. Nag, O. K.; Stewart, M. H.; Deschamps, J. R.; Susumu, K.; Oh, E.; Tsytsarev, V.; Tang, Q.; Efros, A. L.; Vaxenburg, R.; Black, B. J.; Chen, Y.; O'Shaughnessy, T. J.; North, S. H.; Field, L. D.; Dawson, P. E.; Pancrazio, J. J.; Medintz, I. L.; Chen, Y.; Erzurumlu, R. S.; Huston, A. L.; Delehanty, J. B., Quantum Dot–Peptide–Fullerene Bioconjugates for Visualization of in Vitro and in Vivo Cellular Membrane Potential. *ACS Nano* **2017**, *11* (6), 5598-5613.
65. Barry, J. F.; Turner, M. J.; Schloss, J. M.; Glenn, D. R.; Song, Y.; Lukin, M. D.; Park, H.; Walsworth, R. L., Optical magnetic detection of single-neuron action potentials using quantum defects in diamond. *Proceedings of the National Academy of Sciences* **2016**, *113* (49), 14133-14138.
66. Chang, Y.-R.; Lee, H.-Y.; Chen, K.; Chang, C.-C.; Tsai, D.-S.; Fu, C.-C.; Lim, T.-S.; Tzeng, Y.-K.; Fang, C.-Y.; Han, C.-C.; Chang, H.-C.; Fann, W., Mass production and dynamic imaging of fluorescent nanodiamonds. *Nature Nanotechnology* **2008**, *3*, 284.

Chapter 2

Development of a single-particle spectrally-resolve microscope

This chapter describes the development, calibration and validation of a wide-field spectrally-resolve microscope, essential for high throughput QCSE measurements of individual particles. This microscope is heavily utilized for screening the performance of the nanosensors synthesized, and the results of screening will be presented in the next chapter. This chapter is a reprint of the original article published in *Proceedings of SPIE* 10352, 103520L (2017), titled “Development of a high throughput single-particle screening for inorganic semiconductor nanorods as neural voltage sensor” by authors: Y. Kuo, K. Park , J. Li, A. Ingargiola, J. Park, V. Shvadchak, S. Weiss. Reprinted with permission from SPIE.

Development of a High Throughput Single-Particle Screening for Inorganic Semiconductor Nanorods as Neural Voltage Sensor

Yung Kuo^a, Kyoungwon Park^a, Jack Li^a, Antonino Ingargiola^a, Joonhyuck Park^a, Shvadchak Volodymyr^b, Shimon Weiss^{*a,c,d}

^aDept. of Chemistry and Biochemistry, University of California, Los Angeles, 607 Charles E. Young Drive East, Los Angeles, CA, USA 90095

^bInstitute of Organic Chemistry and Biochemistry AS CR, Czech Republic, Prague 166-10

^cCalifornia NanoSystems Institute, 570 Westwood Plaza, Los Angeles, CA, USA 90095

^dDept. of Physiology, David Geffen School of Medicine at UCLA, 10833 Le Conte Avenue, 53-232 CHS, Los Angeles, CA, USA 90095

*sweiss@chem.ucla.edu; tel: 1-310-794-0093; fax: 1-310-267-4672; http://www.openwetware.org/wiki/Weiss_Lab

ABSTRACT

Monitoring membrane potential in neurons requires sensors with minimal invasiveness, high spatial and temporal (sub-ms) resolution, and large sensitivity for enabling detection of sub-threshold activities. While organic dyes and fluorescent proteins have been developed to possess voltage-sensing properties, photobleaching, cytotoxicity, low sensitivity, and low spatial resolution have obstructed further studies. Semiconductor nanoparticles (NPs), as prospective voltage sensors, have shown excellent sensitivity based on Quantum confined Stark effect (QCSE) at room temperature and at single particle level. Both theory and experiment have shown their voltage sensitivity can be increased significantly via material, bandgap, and structural engineering. Based on theoretical calculations, we synthesized one of the optimal candidates for voltage sensors: 12 nm type-II ZnSe/CdS nanorods (NRs), with an asymmetrically located seed. The voltage sensitivity and spectral shift were characterized *in vitro* using spectrally-resolved microscopy using electrodes grown by thin film deposition, which “sandwich” the NRs. We characterized multiple batches of such NRs and iteratively modified the synthesis to achieve higher voltage sensitivity ($\Delta F/F > 10\%$), larger spectral shift (>5 nm), better homogeneity, and better colloidal stability. Using a high throughput screening method, we were able to compare the voltage sensitivity of our NRs with commercial spherical quantum dots (QDs) with single particle statistics. Our method of high throughput screening with spectrally-resolved microscope also provides a versatile tool for studying single particles spectroscopy under field modulation.

Keywords: Quantum Dot, quantum confined Stark effect, nanorod, voltage sensor, action potential, neuron

1. INTRODUCTION

Membrane potential in live cells is an important driving force for numerous biological processes, especially for signal transmission in neurons and muscle cells¹. In a resting neuron, the membrane potential is created by gradients of ion concentrations, such as sodium and potassium concentrations, across the cell membrane that generate a potential difference of roughly -70 mV known as the resting potential. This resting potential can be perturbed upon receiving triggers and depolarizes to +40 mV as a subset of ion channels are triggered to open and allow ion flow across the membrane^{1, 2}. The membrane potential repolarizes as another subset of ion channels work to redistribute ions across the membrane and restore the resting potential. This process is called an action potential, which dictates signal transmission across a neuron, encodes information, and triggers chemical releases and complex biological processes³. In order to monitor action potentials and to understand

signal transmission in live neurons, tools need to be developed to allow non-invasive recording of such electrical events.

Electrical recording using the patch clamp technique has been well-developed for decades. This method allows direct recording of voltage across the cell membrane by using electrodes and a micropipette that forms an electrical seal to the cell membrane with a Giga-Ohm resistance, the so-called gigaseal, enabling measurements without leakage via biological media⁴. However, patch clamp not only requires expensive instruments such as micromanipulator and an amplifier, but also depends on the skill and experience of the user to produce a gigaseal. Regardless of these requirements, patch clamp is incapable of recording membrane potential at multiple sites in a small field-of-view, even with multi-pipette patch clamping, due to the bulkiness of the instrument. On the contrary, voltage sensitive dyes (VSDs) and genetically encoded voltage indicators (GEVIs) are less invasive alternatives for such recordings by translating electrical signals into fluorescence changes. VSDs and/or GEVIs operate via changes in absorption/emission spectra, change in quantum yield (QY), and/or change in absorption coefficients upon membrane depolarization due to Stark effect, electrochromism or quenching via electron transfer⁵. Therefore, with VSDs and/or GEVIs, membrane potentials can be monitored under a fluorescence microscope, which vastly simplifies the instrumentation and skills required for recording membrane potentials. However, in order to report membrane potential with high fidelity in live cells or tissues, fluorescent probes need to have high voltage sensitivity, fast response time, little perturbation to the membrane, low cytotoxicity, and photostability for long-term monitoring^{5, 6}. Despite considerable advances made with VSDs⁷⁻⁹ and GEVIs^{10, 11}, most of the existing probes still suffer from a subset of the problems listed above. Furthermore, VSDs and GEVIs have limited single molecule brightness, which prevents monitoring of membrane potential in sub-diffraction limit structures with super-resolution microscopy. We previously proposed an alternative voltage probe using semiconductor NPs^{12, 13}. Presumably, voltage sensing NPs (vsNPs) could enable single particle detection and neuroscience studies with higher spatial and temporal resolution while maintaining high fidelity.

Semiconductor NPs, or quantum dots (QDs), have been used as biological probes in various applications¹⁴. QDs have high brightness, highly functionalizable surface, engineerable emission wavelength and QY, negligible photobleaching, and manageable cytotoxicity after surface modification. QDs can operate as highly sensitive voltage probes due to the quantum confined Stark effect (QCSE), which causes change in absorption and emission spectra, QY, and fluorescence lifetime. Beside benefits listed previously, QDs have several advantages as voltage sensors: (1) high voltage sensitivity ($\Delta F/F$) by material engineering, (2) large spectral shift ($\Delta\lambda$) enabling ratiometric detection, (3) large lifetime change providing alternative detection scheme, (4) high brightness affording single particle detection and superresolution applications, (5) fast response time (\sim ns), and (6) large two photon absorption cross section allowing deep tissue imaging. In 1997, the QCSE in single QD was observed in cryogenic conditions¹⁵, and the possibility of using QDs as voltage sensors at room temperature was predicted based on the huge shift in emission energy under voltage. Theoretical^{12, 16} and experimental works^{13, 17} have examined the feasibility of using quantum dots or nanorods (NRs) with various band alignment, sizes, and materials as voltage sensors in neurons. The sensitivities of many of these NPs were calculated and/or experimentally inspected under voltage at the single particle level. Park et al¹² have predicted that type-II NRs, such as ZnSe/CdS will exhibit larger voltage sensitivity as compared to type-I CdSe NRs and that the longer the NRs are, the larger their voltage sensitivity is. However, they approximated the seeded NR (a “dot-in-rod” structure) with a single heterostructure. Synthesizing NRs with a single heterostructure would be impractical, as this would require an asymmetric tip growth. In this work, we synthesized type-II seeded ZnSe/CdS NRs using colloidal synthesis. Intrinsic to the synthesis of NRs, there will be inevitable sources of polydispersity. Firstly, it is difficult to control anisotropic growth to maintain high aspect ratio of NRs in this dimension. Most NRs synthesized in previous works^{18, 19} were longer (40- 100 nm), and the aliquots of shorter NRs at early stage of syntheses often have large distribution in aspect ratios. Secondly, synthesis of NRs with high monodispersity, i.e. narrow size distribution, is challenging especially when anisotropic growth is desired. Lastly, for a “dot-in-rod” type-II structure, the position of the dots in the rods^{18, 19} will have a distribution, resulting in distribution in voltage sensitivities. With all the challenges contributing to an inevitable distribution

in voltage sensitivity from NR to NR, even from the same synthesis in the same flask, single-particle statistics is needed for realistic evaluation of the voltage sensitivity. However, the *in vitro* screening method developed in the previous work¹³ for single particle screening had low throughput by design and could not screen large number of particles with significant statistics. Hence, we developed a high throughput methodology allowing investigation of spectral and emission intensity changes of hundreds of NPs under voltage in one field-of-view using a spectrally-resolved microscope. This method involves fabrication of improved microelectrodes¹⁷ to allow application of an electric field in the vertical direction, building and calibrating a spectrally-resolved microscope, and developing an automated program for analysis. With this method, we investigated two types of NPs, ZnSe/CdS NRs and CdSe/ZnS QDs, and tested their voltage sensitivities with respect to changes in fluorescence intensity ($\Delta F/F$) and changes in emission wavelength ($\Delta\lambda$).

2. MATERIALS AND METHODS

2.1. Nanoparticles

Powder of CdSe/ZnS QDs (ID: QSP-620-10) was provided from Ocean NanoTech LLC. ZnSe/CdS NRs were synthesized following previous protocols¹⁸ with small modifications. First, ZnSe QDs were synthesized following previous protocols¹⁸, and the synthesis was stopped when an absorption peak at 364 nm was observed. The ZnSe QDs were purified from excess ligands by 3 consecutive butanol precipitations. A clear solution of ZnSe QDs was obtained by dissolving the pellet in toluene. The concentration of ZnSe seeds was determined by the optical density (OD) at 364 nm using UV-VIS spectrometer and cuvette with 1 cm path length. We used the robotic synthesizer WANDA²⁰ at the Molecular Foundry, Lawrence Berkeley National Laboratory (LBNL) for the synthesis of ZnSe seeded CdS NRs with accurate control of reaction parameters. 24 units (OD*ml) of ZnSe seeds were dissolved in 960 mg octadecanethiol (ODT) and degassed to remove toluene. 270 mg CdO, 1305 mg octadecylphosphonic acid (ODPA), 360 mg hexylphosphonic acid (HPA), 13.5 g trioctylphosphine oxide (TOPO), and 180 mg hexadecylamine (HDA) were mixed and degassed at 100 °C under <50 torr for roughly 1 hr before heated to 230 °C under nitrogen to convert CdO. Further degas at 100 °C under <50 torr for more than 2 hrs was done before the solution of Cd precursors was transferred to WANDA. The ZnSe solution in ODT was heated to 50 °C and injected to the solution of Cd precursors at 330 °C. The NRs were grown at 320 °C for 900 s before the solution was cooled and quenched with 5 ml acetone. The information and transmission electron microscope (TEM) images of NPs used in this work are shown in Table 1.

2.2. Fabrication of microelectrodes

The microelectrodes were fabricated at the UCLA Nanoelectronics Research Facility. As shown in Figure 1, a No. 1 coverslip with a transparent electrode made of indium tin oxide (ITO) was purchase from Structure Probe Inc (product number: 06463-AB) as the substrate. A film of 500 nm SiO₂ insulating layer was deposited at 1.5 Å/s rate using e-beam deposition (CHA Mark 40). QDs or NRs were diluted in toluene and spin-coated on the SiO₂. A layer of polyvinylpyrrolidone (PVP) was introduced to prevent oxidation of the NPs by spin-coating of 5 % PVP solution in 1:1 methanol: deionized water (v/v). After checking the density of QDs or NRs under a wide-field microscope, substrates with low aggregation of NPs were used for further deposition of 500 nm SiO₂. 5 nm Cr and 100 nm gold electrodes were patterned with a shadow mask and deposited using e-beam deposition (CHA Mark 40) at 0.1 Å/s and 1.0 Å/s rate, respectively. The thickness of each layer was measured by a stylus profilometer (Veeco Dektak 8, Bruker). The thickness of the PVP layer was usually 500 nm \pm 50 nm.

2.3. Microscope setup and calibration

A wide-field microscope modified from Zeiss Axiovert S100TV, with home-built illumination and detection optics, was used. A 460 nm laser (Sapphire 460-10, Coherent) was focused onto the back focal plane of a 100x objective (Zeiss Plan-Neofluar, N.A. 1.3, oil immersion) to create wide-field illumination. The laser power was 0.7 mW before entering the objective. A 488 nm dichroic mirror (Di03-R488, Semrock) and a 530 nm long pass filter (E530LP, Chroma) were used. In the detection path, a removable prism could be inserted before an electron multiplied charged couple device (EMCCD) (Ixon DU-897, Andor) for dispersing single particle point

spread functions (PSFs) into spectrally resolved lines. Spectral measurements under electric field were done with a voltage amplifier (STM100, RHK Technology) connected to a function generator (FG2A, Beckman Industrial), which also triggers each frame of EMCCD via a LabView-controlled FPGA board for synchronization. In this work, a movie of 600 frames were recorded at 16 Hz, and a voltage of ~ 60 V (calculated based on the thickness and dielectric constants of each layer in the stack to generate 400kV/cm in the PVP layer) to all the even frames (denoted as V_{on}), while 0 V was applied to all the odd frames (denoted as V_{off}). Wavelength calibration for the prism dispersed image was done using fluorescent beads and QDs with well-known emission wavelength. The fluorescent beads used were FluoSphere (505/515) $0.1\mu\text{m}$ (Molecular Probes), FluoSphere (540/560) $0.1\mu\text{m}$ (Invitrogen), FluoSphere (535/575) $0.02\mu\text{m}$ (Molecular Probes), and FluoSphere (625/645) $0.2\mu\text{m}$ (Molecular Probes).

3. RESULTS

A stack of thin films was fabricated in order to apply electric field of magnitude close to that generated by an action potential and to allow fluorescence imaging using objectives with high numerical aperture (N.A.). The scheme and photograph are shown in Figure 1.

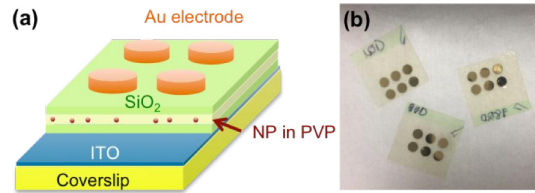


Figure 1. Microelectrodes which allow imaging of single particles under electric field using high N.A. objectives. (a) Schematics of the stack of thin films and microelectrodes fabricated for applying homogeneous electric field on NPs. (b) A photograph of the microelectrodes. The sizes of the coverslips are $18\text{ mm} \times 18\text{ mm}$.

In this work, we investigated two types of NPs and compared their performance as single particle voltage sensors. The information of the two NPs is summarized in Table 1. In each measurement, a wide-field image was taken to mark the location of each single particle, (x, y) (Figure 2a). For spectra measurements under alternating voltage, a movie was acquired while the prism was inserted to disperse each PSF. An example frame extracted from this movie is shown in Figure 2b. The dispersed PSFs span a range of few pixels in y direction and approximately 50 pixels in the x direction, (X_1, Y_1) to (X_{50}, Y_5) .

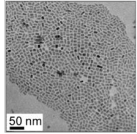
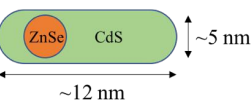
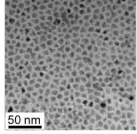

| Nanoparticles investigated | | | |
|---|---|---|---|
| ZnSe/CdS NRs | | CdSe/ZnS QDs | |
| Band alignment | type-II | Band alignment | type-I |
| Size | 5 nm (diameter) x 12 nm (length) | Size | 5 nm |
| TEM micrograph and Scheme | | TEM micrograph and Scheme | |
|  |  |  |  |

Table 1. Information of NPs investigated in this work.

To assign wavelengths to each pixel of the dispersed PSFs along the x direction, the equations below are used.

$$X_n = x + dx(x, \lambda) \quad (1)$$

$$Y_n = (y+s)/m \quad (2)$$

dx : shift of PSF locations in pixels in x direction after inserting the prism; λ : wavelength; s : shift of PSF locations in pixels in y direction after inserting the prism; m : magnification change after inserting the prism.

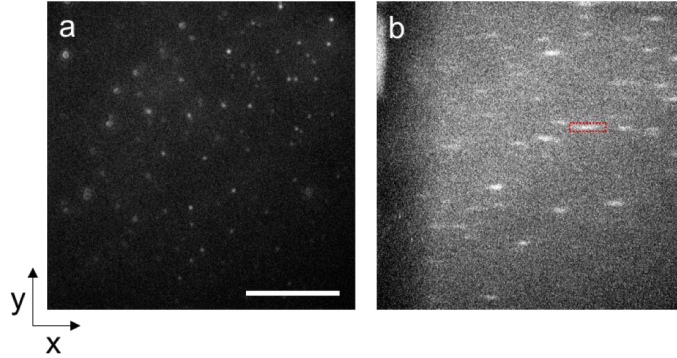


Figure 2. Example images for single particle measurements. (a) wide-field image to make locations of each NP. The scale bar is 10 μm . (b) a prism-dispersed image which allows extraction of wavelength information from each NP. The red box highlights a dispersed PSF of a single particle.

The parameters, s and m , are trivial numbers related to the instrument and remain constant after repetitive insertion and removal of the prism. dx is a function of the original wide-field location of a PSF and the wavelength of the PSF, so it can be acquired by fitting dx of PSFs of fluorescent beads with known emission wavelength. With the fitting results of dx from 4 types of fluorescent beads emitting at 515 nm, 560 nm, 575 nm, and 645 nm and QDs emitting at 750 nm, we were able to calibrate the wavelength for each pixel and use this calibration for subsequent measurements. The reproducibility of s , m and dx were tested after each removal and re-insertion of the prism. The error in dx was found to be smaller than 1 pixel, attesting the stability and reliability of our setup.

After 2D high-pass Gaussian filtering and background subtraction, spectral changes of individual NPs are extracted as function of the modulated voltage. Firstly, region of interests (ROIs) around each dispersed PSF are selected by detection of local maximums in a defined rectangle (red box in Figure 2b as an example). The wavelengths of each pixel in the ROIs are then assigned based on the method mentioned above. A stack of the dispersed PSFs from a single type-I CdSe/ZnS QD for 40 frames are shown in Figure 3a. The red and blue segments mark the V_{on} and V_{off} frames, respectively. In Figure 3a, displacements of the PSFs from frame to frame due to voltage are clearly observed. Secondly, the emission intensity as a function of frames is extracted by integrating the total counts in the ROI (Figure 3b), and a threshold to distinguish between blinking on and off states can be defined based on the intensity trace. To define the blinking threshold, the mean of the intensity trace is used initially, and a new threshold is defined as 0.8 standard deviation above the mean of the blinking-off states. This process is iterated for 5 times or until converged to finalize the blinking threshold. Third, the frames with integrated intensity above the blinking threshold are taken for calculating averaged spectra (Figure 3d). From this QD, we find a ~ 1.3 nm shift in emission wavelength ($\Delta\lambda$), a slight broadening in emission linewidth, and a change of 22.5% in total emission intensity ($\Delta F/F$) under voltage. Besides averaging, spectral peaks can also be extracted from individual frames. Figure 3c shows the peak wavelength as function of frames. The peak wavelength is calculated using the equation below.

$$\text{peak wavelength} = \frac{\sum_n (I(X_n) \times \lambda_n)}{\sum_n I(X_n)} \quad (3)$$

The clear displacements of the red dots (V_{on} frames) from the blue dots (V_{off} frames) confirm the spectral shifts from frame to frame due to voltage. A histogram of peak positions from individual frames that have intensity above the blinking threshold is shown in Figure 3e.

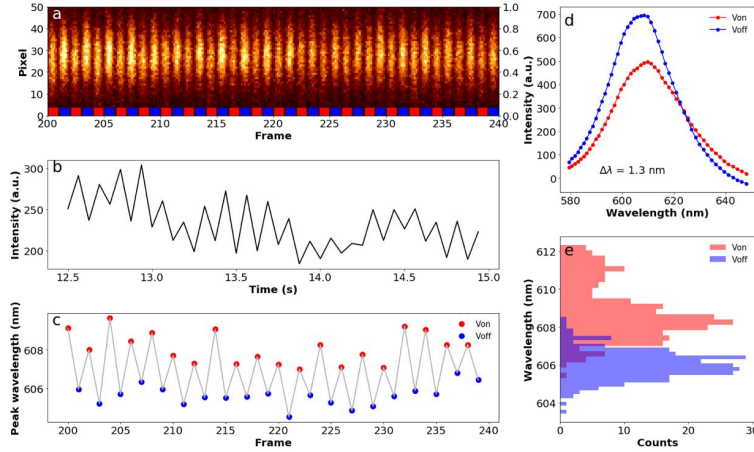


Figure 3. Example results of QCSE responses of a single type-I CdSe/ZnS QD. (a) A kymograph by stacking the dispersed PSFs from frame to frame for 40 frames. The red and blue segments mark the V_{on} and V_{off} frames, respectively. (b) Integrated intensity extracted from the selected ROI as function of time. (c) Peak position extracted by equation (3) as function of frame showing a clear shift from frame to frame due to voltage. Red and blue dots are peak position at V_{on} and V_{off} frames, respectively. (d) Averaged spectra from V_{on} (red) and V_{off} (blue) frames. Only the frames above the blinking threshold are used to calculate the averaged spectra. (e) Histograms of peak positions extracted from individual frames that have intensity above the blinking threshold. A clear separation of the two histogram shows spectral shift from this single particle under voltage.

We also studied the QCSE responses of type-II ZnSe/CdS NRs in the same fashion and obtained corresponding histograms of $\Delta F/F$ and $\Delta\lambda$ (Figure 4). Figure 4 shows that type-II NRs have a wide distribution of $\Delta\lambda$, and there is a significant population with large voltage sensitivity. Furthermore, Type-II NRs have both blue-shifted ($\Delta\lambda < 0$) and red-shifted ($\Delta\lambda > 0$) populations, while type-I QDs have mostly red-shifted population, as predicted previously by theoretical works^{12,13}.

4. DISCUSSION

We developed a high throughput methodology for QCSE response measurements at single particle level. This method allowed us to build statistically meaningful histograms in order to evaluate the performance of QDs or NRs with only few measurements. Figure 4 shows histograms of voltage sensitivity observables, $\Delta F/F$ and $\Delta\lambda$, for type-I CdSe/ZnS QDs and type-II ZnSe/CdS NRs. Since the NPs were spin-coated onto the substrate, and the electric field was not aligned with the long axes of NRs, we find a large population of NRs with small $\Delta F/F$

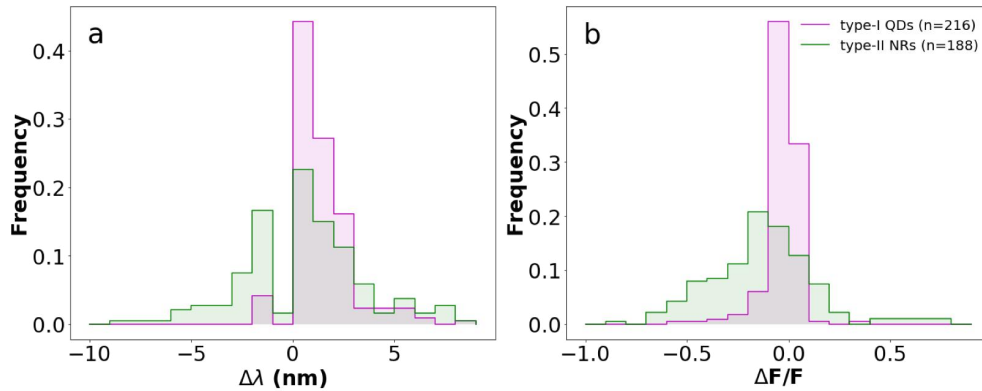


Figure 4. Histograms of single particle QCSE responses, $\Delta F/F$ and $\Delta\lambda$, of type-I QDs and type-II NRs. (a) Histogram of spectral shift, $\Delta\lambda$, of single NPs under voltage, extracted from Fig. 3d. (b) Histogram of change in emission intensity, $\Delta F/F$, of single NPs under voltage, extracted from Fig. 3d. Total numbers of NPs analyzed are 216 and 188 for type-I QDs and type-II NRs, respectively.

or $\Delta\lambda$. We attribute the large population of QDs / NRs with small $\Delta F/F$ or $\Delta\lambda$ to the random alignment between NRs and the electric field (only very few NRs are aligned with the field). In addition, the size inhomogeneity of NRs also contributes to the wide distribution of voltage sensitivities. However, a noticeable difference between the histograms of QDs and NRs is noticed. The NRs sample has a significantly larger population of nanoparticles that exhibit both large positive or negative $\Delta F/F$ (as compared to QDs) and positive (red shift) or negative (blue shift) $\Delta\lambda$. QDs, on the other hand, exhibit smaller and mostly negative $\Delta F/F$ and red-shifted only $\Delta\lambda$, as predicted by theory^{12, 13}.

The larger separation of excited charge carriers in the NRs can also be confirmed with fluorescence lifetime measurements, as shown in several works^{18, 21}. The longer fluorescence lifetimes of type-II NPs (tens of ns up to 100 ns) compared to type-I NPs confirm the decreased overlap integral of the electron and hole wavefunctions. Furthermore, the presence of both blue-shifted ($\Delta\lambda < 0$) and red-shifted ($\Delta\lambda > 0$) populations agrees with the theoretical prediction from asymmetric NRs by Park et al¹². The presence of both populations can be explained by the possibility of asymmetrically located seeds in rods in a type-II structure. Several works have shown that growth of seeded NRs is often anisotropic along the two growing axes^{18, 19}, and the seed is often located at $\sim 1/3$ of the NR length.

With this tool, we have screened two different batches of nanosensors. We expect to perform iterative optimization of our colloidal synthesis based on the results from these measurements. This spectrally resolved wide-field microscope, together with the microelectrode device, constitute a tool for high throughput spectral screening of single particle under modulated field.

ACKNOWLEDGEMENTS

We would like to thank Emory Chan for valuable discussion on NR syntheses and instruction on WANDA operation, Antonio Ingargiola for discussion on data analysis, and Max Ho and Wilson Lin for discussion on thin film fabrication. We thank Ocean Nanotech LLC for providing QDs at no cost. This research was supported by DARPA Fund #D14PC00141, by the European Research Council (ERC) advanced grant NVS #669941, and by the Human Frontier Science Program (HFSP) research grant #RGP0061/2015. Work at the Molecular Foundry was supported by the Office of Science, Office of Basic Energy Sciences, of the U.S. Department of Energy under Contract No. DE-AC02-05CH11231.

REFERENCES

- [1] Alberts, B.; Johnson, A.; Lewis, J.; Raff, M.; Roberts, K.; Walter, P., *Molecular Biology of the Cell*. 6th ed.; Garland science: New York, 2014; p 1464.
- [2] Hille, B., *Ion Channels of Excitable Membranes*. 3rd ed.; Sinauer Associates, Inc.: Sunderland, Massachusetts U.S.A., 2001.
- [3] Bean, B. P., The action potential in mammalian central neurons. *Nat Rev Neurosci* **2007**, *8* (6), 451-465.
- [4] Zhao, Y.; Inayat, S.; Dikin, D. A.; Singer, J. H.; Ruoff, R. S.; Troy, J. B., Patch clamp technique: Review of the current state of the art and potential contributions from nanoengineering. *Proceedings of the Institution of Mechanical Engineers, Part N: Journal of Nanoengineering and Nanosystems* **2008**, *222* (1), 1-11.
- [5] Kulkarni, R. U.; Miller, E. W., Voltage Imaging: Pitfalls and Potential. *Biochemistry* **2017**.
- [6] Chemla, S.; Chavane, F., Voltage-sensitive dye imaging: Technique review and models. *Journal of Physiology-Paris* **2010**, *104* (1), 40-50.
- [7] Loew, L. M., Design and Use of Organic Voltage Sensitive Dyes. In *Membrane Potential Imaging in the Nervous System: Methods and Applications*, Canepari, M.; Zecevic, D., Eds. Springer New York: New York, NY, 2011; pp 13-23.
- [8] Bradley, J.; Luo, R.; Otis, T. S.; DiGregorio, D. A., Submillisecond optical reporting of membrane potential in situ using a neuronal tracer dye. *The Journal of neuroscience : the official journal of the Society for Neuroscience* **2009**, *29* (29), 9197-9209.
- [9] Ebner, T. J.; Chen, G., Use of voltage-sensitive dyes and optical recordings in the central nervous system. *Progress in Neurobiology* **1995**, *46* (5), 463-506.

- [10] Akemann, W.; Mutoh, H.; Perron, A.; Park, Y. K.; Iwamoto, Y.; Knöpfel, T., Imaging neural circuit dynamics with a voltage-sensitive fluorescent protein. *Journal of Neurophysiology* **2012**, *108* (8), 2323.
- [11] Gong, Y.; Wagner, M. J.; Zhong Li, J.; Schnitzer, M. J., Imaging neural spiking in brain tissue using FRET-opsin protein voltage sensors. **2014**, *5*, 3674.
- [12] Park, K.; Weiss, S., Design Rules for Membrane-Embedded Voltage-Sensing Nanoparticles. *Biophysical Journal* **2017**, *112* (4), 703-713.
- [13] Park, K.; Deutsch, Z.; Li, J. J.; Oron, D.; Weiss, S., Single Molecule Quantum-Confined Stark Effect Measurements of Semiconductor Nanoparticles at Room Temperature. *ACS Nano* **2012**, *6* (11), 10013-10023.
- [14] Michalet, X.; Pinaud, F. F.; Bentolila, L. A.; Tsay, J. M.; Doose, S.; Li, J. J.; Sundaresan, G.; Wu, A. M.; Gambhir, S. S.; Weiss, S., Quantum Dots for Live Cells, in Vivo Imaging, and Diagnostics. *Science* **2005**, *307* (5709), 538.
- [15] Empedocles, S. A.; Bawendi, M. G., Quantum-Confined Stark Effect in Single CdSe Nanocrystallite Quantum Dots. *Science* **1997**, *278* (5346), 2114.
- [16] Marshall, J. D.; Schnitzer, M. J., Optical Strategies for Sensing Neuronal Voltage Using Quantum Dots and Other Semiconductor Nanocrystals. *ACS Nano* **2013**, *7* (5), 4601-4609.
- [17] Rowland, C. E.; Susumu, K.; Stewart, M. H.; Oh, E.; Mäkinen, A. J.; O'Shaughnessy, T. J.; Kushto, G.; Wolak, M. A.; Erickson, J. S.; L. Efros, A.; Huston, A. L.; Delehanty, J. B., Electric Field Modulation of Semiconductor Quantum Dot Photoluminescence: Insights Into the Design of Robust Voltage-Sensitive Cellular Imaging Probes. *Nano Letters* **2015**, *15* (10), 6848-6854.
- [18] Dorfs, D.; Salant, A.; Popov, I.; Banin, U., ZnSe Quantum Dots Within CdS Nanorods: A Seeded-Growth Type-II System. *Small* **2008**, *4* (9), 1319-1323.
- [19] Hewa-Kasakarage, N. N.; Kirsanova, M.; Nemchinov, A.; Schmall, N.; El-Khoury, P. Z.; Tarnovsky, A. N.; Zamkov, M., Radiative Recombination of Spatially Extended Excitons in (ZnSe/CdS)/CdS Heterostructured Nanorods. *Journal of the American Chemical Society* **2009**, *131* (3), 1328-1334.
- [20] Chan, E. M.; Xu, C.; Mao, A. W.; Han, G.; Owen, J. S.; Cohen, B. E.; Milliron, D. J., Reproducible, High-Throughput Synthesis of Colloidal Nanocrystals for Optimization in Multidimensional Parameter Space. *Nano Letters* **2010**, *10* (5), 1874-1885.
- [21] Li, J. J.; Tsay, J. M.; Michalet, X.; Weiss, S., Wavefunction engineering: From quantum wells to near-infrared type-II colloidal quantum dots synthesized by layer-by-layer colloidal epitaxy. *Chemical physics* **2005**, *318* (1-2), 82-90.

Chapter 3

Measurements of the quantum confined Stark effect of single semiconductor nanosensors

This chapter describes the synthesis of type-II ZnSe seeded CdS nanorods and the QCSE measurements and comparisons of a variety of nanosensors. This chapter is a reprint of the original article published in *ACS Photonics* in October 2018, titled “Characterizing the quantum-confined Stark effect in semiconductor quantum dots and nanorods for single-molecule electrophysiology.”, by authors: Y. Kuo, J. Li, X. Michalet, A. Chizhik, N. Meir, O. Bar-Elli, E. Chan, D. Oron, J. Enderlein, S. Weiss. DOI: 10.1021/acsp Photonics.8b00617. Reprinted with permission from *ACS Photonics* 5 (12), 4788-4800 (2018). Copyright 2018 American Chemical Society.

Characterizing the Quantum-Confined Stark Effect in Semiconductor Quantum Dots and Nanorods for Single-Molecule Electrophysiology

Yung Kuo,[†] Jack Li,[†] Xavier Michalet,[†] Alexey Chizhik,[‡] Noga Meir,[§] Omri Bar-Elli,[§] Emory Chan,^{||} Dan Oron,[§] Joerg Enderlein,[‡] and Shimon Weiss^{*,†,‡,§,||,△}

[†]Department of Chemistry and Biochemistry, University of California Los Angeles, Los Angeles, California 90095, United States

[‡]III. Institute of Physics–Biophysics, Georg-August-Universität, 37077 Göttingen, Germany

[§]Weizmann Institute of Science, Rehovot 76100, Israel

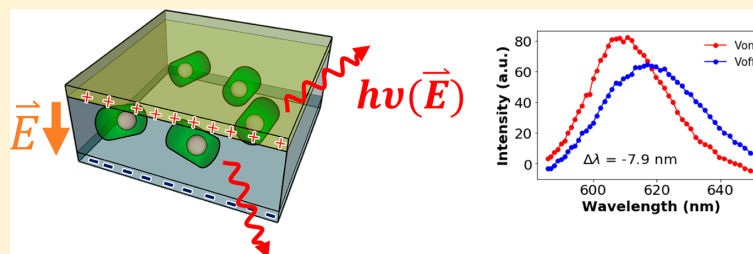
^{||}The Molecular Foundry, Lawrence Berkeley National Laboratory, Berkeley, California 94720, United States

[⊥]California NanoSystems Institute, University of California Los Angeles, Los Angeles, California 90095, United States

[#]Department of Physiology, University of California Los Angeles, Los Angeles, California 90095, United States

[△]Department of Physics, Institute for Nanotechnology and Advanced Materials, Bar-Ilan University, Ramat-Gan 52900, Israel

Supporting Information



ABSTRACT: We optimized the performance of quantum-confined Stark effect (QCSE)-based voltage nanosensors. A high-throughput approach for single-particle QCSE characterization was developed and utilized to screen a library of such nanosensors. Type-II ZnSe/CdS-seeded nanorods were found to have the best performance among the different nanosensors evaluated in this work. The degree of correlation between intensity changes and spectral changes of the exciton's emission under an applied field was characterized. An upper limit for the temporal response of individual ZnSe/CdS nanorods to voltage modulation was characterized by high-throughput, high temporal resolution intensity measurements using a novel photon-counting camera. The measured 3.5 μ s response time is limited by the voltage modulation electronics and represents \sim 30 times higher bandwidth than needed for recording an action potential in a neuron.

KEYWORDS: quantum-confined Stark effect, quantum dot, membrane potential, single molecule, voltage sensor, nanorod

Nanoparticles (NPs) with extremely bright fluorescence have found application in many biological and biophysical studies,^{1,2} such as single-particle imaging and tracking,^{3,4} single-particle sensors,^{2,5} and super-resolution microscopy.^{6,7} In particular, semiconductor quantum dots (QDs) have been used as biological probes in various applications, for example as labeling agents for long-term tracking of single molecules³ and as intracellular sensors for temperature,^{5,8} pH,⁹ etc. Within the past decade, QDs or nanorods (NRs) were also predicted theoretically and observed experimentally to report cellular membrane potential with exceptionally large sensitivities.^{10–14} With the versatile capabilities already shown and with some advanced engineering, QDs/NRs have great potential to become next-generation voltage nanosensors that enable membrane potential imaging

using single particles. In this work, we synthesized, characterized, and optimized QDs and NRs to exhibit enhanced quantum-confined Stark effect (QCSE) using a dedicated high-throughput single-particle screening approach.

As neurons transmit signals via electrical impulses generated by membrane potential modulations, two approaches are traditionally taken to monitor neural activities: (i) direct electrical recording or (ii) utilization of a sensor that transduces the electrical observables into other signals, such as fluorescence. Electrical monitoring involves the patch clamp technique or microelectrode arrays, which are both highly invasive and not suitable for simultaneous recording from the

Received: May 9, 2018

Published: October 15, 2018

large number of neuronal cells needed in order to study how neurons communicate within a network. These techniques are also inadequate to record signals from multiple nanostructures, such as synapses or dendritic spines, within a neuron due to space constraints. Many important brain functions such as transmission of signals, plasticity, learning, and memory^{15–18} are facilitated by complex electrical and chemical events in microscopic structures such as dendritic spines and synapses that have volumes smaller than 1 femtoliter¹⁷ and have extremely dynamic shapes and sizes.^{19–21} Studying local electrical signals from such small volumes requires the development of bright and noninvasive probes that have molecular dimensions (nm), thus allowing for high spatial resolution recording. Optical sensors such as voltage-sensitive dyes (VSDs)^{22–25} and genetically encoded voltage indicators (GEVIs)^{26–28} are examples of the second approach. VSDs and GEVIs can report on changes in membrane potential via changes in their absorption/emission properties.²⁹ Despite the advances made with VSDs, GEVIs, and their hybrids,^{29–33} they cannot monitor electrical events on the nanoscale with single molecules due to limited brightness. Additionally, most VSDs and GEVIs suffer from photobleaching, low voltage sensitivity, toxicity, and/or slow kinetics, and they can perturb membrane capacitance at high concentrations.

While organic dyes and fluorescent proteins may be further improved in the future, nanoparticles (NPs) could offer alternatives. For example, nitrogen-vacancy centers in nanodiamonds could report action potentials (APs) in a giant axon of *Myxicola infundibulum* (worm) via the optically detected magnetic resonance (ODMR) technique.³⁴ QDs can operate as voltage sensors³⁵ via photoinduced electron transfer or the QCSE.^{10,11,14} The physical origin of the QCSE lies in the separation of the confined photoexcited charges in the semiconductor QD or NR, creating a dipole that opposes the external electric field. This, in turn, leads to (red or blue) shifting of the absorption and emission edges that are accompanied by quantum yield (QY) and fluorescence lifetime changes, according to the Fermi golden rule. Therefore, QDs or NRs with sizable QCSE (at room temperature) that are properly inserted into the cell membrane could report on changes in membrane potential via a spectral shift, a change in the emission intensity, and/or a change in the excited state lifetime. QCSE-based QD/NR voltage sensors could also offer several advantages over existing voltage sensors based on organic dyes, fluorescent proteins, or their hybrid: they (1) have high voltage sensitivity (quantified as percent change in fluorescence intensity, $\Delta F/F$), (2) exhibit large spectral shifts ($\Delta\lambda$) enabling ratiometric detection, (3) exhibit changes in excited state lifetime (providing an alternative detection scheme), (4) have high brightness, affording single-particle detection and superresolution recording, (5) have a fast response time (\sim ns) based on QCSE, (6) have a highly functionalizable surface, (7) have emission wavelength and QY that can be engineered, (8) have negligible photobleaching, and (9) have low cytotoxicity (after surface modification). With the extremely fast response time, QDs/NRs will be capable of reporting and resolving the APs, which not only have fast dynamics (sub-ms) but also present in a wide range of frequencies and waveforms, especially in mammalian brains.^{38–43}

However, there are some challenges to overcome before QCSE-based QD/NR voltage sensors can achieve single-particle voltage imaging. First, the larger the QDs or the longer

the NRs, the larger their polarizability and hence their voltage sensitivities.^{10,13} However, for proper membrane potential reporting, the QDs/NRs need to be functionalized and inserted into the 4 nm thick cell membrane. Therefore, a trade-off between magnitude of the QCSE (increasing with NP size and dependent on materials) and ease of membrane insertion (decreasing with increasing NP size) is required. Previous work has shown that small (\sim 3 nm) spherical QDs can be encapsulated into liposomes⁴⁴ and short (<10 nm) NRs, functionalized with transmembrane peptides, can be inserted into both synthetic and cellular membranes.¹⁴ In this work, we characterize QDs/NRs with different materials, sizes, and bandgap alignments and assess the possibility of maximizing the voltage sensitivity of QDs/NRs with material and bandgap engineering without increasing their sizes. Second, QDs/NRs obtained by colloidal synthesis are inevitably polydispersed, especially when multiple materials or anisotropic growth (for NRs) is involved. The polydispersity among particles will introduce a large distribution in their voltage sensitivities, resulting in difficulties in evaluating the single-particle performance of these nanosensors using ensemble spectroscopic methods. These challenges need to be addressed *in vitro* before attempting to utilize QDs/NRs as single-particle voltage nanosensors in live neurons.

In this work, we addressed these challenges in several steps. First, we synthesized type-II ZnSe-seeded CdS NRs (Figure 1)

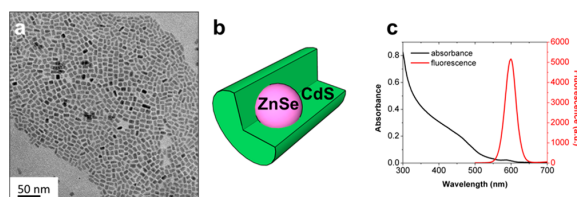


Figure 1. ZnSe/CdS NRs synthesized on WANDA. (a) TEM image of NRs. (b) Schematic of the asymmetric ZnSe/CdS dot-in-rod structure. (c) Absorption and emission spectra of NR (in toluene).

with enhanced QCSE while maintaining small dimensions. A type-II heterostructure increases charge separation by presenting spatially separated band energy minima for electrons and holes across the heterojunction and hence increases voltage sensitivity by QCSE without increasing the dimensions of NRs significantly. In addition, the dot-in-rod structure of the NRs, schematically shown in Figure 1b, is often asymmetric, creating an asymmetric charge separation and a linear dipole that screens the external field.⁴⁵ In previous theoretical work, type-II NRs were predicted to exhibit large voltage sensitivities,^{12,13} and NRs < 12 nm were shown to be easily inserted in membranes after surface functionalization.¹⁴ To address the second challenge, we developed a single-particle high-throughput screening assay, which enables iterative optimization of the synthesis. The screening was based on single-particle spectral shift ($\Delta\lambda$) and relative intensity change ($\Delta F/F$) observables and allowed for statistical evaluation of the properties of individual NRs randomly oriented in the electric field. This approach required (i) the fabrication of thin film microelectrodes that “sandwiched” NRs or QDs to allow application of a homogeneous electric field vertically; (ii) building a spectrally resolved wide-field single-molecule microscope; and (iii) implementing a code for automated data analysis. With this high-throughput *in vitro* screening

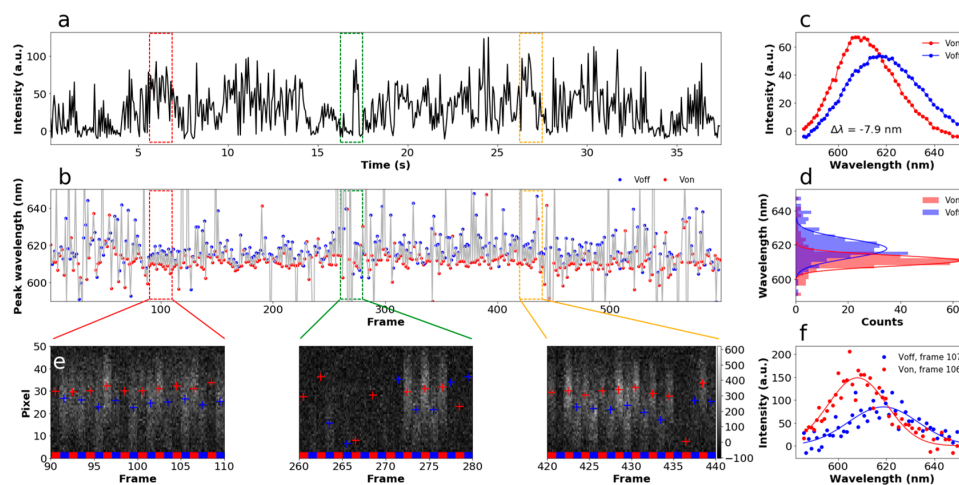


Figure 2. Example of QCSE measurements of a single ZnSe/CdS NR. (a) Intensity trace and (b) spectral peak position trace as a function of frames. (c) Averaged emission spectrum for V_{on} (red) and V_{off} (blue) frames. (d) Histograms of spectral peak positions from individual frames for V_{on} (red) and V_{off} (blue). Fitting the two peak position distributions to Gaussian functions (red and blue lines for V_{on} and V_{off} histograms, respectively) showed that the centers were shifted by 7.5 nm, consistent with the result in (c). (e) Images of the prism-dispersed PSFs from 20 consecutive frames (“zoom-ins”) at three different time periods of the background-subtracted movie. The prism-dispersed PSFs from different frames are stacked side by side, with the blue and red segments marking the V_{off} and V_{on} frames, respectively. The peak positions are marked with red and blue +’s for V_{on} and V_{off} frames, respectively. The clear “up” and “down” displacements between consecutively dispersed PSFs are strong evidence for spectral shifts (converted to nm by a calibration procedure detailed in Supporting Information-4). The intensity of each pixel in (e) is shown in grayscale with the color bar shown on the right. (f) Example of a V_{on} (red) and a V_{off} (blue) spectrum from one single frame and the Gaussian fits of both spectra (blue and red lines). The noisy spectra show that finding peak positions from single frames by fitting is not ideal and, hence, why, in this work, the peak positions are calculated using eq S3.

approach, we compared the voltage sensitivities and screened various QDs and NRs of different material compositions (including doping), sizes, and band alignments and acquired sufficient single-particle statistics for their assessment. Short type-II NRs exhibited larger single-particle voltage sensitivity than longer type-I NRs, validating the concept of QCSE optimization by proper engineering of the NP’s composition and bandgap/heterointerface alignment. This single-particle screen allowed us to systematically and iteratively improve and optimize the NRs’ synthesis and improve homogeneity, quantum yield, and voltage sensitivity. The improved NRs exhibited voltage sensitivity, characterized by an up to 69% relative intensity change ($\Delta F/F$) and a ~ 4.3 nm spectral shift ($\Delta\lambda$), fast response time (<3.5 μs , an upper bound set by the RC time constant of the voltage modulation electronics), and high brightness, affording facile single-particle detection.

RESULTS

Nanorod Synthesis. Reaction parameters that allow precise control of anisotropic growth are critical for NRs of small size (~ 10 nm) as studied here. Poor control would yield NRs with low aspect ratio (hence more symmetric and with reduced QCSE).

Previous work reporting the synthesis of seeded ZnSe/CdS NRs focused on much longer NRs (40 to 100 nm).^{45,46} Simply quenching the reaction after a short amount of time usually yielded polydisperse distributions in the length and width of the NRs. For voltage sensing, shorter NRs are required due to the difficulty in inserting longer NRs (>12 nm) into the membrane.¹⁴ In order to determine the optimal synthesis parameters to obtain shorter NRs with high aspect ratio, and to precisely control reaction parameters, we used a high-throughput robot (WANDA⁴⁷) to systematically vary nano-

crystal growth parameters and screen for NRs with aspect ratios greater than 1.5 and lengths less than 12 nm. Our ~ 12 nm NR synthesis was based on a published procedure⁴⁵ with one modification: we used an alkanethiol in place of trioctylphosphine sulfide (TOPS) as the S precursor to control the reaction kinetics and to slow down the initial growth rate. Thiol precursors of different carbon chain length (from dodecanethiol to octadecanethiol) were tested. The injection and growth temperatures respectively were optimized in multiple optimization runs, in order to achieve slower initial growth rate and hence obtain shorter NRs. The transmission electron microscopy (TEM) image and absorption and emission spectra of the batch of ZnSe/CdS NRs with minimal size distributions and high aspect ratios revealed by TEM are shown in Figure 1. The synthesis was iteratively optimized using a series of screening assays including UV–vis, TEM, and QCSE measurements (details shown below) to yield NRs with a length of <12 nm and an aspect ratio of >1.5 while maintaining a large QCSE response. Particle size analysis of the best batch shown in Figure 1 reports an average of 11.6 ± 1.7 nm for the long NR’s axis, 6.8 ± 1.3 nm for the short axis (diameter) and an average aspect ratio of 1.9 ± 0.5 (see Figure S1).

Setup and Protocol for High-Throughput Single-Particle QCSE Measurements. To characterize NRs’ QCSE-induced spectral shift and intensity change upon external field modulation with sufficient statistical significance, a dedicated setup, methodology, and analysis had to be developed. To apply an electric field of magnitude similar to that generated by the depolarization phase of an AP, we followed the approach of a previous work³⁶ (with a few modifications) to fabricate microelectrode stacks using thin film depositions. The thin film electrodes “sandwiched” the NPs of interest and allowed

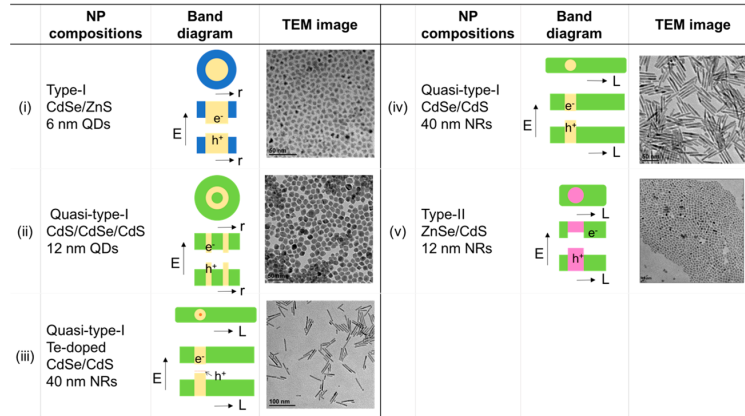


Figure 3. Composition, band diagram, and TEM images of NPs investigated in this study.

application of a homogeneous electric field while allowing imaging with a high numerical aperture (NA) objective. The stack was composed, from bottom to top, of an indium tin oxide (ITO)-coated coverslip, SiO_2 for insulation, NPs of interest, polyvinylpyrrolidone (PVP), SiO_2 for insulation, and a gold electrode (schematically shown in Figure S2). The NPs in such devices were stable for several weeks and up to 2 months after fabrication. NPs in older devices, such as lithographically patterned electrodes, tended to rapidly photobleach, possibly due to oxidation by exposure to air. Compared to the horizontally patterned electrodes, the vertical stack device suffers significantly fewer catastrophic arc discharge or meltdown events.¹¹ This “sandwich device” can be fabricated with either a large NP density (for ensemble measurements) or a smaller density (for single-particle measurements) by controlling the dilution and spin-coating conditions. We used low concentration to test and optimize our NRs as single-particle voltage nanosensors. A dedicated wide-field and spectrally resolved single-molecule microscope (inspired by previous work,⁴⁸ Figure S3) was designed (see Materials and Methods and Supporting Information for details). It allowed us to acquire modulated spectra of hundreds of individual single NPs per measurement while applying voltage alternating from frame to frame. Briefly, the camera acquisition was synchronized to a modulated voltage source that was applied to the test device, creating an electric field alternating from 0 kV/cm (V_{off}) to 400 kV/cm (V_{on}) in consecutive frames. The fluorescence emitted by individual NRs was spectrally dispersed by an Amici prism inserted in the detection path and imaged by a camera. Movies of 600 frames (300 modulations periods; frame rate at 16 Hz) were recorded for all samples.

To analyze the QCSE of single NRs, the spectrally dispersed point spread functions (PSFs) of individual NRs were selected from the mean frame of the entire movie using an algorithm for automatic PSF detection (described in Supporting Information-5), and the following analysis was performed only on the selected NRs. Wavelength calibration for each pixel was performed according to the protocol described in Supporting Information-4, allowing the accurate extraction of the (calibrated) spectrum for each NR, anywhere in the field of view. Thus, the spectrum, the integrated intensity, and the peak wavelength for each NR in each frame could be automatically derived.

An example of a single ZnSe/CdS NR QCSE analysis is shown in Figure 2. The intensity time trace and extracted spectral peak positions of a single NR are shown in Figure 2a and b, respectively. The red and blue dots in Figure 2b respectively highlight the spectral peak positions during frames with (V_{on}) or without (V_{off}) applied voltage. Clear fluctuations of intensity or peak wavelength from frame to frame due to voltage modulation can be observed. While some NRs showed clear “on” and “off” blinking states that can be discriminated by an intensity threshold, this NR is an example of the subpopulation that does not show clear “on” and “off” blinking states (the histogram of total counts from individual frames is shown in Figure S5-2a). Therefore, a “burst analysis” (details described in Supporting Information-5) instead of applying a blinking threshold was implemented for further analysis to avoid the associated bias. For this NR, the averaged emission spectrum at 400 kV/cm is blue-shifted by 7.9 nm (Figure 2c), the fwhm of the emission spectrum is narrowed by 6 nm (Figure S5-2b), and the integrated intensity is increased by 7% ($\Delta F/F$) with respect to the spectrum in the absence of applied field. This blue shift and increased intensity are consistent with the NR’s predicted type-II band structure.^{11,13} To get a preliminary estimation of the NPs’ voltage sensitivities, we implemented an automatic algorithm to calculate the averaged emission intensity change ($\Delta F/F$) and spectral shifts ($\Delta\lambda$) (details described in Supporting Information-5) using the equations below:

$$\langle \Delta F/F \rangle = \frac{\langle F_j^{V_{\text{on}}} \rangle_{F_j > \text{th}} - \langle F_j^{V_{\text{off}}} \rangle_{F_j > \text{th}}}{\langle F_j^{V_{\text{off}}} \rangle_{F_j > \text{th}}} \quad (1)$$

$$\langle \Delta\lambda \rangle = \langle \lambda_j^{V_{\text{on}}} \rangle_{F_j > \text{th}} - \langle \lambda_j^{V_{\text{off}}} \rangle_{F_j > \text{th}} \quad (2)$$

where F is the fluorescence intensity and λ is the peak wavelength. V_{on} and V_{off} denote the frames with (V_{on}) or without (V_{off}) applied voltage, respectively, and th notes the blinking threshold. The histograms of single-particle $\Delta F/F$ and $\Delta\lambda$, calculated using eqs 1 and 2, for all the NPs listed in Figure 3 are shown in Figure S5-3. In Figure S5-3, we found that the majority (~80%) of type-II NRs (sample (v)) have voltage responses ($n = 190$), and the magnitudes of these averaged voltage responses, expressed in $\Delta F/F$ and $\Delta\lambda$, are much larger than that of type-I QDs (sample (i)).

Clear spectral shifts between consecutive frames due to field modulation can also be seen in this NR. In Figure 2e, the spectrally dispersed PSFs between consecutive frames show clear displacements, which are converted to wavelength shifts as described in SI-5. Clear blinking “off” states are also seen in the frames missing clear dispersed PSFs (for example frames 260–271 in the second panel). The histograms of spectral peak positions (Figure 2d) from individual frames, calculated using eq S3, show a large separation of 7.5 nm between the V_{on} and V_{off} frames, which is consistent with the peak shift found in the averaged spectra. The clear separation between the two histograms of peak positions from single V_{on} and V_{off} frames also shows that the spectral shift can be detected from single frames without averaging.

As seen in Figure 2, the fluorescence from a single NP exhibited intermittency (blinking), and in the blinking “on” states, there is a wide distribution in fluorescence intensity (F) and wavelength (λ) even in the absence of voltage (see Figure 2a and b for examples). The wide distributions are primarily due to the relatively slow acquisition rate compared to the blinking rate and possibly due to local charge accumulations, ionization, and spectral diffusion. As a result, for all NPs, $\Delta\lambda$ and $\Delta F/F$ are often not constant throughout the acquisition period but rather appear as “bursts” of large responses following periods of small or noisy responses. The intermittent voltage responses, or “bursts”, were shown to coincide with blinking periods when recorded under a faster frame rate (Supporting Information-5), which shows that blinking is the major cause of intermittent voltage responses. While introducing a blinking threshold could allow extracting the voltage sensitivities, $\Delta\lambda$ and $\Delta F/F$, from only the blinking “on” states, the blinking threshold inevitably creates bias when the “on” and “off” states are not clearly separated, as shown in Figure 2a and Figure S5-2a. Instead, we applied a “burst analysis” to extract large responses, $\Delta F/F$ or $\Delta\lambda$, from time windows of eight or more consecutive frames without applying a binary discriminating threshold. Details for the burst search algorithm are given in Supporting Information-5. Briefly, the $|\Delta F/F|^2$ and the $|\Delta\lambda|^2$ trace (i.e., the “score²” trace) were first calculated between neighboring frames. A “burst” was identified when eight (time threshold) or more consecutive frames had an averaged $|\Delta F/F|^2$ or $|\Delta\lambda|^2$ larger than the score threshold, defined as the 50% percentile of the moving averaged “score²” trace with a window of eight frames. The correlation between the $\Delta\lambda$ and $\Delta F/F$ was small; therefore the burst search was applied separately to $\Delta\lambda$ and $\Delta F/F$ traces. The reasons for small correlations between $\Delta\lambda$ and $\Delta F/F$ are further studied and discussed below. Example $\Delta F/F$ and $\Delta\lambda$ traces from the same particle with identified bursts are shown in Figures S5-6 and S5-7, respectively. After applying the burst search algorithm to all traces from all NPs, the histograms of $\Delta\lambda$ and $\Delta F/F$ of individual “bursts” per NP type are plotted in Figure 4.

Single-Particle QCSE Results. With the setup and analysis for high-throughput QCSE measurements described above, we measured QCSE responses of five different types of NPs and built single-particle histograms to compare the voltage sensitivities, $\Delta\lambda$ and $\Delta F/F$, between NPs with different shapes, sizes, and band alignments. Figure 3 summarizes the properties of the NPs measured in this work, including (i) 6 nm type-I CdSe/ZnS QDs; (ii) 12 nm quasi-type-I CdS/CdSe/CdS QDs;⁴⁹ (iii) 40 nm quasi-type-I Te-doped CdSe/CdS NRs; (iv) 40 nm quasi-type-I CdSe/CdS NRs; and (v) 12

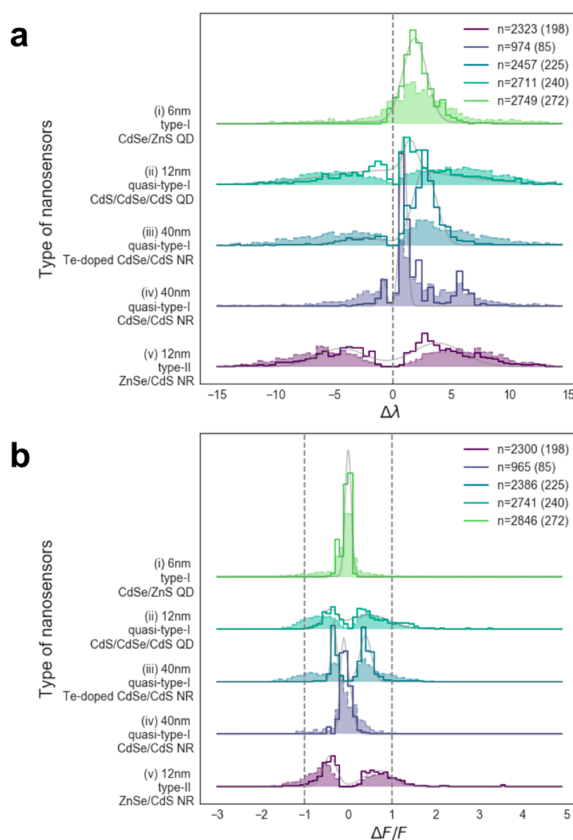


Figure 4. Histograms of (a) $\Delta\lambda$ and (b) $\Delta F/F$ extracted from bursts from five types of NPs described in Figure 3. The number of bursts (n) and number of NPs (number in parentheses) in each histogram are shown in the legends. The solid lines are the histogram weighted by the total intensity counts during each burst, and the shaded areas with dashed lines are the histogram without any weight. Type-II NRs exhibit the largest voltage sensitivities, with positive and negative $\Delta F/F$ and $\Delta\lambda$ responses. The gray lines show the fits of the distributions to a sum of two Gaussians.

nm type-II ZnSe/CdS NRs. Figure 4 shows the histogram of single-particle voltage sensitivities ($\Delta\lambda$ and $\Delta F/F$ from individual “bursts”) measured from these samples. Sample (i) is the typical type-I QDs that are commercially available, in which both the excited hole and electron reside in the CdSe core. Sample (ii) is a core–shell–shell spherical QD, in which the excited hole resides in a shell-shaped quantum well in the CdSe layer, and the excited electron delocalizes across the entire QD. This QD was reported to have suppressed blinking and near-unity QY.⁴⁹ Samples (iii) and (iv) are quasi-type-I NRs with and without Te doping in the CdSe core, which forms a trap for excited holes.⁵⁰ The Te-doped 40 nm CdSe/CdS NRs (sample (iii)) have on average one atom of Te in the CdSe core.

QCSE responses of type-I and type-II NPs are clearly distinct, as shown in Figure 4. Type-I QDs exhibit mostly red shifts ($\Delta\lambda > 0$) under electric field (samples (i)–(iv)), while 47% of bursts from type-II NRs exhibit blue shifts and 53% exhibit red shifts (samples (v), dashed line in Figure 4a). Type-I QDs exhibit very small negative $\Delta F/F$ (samples (i) in Figure 4b); that is, they decrease in intensity under an electric field,

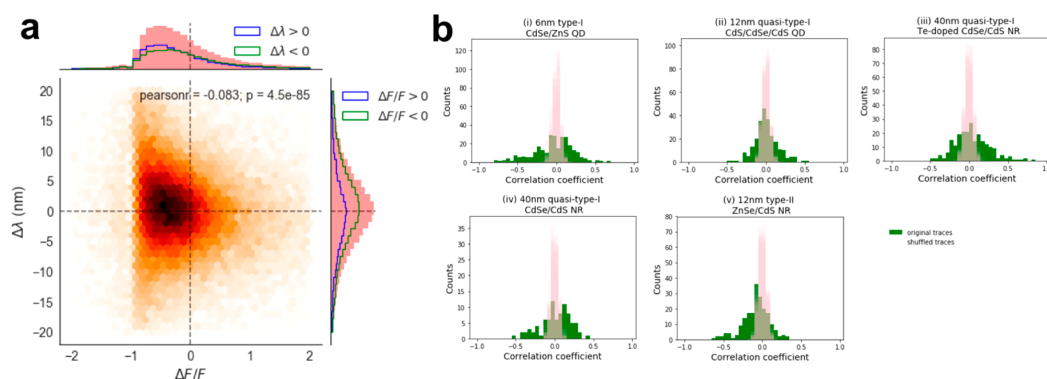


Figure 5. (a) 2D histogram of $\Delta F/F$ and $\Delta\lambda$ constructed from individual modulation cycles from 125 type-II ZnSe/CdS NRs (sample (v)) each contributing ~ 450 modulation cycles on average, including blinking “off” states. The distributions of $\Delta F/F$ and $\Delta\lambda$ are shown on the top and right panel, respectively. We note that this histogram includes all data points including blinking “off” states and therefore is different from the distribution shown in Figure 4, which shows only data points from “bursts”. Within the top (or the right) panel, the histograms of subpopulations, $\Delta\lambda$ (or $\Delta F/F$) > 0 and $\Delta\lambda$ (or $\Delta F/F$) < 0 , are plotted as the blue and green lines, respectively. (b) Histograms of Pearson’s correlation coefficients extracted from individual NPs for each type of NP (green). The distributions are compared to the distributions of Pearson’s correlation coefficients calculated between the same $\Delta F/F$ traces and 10 randomly shuffled $\Delta\lambda$ traces (pink, serving as controls).

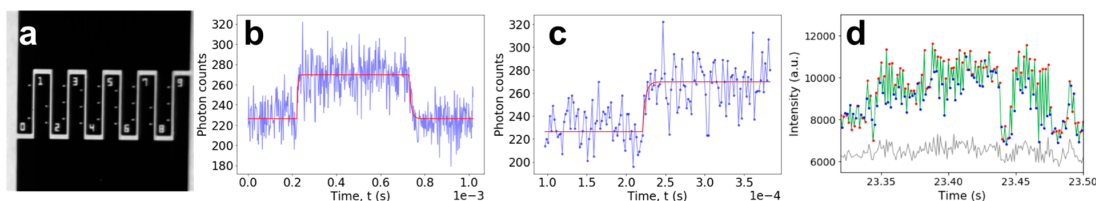


Figure 6. Temporal response of a single type-II NR (sample (v)). (a) Image of the lithographically patterned microelectrode (with $2\ \mu\text{m}$ gap) used in this experiment. (b) Accumulated photon counts from one single NR (from an acquisition of 269 s, blue) as a function of photon arrival time with respect to the voltage trigger. The time bin is $2\ \mu\text{s}$, and the modulation frequency was 1 kHz. The red line is a fit to the photon count trace with eq 3 to extract time constants. (c) Zoom-in on the rising edge in (b), from which the fit (red line) yields a response time of $3.5\ \mu\text{s}$. (d) Single type-II NR response recorded using a spectral splitting dual-view setup (details shown in Supporting Information) at 1 kHz frame rate with alternating applied voltage at 500 Hz. The green trace is the integrated emission intensity from a single NR from the two dual-view channels. The red and blue dots mark the intensity extracted from the V_{on} and V_{off} frames, respectively. The gray line is the sum of the backgrounds extracted locally from pixels near the NR in the two channels.

while 43% of bursts from type-II NRs exhibit positive $\Delta F/F$ and 57% exhibit negative $\Delta F/F$ (samples (v), dashed line in Figure 4b). We note that in the case of decreased intensity by voltage modulation the intensity counts can only decrease to 0 in theory; that is, $\Delta F/F$ has a lower bound of -1 . The bursts that showed $\Delta F/F < -1$ (4.7% of bursts from type-II NR, dashed line in Figure 4b) are due to the events with extremely low counts, resulting in occasional fluctuations below 0 after background subtraction. Therefore, to avoid these events from biasing the distributions of $\Delta F/F$ s and $\Delta\lambda$'s, histograms of both $\Delta F/F$ and $\Delta\lambda$ bursts weighted by the total intensity counts within the bursts are also plotted in Figure 4. Bursts with higher intensity counts have higher signal-to-noise ratio (SNR), and therefore, weighting data points by total intensity counts puts emphasis on good SNR data points. As expected, the histograms weighted in this manner show almost no population with $\Delta F/F$ s < -1 . By fitting the weighted $\Delta\lambda$ distributions with a sum of two Gaussians, two populations centered at $-4.3 \pm 2.0\ \text{nm}$ (1 sigma from Gaussian fitting) and $3.8 \pm 2.2\ \text{nm}$ were found for type-II NRs (sample (v)), and only one major population centered at $1.9 \pm 1.0\ \text{nm}$ was found for type-I QDs (sample (i)) (gray lines in Figure 4a). For $\Delta F/F$ distributions, fitting the weighted $\Delta F/F$ histograms with a sum of two Gaussians yielded two populations centered at 69%

$\pm 32\%$ and $-42\% \pm 16\%$ for type-II NRs (sample (v)) and only one population centered at $0\% \pm 7\%$ for type-I QDs (sample (i)) (gray lines in Figure 4b).

In summary, the type-II NRs synthesized in this work, compared to type-I QDs or 40 nm quasi-type-I NRs, exhibit both signs (positive and negative) of $\Delta F/F$ and $\Delta\lambda$ and much larger absolute $\Delta F/F$ and $\Delta\lambda$ for both the positive and negative populations, which are characteristics of the type-II band alignment and asymmetrically located ZnSe seeds within the CdS NRs. The type-II NRs, with the largest voltage sensitivities among all NPs studied in this work and much smaller size compared to the quasi-type-I NRs, are the optimal voltage sensors among all NPs studied in this work. The average burst width, average burst number per particle, and fractional burst duration (with respect to the entire measurement duration) are shown in Figure S5-8. The distributions of $\Delta F/F$ and $\Delta\lambda$ found by burst search with different time thresholds were also studied and are shown in Figure S5-9. The distributions and averages of $\Delta F/F$ and $\Delta\lambda$ are not affected by the time threshold from 8 frames to 16 frames, and the absolute values of $\Delta F/F$ and $\Delta\lambda$, for both positive and negative $\Delta F/F$ and $\Delta\lambda$, decrease as the time threshold increases to 64 frames due to averaging.

Dependence of NRs' Voltage Sensitivity on Their Orientation with Respect to the Electric Field. It is worth noting that in the “sandwich device” the orientations of NRs were random with respect to the direction of the applied electric field, which may broaden the distributions of voltage sensitivities. Therefore, the correlation between the QCSE spectral shifts and the orientations of the NRs was studied in a lower throughput manner using the interdigitated electrodes (Figure 6a). Randomly oriented type-II NRs (sample (v)) were positioned between the electrodes by drop-casting, and the orientations of the emission transition dipoles of NRs were visualized using defocused imaging.^{51,52} The orientations of emission transition dipoles of the NRs were recorded without applied field, and the emission spectra were measured in the presence and absence of applied field. The results (Supporting Information-6) show five NRs that displayed significant spectral shifts under an applied electric field. Similar results from single NRs composed of the same materials have also been shown recently.⁵³ In our experiment, despite the heterogeneity among the five type-II NRs (sample (v)) studied, a decreasing trend in the QCSE spectral shift could be seen as the angle between the transition dipole and the electric field increased from 0 deg to ~ 90 deg. With this experiment, we found that the emission dipoles of the short type-II NRs are linear and the degree of alignment between the NR and the applied field significantly affects the QCSE spectral shift. The voltage sensitivity diminishes when the NR is orthogonal to the applied field and is maximized when the two are parallel.

Correlation between $\Delta F/F$ and $\Delta\lambda$. To assess the amount of correlation between $\Delta F/F$ and $\Delta\lambda$ from these type-II NRs (sample(v)), $\Delta F/F$ and $\Delta\lambda$ of single modulation cycles and multiple cycle averages are plotted in a two-dimensional histogram (Figure 5a) and a scatter plot (Figure S5-5), respectively. The correlation between $\Delta F/F$'s and $\Delta\lambda$'s from many different particles was very small, as shown by the Pearson's correlation coefficient (-0.083 in Figure 5a and -0.19 in Figure S5-5). However, the correlations between $\Delta F/F$ and $\Delta\lambda$ from single particles are much larger. The $\Delta F/F$ - $\Delta\lambda$ Pearson's correlation coefficients were calculated for all types of NPs studied here, and the results are shown in Figure 5b. The distributions of the correlation coefficients (Figure 5b, green) are compared to negative controls (Figure 5b, pink), calculated as the correlation coefficients between the same $\Delta F/F$ trace and 10 randomly shuffled $\Delta\lambda$ traces ($\Delta\lambda$ distributions before and after shuffling are shown in Figure S5-10). The results show that 56% of type-II NRs (111 NRs out of 198 NRs) were negatively correlated, while 20% were positively correlated with the correlation coefficients at least one standard deviation away from the mean of the controls' correlation coefficients. For type-I QDs, 43% (117 QDs out of 272 QDs) were negatively correlated, while 40% were positively correlated. The results show that for the majority of NPs the $\Delta F/F$ and $\Delta\lambda$ from the same NPs were correlated within the acquisition time, meaning that an intensity change is usually accompanying a wavelength shift with proportional magnitude as predicted by the theory of QCSE. However, for some NPs, the correlation coefficients are positive instead of negative, opposing the prediction by the theory of QCSE. Meanwhile, the correlation between $\Delta F/F$ and $\Delta\lambda$ from different NPs shows that the sign and the magnitude of $\Delta F/F$ and $\Delta\lambda$ could not be predicted purely by the Stark effect, possibly due to different rates of charge trapping and

detrapping in the defect states, different degrees of surface passivation, and different local environments for different particles.

Stability of Single Type-II ZnSe/CdS NRs. As reported previously, QDs and NRs may experience changes in emission wavelength and blinking rate or photobleach after a long period of excitation in ambient air due to photochemical reactions (oxidation) of the surface of the nanocrystals.^{54–57} Therefore, the stability and voltage sensitivity of a single type-II NR (sample (v)) after a long period of excitation were also studied. The emission of a single, type-II NR was recorded using a dual-view spectral splitting setup while the camera recording was synchronized to the alternating applied electric field. The experimental detail and the results are shown in Supporting Information-6. The NR was continuously excited under ambient air, and the fluorescence was recorded for more than 8 h. The voltage sensitivities, including both $\Delta F/F$ and $\Delta\lambda$, despite some fluctuations due to blinking, remain nearly constant in the “blinking on” states for more than 4 h. Over time, the emission blue-shifted, and the NR entered more dark states, while the $\Delta\lambda$ decreased after 5 h. Although exposed to ambient air, this single NR exhibited excellent long life (>8 h) and voltage-sensing stability (~ 4 h). With improved coatings, even longer lifetimes are expected in the future.

Temporal Response of Single Type-II ZnSe/CdS NRs. To capture an AP, a membrane voltage sensor needs to have a sub-ms temporal response and a photon emission rate that allows recording it with sufficient SNR. In principle, the response time of NRs is on the order of their excited state lifetime, which is of the order of a few tens of nanoseconds. Bar-Elli et al. have shown that bright NRs (with a photon emission rate of $\sim 10^5$ Hz) could report voltage at 1 kHz via their spectral shifts, $\Delta\lambda$.⁵³ Here we set up to directly resolve the fluorescence intensity of individual NRs in response to voltage modulations with a custom wide-field photon counting camera (PCC) designed for time-resolved single-molecule imaging.^{58–62}

For this experiment, we deposited NRs in between lithographically patterned horizontal microelectrodes¹¹ with a $2\ \mu\text{m}$ gap (Figure 6a) and imaged them with the PCC while applying a modulated voltage on the electrodes. In contrast to conventional cameras, which accumulate photoelectrons generated during a preset integration time, read out the whole frame at fixed intervals, and suffer from readout noise, the PCC records each photon's arrival times with 156 ps temporal resolution and its location with $50\ \mu\text{m}$ spatial resolution, allowing to define arbitrary “frame” durations postacquisition, and is readout-noise-free. The maximum achievable frame rate is only limited on one hand by the signal and the desired SNR, but also by detector hardware constraints. In the device used for these experiments, the local (single NR) count rate was limited to ~ 40 kHz, while the global count rate (over the whole detector) was limited to ~ 2 MHz. For periodic processes such as those studied here, the availability of precise photon timing allows for accumulation of data from “frames” of duration much shorter than the above limits, the signal being now limited only by the total acquisition time. This allowed us to define frame rates comparable to the fastest complementary metal oxide semiconductor (CMOS) cameras but with single-photon sensitivity due to the absence of readout noise.

Type-II NRs in toluene were drop-casted on the microelectrodes and covered with PVP by spin-coating after toluene

evaporation. During the acquisition of photons by the PCC, 1 kHz square voltage modulation (at 50% duty cycle) was applied to create alternating electric fields alternating between 0 and 400 kV/cm. The triggers for the voltage modulations were simultaneously recorded by the PCC electronics and time stamped with an internal 50 MHz clock synchronized with that used to time-stamp detected photons. A total of 269 904 modulation periods were recorded for the single-particle intensity time trace shown in Figure 6b (total duration: 269 s). Figure 6a shows the electrodes used for this experiment imaged under a microscope with white light illumination. Figure 6b shows the accumulated photon counts after reassignment to a single modulation period. The results shown here represent an assessment of the time resolution when a measurement is not limited by the photon emission rates, for example, when an ensemble of oriented NRs respond collectively to the electric field. The $\Delta F/F$ of this specific NR was 19%.

To extract the temporal response of the NRs, we fitted the signal with the following model:

$$\begin{aligned} F(t < \mu_1) &= F_0 \\ F(\mu_1 < t < \mu_2) &= \Delta F(1 - e^{-(t-\mu_1/\tau_1)}) + F_0 \\ F(t > \mu_2) &= \Delta F(e^{-(t-\mu_2/\tau_2)}) + F_0 \end{aligned} \quad (3)$$

where F is the photon counts, which is a function of time, t . μ_1 and μ_2 are the fitted start time of the NR's intensity rise and decay, respectively. τ_1 and τ_2 are the fitted rise and decay time constant, respectively. F_0 represents the total photon counts in the absence of voltage, and ΔF is the change in photon counts under applied voltage with respect to F_0 . Therefore, $\Delta F/F$ equals $\Delta F/F_0$. Fitting the accumulated trace to eq 3 yielded time constants $\tau_1 = 3.5 \mu\text{s}$ and $\tau_2 = 8.8 \mu\text{s}$ (Figure 6b,c) for the rising and falling edges, respectively. The time constant of 3.5 μs is exactly the rise time of the measuring circuit (including the voltage amplifier and RC time constant of the micro-electrodes, Figures S8-1 and S8-2). The measured response time is therefore an upper bound imposed by the instrument and is ~ 30 times faster than what is needed to resolve an AP. We note that, however, in order to achieve kHz recording for APs using a single NR, the emission rate of this specific NR must exceed 30 kHz to overcome the shot noise to allow for observing a 19% change in intensity measured previously. In the current setup, the global count rate was limited by the PCC, and therefore a single NR emission rate of ~ 4 kHz was recorded, which was well below the saturation emission rate of the NRs. To demonstrate that these NRs could indeed report voltage at a 1 kHz frame rate with sufficient photon emission, the fluorescence from a single NR was recorded using a dual-view spectral splitting setup (details described in the Supporting Information) and an electron-multiplying charged couple device (EMCCD) with a small field of view (50×50 pixels). The results are shown in Figure 6d and Supporting Information-7. The NR exhibited alternating emission intensity and emission peak positions, in single 1 ms frames without averaging, as the applied electric field alternated between 0 and 300 kV/cm from frame to frame (Figure 6d). The result shows that the QCSE from a single NR could be observed using the spectral splitting setup at 1 kHz frame rate, which is consistent with the recently published work.⁵³ With proper functionalization for membrane insertion, a single NR could therefore be

potentially used for monitoring neural activities at ca. millisecond temporal resolution.

DISCUSSION

The optimal voltage sensors for single-particle electrophysiology need to have large voltage sensitivity while maintaining small sizes for membrane insertion. Using a high-throughput QCSE screening assay, we successfully demonstrated that the 12 nm long type-II NRs (sample (v)) exhibit much larger voltage sensitivities ($\Delta F/F$ and $\Delta\lambda$) compared to the other NPs studied in this work, including spherical QDs and 40 nm long quasi-type-I NRs. Type-II band alignment increases the separation of excited holes and electrons and hence QCSE, and therefore, by changing the material compositions of seeded NRs, the voltage sensitivities ($\Delta F/F$ and $\Delta\lambda$) can be increased without increasing the sizes of the NRs. Although the length of our type-II NR is longer than the thickness of a lipid bilayer membrane of ~ 4 nm, a method for functionalizing similar semiconductor NRs for vertical insertion into cellular membranes has been demonstrated experimentally.¹⁴ The voltage response of a type-II NR of similar length has also been calculated by Park et al.,¹³ using self-consistent Schrödinger–Poisson calculations for NRs inserted vertically across the membrane. The result showed that a 12 nm long type-II NR exhibits the largest voltage sensitivity ($\Delta F/F > 190\%/100$ mV) compared to shorter type-II NRs and type-I NRs with the same length. The experimental results presented here validate our previous predictions of the optimal materials and dimensions for NR voltage sensors.

One of the important characteristics required for membrane potential sensors is that they can report the physiological membrane potential, ranging from ~ -70 to 40 mV. Hence, a good membrane potential sensor must have asymmetric responses around zero field. In type-I spherical QDs, the excited dipole is small and isotropic due to quantum confinement in the spherical core (well), while in type-II NRs, excited carriers separate to different ends of the NRs, creating a linear dipole that partially screens the external electric field. While type-I QDs exhibit isotropic responses regardless of the field direction, the linear dipole in an NR results in asymmetric (positive and negative) $\Delta F/F$ and $\Delta\lambda$ responses depending on the direction of the electric field with respect to that of the dipole, as well as larger absolute values of $\Delta F/F$ and $\Delta\lambda$ under both signs.¹³ The results by burst search (Figure 4) and by comparing the $\Delta\lambda$ distributions with that from randomized wavelength (λ) traces (Figure S5-10) both show that type-II NRs exhibit $\Delta\lambda$ of both signs, while type-I QDs and quasi-type-I NRs exhibit primarily positive $\Delta\lambda$'s. The presence of both blue-shifting and red-shifting NR populations was consistent with theoretical predictions¹³ and attests to the type-II nature of these NRs and their asymmetric structure. Previous work has shown that seeded NR growth is often asymmetric and the seed is offset from the center of the NR by $\sim 1/3$ length of the NR⁴⁶ (as illustrated in Figure 1b), resulting in a spatially asymmetric distribution of carrier wave functions. These NRs, with both positive and negative $\Delta F/F$ and $\Delta\lambda$ due to random orientations in the electric field, are capable of reporting not only the field strength but also the field direction, as required for electrophysiology applications.

For type-II NRs, despite some heterogeneity and random orientations in the electric field, the average $\Delta F/F$ is very large (69% for positive $\Delta F/F$ and -42% for negative $\Delta F/F$, Figure 4), and the average $\Delta\lambda$ is $+3.8$ nm and -4.3 nm for an electric

field of 400 kV/cm, which is approximately 1.45 times larger than the electric field swing that will be created during firing of an AP in a neuron. The $\Delta F/F$ from the type-II NRs, even when divided by a factor of 1.45, is much larger than most commercially available VSDs (di-8-ANEPPS: 7.5% per 100 mV;⁶³ di-4-ANEPPS: 4.13% at 560 nm and 2.12% at 620 nm per 150 mV;⁶⁴ RH237: 2–3%;⁶⁵ JPW-6003: 11.9%⁶⁶) or GEVIs and has much higher signal-to-background ratio at the single-particle level.

One potential challenge for using these NRs as voltage sensors is that our QCSE screening results showed broad distributions of voltage sensitivities ($\Delta F/F$ and $\Delta\lambda$) for single type-II ZnSe/CdS NRs (sample (v)). Some NRs exhibited large spectral shifts (red shifts or blue shifts), while some exhibited small or no spectral shifts. Some NRs exhibited large changes (positive or negative) in emission intensity ($\Delta F/F$), while some exhibited small or no changes in $\Delta F/F$. The main reason for the wide distributions is the random orientations of NRs with respect to the electric field direction. The experimental results showed that the misalignment between the NRs and the electric field can diminish the voltage sensitivity and that the random orientations of NRs are responsible for the distributions of voltage sensitivities shown in Figure 4. In the “sandwich device”, the surface roughness of the substrate and the residuals, such as excess ligands, from the solution could cause the NRs to be not completely orthogonal to the vertical applied field and hence a distribution of spectral shifts offset from 0. Other possible causes of the wide distribution in voltage sensitivities are the heterogeneity (in sizes, shape, and QYs) among particles. However, with proper functionalization, we expect better control over the alignment between the NRs and the electric field in applications in lipid membranes, overcoming the issue of broad distributions of voltage sensitivities caused by random orientations of NRs as shown in this work.

Another consideration before using these NRs as voltage sensors is that, according to the theoretical studies by Park and Weiss,¹³ $\Delta F/F$ is dependent on the QY of the NP as well as on the excitation power (which in turn affects the QY via repartitioning between the exciton state and the positive trion state). For a 12 nm type-II ZnSe/CdS NR with 10% QY and 100% partitioning in the exciton state, $\Delta F/F$ is estimated to be >60%, while the same NR with 90% QY and 20% partitioning in the exciton state exhibits a $\Delta F/F$ of only ~5%.¹³ While a larger excitation power could allow a higher emission rate, it also decreases $\Delta F/F$ and the partitioning in the exciton state. A larger QY and less blinking allow the NRs to stay voltage sensitive for longer periods of time, but it also decreases $\Delta F/F$. A careful balancing of the trade-off between $\Delta F/F$, QY, and excitation power is therefore needed in order to record APs based on $\Delta F/F$ readings. As shown in Supporting Information-5, blinking is the major cause of the burst voltage sensitivities for these NRs, besides other minor factors such as local charging, ionization, and spectral diffusion. Increasing the QY will simultaneously reduce the intermittency in voltage sensitivities and increase emission rate. Although the existing NRs are not yet capable of reporting APs, by improving their QY and reducing their blinking, future generations of NRs could become membrane potential sensors for AP recordings.

An interesting finding unexpected by Park and Weiss is that the $\Delta F/F$ responses in the colloidal NRs are more complicated than the QCSE theory could predict. The $\Delta F/F$ caused by the intrinsic QCSE effect, without considering defect or charge

trapping states, is negatively correlated with the $\Delta\lambda$. However, all the NPs studied in this work showed a fraction of the population with positively correlated $\Delta\lambda$ and $\Delta F/F$. The reasons for positively correlated $\Delta\lambda$ and $\Delta F/F$ could be that $\Delta F/F$ was induced by a combined result of the applied electric field and local charges at surface and interface defects⁶⁷ since local charge states can create a local electric field¹⁰ and be modulated by the applied electric field.⁶⁸ Extrinsic charging/ionization at surface and interface defects⁶⁸ could further modulate blinking rates (and hence QY) and contribute to a positive correlation and/or no correlation. These effects will require further studies that correlate spectral, intensity, and lifetime measurements under an applied electric field and at different excitation powers (currently a topic of a follow-up project). Such measurements will allow us to decouple these contributions and further improve type-II NRs as voltage sensors (for example, by growing an additional layer of a high-bandgap coat). Indeed, the high-throughput screening method developed in this work is most suitable for these studies and will be used to minimize extrinsic effects and optimize the intrinsic QCSE signal.

Furthermore, the large $\Delta\lambda$ shift from the type-II NRs (relative to their emission spectral width) is amenable to ratiometric detection using a dual-channel spectral splitting setup^{11,53} as shown by the single NR recording results. $\Delta\lambda$ -based, ratiometric measurements are also immune to the complications associated with the intensity-based measurements described above. Together with further improvements in the sensors' design and performance and in their surface functionalization for membrane insertion,¹⁴ we envision their utilization for parallel, multisite, super-resolved electrophysiological recordings.

METHODS

Materials and Chemicals. All chemicals are used as purchased without further purification. Trioctylphosphine oxide (TOPO, 99%), octadecylphosphonic acid (ODPA), and hexylphosphonic acid (HPA) were purchased from PCI Synthesis. Tri-*n*-octylphosphine (TOP, 97%) was obtained from Strem Chemicals. Cadmium oxide (CdO), octadecylamine (ODA), hexadecylamine (HDA), octadecanethiol (ODT), and a 1.0 M diethylzinc (Zn(Et)₂) solution in hexanes were purchased from Sigma-Aldrich. Selenium powder (99.999%, 200 mesh) was purchased from Alfa Aesar.

Synthesis of ZnSe/CdS NRs. The detailed procedure for the synthesis of ZnSe QDs is described in Dorfs et al.⁴⁵ Briefly, a mixture of Se (63 mg), TOP (2 g), and diethyl zinc solution (0.8 mL, 1 M) was injected into degassed HDA (7 g) at 300 °C in an argon atmosphere. The reaction was kept at 265 °C until a sharp absorption peak around 360 nm was observed (~30 min after injection). After the reaction was cooled to room temperature, ZnSe QDs were purified three times by butanol/methanol precipitation and redissolved in toluene. The concentration of ZnSe in toluene was documented by the optical density (OD) at the absorption peak through a 1 cm cuvette. To synthesize CdS nanorods on ZnSe seeds using WANDA, CdO (270 mg), ODPA (1305 mg), HPA (360 mg), and TOPO (13.5 g) were first degassed at 100 °C under vacuum for 2 h, and the solution was heated to 230 °C until the CdO powder was fully dissolved, rendering a colorless solution. The solution was cooled to room temperature to add 180 mg of ODA, and the solution was degassed under vacuum at 100 °C for an additional 2 h. To prepare the S precursor

solution with ZnSe, 1440 mg of ODT was mixed with 36 units [OD (under 1 cm path length) \times mL] of ZnSe solution in toluene and heated under vacuum to remove the toluene and moisture. After degassing, both Cd precursor solution and S precursor with ZnSe were transferred under vacuum into a glovebox and dispensed gravimetrically into the 40 mL glass vials used as reaction vessels for the robot. The filled vials were loaded into the eight-reactor array of WANDA, an automated nanocrystal synthesis robot at the Molecular Foundry.⁴⁷ WANDA was used to run up to eight reactions in series with individually controlled heating/cooling profiles, stirring rate, injections, and aliquot schedules. Below is the description of an exemplary run. A 1.133 mL amount of a S/ZnSe solution (heated to 50 °C to prevent solidification) was injected into 15 615 mg of a Cd solution at 330 °C at a dispense rate of 1.5 mL/s. The temperature after injection was set at 320 °C for CdS NR growth. The heating was stopped 15 min after injection. To thermally quench the reaction, each reaction was then rapidly cooled to 50 °C using a stream of nitrogen, after which 5 mL of acetone was injected.

Postsynthesis Treatment of ZnSe/CdS NR. The obtained product was purified three times by methanol precipitation and toluene wash/centrifugation to remove free ligands and unreacted precursors, and a half monolayer of Zn was grown on the NRs' surface to introduce a metal-rich surface and coordinating ligands for further functionalization while maintaining the QY (30–40%) of these NRs during and after functionalization. Briefly, the purified ZnSe/CdS NRs were mixed with TOPO, oleic acid, and oleylamine. Following degassing, the reaction solution was heated to 250–280 °C under argon, and a TOP solution of zinc acetate or zinc undecylate was infused to the reaction flask with a needle mounted syringe. The reaction was stopped by removing the heating mantle 20 min later.

Wide-Field Spectrally Resolved Microscopy for QCSE Measurements. A wide-field microscope based on a Zeiss Axiovert S100TV, with home-built illumination and detection optics, was used. A 460 nm laser (Sapphire 460-10, Coherent) was focused onto the back focal plane of a 100 \times objective (Zeiss Plan-Neofluar, NA 1.3, oil immersion) to create wide-field illumination. The laser power was 0.7 mW before entering the objective. A 488 nm dichroic mirror (Di03-R488, Semrock) and a 530 nm long-pass filter (E530LP, Chroma Technologies) were used. In the detection path, a removable Amici prism could be inserted before the EMCCD (Ixon DU-897, Andor) for spectrally dispersing PSFs. For each QCSE measurement, a wide-field image without the Amici prism was first acquired to locate each NP. After inserting the prism, a movie was acquired while synchronously alternating the voltage applied to the sandwich device as described below. Alternating the voltage between 0 (V_{off}) and \sim 60 V (V_{on}) (variable depending on the final thickness of SiO₂, PVP, and SiO₂ layers in each device) was done by a function generator (FG2A, Beckman Industrial) creating a square wave at 8 Hz with 50% duty cycle and amplified with an additional offset of \sim 30 V (variable, to offset the voltage in half-periods to 0 V) by a high-bandwidth voltage amplifier (STM100, RHK Technology). The exact voltage applied for V_{on} was calculated to impose an electric field of 400 kV/cm in the PVP layer, assuming that the two SiO₂ layers and the one PVP layer were acting as three capacitors in series with dielectric constants of 3.9 and 2.33 for SiO₂ and PVP, respectively. Synchronization of the function generator and the EMCCD camera was

achieved by a programmable FPGA board (410-087, Digilent Inc.), which identified downward and upward zero-voltage crossings from the voltage generator and output TTL triggers at each crossing. As a result, two frames were recorded for each modulation period (one frame with voltage on, one frame with voltage off). Therefore, the resulting exposure time for each frame was 62.5 ms, and the frame rate was 16 Hz. All movies consisted of 600 frames. The algorithms for extracting QCSE parameters from these movies are described briefly below and in detail in [Supporting Information-5](#).

Wide-Field Photon Counting Microscopy Using a Photon-Counting Camera. An inverted wide-field microscope based on an Olympus IX71 with home-built excitation and detection optics was constructed. The excitation source was a 532 nm continuous wave laser (MGL-III-532-150 mW, Opto Engine). The laser was reflected by a 488/532 long-pass dichroic mirror (Omega Optical, transmission spectrum shown in [Supporting Information-9](#)) and focused onto the back focal plane of a 60 \times objective with an NA of 1.45 (Plan Apo TIRFM, Olympus) to create wide-field illumination. The excitation power was 1.9 mW before entering the objective. A 596/60 band-pass filter (S96DF60, Omega Optical) was used as the emission filter. Details for the hardware and software for the PCC are similar to those presented in Colyer et al.⁶² with the following differences: the detector comprised a GaAs photocathode cooled to 12 °C, with a quantum efficiency of \sim 30% in the detection wavelength range and a cross-strip anode for position sensing.⁶⁹ A dilute NR solution in toluene were drop-casted onto lithographically patterned electrodes, allowed to dry in air, and covered with a layer of PVP by spin-coating. After locating NRs in between the electrodes under a microscope, square wave voltage was applied via the same hardware used for QCSE measurements, while the emitted photons from NRs were detected and time-stamped by the PCC. Since the detector does not accumulate photons into “frames” but instead collects position and time information for each photon, synchronization of acquired photons was performed with the help of TTL triggers emitted by the voltage function generator, recorded as a separate time-stamped signal by the PCC electronics. Because of hardware limitations, only one of every eight trigger signals was recorded, which provided plenty of information for post-acquisition synchronization, each time-stamp being recorded with 20 ns resolution.

Fabrication of Sandwich Devices. An 18 mm \times 18 mm ITO-coated coverslip (#1.5, 30–60 ohms per square resistivity, SPI Supplies) was used as the starting substrate. A 500 nm layer of SiO₂ was deposited using e-beam evaporation (Mark 40, CHA) at a rate of 1.5 Å/s. The resistance of the substrate after SiO₂ deposition was tested and confirmed to be infinite using a multimeter. QDs or NRs in toluene were spin-coated on top of the SiO₂ layer, followed by spin-coating of 5% w/w PVP (40k Sigma-Aldrich) in a 1:1 methanol and H₂O solution to create a layer of PVP of 400–500 nm (measured by a stylus profilometer, Veeco Dektak 8, Bruker). Next, a second 500 nm SiO₂ layer was deposited on top of the PVP layer for insulation, followed by the second electrode deposition of a 5 nm Cr layer (0.1 Å/s) and a 100 nm Au layer (1 Å/s) using e-beam evaporation (Mark 40, CHA). The deposition of the second electrode was through a shadow mask that created six electrodes of 3 mm diameter on each coverslip. The thicknesses of each layer were measured with the stylus profilometer (Veeco Dektak 8, Bruker) after each deposition or

spin-coating to assist calculation of the voltage required for QCSE measurements.

■ ASSOCIATED CONTENT

📄 Supporting Information

The Supporting Information is available free of charge on the ACS Publications website at DOI: 10.1021/acsphotonics.8b00617.

NR size analysis, schematics of the “sandwich device”, schematics of the wide-field spectrally resolved microscope, wavelength calibration for the spectrally resolved microscope, data analysis for extracting QCSE results, dependences of QCSE on the orientations of NRs with respect to the electric field and the exposure time, single-particle recording at 1 kHz, characterization of the instrument's RC time constant, dichroic mirror's transmission spectrum (PDF)

■ AUTHOR INFORMATION

Corresponding Author

*E-mail: sweiss@chem.ucla.edu.

ORCID

Yung Kuo: 0000-0001-6704-6722

Noga Meir: 0000-0002-7467-373X

Dan Oron: 0000-0003-1582-8532

Joerg Enderlein: 0000-0001-5091-7157

Shimon Weiss: 0000-0002-0720-5426

Author Contributions

Y.K. conducted all experiments, analyzed all the data, and wrote the manuscript. J.J.L. and Y.K. synthesized ZnSe/CdS NRs using WANDA. ZnSe QDs were synthesized by J.J.L. X.M. built the optical setup with the PCC with the excitation source added by Y.K. X.M. and Y.K. performed related data analysis. A.C. performed defocused imaging experiments. N.M. synthesized the 40 nm NRs. E.C. contributed to NR syntheses and provided training for WANDA operation. D.O. provided two types of NRs. X.M., A.C., O.B., D.O., and J.E. contributed to discussions. S.W. and Y.K. designed the experiments. S.W., X.M., and D.O. helped in writing and revising the manuscript. All authors have given approval to the final version of the manuscript.

Notes

The authors declare no competing financial interest.

■ ACKNOWLEDGMENTS

We would like to thank Antonio Ingargiola and Kyoungwon Park for discussions on data analysis, Max Ho and Wilson Lin for discussions on thin film fabrication, Andrew Wang and Ocean Nanotech LLC for providing the CdSe/ZnS QDs at no cost, and Prof. Wan Ki Bae for providing the CdS/CdSe/CdS QDs. This research was supported by DARPA Fund No. D14PC00141, by the European Research Council (ERC) advanced grant NVS 669941, by the Human Frontier Science Program (HFSP) research grant RGP0061/2015, and by the BER program of the Department of Energy Office of Science, grant DE-FC03-02ER63421. Work at the Molecular Foundry was supported by the Office of Science, Office of Basic Energy Sciences, of the U.S. Department of Energy under Contract No. DE-AC02-05CH11231. This work was also supported by STROBE: A National Science Foundation Science & Technology Center under Grant No. DMR 1548924.

■ REFERENCES

- (1) Michalet, X.; Pinaud, F. F.; Bentolila, L. A.; Tsay, J. M.; Doose, S.; Li, J. J.; Sundaresan, G.; Wu, A. M.; Gambhir, S. S.; Weiss, S. Quantum Dots for Live Cells, in Vivo Imaging, and Diagnostics. *Science* **2005**, *307* (5709), 538.
- (2) Wen, S.; Xiaohua, Li; Huimin, M. Fluorescent probes and nanoparticles for intracellular sensing of pH values. *Methods Appl. Fluoresc.* **2014**, *2* (4), 042001.
- (3) Chang, Y.-P.; Pinaud, F.; Antelman, J.; Weiss, S. Tracking biomolecules in live cells using quantum dots. *J. Biophotonics* **2008**, *1* (4), 287–298.
- (4) Bhatia, D.; Arumugam, S.; Nasilowski, M.; Joshi, H.; Wunder, C.; Chambon, V.; Prakash, V.; Grazon, C.; Nadal, B.; Maiti, P. K.; Johannes, L.; Dubertret, B.; Krishnan, Y. Quantum dot-loaded monofunctionalized DNA icosahedra for single-particle tracking of endocytic pathways. *Nat. Nanotechnol.* **2016**, *11*, 1112.
- (5) Tanimoto, R.; Hiraiwa, T.; Nakai, Y.; Shindo, Y.; Oka, K.; Hiroi, N.; Funahashi, A. Detection of Temperature Difference in Neuronal Cells. *Sci. Rep.* **2016**, *6*, 22071.
- (6) Xu, J.; Tehrani, K. F.; Kner, P. Multicolor 3D Super-resolution Imaging by Quantum Dot Stochastic Optical Reconstruction Microscopy. *ACS Nano* **2015**, *9* (3), 2917–2925.
- (7) Yang, X.; Zhanghao, K.; Wang, H.; Liu, Y.; Wang, F.; Zhang, X.; Shi, K.; Gao, J.; Jin, D.; Xi, P. Versatile Application of Fluorescent Quantum Dot Labels in Super-resolution Fluorescence Microscopy. *ACS Photonics* **2016**, *3* (9), 1611–1618.
- (8) Jiang, X.; Qu, X.; Li, B. Q. In *Thermal mapping with quantum dots in a living cell*; 2016 IEEE 10th International Conference on Nano/Molecular Medicine and Engineering (NANOMED), Oct 30, 2016–Nov 2, 2016; 2016; pp 14–18.
- (9) Medintz, I. L.; Stewart, M. H.; Trammell, S. A.; Susumu, K.; Delehanty, J. B.; Mei, B. C.; Melinger, J. S.; Blanco-Canosa, J. B.; Dawson, P. E.; Mattoussi, H. Quantum-dot/dopamine bioconjugates function as redox coupled assemblies for in vitro and intracellular pH sensing. *Nat. Mater.* **2010**, *9*, 676.
- (10) Empedocles, S. A.; Bawendi, M. G. Quantum-Confined Stark Effect in Single CdSe Nanocrystallite Quantum Dots. *Science* **1997**, *278* (5346), 2114.
- (11) Park, K.; Deutsch, Z.; Li, J. J.; Oron, D.; Weiss, S. Single Molecule Quantum-Confined Stark Effect Measurements of Semiconductor Nanoparticles at Room Temperature. *ACS Nano* **2012**, *6* (11), 10013–10023.
- (12) Marshall, J. D.; Schnitzer, M. J. Optical Strategies for Sensing Neuronal Voltage Using Quantum Dots and Other Semiconductor Nanocrystals. *ACS Nano* **2013**, *7* (5), 4601–4609.
- (13) Park, K.; Weiss, S. Design Rules for Membrane-Embedded Voltage-Sensing Nanoparticles. *Biophys. J.* **2017**, *112* (4), 703–713.
- (14) Park, K.; Kuo, Y.; Shvadchak, V.; Ingargiola, A.; Dai, X.; Hsiung, L.; Kim, W.; Zhou, H.; Zou, P.; Levine, A. J.; Li, J.; Weiss, S. Membrane insertion of—and membrane potential sensing by—semiconductor voltage nanosensors: Feasibility demonstration. *Science Advances* **2018**, *4* (1), e1601453.
- (15) Nimchinsky, E. A.; Sabatini, B. L.; Svoboda, K. Structure and Function of Dendritic Spines. *Annu. Rev. Physiol.* **2002**, *64* (1), 313–353.
- (16) Hering, H.; Sheng, M. Dendritic spines: structure, dynamics and regulation. *Nat. Rev. Neurosci.* **2001**, *2* (12), 880–888.
- (17) Rochefort, N. L.; Konnerth, A. Dendritic spines: from structure to in vivo function. *EMBO Rep.* **2012**, *13* (8), 699–708.
- (18) Sala, C.; Segal, M. Dendritic Spines: The Locus of Structural and Functional Plasticity. *Physiol. Rev.* **2014**, *94* (1), 141.
- (19) Bonhoeffer, T.; Yuste, R. Spine Motility: Phenomenology, Mechanisms, and Function. *Neuron* **2002**, *35* (6), 1019–1027.
- (20) Yoshihara, Y.; De Roo, M.; Muller, D. Dendritic spine formation and stabilization. *Curr. Opin. Neurobiol.* **2009**, *19* (2), 146–153.
- (21) Dailey, M. E.; Smith, S. J. The Dynamics of Dendritic Structure in Developing Hippocampal Slices. *J. Neurosci.* **1996**, *16* (9), 2983.

- (22) Chemla, S.; Chavane, F. Voltage-sensitive dye imaging: Technique review and models. *J. Physiol.* **2010**, *104* (1), 40–50.
- (23) Fairless, R.; Beck, A.; Kravchenko, M.; Williams, S. K.; Wissenbach, U.; Diem, R.; Cavalie, A. Membrane Potential Measurements of Isolated Neurons Using a Voltage-Sensitive Dye. *PLoS One* **2013**, *8* (3), e58260.
- (24) Woodford, C. R.; Frady, E. P.; Smith, R. S.; Morey, B.; Canzi, G.; Palida, S. F.; Araneda, R. C.; Kristan, W. B.; Kubiak, C. P.; Miller, E. W.; Tsiens, R. Y. Improved PeT Molecules for Optically Sensing Voltage in Neurons. *J. Am. Chem. Soc.* **2015**, *137* (5), 1817–1824.
- (25) Wuskell, J. P.; Boudreau, D.; Wei, M.-d.; Jin, L.; Engl, R.; Chebolu, R.; Bullen, A.; Hoffacker, K. D.; Kerimo, J.; Cohen, L. B.; Zochowski, M. R.; Loew, L. M. Synthesis, spectra, delivery and potentiometric responses of new styryl dyes with extended spectral ranges. *J. Neurosci. Methods* **2006**, *151* (2), 200–215.
- (26) St-Pierre, F.; Chavarha, M.; Lin, M. Z. Designs and sensing mechanisms of genetically encoded fluorescent voltage indicators. *Curr. Opin. Chem. Biol.* **2015**, *27*, 31–38.
- (27) Han, Z.; Jin, L.; Platisa, J.; Cohen, L. B.; Baker, B. J.; Pieribone, V. A. Fluorescent Protein Voltage Probes Derived from ArcLight that Respond to Membrane Voltage Changes with Fast Kinetics. *PLoS One* **2013**, *8* (11), e81295.
- (28) St-Pierre, F.; Marshall, J. D.; Yang, Y.; Gong, Y.; Schnitzer, M. J.; Lin, M. Z. High-fidelity optical reporting of neuronal electrical activity with an ultrafast fluorescent voltage sensor. *Nat. Neurosci.* **2014**, *17* (6), 884–889.
- (29) Kulkarni, R. U.; Miller, E. W. Voltage Imaging: Pitfalls and Potential. *Biochemistry* **2017**, *56*, 5171.
- (30) Loew, L. M. Design and Use of Organic Voltage Sensitive Dyes. In *Membrane Potential Imaging in the Nervous System: Methods and Applications*; Canepari, M.; Zecevic, D., Eds.; Springer New York: New York, NY, 2011; pp 13–23.
- (31) Peterka, D. S.; Takahashi, H.; Yuste, R. Imaging voltage in neurons. *Neuron* **2011**, *69* (1), 9–21.
- (32) Gong, Y.; Wagner, M. J.; Zhong Li, J.; Schnitzer, M. J. Imaging neural spiking in brain tissue using FRET-opsin protein voltage sensors. *Nat. Commun.* **2014**, *5*, 3674.
- (33) Gong, Y.; Huang, C.; Li, J. Z.; Grewe, B. F.; Zhang, Y.; Eismann, S.; Schnitzer, M. J. High-speed recording of neural spikes in awake mice and flies with a fluorescent voltage sensor. *Science* **2015**, *350*, 1361.
- (34) Barry, J. F.; Turner, M. J.; Schloss, J. M.; Glenn, D. R.; Song, Y.; Lukin, M. D.; Park, H.; Walsworth, R. L. Optical magnetic detection of single-neuron action potentials using quantum defects in diamond. *Proc. Natl. Acad. Sci. U. S. A.* **2016**, *113* (49), 14133–14138.
- (35) Efros, A. L.; Delehanty, J. B.; Huston, A. L.; Medintz, I. L.; Barbic, M.; Harris, T. D. Evaluating the potential of using quantum dots for monitoring electrical signals in neurons. *Nat. Nanotechnol.* **2018**, *13* (4), 278–288.
- (36) Rowland, C. E.; Susumu, K.; Stewart, M. H.; Oh, E.; Mäkinen, A. J.; O’Shaughnessy, T. J.; Kushto, G.; Wolak, M. A.; Erickson, J. S.; Efros, A.; Huston, A. L.; Delehanty, J. B. Electric Field Modulation of Semiconductor Quantum Dot Photoluminescence: Insights Into the Design of Robust Voltage-Sensitive Cellular Imaging Probes. *Nano Lett.* **2015**, *15* (10), 6848–6854.
- (37) Nag, O. K.; Stewart, M. H.; Deschamps, J. R.; Susumu, K.; Oh, E.; Tsytarev, V.; Tang, Q.; Efros, A. L.; Vaxenburg, R.; Black, B. J.; Chen, Y.; O’Shaughnessy, T. J.; North, S. H.; Field, L. D.; Dawson, P. E.; Pancrazio, J. J.; Medintz, I. L.; Chen, Y.; Erzurumlu, R. S.; Huston, A. L.; Delehanty, J. B. Quantum Dot–Peptide–Fullerene Bioconjugates for Visualization of In Vitro and In Vivo Cellular Membrane Potential. *ACS Nano* **2017**, *11* (6), 5598–5613.
- (38) Bean, B. P. The action potential in mammalian central neurons. *Nat. Rev. Neurosci.* **2007**, *8* (6), 451–465.
- (39) Connors, B. W.; Gutnick, M. J. Intrinsic firing patterns of diverse neocortical neurons. *Trends Neurosci.* **1990**, *13* (3), 99–104.
- (40) Connor, J. A. Neural repetitive firing: a comparative study of membrane properties of crustacean walking leg axons. *J. Neurophysiol.* **1975**, *38* (4), 922.
- (41) Tateno, T.; Harsch, A.; Robinson, H. P. C. Threshold Firing Frequency–Current Relationships of Neurons in Rat Somatosensory Cortex: Type 1 and Type 2 Dynamics. *J. Neurophysiol.* **2004**, *92* (4), 2283.
- (42) Zhou, F. M.; Hablitz, J. J. Layer I neurons of rat neocortex. I. Action potential and repetitive firing properties. *J. Neurophysiol.* **1996**, *76* (2), 651.
- (43) Descalzo, V. F.; Nowak, L. G.; Brumberg, J. C.; McCormick, D. A.; Sanchez-Vives, M. V. Slow Adaptation in Fast-Spiking Neurons of Visual Cortex. *J. Neurophysiol.* **2005**, *93* (2), 1111.
- (44) Zheng, W.; Liu, Y.; West, A.; Schuler, E. E.; Yehl, K.; Dyer, R. B.; Kindt, J. T.; Salaita, K. Quantum Dots Encapsulated within Phospholipid Membranes: Phase-Dependent Structure, Photostability, and Site-Selective Functionalization. *J. Am. Chem. Soc.* **2014**, *136* (5), 1992–1999.
- (45) Dorfs, D.; Salant, A.; Popov, I.; Banin, U. ZnSe Quantum Dots Within CdS Nanorods: A Seeded-Growth Type-II System. *Small* **2008**, *4* (9), 1319–1323.
- (46) Hewa-Kasakarage, N. N.; Kirsanova, M.; Nemchinov, A.; Schmall, N.; El-Khoury, P. Z.; Tarnovsky, A. N.; Zamkov, M. Radiative Recombination of Spatially Extended Excitons in (ZnSe/CdS)/CdS Heterostructured Nanorods. *J. Am. Chem. Soc.* **2009**, *131* (3), 1328–1334.
- (47) Chan, E. M.; Xu, C.; Mao, A. W.; Han, G.; Owen, J. S.; Cohen, B. E.; Milliron, D. J. Reproducible, High-Throughput Synthesis of Colloidal Nanocrystals for Optimization in Multidimensional Parameter Space. *Nano Lett.* **2010**, *10* (5), 1874–1885.
- (48) Zhang, Z.; Kenny, S. J.; Hauser, M.; Li, W.; Xu, K. Ultrahigh-throughput single-molecule spectroscopy and spectrally resolved super-resolution microscopy. *Nat. Methods* **2015**, *12* (10), 935–938.
- (49) Jeong, B. G.; Park, Y.-S.; Chang, J. H.; Cho, I.; Kim, J. K.; Kim, H.; Char, K.; Cho, J.; Klimov, V. I.; Park, P.; Lee, D. C.; Bae, W. K. Colloidal Spherical Quantum Wells with Near-Unity Photoluminescence Quantum Yield and Suppressed Blinking. *ACS Nano* **2016**, *10* (10), 9297–9305.
- (50) Meir, N.; Martín-García, B.; Moreels, I.; Oron, D. Revisiting the Anion Framework Conservation in Cation Exchange Processes. *Chem. Mater.* **2016**, *28* (21), 7872–7877.
- (51) Patra, D.; Gregor, I.; Enderlein, J. Image Analysis of Defocused Single-Molecule Images for Three-Dimensional Molecule Orientation Studies. *J. Phys. Chem. A* **2004**, *108* (33), 6836–6841.
- (52) Patra, D.; Gregor, I.; Enderlein, J. Defocused imaging of quantum-dot angular distribution of radiation. *Appl. Phys. Lett.* **2005**, *87*, 101103.
- (53) Bar-Elli, O.; Steinitz, D.; Yang, G.; Tenne, R.; Ludwig, A.; Kuo, Y.; Triller, A.; Weiss, S.; Oron, D. Rapid Voltage Sensing with Single Nanorods via the Quantum Confined Stark Effect. *ACS Photonics* **2018**, *5*, 2860.
- (54) van Sark, W. G. J. H. M.; Frederix, P. L. T. M.; Van den Heuvel, D. J.; Gerritsen, H. C.; Bol, A. A.; van Lingen, J. N. J.; de Mello Donegá, C.; Meijerink, A. Photooxidation and Photobleaching of Single CdSe/ZnS Quantum Dots Probed by Room-Temperature Time-Resolved Spectroscopy. *J. Phys. Chem. B* **2001**, *105* (35), 8281–8284.
- (55) Yamashita, S.-i.; Hamada, M.; Nakanishi, S.; Saito, H.; Nosaka, Y.; Wakida, S.-i.; Biju, V. Auger Ionization Beats Photo-Oxidation of Semiconductor Quantum Dots: Extended Stability of Single-Molecule Photoluminescence. *Angew. Chem., Int. Ed.* **2015**, *54* (13), 3892–3896.
- (56) Lee Steven, F.; Osborne Mark, A. Brightening, Blinking, Bluing and Bleaching in the Life of a Quantum Dot: Friend or Foe? *ChemPhysChem* **2009**, *10* (13), 2174–2191.
- (57) Qin, H.; Meng, R.; Wang, N.; Peng, X. Photoluminescence Intermittency and Photo-Bleaching of Single Colloidal Quantum Dot. *Adv. Mater.* **2017**, *29* (14), 1606923.
- (58) Michalet, X.; Colyer, R. A.; Scalia, G.; Weiss, S.; Siegmund, O. H. W.; Tremsin, A. S.; Vallerger, J. V.; Villa, F.; Guerrieri, F.; Rech, I.; Gulinatti, A.; Tisa, S.; Zappa, F.; Ghioni, M.; Cova, S. New photon-

counting detectors for single-molecule fluorescence spectroscopy and imaging. *Proc. SPIE* **2011**, 8033, 803316.

(59) Michalet, X.; Colyer, R. A.; Antelman, J.; Siegmund, O. H. W.; Tremsin, A.; Vallerga, J. V.; Weiss, S. Single-quantum dot imaging with a photon counting camera. *Curr. Pharm. Biotechnol.* **2009**, *10* (5), 543–558.

(60) Tremsin, A. S.; Siegmund, O. H. W.; Vallerga, J. V.; Raffanti, R.; Weiss, S.; Michalet, X. High Speed Multichannel Charge Sensitive Data Acquisition System with Self-Triggered Event Timing. *IEEE Trans. Nucl. Sci.* **2009**, *56* (3), 1148–1152.

(61) Michalet, X.; Siegmund, O. H. W.; Vallerga, J. V.; Jelinsky, P.; Millaud, J. E.; Weiss, S. Photon-Counting H33D Detector for Biological Fluorescence Imaging. *Nuclear instruments & methods in physics research. Nucl. Instrum. Methods Phys. Res., Sect. A* **2006**, *567* (1), 133–133.

(62) Colyer, R. A.; Siegmund, O. H. W.; Tremsin, A. S.; Vallerga, J. V.; Weiss, S.; Michalet, X. Phasor imaging with a widefield photon-counting detector. *J. Biomed. Opt.* **2012**, *17* (1), 016008.

(63) Hardy, M. E. L.; Lawrence, C. L.; Standen, N. B.; Rodrigo, G. C. Can optical recordings of membrane potential be used to screen for drug-induced action potential prolongation in single cardiac myocytes? *J. Pharmacol. Toxicol. Methods* **2006**, *54* (2), 173–182.

(64) Kao, W. Y.; Davis, C. E.; Kim, Y. I.; Beach, J. M. Fluorescence Emission Spectral Shift Measurements of Membrane Potential in Single Cells. *Biophys. J.* **2001**, *81* (2), 1163–1170.

(65) Choi, B.-R.; Salama, G. Simultaneous maps of optical action potentials and calcium transients in guinea-pig hearts: mechanisms underlying concordant alternans. *J. Physiol.* **2000**, *529* (1), 171–188.

(66) Matiukas, A.; Mitrea, B. G.; Qin, M.; Pertsov, A. M.; Shvedko, A. G.; Warren, M. D.; Zaitsev, A. V.; Wuskell, J. P.; Wei, M.-d.; Watras, J.; Loew, L. M. Near-infrared voltage-sensitive fluorescent dyes optimized for optical mapping in blood-perfused myocardium. *Heart Rhythm* **2007**, *4* (11), 1441–1451.

(67) Yuan, G.; Gomez, D.; Kirkwood, N.; Boldt, K.; Mulvaney, P. Two Mechanisms Determine Quantum Dot Blinking. *ChemRxiv* **2017**.

(68) Park, S.-J.; Link, S.; Miller, W. L.; Gesquiere, A.; Barbara, P. F. Effect of electric field on the photoluminescence intensity of single CdSe nanocrystals. *Chem. Phys.* **2007**, *341* (1), 169–174.

(69) Siegmund, O.; Vallerga, J.; Tremsin, A.; McPhate, J.; Michalet, X.; Weiss, S.; Frisch, H.; Wagner, R.; Mane, A.; Elam, J.; Varner, G., Large Area and High Efficiency Photon Counting Imaging Detectors with High Time and Spatial Resolution for Night Time Sensing and Astronomy. In *Advanced Maui Optical and Space Surveillance Technologies Conference*, Maui, HI, 2012.

Supplementary information:

Characterizing the Quantum Confined Stark Effect in Semiconductor Quantum Dots and Nanorods for Single-Molecule Electrophysiology

Yung Kuo¹, Jack Li¹, Xavier Michalet¹, Alexey Chizhik², Noga Meir³, Omri Bar-Elli³, Emory

*Chan⁴, Dan Oron³, Joerg Enderlein², Shimon Weiss^{1,5,6,7} **

Number of pages: 18

Number of figures: 22

Number of tables: 0

Supplementary information list:

1. NR size analysis
2. Schematics of the “sandwich device”
3. Schematics of the wide-field spectrally-resolved microscope
4. Wavelength calibration for the spectrally-resolved microscope
5. Data analysis for extracting QCSE results
6. Dependences of QCSE on the orientations of NRs with respect to the electric field and the exposure time
7. Single particle recording at 1 kHz
8. Characterization of the instrument’s RC time constant
9. Dichroic mirror’s transmission spectrum
10. References

1. NR size analysis

The size analyses for type-II ZnSe/CdS nanorods (NRs) were done using a home-written python code. The algorithm includes the following steps: (i) decreasing contrast of original image; (ii) setting threshold for segmentation; (iii) finding the major and minor axes of each nanoparticle (NP) by fitting an ellipse tangential to the 4 borders of each NR. The size analyses for spherical NPs were done with ImageJ.

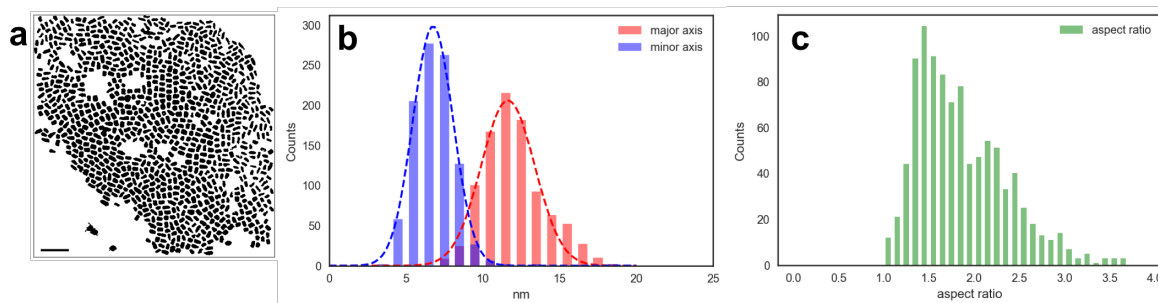


Fig. S1: Results of size analysis for type-II ZnSe/CdS NRs. (a) A binary image showing segmentation of NRs and background, processed by a home-written python code. The original image is Fig. 1a. The scale bar is 50 nm. (b) Histograms of major and minor axes acquired via size analysis. By fitting the distributions with Gaussians, the average of the major (long) axis was found to be $11.6 \text{ nm} \pm 1.7 \text{ nm}$ (1 sigma from Gaussian fitting), and the average of the minor (short) axis was found to be $6.8 \text{ nm} \pm 1.3 \text{ nm}$ (1 sigma from Gaussian fitting). (c) Histogram of aspect ratios acquired via size analysis. The averaged aspect ratio was calculated to be 1.9 ± 0.5 (1 standard deviation).

2. Schematics of the “sandwich device”

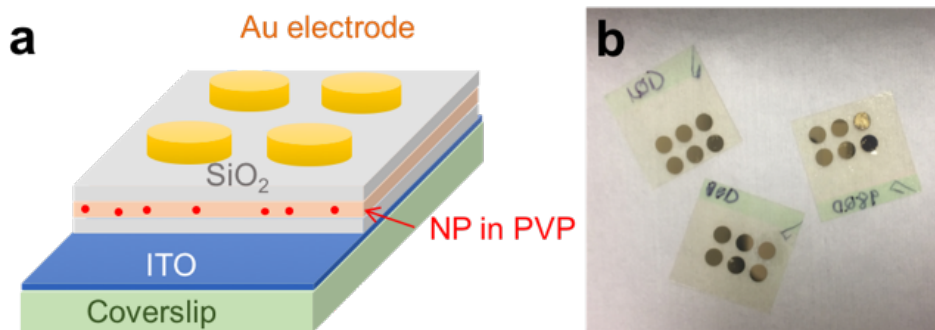


Fig. S2: (a) A schematics of the “sandwich device”. This geometry ensures a homogeneous electric field across the NPs in the spin-coated PVP layer of 400-500 nm thickness. The PVP layer and NPs are “sandwiched” between two 500 nm SiO₂ insulation layers. The bottom indium tin oxide (ITO) electrode (blue, bottom) has a resistivity of 30-60 Ohms per square. The top Cr/Au electrode (yellow circles (top) has thicknesses of 0.5 and 100 nm respectively. The Au electrodes are patterned as circles with a diameter of 3 mm by shadow masking. (b) A photo of the “sandwich device”. The coverslip dimensions are 18 x 18 mm.

3. Schematics of the wide-field spectrally-resolved microscope

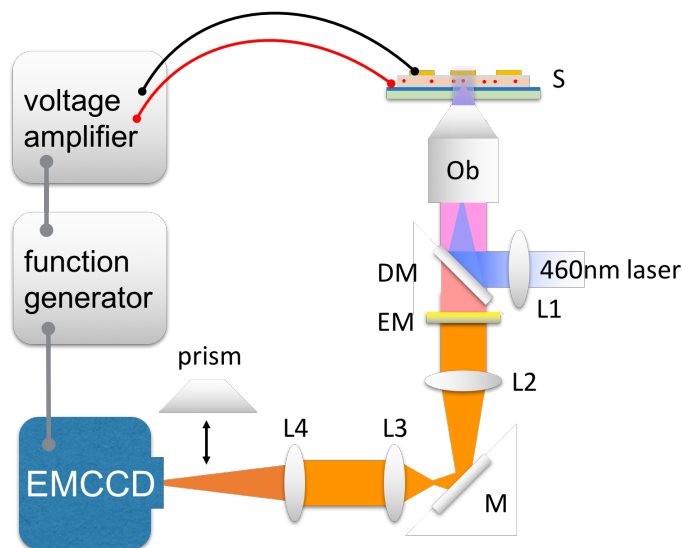


Fig. S3: Schematics of the wide-field spectrally-resolved microscope. Ob: 100x objective, N.A. 1.3. S: sample, i.e. sandwich device. DM: 488nm dichroic long pass filter. EM: emission filter. L1-L4: lenses. M: mirror. EMCCD: electron-multiplying charged couple device. In a QCSE measurement, the prism is inserted to disperse individual point spread functions (PSFs) into spectrally resolved lines, and the EMCCD acquisition is synchronized to the square voltage applied to the sample via TTL triggering generated by a programmable FPGA board detecting the rising and falling of voltage waves.

4. Wavelength calibration for the spectrally-resolved microscope

The equations below were used to assign wavelengths to each pixel of the dispersed point spread functions (PSFs) along the dispersion direction, x :

$$X_n = x + dx(x, \lambda) \tag{S1}$$

$$Y_n = (y+s)/m \tag{S2}$$

where dx is the shift of PSF locations in pixels in x direction after inserting the prism; λ is the wavelength in nm; s is the shift of PSF locations in pixels in y direction after inserting the prism;

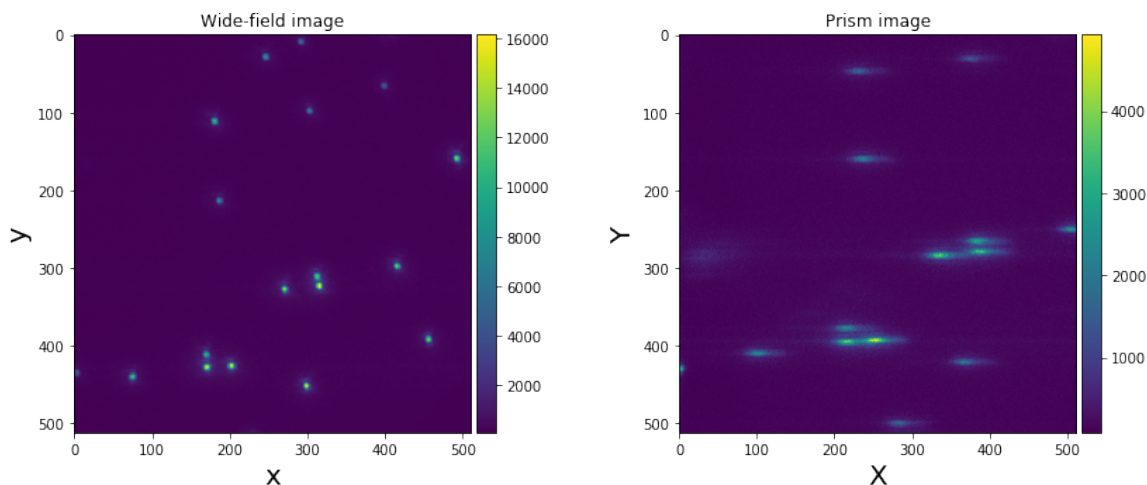


Fig. S4-1: Wide-field image (left) and prism-dispersed image (right) of spin-coated FluoSphere (625/645).

m is the magnification change after inserting the prism. The parameters, s and m , are trivial numbers related to the instrument and remain constant after repetitive insertion and removal of the prism. dx is a function of the original wide-field location of a PSF and the wavelength of the PSF, so it can be acquired by fitting dx of PSFs of fluorescent beads with known emission wavelength. 4 kinds of fluorescent beads or quantum dots (QDs) were used for this calibration: FluoSphere (505/515) 0.1 μm (Molecular Probes), FluoSphere (540/560) 0.1 μm (Invitrogen), FluoSphere (625/645) 0.2 μm (Molecular Probes) and QDs emitting at 750 nm.

As shown in Fig. S4-1, two images, a wide-field image and a prism-dispersed image, were taken for each sample of spin-coated beads or QDs. Each fluorescent bead/QD has a wide-field location, (x, y) . After inserting the prism, the dispersed PSFs span a range of few pixels in the y direction and approximately 50 pixels in the x direction, (X_1, Y_1) to (X_{50}, Y_5) . The wide-field location, (x,y) corresponding to each dispersed PSF, can be found by a trivial search in the proximity (provided that the sample is dilute enough). By extracting the intensity profile in pixel X_1 to X_{50} , the emission spectrum of a single fluorescent bead can be recovered, and the pixel with largest intensity, X_i , is assigned to the peak wavelength, 515, 560, 645, or 750 nm. Therefore, dx as functions of x for each wavelength can be extracted and fitted with a line (Fig. S4-2a). We found that both dx and dy depend linearly on x and y , respectively (Fig. S4-2a), while only dx depends on λ , as eq. S1 and S2 state. This imaging and fitting protocol was repeated several times for each bead type. After averaging and plotting the results (Fig. S4-2b), a clear quadratic depends of $dx(x)$ on the wavelength (λ) could be seen.

With this calibration at hand, we were able to calibrate quantum confined Stark effect (QCSE) spectra for each individual NPs: dx_1 - dx_{50} and x were identified for each NP, and the wavelengths were assigned to each pixel of X_1 to X_{50} .

The custom python code used for wavelength analysis is published in a public github repository: <https://github.com/yungkuo/wavelength-calibration> where interested readers can download and reproduce the entire data analysis workflow. In this repository, there are two .ipynb

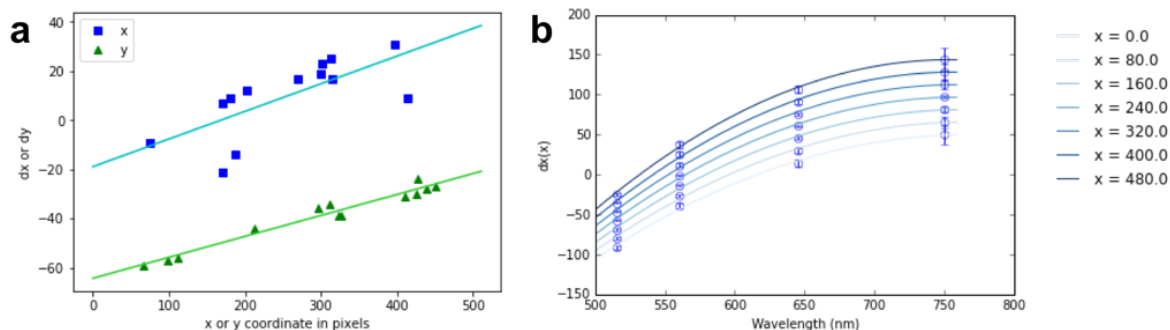


Fig. S4-2: (a) Linear dependence of dx on x and dy on y . The (dx,x) and (dy,y) data points were extracted from the PSFs in Fig S4-1. (b) Quadratic dependence of dx on λ . The data points were extracted from several measurements for each bead type.

(ipynb notebook) files. One notebook demonstrates the wavelength calibration process, and the other tests spectra recovery for individual fluorescent beads locating in various locations in the field of view using the calibration results. There is a .py file containing low-level functions, such as defining ROI and detecting PSFs. The calibration notebook can be visualized at ([link](#)).

5. Data analysis for extracting QCSE results

In each measurement, a wide-field image was taken to mark the location of each single particle, (x, y) (Fig. S5-1a is an example). For spectra measurements under alternating voltage, a movie was acquired while the prism was inserted to disperse each PSF. An example frame extracted from the movie is shown in Fig. S5-1b.

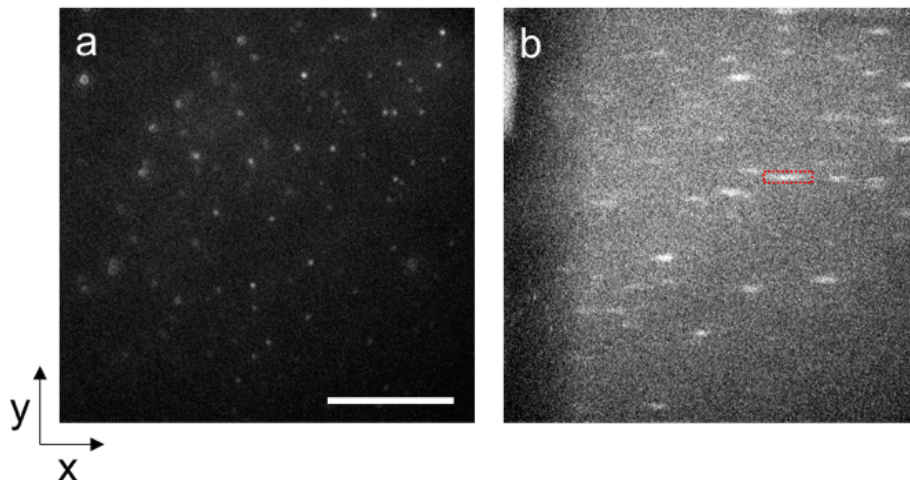


Fig. S5-1: Example images for single particle QCSE measurements. (a) wide-field image to mark locations of each NP. The scale bar is 10 μm . (b) a prism-dispersed image which allows extraction of wavelength information from each NP. The red box highlights a dispersed PSF of a single particle.

The data analysis was automated by home-written python code. The detail process for each step are listed below:

- a. Background subtraction - A 2D low pass filter was applied to each frame to define slow varying background. The sigma for the low pass filter was defined to be 20 pixels for the wide-field image and 30 for the prism-dispersed image. Background was subtracted from each frame of the movie.
- b. Automatic detection of individual PSFs - An algorithm searching for local maximum in regions of interest (ROIs) of 7×7 pixels along with a threshold to the total intensity within the ROI was applied to locate PSFs in the wide-field image. An ROI of 7×21 pixels was used for the same search in the prism-dispersed image. The PSF search was performed on the mean image of the background subtracted movie. If a pixel is the local maximum within the 7×7 or 7×21 pixel ROI, and if the integrated intensity of all pixels within this ROI is larger than a set threshold, this pixel is identified as the location of the PSF. The threshold was defined as the integrated intensity within a bigger ROI (21×21 or 21×63 pixels) surrounding the PSF plus [a x the standard deviation of intensity among all pixels within this bigger ROI]. a is 1.4 for wide-field image and 1.3 for prism-dispersed image.
- c. Matching the dispersed PSFs with wide-field PSFs - Each dispersed PSF was matched to the closest wide-field PSF. The estimations for dx and dy were provided as pre-requisite parameters for the search. PSFs that had no matching pairs within a reasonable (dx, dy) distance were omitted from further analysis.
- d. Assigning wavelengths to each dispersed PSFs - As stated in SI-4, each pixel where the dispersed PSFs spanned was assigned with a wavelength calculated from x and dx .
- e. Extraction of wavelength, intensity, and blinking information as functions of voltage - From the selected ROI (see the red box in Fig. S5-1b for an example), we could extract intensity

trace by integrating counts over all the pixels within the ROI from each frame. Here, we defined ROI to be 7x51 pixels to ensure inclusion of the entire dispersed PSFs. The peak wavelength was defined by equation S3 below:

$$\text{Peak wavelength} = \frac{\sum_n (I(X_n) \times \lambda_n)}{\sum_n I(X_n)} \quad (\text{S3})$$

where $I(X_n)$ is the integrated intensity of pixels (X_n, Y_1) to (X_n, Y_7) . n indicates the pixel number within the ROI, and therefore n is an integer number in the range of 1 to 51. λ_n is the wavelength in nm corresponding to pixel X_n .

With equation S3, peak wavelengths as a function of frames could be extracted without the need to fit the spectra of individual frames, which was advantageous since some frames had low signal-to-noise ratio for some of the NPs.

- f. Averaging the intensity percentage change ($\Delta F/F$) and wavelength shift ($\Delta\lambda$) in response to voltage - After acquiring the intensity and wavelength traces as function of frame from each particle, a blinking threshold was applied to select the “blinking on” states for further analysis. The blinking threshold was obtained by iterative optimizations (with 15 iterations). It was initially defined as the mean of intensity in the entire trace, excluding the first 2 frames as the voltage was not stable in those frames. The blinking threshold was then defined as the mean plus 1.3 x the standard deviation of intensities below the initial threshold. This optimization process was iterated 15 times to obtain a final blinking threshold although it usually converged within 5 iterations. An example of the blinking threshold is shown in Fig. 2a (cyan line). The intensities, spectra, and peak wavelengths from V_{on} (even: 0, 2, 4... etc.) and V_{off} (odd: 1, 3, 5...etc.) frames that were above the blinking threshold could then be extracted and averaged. The histograms of emission intensities from V_{on} and V_{off} frames and the blinking threshold are shown in Fig. S5-2a. As shown in Fig. S5-2, the blinking ‘on’ and ‘off’ states are not clearly separated for this single NR.

Examples of the averaged spectra from V_{on} and V_{off} frames are shown in Fig. 2c and in Fig. S5-2b. In Fig. S5-2b, Gaussian fittings are applied to the averaged spectra from V_{on} and V_{off}

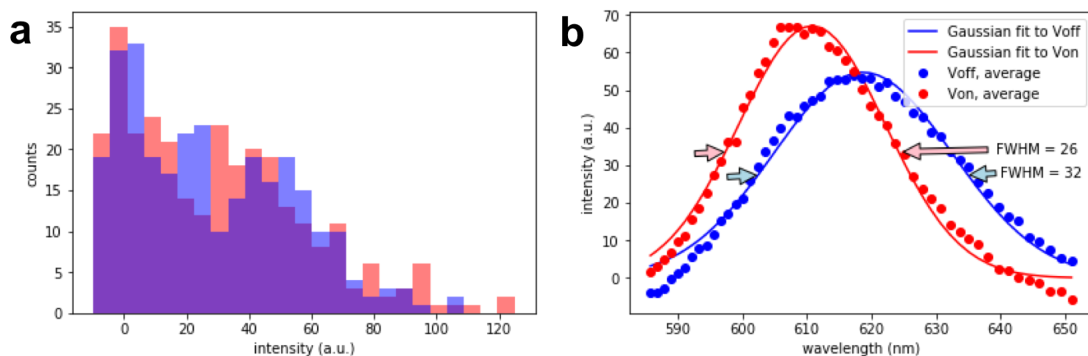


Fig. S5-2: (a) Histograms of emission intensities from single frames (V_{on} , red) and (V_{off} , blue) from the single type-II NR shown in Fig. 2. This particular NR shows no clear separation between blinking ‘on’ and ‘off’ states. (b) Gaussian fittings to the averaged spectra shown in Fig. 2c show that the emission peak blue-shifted 7.9 nm and the FWHM narrowed by 6 nm in the V_{on} frames with respect to that in the V_{off} frames.

frames, respectively. Fitting results show that the emission peak was blue-shifted 7.9 nm and the full width at half maximum (FWHM) was narrowed by 6 nm in the V_{on} frames with respect to that in the V_{off} frames.

After applying blinking threshold and averaging, the results (including $\Delta F/F$ and $\Delta\lambda$ as shown in Fig. 2) from each single particle were recorded, and histograms were plotted, as shown in Fig. S5-3.

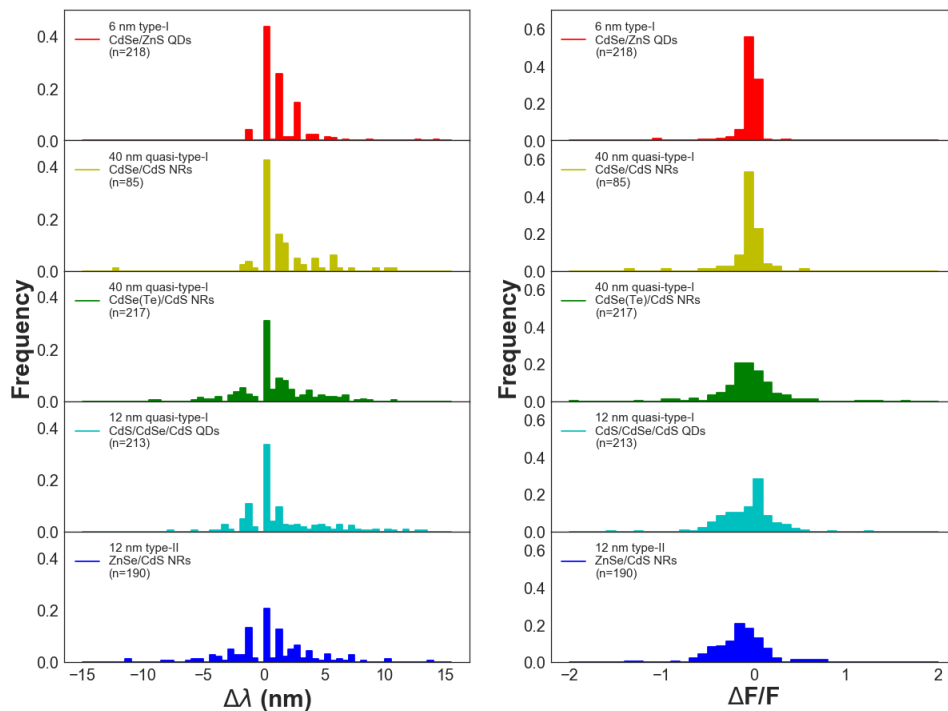


Fig. S5-3: Histograms of single particle $\Delta F/F$ and $\Delta\lambda$. The n numbers shown in legends indicate the number of particles included in the histograms.

- g. Searching ΔF and $\Delta\lambda$ “bursts” in the intensity (F) and wavelength (λ) time traces – We found that all single NPs exhibited periods of large $\Delta F/F$ or $\Delta\lambda$ and periods of smaller $\Delta F/F$ or $\Delta\lambda$. We dub periods of large $\Delta F/F$ or $\Delta\lambda$ as “bursts”. These bursts showed that NPs’ voltage sensitivity was intermittent, primarily due to the fast blinking rate compared to the acquisition rate and also possibly due to local transient charging, ionization, or spectral diffusion. Therefore, averaging spectra from all the V_{on} or V_{off} frames within the entire course of acquisition would not be a fair representation of the voltage sensitivity (for both $\Delta F/F$ and $\Delta\lambda$) as the time scale of $\Delta F/F$ and $\Delta\lambda$ changes was much smaller than the total acquisition period. To validate that the blinking is the major cause of such intermittent voltage responses, we recorded the fluorescence response of a single type-II NR (sample (v)) with a faster acquisition rate using a dual-view spectral splitting setup. In the setup, the emission from a single NR was split into two channels, a transmitted and a reflected channel, using a dichroic mirror (FF593-Di03, Semrock). Using this setup, the relative wavelength shifts could be extracted via the ratio between the two channels (instead of spectrally dispersing the signal and analyzing the spectrum’s peak position), resulting in an increased signal-to-noise ratio (SNR) under fast acquisition. The result (Fig. S5-4a) shows that the intermittent voltage sensitivities correlates with the blinking periods. In the 2-dimensional (F, ΔF) histogram (Fig. S5-4b), 2 populations can be identified, corresponding to the bright and dark states, with large and small voltage responses ($F \sim 0$ and $\Delta F \sim 0$), respectively. Meanwhile, the 2-dimensional (F, $\Delta\lambda$) histogram (Fig. S5-4c) shows essentially one population because the $\Delta\lambda$ during dark state could not be

extracted due to low fluorescence intensity. The population with $\Delta\lambda$ centered around -1 nm corresponds to the $\Delta\lambda$ observed in the bright state. To show that the ΔF intermittency is primarily caused by blinking, the autocorrelation of the intensity (F) trace and the cross correlation between the intensity (F) trace and the ΔF trace are plotted in Fig. S5-4d. The normalized autocorrelation or cross correlation curves have the following definitions:

$$G(\tau) = \sum_{t=0}^{frame} \frac{f(t+\tau)*h(t)}{\langle f(t) \rangle_t \langle h(t) \rangle_t} \quad (S4)$$

in which $f(t)$ or $h(t)$ are the F or ΔF trace, and $\langle \cdot \rangle_t$ denotes the time average.

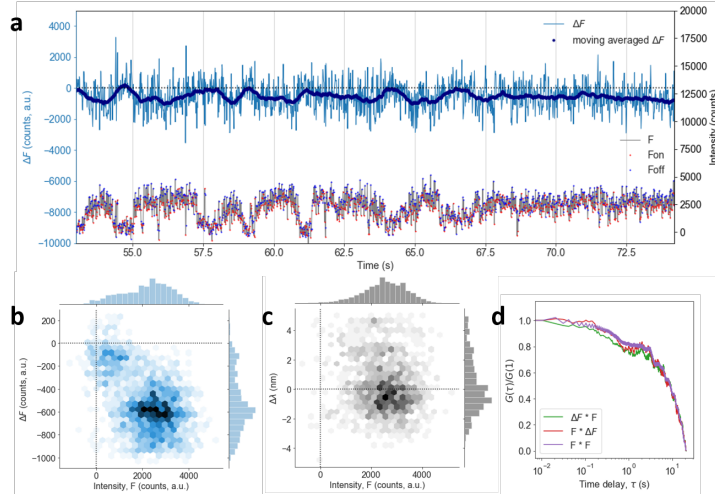


Fig. S5-4: Fluorescence responses of a single type-II NR (sample(v)) under alternating voltage modulations at 47 Hz. The camera frame rate was 94 Hz. (a) The fluorescence intensity (gray) and ΔF (blue) time traces. The darker blue trace is the moving average of ΔF with a window of 50 frames. ΔF fluctuations clearly correlate with the blinking periods. (b) The 2-dimensional histogram of ΔF and F showing 2 populations corresponding to large and small ΔF during the bright and dark states, respectively. (c) The 2-dimensional histogram of $\Delta\lambda$ and F. (d) The normalized cross correlation between the ΔF and F trace and the normalized autocorrelation of the F trace.

Because of the intermittent responses, we implemented a burst search algorithm to extract bursts of $\Delta F/F$ or $\Delta\lambda$ in the entire time traces, and the bursts statistics of $\Delta F/F$ and $\Delta\lambda$ were evaluated. The burst search algorithm was modified from the work by Ingargiola *et al.*¹. Before performing the burst search, the 2D distribution of $\Delta F/F$ v.s. $\Delta\lambda$ was plotted to examine the correlation between $\Delta F/F$ and $\Delta\lambda$. Fig. 5a shows an example of the 2D distribution of $\Delta F/F$ and $\Delta\lambda$ constructed from every modulation cycle from 125 single type-II ZnSe/CdS NRs. Each data point of $\Delta F/F$ and $\Delta\lambda$ in the histogram in Fig. 5a was extracted from 1 modulation cycle including the blinking ‘off’ states. We avoided applying blinking threshold to exclude blinking ‘off’ states, which inevitably introduces bias due to unclear separation of the blinking ‘on’ and ‘off’ states judged only by the fluorescence intensity.

Because the ΔF ’s during blinking ‘off’ states are ~ 0 (with small deviation from 0 due to noise fluctuation), and $\Delta F/F$ ’s are unreasonably large due to small F, Fig. 5a plotted the clipped population with $2 > \Delta F/F > -2$. Likewise, only the population with $20 \text{ nm} > \Delta\lambda > -20 \text{ nm}$ were plotted to exclude unreasonably large $\Delta\lambda$ ’s due to low fluorescence signals during the blinking ‘off’ states for λ calculation. As a result, a total of 55,863 data points from single cycles from 125 NRs are plotted in Fig. 5a.

In Fig. 4, the median of $\Delta F/F$ is around -29%, indicating that the majority of NRs exhibited decreased quantum yield (QY) in response to voltage modulation, while $\Delta\lambda$ has equal populations showing positive (red shifts) and negative (blue shifts) shifts. The equal populations of $\Delta\lambda$ in the negative and positive regions, as well as some population with $\Delta\lambda \sim 0$, are results of randomly oriented NRs with respect to the applied field. A very small correlation between $\Delta\lambda$ and $\Delta F/F$ is shown in Fig. 5a, as estimated by the Pearson's r value (-0.083) (top right). The small correlation shows that (1) $\Delta\lambda$ and $\Delta F/F$ bursts do not always happen at the same time and (2) large $\Delta\lambda$ are not always accompanied by large $\Delta F/F$. A low correlation between averaged $\Delta F/F$ and $\Delta\lambda$ was also reported by Bar-Elli *et al*² in other type-II ZnSe/CdS NRs. The distribution of averaged $\Delta F/F$ and $\Delta\lambda$ per particle is shown in Fig. S5-5, which also demonstrates the absence of clear correlation. Therefore, in the following analysis, the burst searching algorithm was applied to $\Delta\lambda$ and $\Delta F/F$ traces independently.

For the $\Delta F/F$ burst search, a $\Delta F/F$ time trace was first calculated from the fluorescence intensity trace. The data from the first two frames were always discarded due to unstable voltage from the function generator. In $\Delta F/F$ traces, values larger or smaller than the median of the trace ± 5 were caused by the low photon counts (very small F in the denominator) during the dark state and were set to 0. $|\Delta F/F|$ was then defined as the *score* for burst search. In the

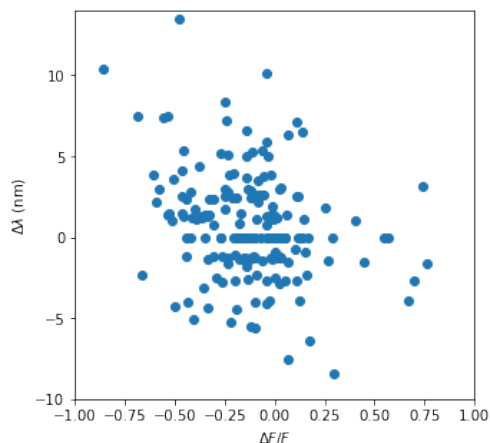


Fig. S5-5: 2D distribution of averaged $\Delta\lambda$ and $\Delta F/F$ from single type-II ZnSe/CdS NRs. The $\Delta\lambda$ and $\Delta F/F$ were calculated using the protocol described in SI-5f. The Pearson's correlation coefficient between $\Delta\lambda$ and $\Delta F/F$ extracted from this plot is -0.19.

burst search, firstly, a window size defining the minimum burst length (t_{\min}) was defined. If the *score* was larger than the score threshold, $\Delta_{0.5, 8}$, defined as the median of the moving averaged *score* trace with a window of 8 frames, the frame was marked as the “start” of a “burst”. The burst stopped when the average *score* dropped below the threshold. If the “burst” length (the number of frames from “start” to “stop”) was larger than t_{\min} , this “burst” was recorded. After finding a burst, the “start”, “stop”, “total score” (i.e. sum of $\Delta F/F$ in the burst), and the total intensity counts within the burst were recorded. An example result for the $\Delta F/F$ burst search applied to a type-II ZnSe/CdS NR is shown in Fig. S5-6.

The same protocol with modifications was applied for the $\Delta\lambda$ bursts search. In a wavelength (λ) trace, the λ 's that were 30 nm larger or smaller than the median of the entire λ trace were replaced with the λ value of its previous frame, and hence $\Delta\lambda$ would be 0. This manipulation was implemented to avoid frames that had unreasonable λ values due to the low signal in the

dark states. After processing λ , $\Delta\lambda$ ($score$) was calculated. The burst search protocol was the same as $\Delta F/F$ burst search. An example result for the $\Delta\lambda$ burst search applied to the same type-II ZnSe/CdS NR in Fig. S5-6 is shown in Fig. S5-7.

- h. Bursts histograms– Having extracted $\Delta\lambda$ score, $\Delta F/F$ score, burst width, and total intensity counts within a burst, histograms of $\Delta\lambda$ and $\Delta F/F$ (with and without intensity weighting) were plotted (see Fig. 3). The average width of bursts, average number of bursts per particle, and percent burst duration as compared to the entire course of acquisitions are shown in Fig. S5-8.



Fig. S5-6: An example result for $\Delta F/F$ burst search applied to the intensity trace from a type-II ZnSe/CdS NR. The blue line is the $\Delta F/F$ $score^2$. The black dashed line is the $8\times$ moving averaged $score^2$ with a window of 8 frames. The red dashed line is the $8\times$ threshold above which the “start” of a burst will be identified. For this NR, 7 bursts above the threshold (and above the time threshold of 8 frames) were detected and marked by the blue shaded areas. The green line is the intensity (F) trace with the scale indicated on the right, and the blue and the red dots mark the F 's at V_{on} and V_{off} frames, respectively.

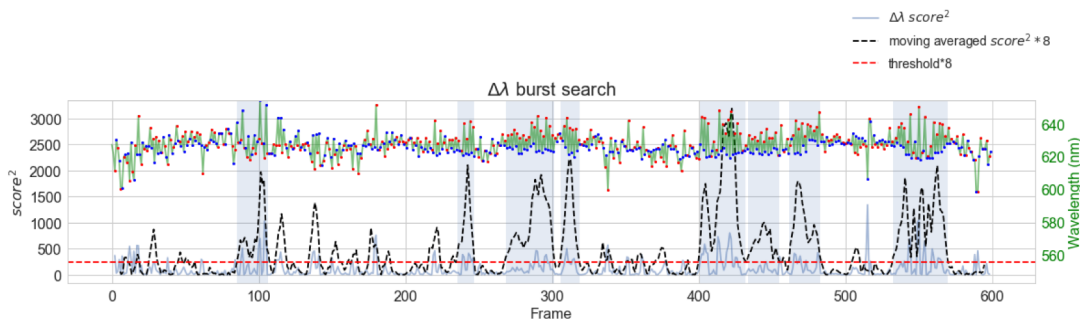


Fig. S5-7: An example result for $\Delta\lambda$ burst search applied to the wavelength (λ) trace from a type-II ZnSe/CdS NR (the same NR as in Fig. S5-6). The blue line is the $\Delta\lambda$ $score^2$. The black dashed line is the $8\times$ moving averaged $score^2$ with a window of 8 frames. The red dashed line is the $8\times$ threshold above which the “start” of a burst will be identified. In this NR, 8 bursts above the threshold (and above the time threshold of 8 frames) are detected and marked by the blue shaded areas. The green line is the wavelength (λ) trace with the scale indicated on the right, and the blue and the red dots mark the λ 's at V_{on} and V_{off} frames, respectively.

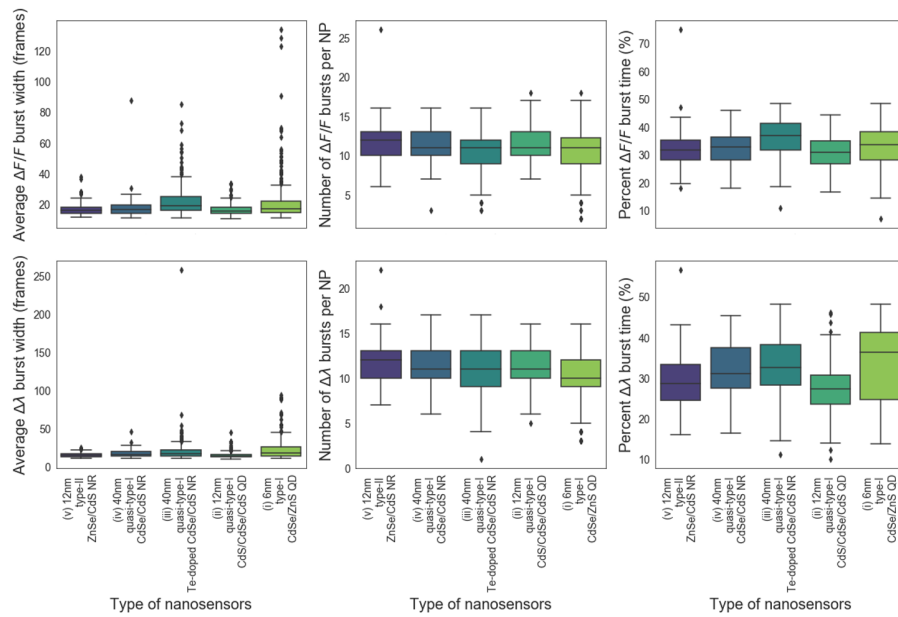


Fig. S5-8: Statistical results from both $\Delta\lambda$ and $\Delta F/F$ burst searches, including the average width of bursts, average number bursts per NP, and percent burst duration within the entire course of acquisitions

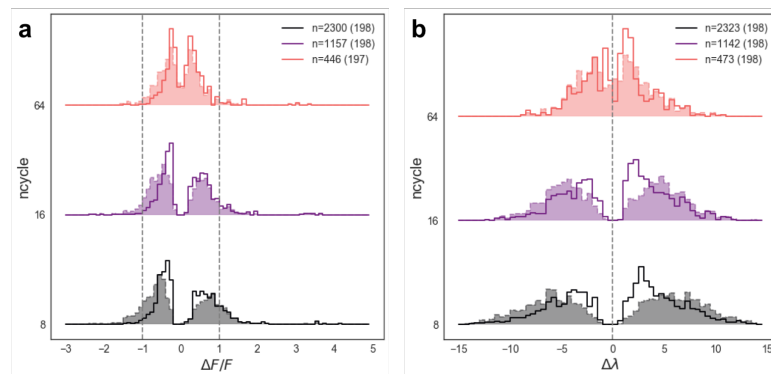


Fig. S5-9: Histograms of (a) $\Delta\lambda$ and (b) $\Delta F/F$ extracted from bursts from type-II NR (sample (v)) with different minimum burst durations used during burst search. The t_{min} were defined as 8, 16, and 32 frames for $ncycle = 8, 16$ and 64, respectively. The $ncycle$ is the window size for calculating moving average. The number of bursts (n) and number of NPs (number in parenthesis) in each histogram are shown in the legends. The solid lines are the histogram weighted by the total intensity counts during each burst (as shown in Fig. 4), and the shaded area with dashed lines are the standard histograms

The effect of a minimum burst duration on the distribution of $\Delta\lambda$ and $\Delta F/F$ is shown in Fig. S5-9.

Fig. 5-10 shows the effect of randomizing the wavelength (λ) traces on the $\Delta\lambda$ distribution. The randomized wavelength (λ) traces were used as a negative control for calculating the Pearson's correlation coefficients between $\Delta F/F$ and $\Delta\lambda$ traces. To get a randomly shuffled $\Delta\lambda$ trace, the wavelength (λ) trace, excluding the first 2 frames was randomly permuted, and the $\Delta\lambda$ trace was calculated between neighboring frames following the same procedure for calculating the original $\Delta\lambda$ trace as shown above. The effects of the randomized wavelength (λ) traces on the $\Delta\lambda$ distributions are shown in Fig. S5-10, confirming that shuffling completely randomized the wavelength (λ) traces, and the $\Delta\lambda$'s between neighboring frames is normally distributed around 0.

All the above-mentioned analyses were done using custom python code, available on github (<https://github.com/yungkuo/wide-field-QCSE-analysis>), and the raw data can be found at 10.6084/m9.figshare.5566948.

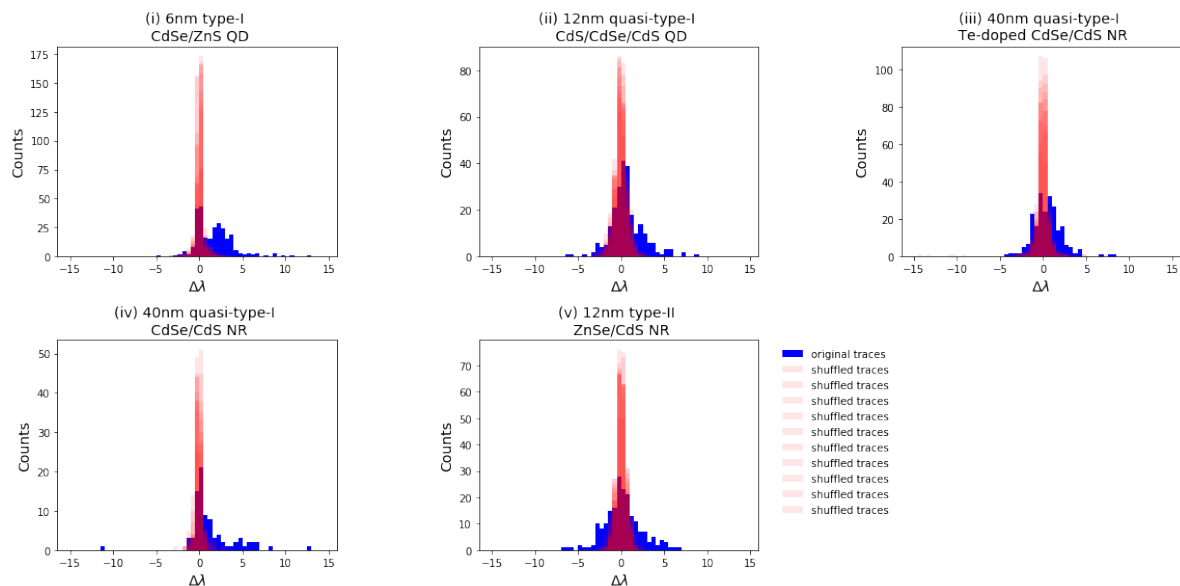


Fig. S5-10: $\Delta\lambda$ distributions for each type of NPs (blue), compared to 10 different $\Delta\lambda$ distributions calculated from randomized wavelength traces for each type of NPs (red).

6. Dependences of QCSE on the orientations of NRs with respect to the electric field and the exposure time

In the “sandwich device” shown in Supporting Information-2, the orientations of NRs were random with respect to the orientation of the applied electric field, which might contribute to widen the distributions of the voltage sensitivities, $\Delta F/F$ and $\Delta\lambda$, measured. Therefore, the correlation between the orientations of the emission transition dipoles of NRs with respect to the field direction and the emission spectra were studied using defocused imaging microscopy³. In the experiment, diluted type-II NR (sample(v)) solution in toluene was dropped casted on the interdigitated electrodes shown in Fig. 6a. After the toluene evaporated completely, a voltage of 20V was applied to create an electric field of 400 kV/cm via a voltage amplifier (BPC 303, Thorlabs). The microscopic defocused image was acquired using a high NA objective (Apo N, 60 \times /1.49 NA oil immersion, Olympus) with a 460 nm laser (SC400-4-20, Fianium) as excitation, and the fluorescence was filtered by an emission filter (Edge Basic Long Wave Pass 561, Semrock) before recorded by a camera (iXon Ultra, DU-897U, Andor). Each spectrum was acquired for 5 seconds using a spectrograph (SR 303i, Andor) and a CCD camera (iXon DU897 BV, Andor.) under $\sim 2 \mu\text{W}$ excitation. The microscope setup and the analysis for the emission dipole are described in detail in ref^{3, 4}. The results are shown in Fig. S6. For spectra data analysis, the spectra were fitted to a Lorentzian to find the peak wavelength.

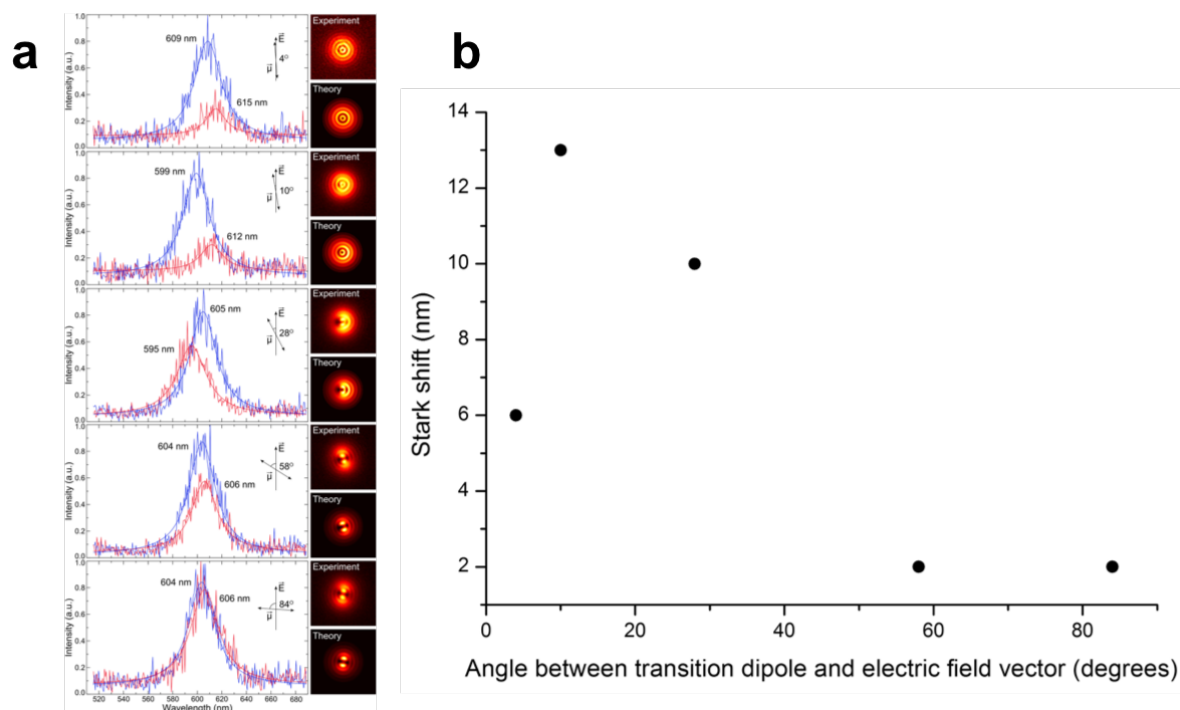


Fig. S6-1: (a) Emission spectra of 5 randomly oriented type-II NRs (sample (v)) in the presence and absence of applied electric field. The orientations of the emission transition dipoles of these NRs are shown as $\vec{\mu}$ by black arrows, and the direction of the applied electric field is shown as \vec{E} . The images acquired by defocused imaging experimentally and theoretically are shown on the right. (b) The QCSE spectral shift as a function of the angle between the emission transition dipole and the applied electric field.

The stability and voltage sensitivities of the type-II NRs (sample (v)) after a long period of excitation were studied. In this experiment, the type-II NRs were dropped casted from toluene solution onto an interdigitated electrode with 2 μm gap (Fig. 6a). After the toluene has evaporated, the NRs were excited with a wide-field illumination using a 405 nm laser at $\sim 10 \text{ W/cm}^2$. The fluorescence was filtered by a bandpass filter (HQ 590/80M, Chroma Technologies) and then split by a dichroic mirror (FF593-Di03, Semrock) into two channels, a reflected channel with wavelength $< 593 \text{ nm}$ and a transmitted channel with wavelength $> 593 \text{ nm}$, before collected by an EMCCD camera (Ixon DU-860, Andor). An alternating square voltage of 0 V and 60 V was applied to generate an electric field of 0 kV/cm and 300 kV/cm between the electrodes. The camera acquisition was synchronized in the same fashion as for the wide-field QCSE measurements described in Method. The frame rate was 30.49 Hz, which was acquired by measuring the triggering signals sent to the camera using an oscilloscope, and hence the accumulation time was $\sim 33 \text{ ms}$.

From the recorded movie, the signals from a single NR from a 5 pixel \times 5 pixel region were summed in individual frames in both channels to generate two intensity time traces. The background for each channel was calculated locally from a 9 pixel \times 9 pixel region around the point-spread-function of the NR. Within the 9 pixel \times 9 pixel region, the 25 pixels with the lowest averaged intensity were selected, and the intensity of these 25 pixels were summed in individual frames to generate a background time trace. The resulted fluorescence time trace of a single type-II NR (sample (v)) recorded for 8 hrs is shown in Fig. S6-2. The odd frames (1, 3, 5, ... etc.)

marked as blue were the frames acquired under no electric field, and the even frames (0, 2, 4, ... etc.) marked as red were recorded under an electric field of 300 kV/cm.

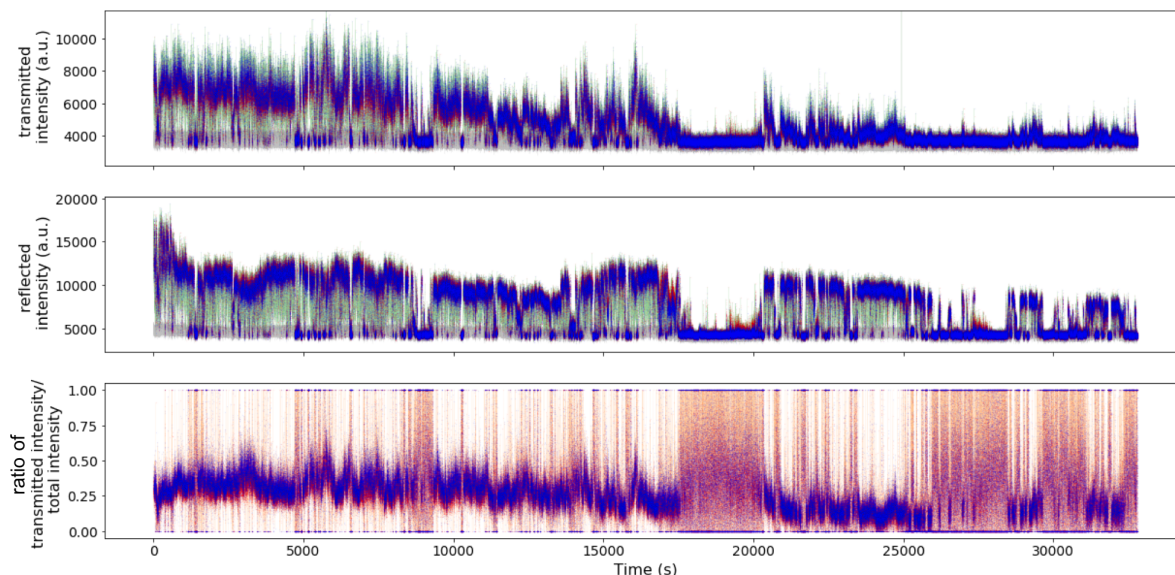


Fig. S6-2: Fluorescence time traces of a single type-II NR (sample (v)) acquired using a dual-view spectral splitting setup. (top) The intensity time trace of the transmitted red channel. (middle) The intensity time trace of the reflected blue channel. (bottom) The ratio time trace calculated by the intensity of the transmitted red channel divided by the total intensity of the two channels after background subtraction. The V_{on} and V_{off} frames are marked with red and blue, respectively, and the backgrounds in each channel are shown as the gray traces in the top and middle panel. In the bottom panel, the ratio trace was clipped to be between 0 and 1. The ratios below 0 and above 1 were insignificant results from the low intensity of the dark state.

The intensity ratio of the transmitted red channel over the sum of both channels can be used to calculate the emission peak wavelength with simple assumptions, including Gaussian emission peak and the full width at half maximum (FWHM) of the emission peak. We assumed that the FWHM was 30 nm based on the single particle emission bandwidth (shown in Figs. 2C and S5-2b), and the transmission spectrum of the dichroic mirror was obtained from the manufacture (Fig. S6-3a, overlaid with the assumed Gaussian emission peak centered at 593 nm). The transmitted intensity ratio as function of the emission peak wavelength is shown in Fig. S6-3b.

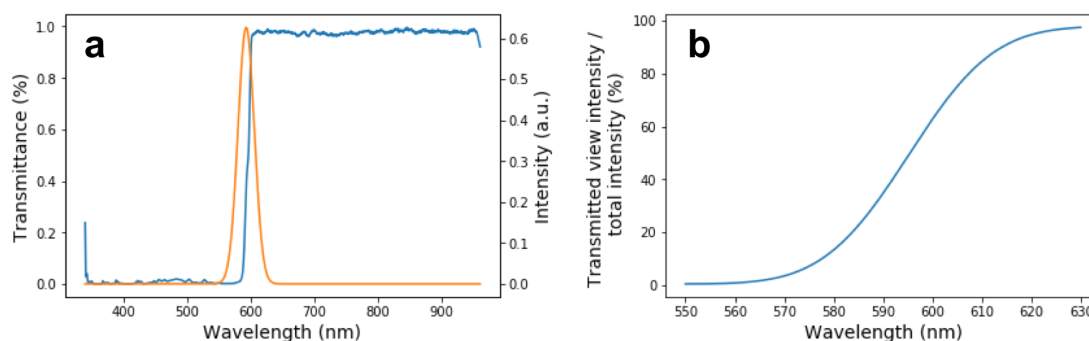


Fig. S6-3: (a) Assumed Gaussian emission spectrum of a single type-II NR (orange) and the transmission spectrum of the dichroic mirror (blue). (b) The calculated transmitted intensity ratio as function of the emission peak wavelength.

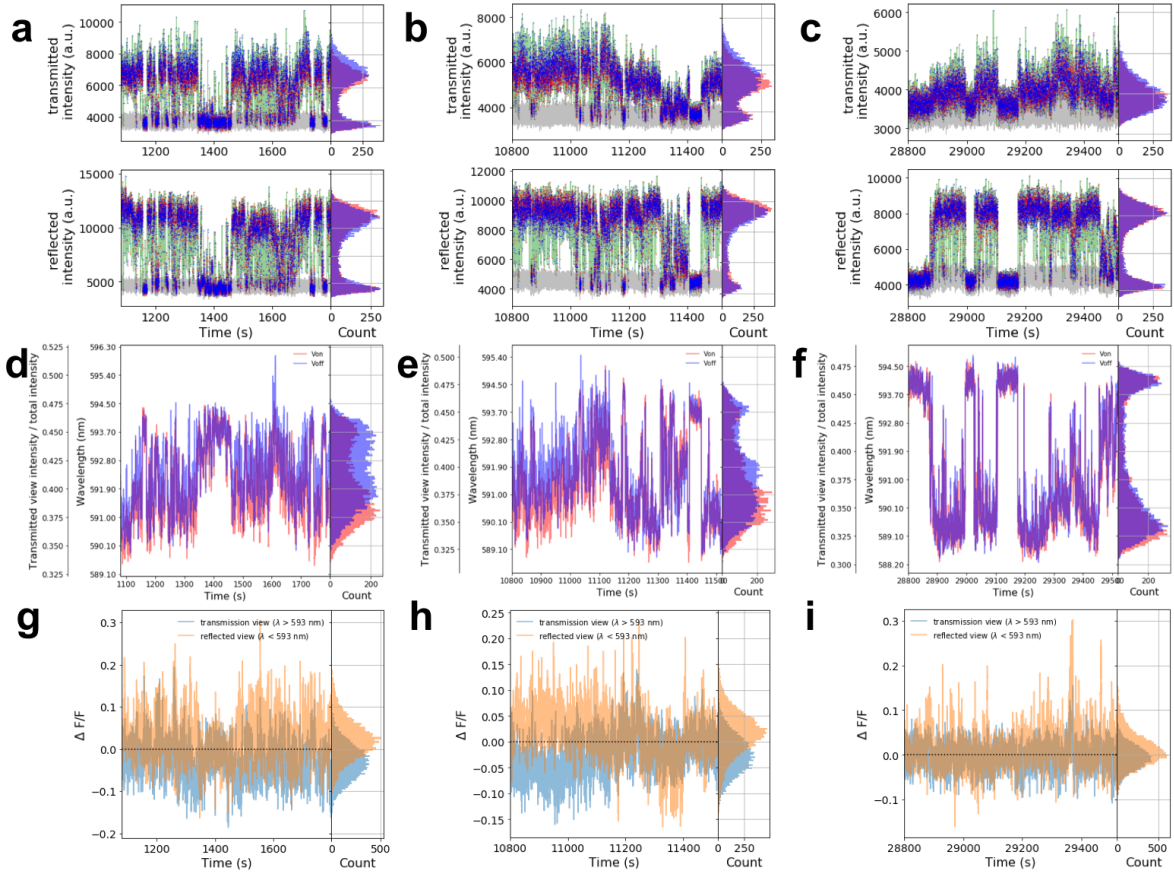


Fig. S6-4: Zoomed-in time traces of the single type-II NR shown in Fig. S6-2 within 1 hr (a,d,g), after 3 hrs (b,e,h), and after 8 hrs (c,f,i) of continuous excitation. (a, b, c) The intensity time traces and intensity histogram of the transmitted and reflected channels with the V_{on} and V_{off} frames marked in red and blue, respectively. The background of each channel is plotted in gray. (d,e,f) Emission peak wavelength calculated from the transmitted intensity ratio in V_{on} (red) and V_{off} (blue) frames and the histogram. (g,h,i) $\Delta F/F$ traces calculated from adjacent frames in the transmitted channel (blue) and reflected channel (orange) and the histogram.

In Fig. S6-4, we show the time traces and the calculated λ (Fig. S6-4d, e, f) and $\Delta F/F$ (Fig. S6-4g, h, i) traces at 3 different time periods, 0.4, 3, and 8 hrs. The $\Delta F/F$ was calculated from adjacent frames using the equation below

$$\left(\frac{\Delta F}{F}\right)_j = F_j^{V_{on}} / (F_j^{V_{on}} - F_{j+1}^{V_{off}}) \quad (S4)$$

This single type-II NR displayed significant spectral shift as seen by the displacement between the λ trace at V_{on} frames (red) and the λ trace at V_{off} frames (blue) (Fig. S6-4d). The spectral shift can also be seen in Fig. S6-4a, in which the intensity in the transmitted channel decreased, while the intensity in the reflected channel increased, when an electric field is applied (V_{on}). In Fig. S6-4g, the $\Delta F/F$ s are positive in the reflected channel and negative in the transmitted channel, which shows that this single type-II NR exhibited blue shifts when an electric field was applied.

It is worth noticing that in the histograms in Fig. S6-4d, e, f, there are two populations, one centers at ~ 591.9 nm and gradually blue shifts, and the other centers at ~ 593.7 nm. The population centered at ~ 593.7 nm has a percent transmittance of $\sim 45\%$ and is clearly originated from the dark states (or dim states). During the dark states or dim states, the NR did not exhibit spectral shift as

seen by the overlapping populations centering at ~ 593.7 nm in the λ histograms at V_{on} and V_{off} in Fig. S6-4 d, e, f. On the contrary, during the bright state, the λ histograms have significant displacement between the V_{on} and V_{off} frames, despite gradually shifting blue after 3 hrs of continuous excitation (Fig. S6-4 d, e, f).

This single type-II NR maintain relative constant $\Delta F/F$ and $\Delta\lambda$ in the first 4 hrs of continuous excitation under ambient air, despite some noisy fluctuations due to blinking and possible spectral diffusion (Figs. S6-2 and S6-4). After 4 hrs of continuous excitation, the NR exhibited blue shifted emission and entered dark state for longer amounts of time. After 8 hrs of continuous excitation, the emission of this NR blue shifted ~ 4 nm as compared to the original emission wavelength. However, this NR still exhibited some voltage sensitivity, $\Delta\lambda$, although the $\Delta\lambda$ was much smaller than the original $\Delta\lambda$ before prolonged excitation.

As shown in many past works, the stability of QDs or NRs can be increased significantly by covering the QDs or NRs in a polymer^{5,6}. We demonstrated the stability of the type-II NRs in ambient air in order to observe the photochemical effect on the QCSE, and the NR showed excellent long life (> 8 hrs) and voltage-sensing stability (~ 4 hrs). Improved high bandgap coatings and immersion in the lipid environment of the membrane can improve stability further.

7. Single particle recording at 1 kHz

To demonstrate that the type-II NRs (sample (v)) could afford recordings at kHz with sufficient emission rate, the fluorescence of a single NR was recorded using a dual-view setup similar to that described in Supporting Information-6 with some modifications. The wide-field excitation was from a 532 nm laser (CNI Optoelectronics Technology) at ~ 250 W/cm², and the emission was split with a 594 nm dichroic mirror (Di02-R594, Semrock) resulting in a “red” transmitted part of the signal (transmitted channel) and a “green” reflected part of the signal (reflected channel). An alternating voltage between 0 V and 60 V at 500 Hz and 50 % duty cycle (square wave) was applied across 2 μm interdigitated electrodes (Fig. 6a). Fluorescence recording was performed by an EMCCD camera (Ixon DU-860, Andor) at 2 frames per voltage cycle, synchronized to the applied voltage (1 kHz frame rate). The recorded intensity time traces and the ratio between the background-subtracted, transmitted channel over the total intensity of the two background-subtracted channels were plotted in Fig. S7. In Fig. 6d and Fig. S7a, clear displacements between the intensity from V_{on} frames and V_{off} frames could be seen, especially in the reflected channel. The clear shift between the wavelength histograms from V_{on} frames and V_{off} frames is seen in Fig. S7b, which shows that (1) the spectral shift can be observed from a single NR at 1 kHz recording and (2) the dual-view spectral splitting setup is suitable for spectrally-resolved recording of the fluorescence from a single NR at 1 kHz. Moreover, the intensity change ($\Delta F/F$) could also be observed as shown in Fig. S7c.

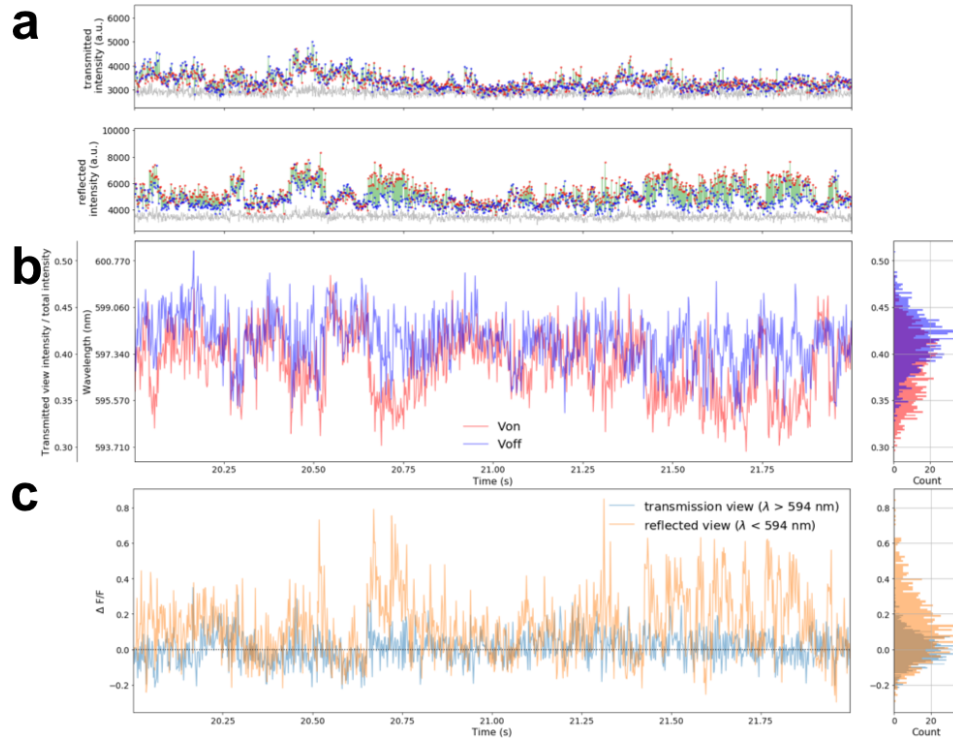


Fig. S7: Time traces of a single type-II NR recorded at 1 kHz. (a) The intensity time traces of the transmitted and reflected channels with the V_{on} and V_{off} frames marked in red and blue, respectively. The background of each channel is plotted in gray. (b) Emission peak wavelength calculated from the transmitted intensity ratio in V_{on} (red) and V_{off} (blue) frames and the histogram. (c) $\Delta F/F$ traces calculated from adjacent frames in the transmitted channel (blue) and reflected channel (orange) and the histogram.

8. Characterization of the instrument's RC time constant

To characterize the rise time of our instrument used for the photon counting experiment, the microelectrode was connected in series to a resistor of $372\text{ M}\Omega$ to form an RC circuit. The voltage drop across the resistor was recorded with an oscilloscope (DS1102E, Rigol Technologies) while square wave was applied. The RC time constant for this circuit was found to be $49.577\text{ }\mu\text{s}$ by fitting (Fig. S7-1), from which a capacitance of 133 pF was extracted.

In actual experiments that tested the response time of NRs, a resistor of $100\text{ }\Omega$ was used, with $RC=13\text{ ns}$, which was much smaller than the instrumental time constant. The instrument time constant was derived from a fit to the rising edge (Fig. S7-2) of the recorded voltage. The rise time was found to be $3.575\text{ }\mu\text{s}$.

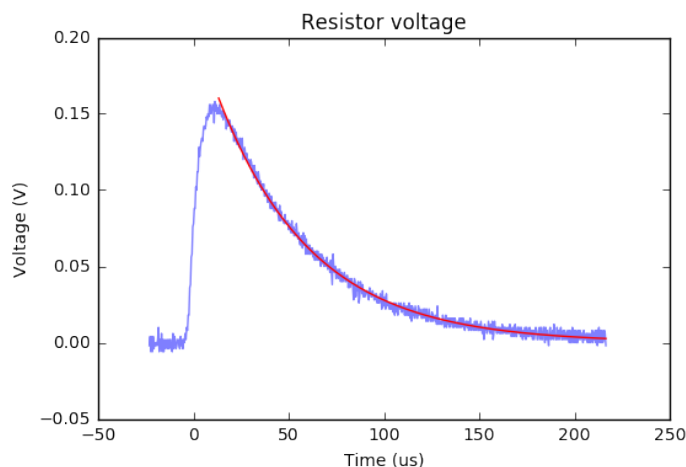


Fig. S8-1: Voltage trace recorded across the resistor ($372\text{ M}\Omega$) in series with the microelectrode for characterizing the RC time constant of the instrument. The resistor voltage trace is in response to a square voltage modulation from 0 V to 80 V, generated and amplified by the instruments described in Methods. The blue line is the recorded voltage across the resistor by an oscilloscope, and the red line is the best fit to the blue line with an exponential decay to extract the RC time constant.

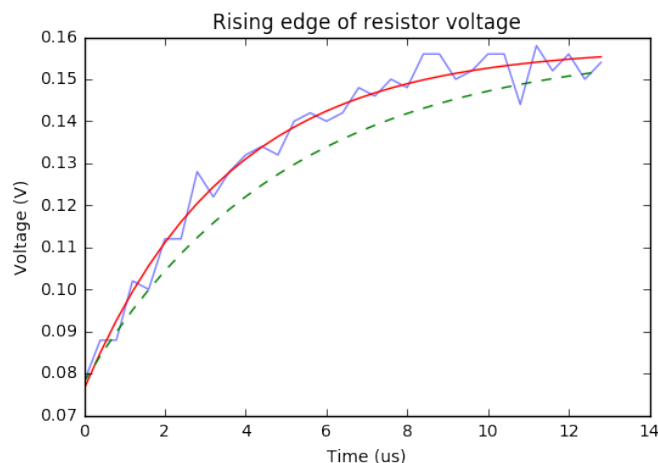
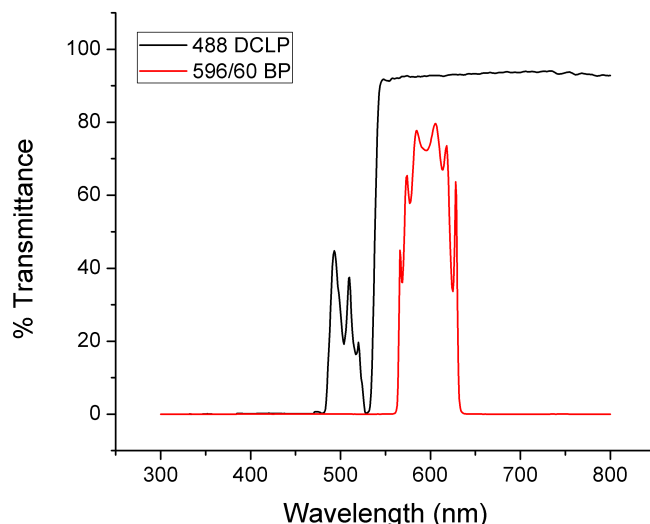


Fig. S8-2: Voltage trace recorded across the resistor ($100\text{ }\Omega$) in series with the microelectrode for characterizing the rise time of the instrument. The resistor voltage trace is in response to a square voltage modulation generated and amplified by the instruments described in Methods. The blue line is the recorded voltage across the resistor by an oscilloscope, the red line is the best fit to the blue line with an exponential rise to extract the time constant, and the green dashed line is the initial guess of the fit.

9. Dichroic mirror's transmission spectrum

Since the manufacture information of the dichroic mirror and emission filter used in the wide-field photon counting setup is no longer available, we provide their transmission spectrum measured by a UV-VIS spectrometer.



10. References

1. Park, K.; Kuo, Y.; Shvadchak, V.; Ingargiola, A.; Dai, X.; Hsiung, L.; Kim, W.; Zhou, H.; Zou, P.; Levine, A. J.; Li, J.; Weiss, S., Membrane insertion of— and membrane potential sensing by— semiconductor voltage nanosensors: Feasibility demonstration. *Science Advances* **2018**, *4* (1).
2. Bar-Elli, O.; Steinitz, D.; Yang, G.; Tenne, R.; Ludwig, A.; Kuo, Y.; Triller, A.; Weiss, S.; Oron, D., Rapid Voltage Sensing with Single Nanorods via the Quantum Confined Stark Effect. *ACS Photonics* **2018**.
3. Patra, D.; Gregor, I.; Enderlein, J., Image Analysis of Defocused Single-Molecule Images for Three-Dimensional Molecule Orientation Studies. *The Journal of Physical Chemistry A* **2004**, *108* (33), 6836-6841.
4. Patra, D.; Gregor, I.; Enderlein, J.; Sauer, M., Defocused imaging of quantum-dot angular distribution of radiation. *Applied Physics Letters* **2005**, *87* (10), 101103.
5. Yang, C.; Zhang, G.; Feng, L.; Li, B.; Li, Z.; Chen, R.; Qin, C.; Gao, Y.; Xiao, L.; Jia, S., Suppressing the photobleaching and photoluminescence intermittency of single near-infrared CdSeTe/ZnS quantum dots with p-phenylenediamine. *Optics Express* **2018**, *26* (9), 11889-11902.
6. Lee Steven, F.; Osborne Mark, A., Brightening, Blinking, Bluing and Bleaching in the Life of a Quantum Dot: Friend or Foe? *ChemPhysChem* **2009**, *10* (13), 2174-2191.

Chapter 4

Functionalization of voltage sensitive nanorods for membrane insertion

This chapter is the unpublished manuscript titled “Improved surface functionalization and characterization of membrane targeted semiconductor voltage nanosensors”. This chapter describes the functionalization of type-II nanorods for membrane insertion and the capability of recording membrane potential using such functionalized nanorods. The authors of this manuscript are Joonhyuck Park, Yung Kuo, Jack Li, Yi-Lin Huang, Evan Miller, and Shimon Weiss. Joonhyuck Park conducted all experiments, analyzed the data, and wrote the manuscript. I developed the assay and built the setup for modulating the membrane potential of valinomycin-treated cells by manipulating the potassium concentrations in the extracellular media. Jack Li and I synthesized ZnSe/CdS NRs using WANDA. Shimon Weiss, Joonhyuck Park, and I designed the experiments. Shimon Weiss, Evan Miller and I helped in writing and revising the manuscript. All authors have given approval to including this manuscript in this dissertation.

Introduction

We previously demonstrated that semiconductor quantum dots and nanorods exhibit a measurable quantum confined Stark effect (QCSE) at room temperature at the single nanoparticle level.¹ We have theoretically evaluated their potential utilization as membrane voltage sensors and examined modes of detections based on intensity changes ($\Delta F/F$), spectral shifts ($\Delta\lambda$), and excited-state lifetime changes ($\Delta\tau$).² We showed that when functionalized with trans-membrane peptides, voltage-sensing nanorods (vsNRs) can be inserted into cellular membranes to report the membrane potential³ via fluorescence intensity or spectral changes. More recently, we have shown that type-II ZnSe/CdS seeded nanorods (CdS nanorods while embedding the ZnSe QDs inside, same composition NRs in this paper) exhibit the largest QCSE among a small library of different compositions and shapes nanoparticles. The QCSE could be directly monitored by $\Delta\lambda$ measurements, but $\Delta F/F$ measurements were also affected by extrinsic effects, most likely via quantum yield (QY) modulation due to charging and/or ionization at surface- and interface- defects.⁴⁻⁶

Here we further developed and improved voltage sensing nanorods (vsNRs) that can optically and non-invasively record the cellular membrane potential at multiple sites, over a large field-of-view, at the ensemble level. These vsNRs could offer unique advantages for sensing the membrane potential: (i) they are very bright and could, in principle, afford single-particle detection; (ii) they display modulated QY as function of voltage change across cell membrane; (iii) with an improved surface coating composed of a mixture of alpha-helical peptides and zwitterionic decorated lipolic acids (zw-LA), they could target the cell membrane with high loading efficiency and minimal non-specific binding. The mixture of peptides and zw-LAs, which contain both positive and

negative charges over wide pH range, provide better colloidal stability to the nanoparticles and decreased non-specific adsorption as compared to peptide-only coating³.

Experimental results

ZnSe/CdS type-II semiconductor nanorods(NRs) were synthesized by the heat-up method.⁷ Briefly, premade ZnSe quantum dots (QDs) were mixed into a solution of cadmium phosphonates and octadecanethiol (cadmium and sulfur precursors). The phosphonic acids in the mixture promote the anisotropic growth of CdS nanorods while embedding the ZnSe QDs inside ('seeded NRs').⁷ The mixture was heated up to ~320 °C for 15 minutes to grow NRs and cooled to room temperature (r.t.) yielding NRs of 11.8 ± 2.3 nm in length and 6.5 ± 1.5 nm in diameter.

To deliver NRs to cell membranes, we improved the previously reported peptide-coating approach.³ In addition to the modified alpha-helical trans-membrane peptides^{3, 8}, we also added zwitterionic decorated lipoic acids (zw-LA)⁸ to provide colloidal stability. Ligand exchange reaction of the mixture was performed through multiple steps (See Methods section for detail). Briefly, as-synthesized NRs (asNRs) were first treated with the ligand stripping agent (triethylxonium tetrafluoroborate) to remove the original hydrophobic ligands⁹, such as alkylphosphonic acids, alkylphosphine oxides or alkylamines on the surface of NRs. IR spectroscopy was used to monitor the ligand stripping efficiency. As can be seen in Fig. S1, the C-H vibration ($2852, 2922\text{ cm}^{-1}$) and the bending peaks (1466 cm^{-1}) were diminished after the stripping treatment. Next, octanoic acid was added to the NRs solution to provide temporal colloidal stability. After removing excess amount of octanoic acid, pyridine was added (acting both as a surface

ligand and as a solvent). Pyridine capped NRs were then mixed with the mixture of 1:3 of zw-LA : alpha-helical peptides and redispersed in DMSO. The optical properties of these zw-LA-and-peptides (ZAP) functionalized NRs were preserved after the ligand exchange process as characterized by UV-Vis absorption and fluorescence spectroscopy (emission peak: 605 nm, Figure 1a). The quantum yield (QY) of the functionalized ZAP-NRs was only

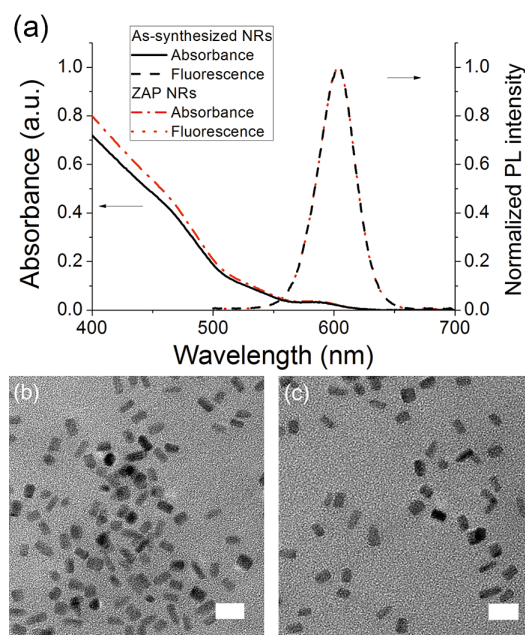


Fig. 1: (a) Absorption (black solid) and fluorescence (red dash-dotted) spectra of as-synthesized (black dashed) and ZAP-NRs (red dotted). TEM images of (b) as-synthesized ZnSe/CdS nanorods and (c) ZAP-NRs (scale bar: 20 nm).

slightly reduced (to 39%) as compared to the original QY of the asNRs (55%). Transmission electron microscopy (TEM) images of the asNRs and the ZAP-NRs showed no substantial change in size after functionalization (long axis = 11.8 ± 2.3 nm and short axis = 6.5 ± 1.5 nm for asNRs, long axis = 12.0 ± 2.4 nm and short axis = 6.7 ± 1.9 nm for ZAP-NRs, see Figs. 1b,c). The 1:3 ratio of zw-LAs to alpha-helical peptides was chosen since it was able to provide both colloidal stability and membrane loading efficiency. This ratio is similar to the previously reported primary amine functionalized ligands to zw-LAs ratio used to minimize non-specific adsorption.⁸

Interestingly, ZAP-NRs were colloidal stable at 10% and down to 1% DMSO(aq) but started to form aggregates at 0.2% DMSO(aq) as shown by DLS measurements (Fig. 2e). We argue that the amphiphilic nature of the peptides affords the dispersion of ZAP-NRs in DMSO, while the zw-LAs afford their partial solubilization in DI water (Fig. S2).

Membrane loading ability and specificity of ZAP-NRs were assessed by confocal microscopy (Figs. 2b-d). HEK293T cells were sequentially incubated with 30 nM ZAP-NRs for 1 hour and then with 2 μ M DiR membrane staining dye for 15 minutes (see details in SI). Next, cells were fixed with 4% paraformaldehyde for 15 minutes at r.t.

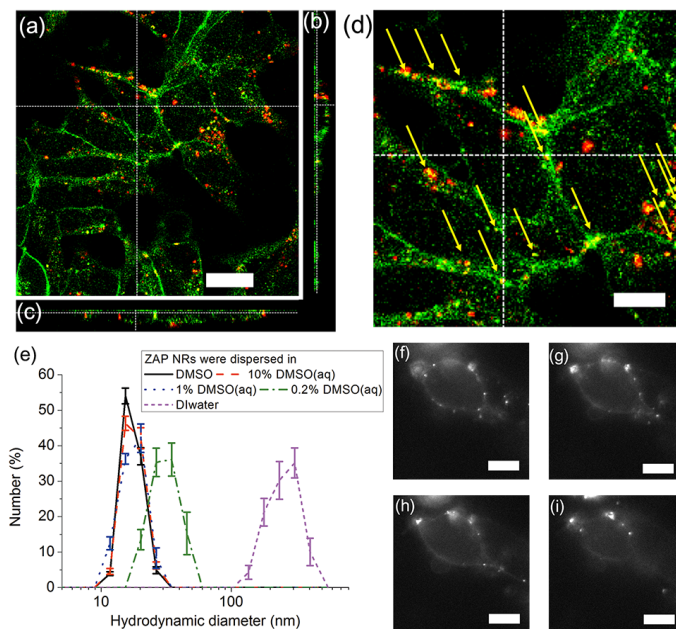


Fig. 2: (a) Confocal microscope image of both ZAP-NRs (red) and DiR dye (green) labeled HEK293T cells (scale bar: 20 μ m). Cross-section images of (b) yz and (c) xz plane through the white dotted line in (b). (d) Yellow arrows indicated colocalized ZAP NRs (red signals) with membrane labeling dyes (green signals) (scale bar: 10 μ m). (e) DLS-derived hydrodynamic diameters of ZAP-NRs in: DMSO (black solid), 10% DMSO(aq) (red dashed), 1% DMSO(aq) (blue dotted), 0.2% DMSO(aq) (green dash-dotted), DI water (violet short dashed). (f-i) Wide-field fluorescence images of ZAP-NRs labeled HEK293T cells at different heights from the focal plane (scale bar: 10 μ m).

At the diffraction-limited resolution of the confocal microscope, ZAP-NRs (red) and DiR dye (green) seem to be co-localized at the cell membrane (Fig. 2a and a zoom-in Fig 2d), as supported by *y-z* and *x-z* cross-section images (Figs. 2b, 2c) through the *yz*- or *xz*-planes. Wide-field fluorescence images at different focal planes also support co-localization (Figs. 2f-i).

We were able to observe the ZAP-NRs associated with the membrane after 1 hour incubation, while negatively- or positively-charged QDs were internalized much faster under similar conditions.⁸ We note, however, that these observations only report on the association of ZAP-NRs to membranes; they do not provide evidence for membrane insertion. Nonetheless, functional assays (reported below) do suggest that at least some

portion of the ZAP-NRs are inserted into the membrane.

To assess voltage sensitivity (at the ensemble level), ZAP-NRs were loaded into lipid

vesicles prepared in a HEPES buffer (20 mM, pH 7.4) with $[K^+] = 140$ mM and then placed into a isosmotic HEPES buffer (20 mM, pH 7.4) with $[K^+] = 2.7$ mM. This preparation establishes a potential of -101.4 mV (as determined by the Nernst equation) across the membrane. Valinomycin, a naturally occurring potassium ionophore (extracted from *Streptomyces* cells) was added at $t = 60$ sec to the vesicles. Once valinomycin was introduced, K^+ ions flowed (from inside to outside of the vesicles) to equalize the $[K^+]$ concentration gradient, thus abolishing the established membrane potential.¹⁰ Vesicle membrane labeling by ZAP-NRs was confirmed by fluorescence microscopy (Fig. S3). The ZAP-NRs photoluminescence (PL) intensity was monitored at 605 nm for 120 sec during this process (Figs. 3a, S4). Valinomycin was added at $t = 60$ sec. A clear drop in ZAP-NRs' PL is seen at this time point (red curve), from which we could calculate $\Delta F/F = 1.1 \pm 0.2$ % per 100 mV. The control experiments (no valinomycin added in same buffer condition (Figs. 3a, black circle) or no established membrane potential – by having the same $[K^+] = 2.7$ mM inside and outside of the vesicle – with valinomycin (Figs. 3b, blue circle) show no change in PL intensity (black and blue curves respectively, Figs. 3a,b). When a full PL spectrum of the ZAP-NRs was recorded, a similar drop of 1% was

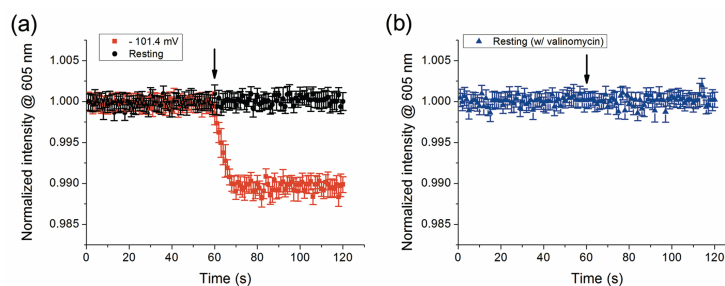


Fig. 3: (a) Time-lapse PL intensity measurement of ZAP-NRs labeled vesicles (a) under membrane potential of -101.4 mV (with $[K^+] = 2.7$ mM outside and $[K^+] = 140$ mM inside of the vesicle, red square). This potential was abolished at $t = 60$ sec after valinomycin addition (arrow). If valinomycin is not added, there is no change in the membrane potential (black circle). (b) Control experiment (blue triangle): time-lapse PL intensity measurement of ZAP-NRs labeled vesicle under resting conditions, with $[K^+] = 2.7$ mM outside and inside of the vesicle; valinomycin was added at $t = 60$ sec (arrow).

observed after the addition of valinomycin (Fig. S4).

Monitoring PL changes as function of time also allowed us to monitor the time it takes to establish the resting potential after the introduction of the $[K^+]=140$ mM vesicles into the $[K^+]=2.7$ mM buffer. The time for balancing the K^+ ion concentration between inside and outside of the vesicle was determined to be 9 secs. This time constant is mainly governed by K^+ ion transfer rate through the ionophore. The drop in PL intensity around $t=60$ secs (Fig. 3a, after the addition of valinomycin) can be governed by the mixing/diffusion of valinomycin, binding constant of valinomycin to the membrane, and the

K^+ ion transfer rate through the ionophore. A previous work reported 25 seconds for balancing the difference of $[K^+]$ between inside and outside of a human red blood cell membrane in the presence of valinomycin.¹¹ We note that PL quenching results for a quasi-type II QDs in PMMA matrix placed between electrodes and subjected to a synthetic voltage sweep of 20 mV yielded $\sim\Delta F/F=2\%$.¹² However, the actual field strength in this work could be quite different as compared to our experiment due to

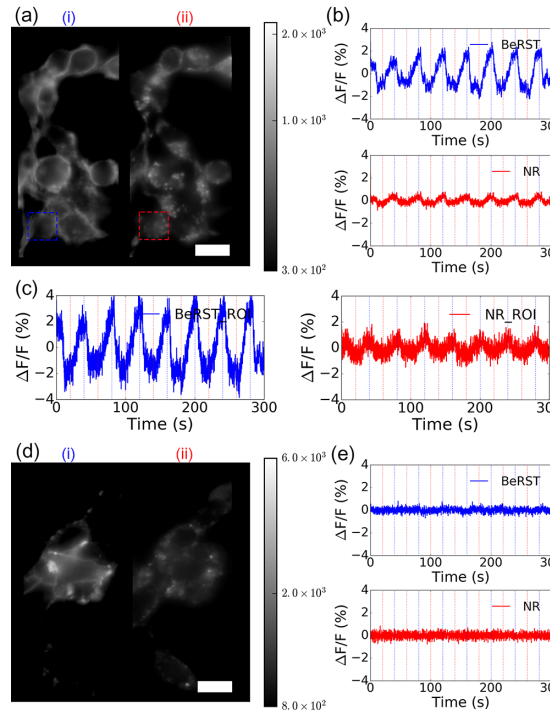


Fig. 4: Chemical modulation of membrane potential of live HEK293T cells. (a) Dual-channel fluorescence microscope images of labeled live HEK293T cells after the addition of valinomycin for (i) the voltage sensitive BeRST dye channel and for (ii) the ZAP-NRs channel. (d) Dual-channel fluorescence microscope images of labeled fixed HEK293T cells for (i) BeRST channel and for (ii) ZAP-NRs channel. (b) and (e) show $\Delta F(t)/F$ for the sum ('ensemble average') of all pixels above a threshold (see method) for BeRST (blue) and ZAP-NRs (red) from (a) and (d) respectively. (c) show $\Delta F(t)/F$ from certain region of interest (one of HEK293T cells) for BeRST (blue) and ZAP-NRs (red) from dotted-area (blue dotted area: BeRST, red dotted area: ZAP NRs in (a)). Blue or red dotted vertical lines indicate time points for either $[K^+]=2.7$ mM and $[K^+]=140$ mM buffer alternation (every 20 seconds, starting with $[K^+]=2.7$ mM at time = 0 s). Scale bar: 20 μ m

differences in local environments.

To evaluate the membrane potential sensitivity of ZAP-NRs under periodic membrane potential modulation, we pre-cultured HEK293T cells in a flow chamber, loaded ZAP-NRs, and recorded PL changes under periodic buffer exchange (of HEPES buffers containing either $[K^+] = 2.7$ mM or $[K^+] = 140$ mM, every 20 seconds, for 7 cycles). This chemical modulation method establishes cell membrane potential modulation in the presence of valinomycin.^{11, 13} HEK293T cells were cultured in poly-L-lysine pretreated flow chambers with 6 channels. Cells were first treated with 5 μ M of valinomycin for 5 minutes. 1 μ L ZAP-NRs (3 μ M stock, final concentration would be 30 nM) were then added to the culture medium of each chamber and incubated for 15 minutes. To confirm and calibrate the chemical voltage induction in live HEK293T cells, near infrared (NIR) voltage sensitive dye BeRST¹⁴ (final concentration would be 200 nM) were added to the cells and incubated for 15 minutes. After each labeling step, excess of ZAP-NRs and dyes was removed by a washing step with Dulbecco Modified Eagle Medium (DMEM) growth media (with 10% fetal bovine serum). Control samples were fixed with 4% paraformaldehyde for 10 minutes at room temperature (which disturbs the integrity of cell membrane and abolishes its membrane potential).

The flow chamber was placed on an inverted fluorescence microscope and connected to an automated controlled flow setup. The high ($[K^+] = 140$ mM) and low ($[K^+] = 2.7$ mM) concentrations of potassium buffers were continuously alternated every 20 seconds while a dual-view (for both BeRST and ZAP-NRs channels) movie was acquired for a duration of 300 seconds. The slow rise of the signal during each period (~10 seconds) is likely due to K^+ ion transfer rate through the ionophore after buffer exchange (denoted by dotted red or blue lines in Fig. 4b, 4c, and 4e, overlay graphs of

BeRST/ZAP NRs signals in Fig. S10). As we mentioned before, a previous report cites a similar 25 seconds to balance the difference of $[K^+]$ between inside and outside of human red blood cell membrane.¹¹

An 'ensemble level' $\Delta F(t)/F$ was calculated from the movie in the following way: First, all pixels above a threshold per single frame were averaged. This quantity was then averaged over all frames (time points) to yield F . Next, $\Delta F(t)$ was defined as the difference between the averaged intensity over all pixels for a single frame (for each time point) and F . This operation was performed for each spectral channel, yielding $\Delta F/F=3.5\pm 0.3\%$ for BeRST and $\Delta F/F=1.0\pm 0.3\%$ for ZAP-NRs per ~ 200 mV (Fig. 4b). The signal-to-noise ratio was defined as the ratio of an averaged $\Delta F(t)/F$ value over 7 cycles from valinomycin treated sample (Fig. 4b) to an averaged $\Delta F(t)/F$ value over 7 cycles from control sample (Fig. 4e). The $\Delta F/F$ cited above were obtained for signal-to-noise ratios of ~ 11 and ~ 3 respectively, and for a membrane potential sweep of -101.4 mV to $+101.4$ mV (as determined by the Nernst equation). To get the signal from a HEK293T cell, $\Delta F/F$ operation from certain region of interest (ROI, blue dotted area for BeRST channel and red dotted area for ZAP-NR channel in Figure 4a) was performed, yielding $\Delta F/F=4.9\pm 0.5\%$ for BeRST and $\Delta F/F=1.8\pm 0.5\%$ for ZAP-NRs (Figure 4c). As the absolute value of $\Delta F/F$ from the ROI of dual-labeled HEK293T cells under voltage sweep increased, the standard deviation of $\Delta F/F$ was also increased. Several control experiments were performed in order to validate the above result: (i) the same experiment ($[K^+]$ modulation) was performed for ZAP-NRs labeled, and valinomycin pretreated, HEK293T cells after fixation (with 4% paraformaldehyde solution in r.t. for 10 minutes). Fixation disturbed the integrity of membrane and abolishes its membrane potential. Indeed, no signal modulation was observed for fixed cells (Figs. 4d and 4e). This control eliminates the

possibility that the signal originates from direct photophysical property change due to the $[K^+]$ modulation itself, but it rather due to the membrane potential modulation; (ii) the same experiment ($[K^+]$ modulation) was performed for either ZAP-NRs-only or BeRST-only labeled live valinomycin pretreated HEK293T cells to eliminate the possibility that the ZAP-NRs signal (in doubly-labeled cells) originates from the BeRST signal (Fig. S5); (iii) the same experiment ($[K^+]$ modulation) was performed for Di-8-ANEPPS-labeled valinomycin pretreated live HEK293T cells. Di-8-ANEPPS is a well characterized and calibrated commercially available voltage sensitive dye (VSD), demonstrating similar PL modulation upon $[K^+]$ modulation for cells treated with valinomycin (Fig. S6). As voltage applied, $\Delta F/F$ for Di-8-ANEPPS would decreased in a conventional setup, whereas $\Delta F/F$ for BeRST increased.¹⁵⁻¹⁷ However, since we optimized the dichroic cut-off for ZAP-NRs spectra, and not for for Di-8-ANEPPS, the observed $\Delta F/F$ for the latter was 2.1 ± 0.4 %; (iv) Solution-based (*in vitro*) PL measurements of ZAP-NRs as function of $[K^+]$ (in the range $[K^+]=0.5$ mM to $[K^+]=200$ mM) and pH (in the range pH=5 to pH=10) were performed. No significant PL changes were observed (Fig. S7a and S7b); (v) Experiments with no $[K^+]$ modulation were performed on live HEK293T cells treated with valinomycin and doubly labeled with ZAP-NRs and BeRST. No PL modulations were observed (Fig. S8a-c); Lastly, (vi) no significant PL changes were observed for non-specifically adsorbed ZAP-NRs to glass surfaces (Fig. S8d-f) upon $[K^+]$ modulation, and no significant autofluorescence changes were observed for unlabeled live HEK293T cells upon $[K^+]$ modulation (Fig. S8g-i).

Discussion

The results shown in Fig. 4 and the series of control experiments suggest that the

$\Delta F/F$ signal reports on membrane potential modulation at the ensemble level. Although the magnitude of $\Delta F/F$ is very small ($\sim 1\%$), this result is statistically significant, and quite surprising.

We previously demonstrated that quasi-type-II CdSe/CdS seeded NRs can report on membrane potential via the quantum confined Stark effect (QCSE) at the single particle level and measured the QCSE for type-II ZnSe/CdS seeded NRs at the single particle level under *in vitro* conditions.³⁻⁴ In the later cases, single particle QCSE measurements exhibited slightly different distributions of positive (43%) and negative (57%) $\Delta F/F$ for randomly oriented type-II ZnSe/CdS seeded NRs. This slight asymmetry could possibly explain the small $\Delta F/F$ measured here on the ensemble level.

We also observed, in disagreement with QCSE predictions, positive correlation between spectral shifts ($\Delta\lambda$) and PL changes ($\Delta F/F$) for type-II ZnSe/CdS seeded nanorods⁴. We hypothesized that extrinsic charging/ionization at surface- and interface-defects¹⁸ could possibly modulate blinking rates (and hence QY) and contribute to the positive $\Delta\lambda$ - $\Delta F/F$ correlation. Such contributions could add up at the ensemble level and therefore be responsible for the ensemble signal observed here. Further studies that correlate spectral, intensity and lifetime measurements under applied electric field and at different excitation powers are currently the topic of a follow-up project.

Conclusions

We have demonstrated QY modulation, at the ensemble level, of functionalized and membrane-targeted type-II ZnSe/CdS seeded nanorods for vesicles treated with valinomycin and for wild type HEK cells under alternating buffers with varying K^+ concentrations. $\Delta F/F$ of $\sim 1\%$ per 200 mV were achieved. Although the mechanism for

these QY modulations is not confirmed as of yet (and is currently under investigation), it is likely not due to the QCSE. Regardless of the mechanism (QCSE or charging/quenching), voltage-sensing nanorods could possibly open up a new nano-neuroscience avenue for highly sensitivity, noise-immune action potential visualization across a large neural network.

Acknowledgements:

We acknowledge Dr. H. Ronald Kaback for assisting with the chemically driven cell membrane modulation assay. We acknowledge Dr. Emory Chan for help with the WANDA instrument. We acknowledge the help of Antonino Ingargiola for processing data from the modulation assay. We also acknowledge the use of instruments at the Electron Imaging Center for NanoMachines supported by the NIH (1S10RR23057 and GM071940 to Z.H.Z.) and the Advanced Light Microscopy/Spectroscopy core, both at the California NanoSystems Institute in the University of California, Los Angeles. Lastly, we acknowledge the participation in the USER Program (#1726 and #3244) of the Molecular Foundry at the Lawrence Berkeley National Laboratory, which was supported by the U.S. Department of Energy Office of Science, Office of Basic Energy Sciences under contract no. DE-AC02-05CH11231. S.W. acknowledges funding from the United States–Israel Binational Science Foundation (#2010382), the Human Frontier Science Program (#RGP0061/2015), the Defense Advanced Research Projects Agency/Biological Technologies Office award no. #D14PC00141, the European Research Council (ERC) advanced grant NVS #669941, and the BER program of the Department of Energy Office of Science, grant # DE-FC03-02ER63421. This work was also supported by STROBE: A National Science Foundation Science & Technology Center under Grant No. DMR 1548924.”

Materials and Methods

Materials: All chemicals are used as purchased without further purification. Trioctylphosphine oxide (TOPO, 99%), Octadecylphosphonic acid (ODPA) and

hexylphosphonic acid (HPA) were purchased from PCI Synthesis. Tri-n-octylphosphine (TOP, 97%) was obtained from Strem Chemicals. Cadmium oxide (CdO), octadecylamine (ODA), hexadecylamine (HDA), octadecanethiol (ODT), 1.0 M diethylzinc ($\text{Zn}(\text{Et})_2$) solution in hexanes, trimethyloxonium tetrafluoroborate (>95%), potassium chloride (KCl), (\pm)-alpha-lipoic acid (99%), N,N-dimethylethylenediamine (>98%), 1,3-propanesultone (>98%), tris(2-carboxyethyl)phosphine (TCEP) hydrochloride, anhydrous chloroform, tetramethylammonium hydroxide solution (25% in methanol), dimethyl sulfoxide, and valinomycin (>97%) were purchased from Sigma-Aldrich. Selenium powder (99.999%, 200 mesh) was purchased from Alfa aesar. Di-8-anepps (D3167), DiR membrane labeling dye (D12731), Phenol-free DMEM, fetal bovine serum, penicillin/streptomycin, and trypsin solution were purchased from Thermo Fisher Scientific. The CG25 peptides were purchased from LifeTein. DOTAP (10 mg/mL in chloroform), DMPC (25 mg/mL in chloroform), and DC-cholesterol (10 mg/mL in chloroform) were purchased from Avanti Polar Lipids.

Preparation of ZnSe/CdS type-II nanorods

The procedure for synthesis of ZnSe quantum dots was adopted from a previous work.⁶ The procedure for synthesis of ZnSe quantum dots was adopted from a previous work.⁶ Briefly, a mixture of Se (63 mg), TOP (2 g) and diethyl zinc solution (0.8 ml, 1 M) was injected into degassed HDA (7 g) at 300 °C in argon atmosphere. The reaction was kept at 265 °C until the desired absorption peak at 360 nm was observed (~30 mins after injection). After the flask was cooled to room temperature, ZnSe quantum dots were purified 3 times by butanol/methanol precipitation and redispersed in toluene. The concentration of ZnSe in toluene was documented by the optical density (OD) at the absorption peak through a 1 cm cuvette.

ZnSe seeded CdS nanorods were synthesized using WANDA.¹⁹ CdO (270 mg), ODPA (1305 mg), HPA (360 mg), and TOPO (13.5 g) were first degassed at 100 °C under vacuum for 2 hrs. The mixture was heated to 230 °C under nitrogen blanket until CdO powder was dissolved and a colorless solution was obtained. The solution was cooled down to 100 °C, ODA was added (180 mg), and the solution was degassed under vacuum for additional 2 hrs. To prepare the S precursor solution with ZnSe, 1440 mg of ODT were mixed with 36 units [OD (under 1 cm path length) × ml] of ZnSe solution in toluene and degassed 100 °C under vacuum to remove the toluene and moisture. After degassing, both Cd precursor solution and S precursor with ZnSe were transferred under vacuum into a glove box and dispensed gravimetrically into the 40 ml glass vials used as reaction vessels for the robot. The filled vials were loaded into the eight-reactor array of WANDA, an automated nanocrystal synthesis robot at the Molecular Foundry. WANDA was used to run up to eight reactions in serial with individually controlled heating/cooling profiles, stirring rate, injections and aliquot schedules. Below is the description of an exemplary run. 1.133 ml of S/ZnSe solution (heated to 50 °C to prevent solidification) was injected into 15.615 g of Cd solution at 330 °C at a dispense rate of 1.5 ml/sec. The temperature after injection was set at 320 °C for CdS NR growth. The heating was stopped 15 mins after injection. To thermally quench the reaction, each reaction was then rapidly cooled to 50°C using a stream of nitrogen, after which 5 ml of acetone was injected.

Functionalization of NRs by zwitterionic decorated lipoic acids (zw-LA) and alpha-helical peptides

100 mg of as synthesized NRs were mixed with 0.5 mL of stripping agent solution (0.1 M trimethyloxonium tetrafluoroborate in hexane) and the solution was

heated to 55 °C for 5 minutes. It was then spun down (10,000 rcf, 2 minutes) and the clear supernatant solution containing the NRs was recovered. Next, the solvent was completely removed by vacuum at 50 °C. 0.5 mL of octanoic acid was added to the dried NRs and sonicated for 5 minutes. 0.1 mL of methanol was added to the NRs solution and the mixture was spun down (10,000 rcf, 2 minutes). The NRs' precipitate was redispersed in 0.5 mL of pyridine. 0.2 mL of hexane was added to the NRs solution and spun down (10,000 rcf, 2 minutes). The NRs were then redispersed in 0.5 mL of pyridine. The extinction coefficient of the NRs was determined by ICP-AES measurement to be $\epsilon = 8 \times 10^6 \text{ L mol cm}^{-1}$. NRs' absorbance at 400 nm (in pyridine) was used to construct a concentration calibration curve. For the preparation of 3 μM NRs stock solution, 0.1 nmol NRs in 1 mL pyridine solution was placed in glass vial. 3 μmol of the alpha helical peptides (CG25, sequence: $\text{C}_{13}(\text{myristoyl})\text{-CLTCALTCMECTLKCWYKRGCRGCG-carboxylate}$) in 1.8 mL DMSO and 10 μL of the zwitterionic decorated lipoic acids (zw-LA)⁷ (from 0.1 M stock solution in DI water), which were reduced by adding 40 μL of tris(2-carboxyethyl)phosphine (TCEP, 0.5 M stock solution in DI water, pH 7.0) to the solution. The reduced peptides / zw-LA mixture was added to the NRs solution in pyridine and vigorously stirred for 10 minutes. 5 μL of 5% tetramethylammonium hydroxide (TMAOH) solution in methanol was then added to the crude NR solution and the mixture was then spun down (10,000 rcf, 2 minutes). The precipitate of NRs was redispersed in 33 μL DMSO and to yield 3 μM of functionalized NRs solution. NRs' QY was determined by comparison to the known QY of the reference rhodamine 101 (Rhodamine 640) dye. PL spectrum of the sample was measured by PTI QuantaMaster spectrofluorometer (HORIBA).

Cell Culture

HEK293T cells (human embryonic kidney cell line) were maintained in DMEM media (GIBCO) supplemented with 10% (v/v) fetal bovine serum (FBS) and 1% (v/v) penicillin/streptomycin (growth media) for cell adhesion. Culture media was replaced 24 hours prior to imaging and $[K^+]$ modulation experiments with phenol red-free DMEM media supplemented with 10% (v/v) fetal bovine serum (FBS) and 1% (v/v) penicillin/streptomycin (imaging media)

Membrane loading of ZAP-NRs for $[K^+]$ modulation experiments

Cultured HEK293T cells (~5,000 cells per channel, 6-channels μ -slide chamber, ibidi) were co-incubated with 5 μ M valinomycin for 5 minutes at 37°C. Excess amount of valinomycin was removed by washing 3 times with phenol red-free DMEM media. 30 nM of ZAP-NRs were directly added in the DMEM media and incubated for 15 minutes at room temperature. For dual labeled with BeRST dye, 200 nM of BeRST in DMSO was incubated for 15 minutes sequentially. Control samples were identically prepared skipping the valinomycin loading step. For fixation, cells were incubated in 4% paraformaldehyde (in 0.01M PBS buffer, pH 7.4) for 10 minutes at room temperature and washed twice with 0.01M PBS buffer. For $[K^+]$ modulation experiments, two reservoirs containing $[K^+]=140$ mM KCl and $[K^+]=2.7$ mM KCl with 274.6 mM sucrose in HEPES buffer (20 mM, pH 7.4) were connected to a single inlet tube (via a T-connector) of the flow chamber and controlled via computer-controlled valves. The constant flow rate (5 mL/min) was controlled by peristaltic pump. The outlet of the chamber was connected via another single tube to the waste reservoir. A home-written Labview code controlled the valves via a USB DAQ (USB-6001, National Instruments) and provided a trigger

signal to the EMCCD (Ixon EM⁺ EMCCD, Andor). An ‘ensemble level’ $\Delta F(t)/F$ was calculated in the following way: An ‘ensemble level’ $\Delta F(t)/F$ was calculated from the movie in the following way: First, all pixels above a threshold (Fig S9) per single frame were averaged. This quantity was then averaged over all frames (time points) to yield F . Next, $\Delta F(t)$ was defined as the difference between the averaged intensity over all pixels for a single frame (for each time point) and F .

Optical imaging

For dual-view setup in chemical modulation assay using two different potassium buffers, The microscope setup was based on a Nikon Ti inverted microscope equipped with LED light source (Aura, Lumencor) and excitation filter (ET470/40x, Chroma Technology Corp). The emissions of the NRs and BeRST dye were collected by x60 oil immersion, 1.4 NA objective was used for all imaging experiments. A 530 nm LP emission filter filter (E530LP, Chroma Technology Corp) and multiband dichroic mirror (FF545/650-Di01, Semrock) were used to block the LED excitation and pass the emission to the dual-view Optosplit unit (Optosplit II, Cairn Research) which was mounted in front of Andor iXon EMCCD camera (Andor iXon EM⁺, Andor). The optosplit was configured with a 640 nm dichroic (FF640-FDi01, Semrock) and 700 nm LP filters (FELH0700, Thorlab) for the BeRST channel, and with 585/40 bandpass filter (FF01-585/40, Semrock) for ZAP-NRs channel. The excitation intensity was adjusted to 0.2 mW/cm² in front of the objective lens. Wide-field fluorescence images of ZAP-NRs labeled cells were acquired with a Nikon Ti inverted microscope equipped with LED light source (Aura, Lumencor) and TxRed filter cube (BP 560/40 for excitation, 595DC, BP 630/60 for emission). Images were recorded with an Ador iXon EMCCD camera (Andor iXon EM⁺, Andor).

Co-localization by confocal microscopy

HEK293T cells were cultured in glass-bottom dishes (diameter: 35 mm; 3×10^5 cells per dish) were incubated with 30 nM ZAP-NRs for 1 hour and with 2 μ M DiR dye (D12731, Thermo Fisher Scientific) for 15 minutes at 37 °C, sequentially. Excess amounts of both the dyes and the NRs were removed by 3 successive washing steps with phenol red-free DMEM media. The cells were fixed with 4% paraformaldehyde (in 0.01M PBS buffer, pH 7.4) for 10 minutes at room temperature. Fixed cells were washed 3 times with PBS buffer (0.01 M, pH 7.4) and placed in phenol red-free DMEM media. Confocal images were recorded by an inverted Leica TCS-SP8-SMD Confocal Microscope at the CNSI's Advanced Light Microscopy/ Spectroscopy core facility.

DLS measurements

10 nM ZAP-NRs (as final concentration) samples were dispersed in 0.2, 1, 10 % DMSO (aq) solution. For control samples, 100% DMSO and DI water were used as solvents. The Wyatt DynaPro Plate Reader II (Wyatt Technology) was used to acquire DLS data and extract hydrodynamic radii of the samples.

GUVs preparation and ZAP-NRs loading for $[K^+]$ modulation experiments

Giant unilamellar vesicles (GUVs) were prepared according to the following protocol: 6 μ L of 1,2-dioleoyl-3-trimethylammonium-propane (chloride salt) (DOTAP, 10 mg/mL in chloroform), 6 μ L of 1,2-dimyristoyl-sn-glycero-3-phosphocholine (DMPC, 25 mg/mL in chloroform), 6 μ L of (3 β -[N-(N',N'-dimethylaminoethane)-carbamoyl]cholesterol hydrochloride, DC-cholesterol, 10 mg/mL in chloroform) were

mixed in glass vial and chloroform was removed under vacuum at room temperature. 1 mL HEPES buffer (20 mM, pH 7.4) with KCl ($[K^+]=140$ mM) was added to the dried lipids in the glass vial and incubated at 37°C for 24 hours. The vial was vigorously shaken and stored at 37°C for 24 hours to form GUVs. For ZAP-NRs labeling, 1 μ L of ZAP NRs stock solution (3 μ M) were treated to the GUVs and incubated for 5 minutes. To build up the membrane potential, the 1 μ L of GUV solution was diluted in 1 mL HEPES buffer (20 mM, pH 7.4) with KCl ($[K^+]=2.7$ mM with with 274.6 mM sucrose) Valinomycin was added after 60 seconds from the starting time for acquiring PL data of ZAP NRs loaded GUVs. Time-lapse PL intensity of each sample for 120 seconds at ZAP NRs peak wave length (605 nm) was measured by PTI QuantaMaster spectrofluorometer (HORIBA).

In-vitro PL measurements of ZAP-NRs as function of $[K^+]$ and pH

PL measurements of ZAP-NRs as function of $[K^+]$: 300 nM of ZAP-NRs were placed in 0, 0.5, 1, 2, 5, 10, 20, 50, 100, and 200 mM of potassium chloride contained HEPES buffer. To maintain constant ionic strength, 400, 399, 398, 396, 390, 380, 360, 300, 200, and 0 mM of sucrose were dissolved and added to each HEPES buffer, respectively. PL spectrum of each sample was measured by PTI QuantaMaster spectrofluorometer (HORIBA).

PL measurements of ZAP-NRs as function of pH: 300 nM of ZAP-NRs were placed in pH 4, 6, 7.4, 8, 10 buffer (for pH 4; 50 mM acetate buffer, for pH 6, 7.4; 50 mM MES buffer, for pH 8, 10; 50 mM PBS buffer). PL spectrum of each sample was measured by PTI QuantaMaster spectrofluorometer (HORIBA).

References

1. Park, K.; Deutsch, Z.; Li, J. J.; Oron, D.; Weiss, S., Single Molecule Quantum-Confined Stark Effect Measurements of Semiconductor Nanoparticles at Room Temperature. *ACS Nano* **2012**, *6* (11), 10013-10023.
2. Park, K.; Weiss, S., Design Rules for Membrane-Embedded Voltage-Sensing Nanoparticles. *Biophys. J.* **2017**, *112* (4), 703-713.
3. Park, K.; Kuo, Y.; Shvadchak, V.; Ingargiola, A.; Dai, X.; Hsiung, L.; Kim, W.; Zhou, H.; Zou, P.; Levine, A. J.; Li, J.; Weiss, S., Membrane insertion of—and membrane potential sensing by—semiconductor voltage nanosensors: Feasibility demonstration. *Science Advances* **2018**, *4* (1).
4. Kuo, Y.; Li, J.; Meir, N.; Michalet, X.; Chan, E.; Oron, D.; Weiss, S., Optimizing the Quantum Confined Stark Effect in Nanorods for Single-Molecule Electrophysiology. *ArXiv e-prints* **2018**.
5. Bar-Elli, O.; Steinitz, D.; Yang, G.; Tenne, R.; Ludwig, A.; Kuo, Y.; Triller, A.; Weiss, S.; Oron, D., Rapid Voltage Sensing with Single Nanorods via the Quantum Confined Stark Effect. *ACS Photonics* **2018**, *5* (7), 2860-2867.
6. Efros, A. L.; Delehanty, J. B.; Huston, A. L.; Medintz, I. L.; Barbic, M.; Harris, T. D., Evaluating the potential of using quantum dots for monitoring electrical signals in neurons. *Nat. Nanotechnol.* **2018**, *13* (4), 278-288.
7. Dorfs, D.; Salant, A.; Popov, I.; Banin, U., ZnSe Quantum Dots Within CdS Nanorods: A Seeded-Growth Type-II System. *Small* **2008**, *4* (9), 1319-1323.
8. Park, J.; Nam, J.; Won, N.; Jin, H.; Jung, S.; Jung, S.; Cho, S.-H.; Kim, S., Compact and Stable Quantum Dots with Positive, Negative, or Zwitterionic Surface: Specific Cell Interactions and Non-Specific Adsorptions by the Surface Charges. *Adv. Funct. Mater.* **2011**, *21* (9), 1558-1566.
9. Rosen, E. L.; Buonsanti, R.; Llordes, A.; Sawvel, A. M.; Milliron, D. J.; Helms, B. A., Exceptionally Mild Reactive Stripping of Native Ligands from Nanocrystal Surfaces by Using Meerwein's Salt. *Angew. Chem. Int. Ed.* **2012**, *51* (3), 684-689.
10. Montana, V.; Farkas, D. L.; Loew, L. M., Dual-wavelength ratiometric fluorescence measurements of membrane potential. *Biochemistry* **1989**, *28* (11), 4536-4539.
11. Bifano, E. M.; Novak, T. S.; Freedman, J. C., Relationship between the shape and the membrane potential of human red blood cells. *J. Membr. Biol.* **1984**, *82* (1), 1-13.
12. Rowland, C. E.; Susumu, K.; Stewart, M. H.; Oh, E.; Mäkinen, A. J.; O'Shaughnessy, T. J.; Kushto, G.; Wolak, M. A.; Erickson, J. S.; L. Efros, A.; Huston, A. L.; Delehanty, J. B., Electric Field Modulation of Semiconductor Quantum Dot Photoluminescence: Insights Into the Design of Robust Voltage-Sensitive Cellular Imaging Probes. *Nano Lett.* **2015**, *15* (10), 6848-6854.
13. Kao, L.; Azimov, R.; Shao, X. M.; Frausto, R. F.; Abuladze, N.; Newman, D.; Aldave, A. J.; Kurtz, I., Multifunctional ion transport properties of human SLC4A11: comparison of the SLC4A11-B and SLC4A11-C variants. *Am. J. Physiol. Cell Physiol.* **2016**, *311* (5), C820-C830.
14. Huang, Y.-L.; Walker, A. S.; Miller, E. W., A Photostable Silicon Rhodamine Platform for Optical Voltage Sensing. *J. Am. Chem. Soc.* **2015**, *137* (33), 10767-10776.

15. DiFranco, M.; Capote, J.; Vergara, J. L., Optical Imaging and Functional Characterization of the Transverse Tubular System of Mammalian Muscle Fibers using the Potentiometric Indicator di-8-ANEPPS. *J. Membr. Biol.* **2005**, *208* (2), 141-153.
16. Kao, W. Y.; Davis, C. E.; Kim, Y. I.; Beach, J. M., Fluorescence Emission Spectral Shift Measurements of Membrane Potential in Single Cells. *Biophys. J.* **2001**, *81* (2), 1163-1170.
17. Manno, C.; Figueroa, L.; Fitts, R.; Ríos, E., Confocal imaging of transmembrane voltage by SEER of di-8-ANEPPS. *J. Gen. Physiol.* **2013**, *141* (3), 371-387.
18. Park, S.-J.; Link, S.; Miller, W. L.; Gesquiere, A.; Barbara, P. F., Effect of electric field on the photoluminescence intensity of single CdSe nanocrystals. *Chem. Phys.* **2007**, *341* (1), 169-174.
19. Chan, E. M.; Xu, C.; Mao, A. W.; Han, G.; Owen, J. S.; Cohen, B. E.; Milliron, D. J., Reproducible, High-Throughput Synthesis of Colloidal Nanocrystals for Optimization in Multidimensional Parameter Space. *Nano Lett.* **2010**, *10* (5), 1874-1885.

Supporting information

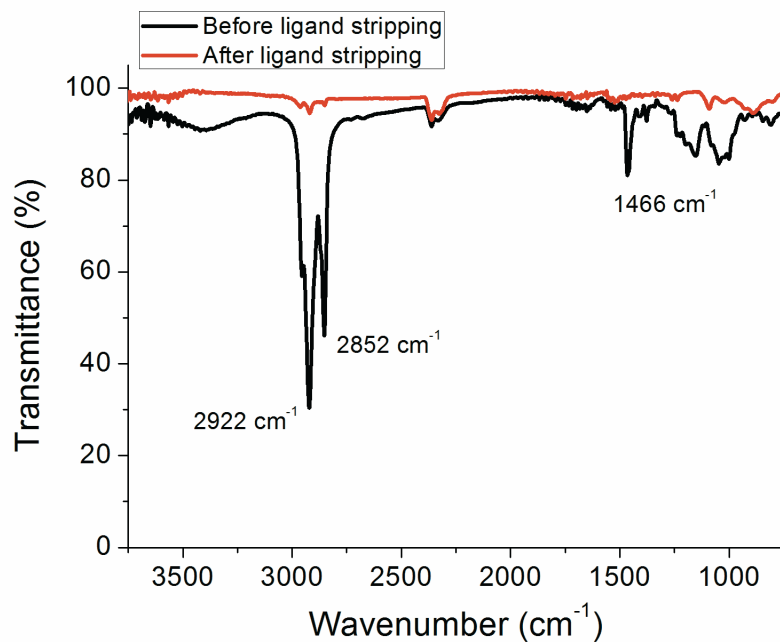


Fig. S1: Infrared (IR) spectrum of ZnSe/CdS nanorods before (black) and after (red) the ligand stripping process with trimethyloxonium tetrafluoroborate (Meerwein's salt; see Materials and Method).

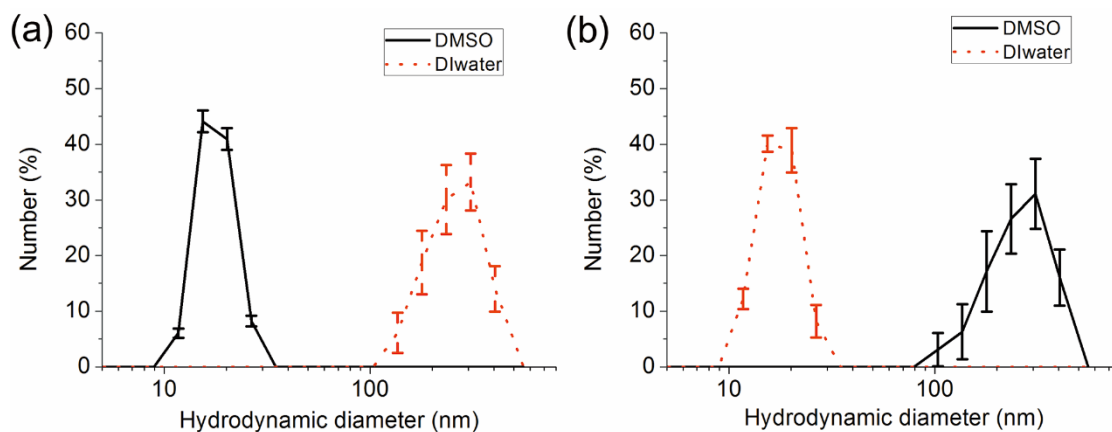


Fig. S2: Dynamic light scattering (DLS) plots of hydrodynamic diameters of (a) peptide coated ZnSe/CdS NRs and (b) zwitterionic ligand coated ZnSe/CdS NRs (ZAP-NRs) in either DMSO (black solid line) or DIwater (red dotted line).

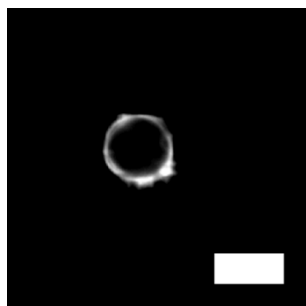


Fig. S3: Wide-field fluorescence image of ZAP-NRs-labeled giant unilamellar vesicle (GUV, scale bar: 10 μm).

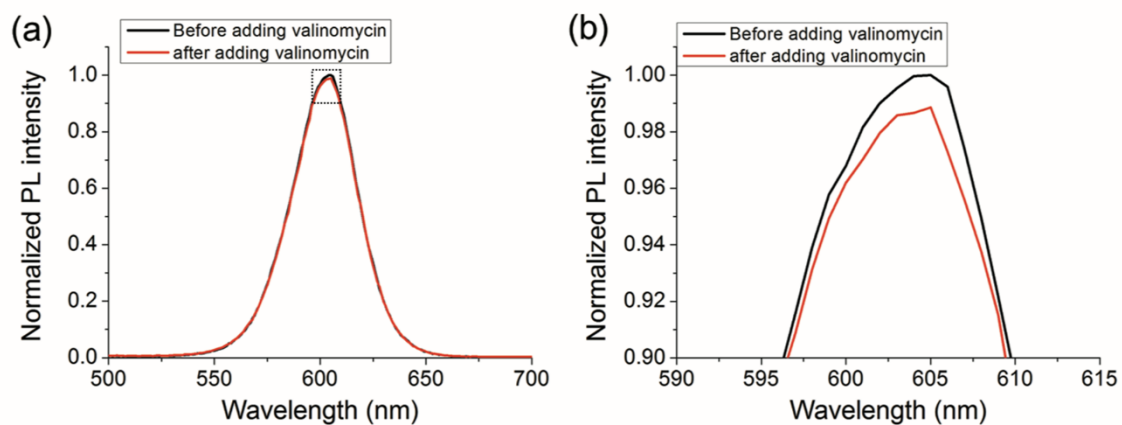


Fig. S4: (a) PL spectra of ZAP-NRs-labeled vesicles with $[\text{K}^+] = 140 \text{ mM}$ inside and $[\text{K}^+] = 2.7 \text{ mM}$ outside potassium contained buffers (establishing $\Delta V = -101.4 \text{ mV}$ across the membrane) before (black) and after (red) addition of valinomycin. (b) zoom-in to the black dotted area in (a).

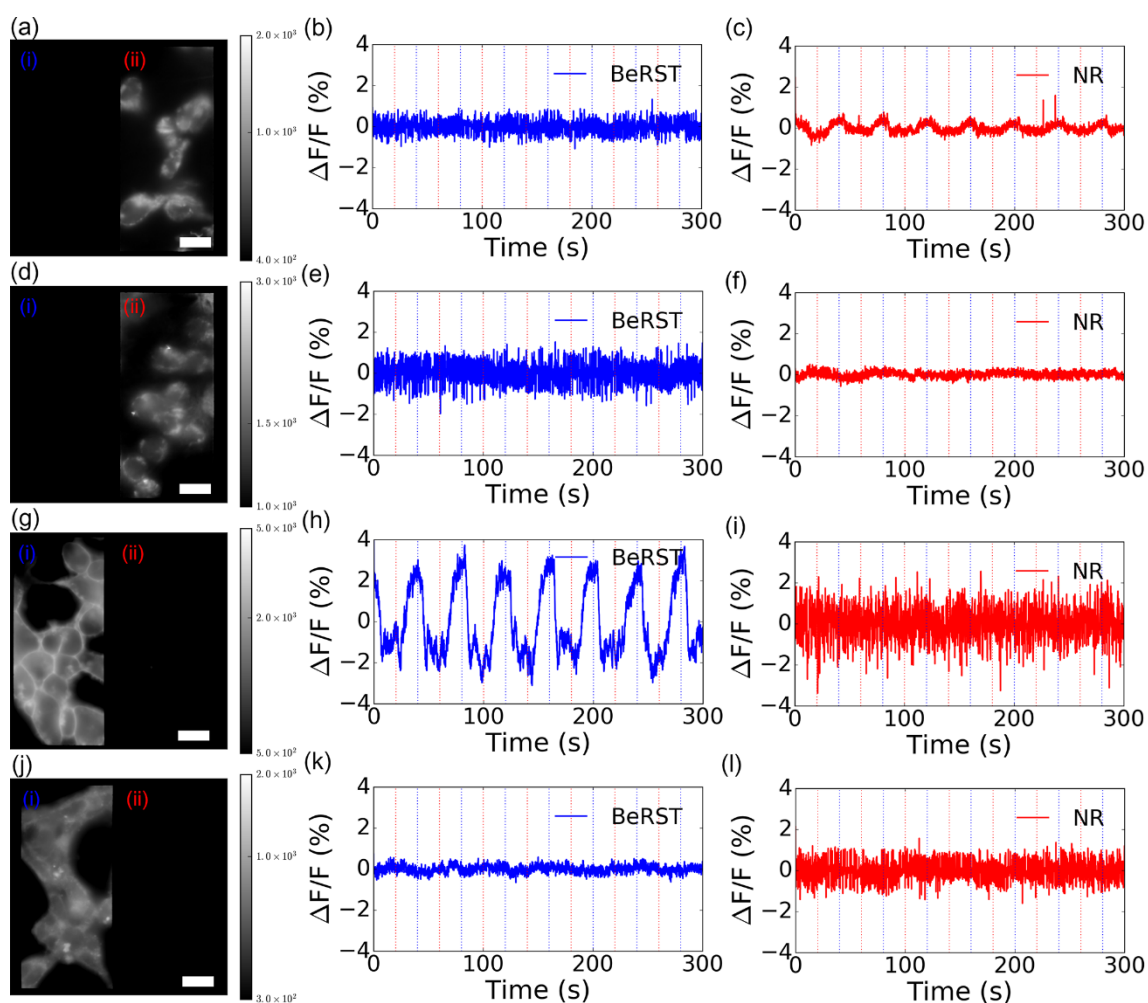


Fig. S5: Control experiments for chemical modulation of HEK293T cells membrane potential. Left column (a,d,g,j): Dual-channel fluorescence microscope images of labeled HEK293T cells for (i) the voltage sensitive BeRST dye channel and for (ii) the ZAP-NRs channel. Center column (b,e,h,k): $\Delta F(t)/F$ for the sum ('ensemble average') of all pixels above a threshold (see M&M) for BeRST (blue). Right column (c,f,i,l): $\Delta F(t)/F$ for the sum ('ensemble average') of all pixels above a threshold (see M&M) for ZAP-NRs (red). Different rows represent different control conditions. Top row (a,b,c): live HEK293T cells with valinomycin. Second row (d,e,f): fixed HEK293T cells. Third row (g,h,i): live HEK293T cells with valinomycin. Last row (j,k,l): fixed HEK293T cells. Red or blue dotted vertical lines indicate time points for $[K^+] = 140$ mM and $[K^+] = 2.7$ mM buffer alternation (every 20 seconds). Scale bar: 20 μ m

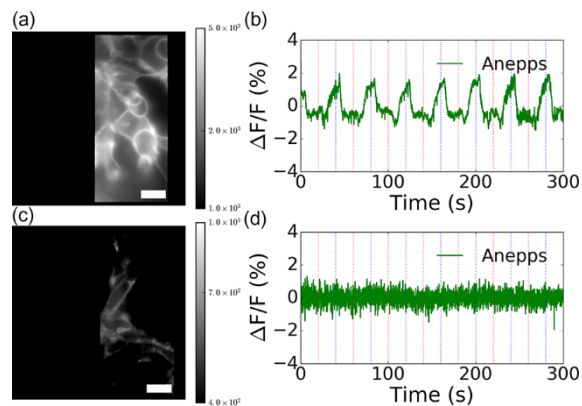


Fig. S6: Control experiments for chemical modulation of HEK293T cells membrane potential. Left column (a,c): Dual-channel fluorescence microscope images of labeled HEK293T cells for the voltage sensitive di-8-anepps dye channel (right side of the image). Right column (b,d): $\Delta F(t)/F$ for the sum ('ensemble average') of all pixels above a threshold (see M&M) for di-8-anepps (green). Different rows represent different control conditions. Top row (a,b): live HEK293T cells with valinomycin. Bottom row (c,d): fixed HEK293T cells. Red or blue dotted vertical lines indicate time points for $[K^+]=140$ mM and $[K^+]=2.7$ mM buffer alternation (every 20 seconds). Scale bar: 20 μ m

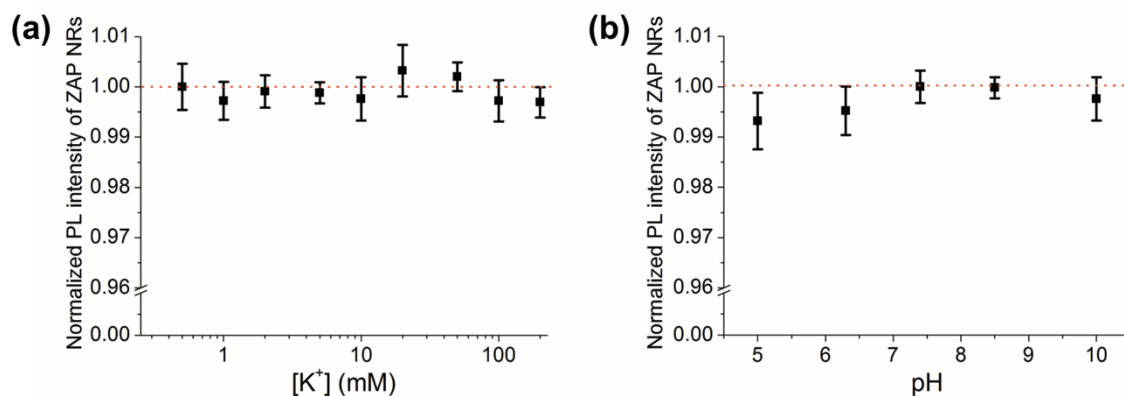


Fig. S7: *In-vitro* PL measurements of ZAP-NRs as function of (a) $[K^+]$ in the range $[K^+]=0.5$ mM to $[K^+]=200$ mM and (b) pH in the range pH=5 to pH=10.

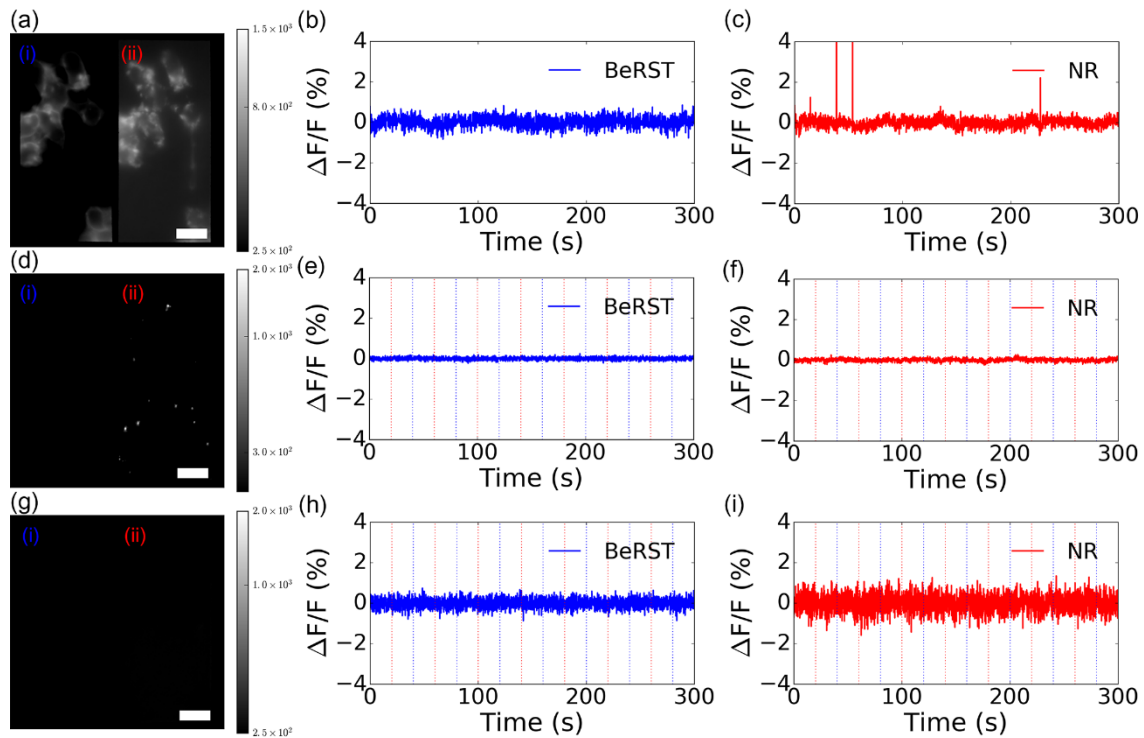


Fig. S8: Control experiments for chemical modulation of HEK293T cells membrane potential. Left column (a,d,g): Dual-channel fluorescence microscope images of labeled HEK293T cells for (i) the voltage sensitive BeRST dye channel and for (ii) the ZAP-NRs channel. Center column (b,e,h): $\Delta F(t)/F$ for the sum ('ensemble average') of all pixels above a threshold (see M&M) for BeRST (blue). Right column (c,f,i): $\Delta F(t)/F$ for the sum ('ensemble average') of all pixels above a threshold (see M&M) for ZAP-NRs (red). Different rows represent different control conditions. Top row (a,b,c): live HEK293T cells with valinomycin and no $[K^+]$ modulation. Second row (d,e,f): non-specifically adsorbed on the poly-L-lysine coated glass substrate. Last row (g,h,i): unlabeled HEK293T cells. Red or blue dotted vertical lines indicate time points for $[K^+] = 140$ mM and $[K^+] = 2.7$ mM buffer alternation (every 20 seconds). Scale bar: 20 μ m

Chapter 5

Membrane potential reporting in live cells using functionalized nanorods

This chapter describes the functionalization of the synthesized nanorods and the detailed characterization and analysis of their membrane insertion efficiency. The functionalized nanorods were tested for capability of reporting membrane potential in voltage-clamped human embryonic kidney (HEK) cells. This chapter is a reprint of the original article from *Science Advances* **2018**, *4* (1), e1601453, titled “Membrane insertion of—and membrane potential sensing by—semiconductor voltage nanosensors: Feasibility demonstration.”, by authors: Park, K.; Kuo, Y.; Shvadchak, V.; Ingargiola, A.; Dai, X.; Hsiung, L.; Kim, W.; Zhou, H.; Zou, P.; Levine, A. J.; Li, J.; Weiss, S. DOI: 10.1126/sciadv.1601453 © The Authors, some rights reserved; exclusive licensee American Association for the Advancement of Science. Distributed under a Creative Commons Attribution NonCommercial License 4.0 (CC BY-NC) <http://creativecommons.org/licenses/by-nc/4.0/>. Reprinted with permission from AAAS.

APPLIED PHYSICS

Membrane insertion of—and membrane potential sensing by—semiconductor voltage nanosensors: Feasibility demonstration

Kyoungwon Park,¹ Yung Kuo,¹ Volodymyr Shvadchak,² Antonino Ingargiola,¹ Xinghong Dai,³ Lawrence Hsiung,⁴ Woogyeon Kim,⁵ Z. Hong Zhou,^{3,6} Peng Zou,^{7*} Alex J. Levine,^{1,8} Jack Li,¹ Shimon Weiss^{1,6,9†}

We developed membrane voltage nanosensors that are based on inorganic semiconductor nanoparticles. We provide here a feasibility study for their utilization. We use a rationally designed peptide to functionalize the nanosensors, imparting them with the ability to self-insert into a lipid membrane with a desired orientation. Once inserted, these nanosensors could sense membrane potential via the quantum confined Stark effect, with a single-particle sensitivity. With further improvements, these nanosensors could potentially be used for simultaneous recording of action potentials from multiple neurons in a large field of view over a long duration and for recording electrical signals on the nanoscale, such as across one synapse.

INTRODUCTION

Recent advances in inorganic colloidal synthesis methods have afforded the construction of functional semiconductor (SC) nanoparticles (NPs) with ever-increasing control over size, shape, composition, and sophisticated heterostructures that exhibit unique photophysical, chemical, and electronic properties (1–4). This precise command of nanoscale materials synthesis has allowed for the exquisite engineering of excited-state wavefunctions (5–7), charge confinement, spatiotemporal control of charge-separated states (8), and manipulation of Fermi levels and redox potentials. As a result, SC NPs have proved to be very useful in numerous applications in optoelectronics (9, 10), biological imaging (11), sensing (12–14), catalysis (15), and energy harvesting (16).

Integrating inorganic nanomaterials with naturally evolved or synthetically evolved biological machineries could, in principle, yield highly sophisticated hybrid nanobiomaterials that outperform biological-only or inorganic-only materials (17). These materials could be self-assembled by biomolecular recognition while maintaining the superior properties of inorganic materials (18, 19). Self-assembly of inorganic components by biomolecular recognition could align components in defined geometries, spatial orientations, and structures. In addition, careful design and control of the organic-inorganic interface could afford hybridization of electronic states, enhancement of radiationless energy transfer or electron transfer, or matching of Fermi levels with redox potentials.

Numerous functionalization and bioconjugation methods have been developed for the integration of inorganic-biological hybrid

nanomaterials that are water-soluble and biologically active (20, 21). These hybrid nanomaterials have been used for in vitro biosensing, intracellular biological imaging (22), single-protein tracking in live cells (20), and in vivo molecular imaging with favorable in vivo bio-distribution and targeting properties (including renal clearance) (11, 23, 24).

Much fewer attempts have been made to functionalize nanomaterials in a way that will allow their integration into the membrane. The ability to impart membrane protein-like properties to NPs could afford their targeting and insertion into the lipid bilayer and the construction of membrane-embedded hybrid nanomaterials with useful functions. For example, a few attempts have been made to target and insert (very small, <3 nm) SC quantum dots (QDs) into the lipid bilayer. Al-Jamal *et al.* (25) incorporated very small QDs in between the two lipid layers of the vesicle's bilayer, as proven by fluorescence microscopy. Kloepper *et al.* (26) reported the transmission electron microscopy (TEM) micrographic evidence of QDs inserted into vesicles' membranes. Gopalakrishnan *et al.* (27) successfully delivered lipophilic QDs (that were first loaded to vesicles' membranes) into membranes of human embryonic kidney (HEK) 293 cells via vesicle fusion. Wi *et al.* (28) investigated the maximum allowed QDs' size both experimentally and theoretically that could still afford membrane insertion. Recently, insertion of other types of nanomaterials into the membrane was demonstrated. Synthetic ion channels made from DNA nanostructures (29, 30) and ion channels made from carbon nanotubes (31) were successfully inserted into lipid bilayers while maintaining functional ion transport across the membrane.

Following works on asymmetric type-II (conduction band and valence band minima are spatially separated) seeded nanorods (NRs) at low temperature on the single-particle level (6, 32) and at room temperature on the ensemble level (33), we recently demonstrated that these NRs exhibit a large quantum-confined Stark effect (QCSE) at room temperature on the single-particle level (34). Marshall and Schnitzer (35) calculated the QCSE of simple type-I QDs (conduction band and valence band minima spatially overlapped) and showed that they have high enough sensitivity to detect action potential with superior signal-to-noise (S/N) ratio to the conventional voltage sensitive dyes. Although recently developed voltage indicators provide much improved sensitivity (36, 37), QCSE of asymmetric type-II NRs is predicated to exhibit

Copyright © 2018
The Authors, some
rights reserved;
exclusive licensee
American Association
for the Advancement
of Science. No claim to
original U.S. Government
Works. Distributed
under a Creative
Commons Attribution
NonCommercial
License 4.0 (CC BY-NC).

¹Department of Chemistry and Biochemistry, University of California, Los Angeles, Los Angeles, CA 90095, USA. ²Institute of Organic Chemistry and Biochemistry AS CR, Prague 166-10, Czech Republic. ³Department of Microbiology, Immunology, and Molecular Genetics, University of California, Los Angeles, Los Angeles, CA 90095, USA. ⁴Department of Chemical and Biomolecular Engineering, University of California, Los Angeles, Los Angeles, CA 90095, USA. ⁵Department of Ecology and Evolutionary Biology, University of California, Los Angeles, Los Angeles, CA 90095, USA. ⁶California NanoSystems Institute, University of California, Los Angeles, Los Angeles, CA 90095, USA. ⁷Department of Chemistry and Chemical Biology, Harvard University, MA 02138, USA. ⁸Department of Physics, University of California, Los Angeles, Los Angeles, CA 90095, USA. ⁹Department of Physiology, University of California, Los Angeles, Los Angeles, CA 90095, USA.

*Present address: College of Chemistry and Molecular Engineering, Peking University, China.

†Corresponding author. Email: sweiss@chem.ucla.edu

even higher voltage sensitivity (38). However, to the best of our knowledge, no attempts have been made to target and insert rod-shaped NPs into the lipid bilayer. In particular, membrane insertion of NRs with length larger than the membrane thickness (~ 4 nm) has not been demonstrated thus far. We present here an approach to insert and position NRs in the membrane by imparting them with membrane protein-like properties and report on membrane voltage-sensing experiments with these NPs.

RESULTS

NRs strongly change their emission in the electric field oriented along their long axis. The optimal strategy to use them for detection of transmembrane potential is to insert them perpendicularly to the membrane surface (Fig. 1A). Selective binding of cylindrical NRs to membranes in perpendicular orientation requires different lipophilic coating of the sides of the cylinder and hydrophilic coating of the tops. To make this nonhomogeneous coating, we decided to use different curvature of the surfaces. The tops of NRs that should bear more hydrophilic coating have higher curvature than cylinder sides. Our previously developed peptide-coating technique [developed for solubilizing QDs in hydrophilic environments (11, 39–43)] used flexible peptides that afforded uniform coating. For facet-selective coating, we designed a peptide consisting of hydrophobic rigid helical domain and more flexible hydrophilic domain (Fig. 1B). Preferential binding of rigid helical domain to the sides of the NR cylinder should lead to a significant difference in the lipophilicity of the sides and tops of the NR necessary for perpendicular insertion into membranes. The sequence of this prototype peptide is myristoyl-CLTCAITCMECTLKWCWKYKRGCRGCG-COOH, where the KRGCRGCG part served as the hydrophilic flexible segment, and other amino acids form an approximately 2.5-nm-long helix that is able to cover half of the NR cylinder side (Fig. 1). By simple geometrical considerations, we assess that ~ 8 to 12 peptides could self-assemble on a single NR (Fig. 1C) and cover it. Binding of the peptide to the NRs is

mediated by seven Cys residues: five on one face of the helical part and two in the flexible segment. To control the immersion depth of the peptide-covered NRs and to prevent insertion with a tilted orientation, we incorporated a KCWYK segment containing amino acids that preferentially localize at the membrane-water interface (44). Only a short segment of aliphatic amino acids was incorporated into the peptide sequence, including three hydroxyl-containing Thr residues and one acidic residue in the hydrophobic helical segment, to avoid aggregation in solution. More details regarding the peptide design are given in section S1. The α -helicity of the peptide was confirmed by circular dichroism spectroscopy (section S2 and fig. S1) in octanol solution ($\epsilon_r = 5.1$ versus membrane ≈ 5).

To test the selective binding (perpendicular) of peptide-coated NRs (pcNRs) to membranes, we introduced them into small unilamellar vesicles (SUVs) and then imaged them by EM. Quasi type-II CdSe-seeded CdS rod [same recipe applied to the sample #3 of Park *et al.* (34)] with dimensions of 4 ± 0.3 nm in diameter and 10 ± 2.2 nm in length were used for this study. The wavelength's peak position (λ_{max}) and full width at half maximum are 604 nm and 30 nm, respectively. This seeded rod exhibits 4 nm of red shift at 400 kV/cm of the electric field in air ($\epsilon_r = 1$). The asymmetric QCSE feature indicates the asymmetric localization of CdSe seed with respect to the center of the CdS rod (34). This rod is selected because the chemistry is well developed to yield narrow size distribution and its QCSE is confirmed at room temperature (34). The pcNRs containing SUVs were then flash-frozen and imaged by cryoEM (Fig. 2A and Materials and Methods). Because cryoEM images are two-dimensional projections, the exact z positions of pcNRs are not exactly known. For this reason, the level of insertion of pcNRs was assessed only for particles close to the vesicle's "equator." We analyzed more than 500 pcNRs and classified them into four categories (Fig. 2, B and C). The a-type represents an ideal, symmetric, and perpendicular insertion (the NR symmetrically traverses the membrane), which was observed for 16.4% of all analyzed pcNRs. The b-type represents partial (asymmetric) but perpendicular insertion (18% of all analyzed pcNRs). The c-type represents partial, tilted insertion and is the most abundant (41.7% of all analyzed pcNRs). The d-type represents horizontal insertion in between the two leaflets of the membrane (23.9% of all analyzed pcNRs). The histogram in Fig. 2C shows the partitioning in insertion geometries. If all cases of c-type insertion are ignored (because it is hard to classify parallel versus perpendicular insertion for these cases), then vertically oriented pcNRs (a- and b-type) constitute 59% of all a-type, b-type, and d-type insertions. Although these percentages are only a rough estimate for the partitioning between the different insertion configurations (because of the ambiguity in z positioning) and the captured cryoEM images only show frozen snapshots of NRs inserted into membranes, this estimate for partitioning is also reproduced in an independent fluorescence anisotropy measurement. The NRs were loaded into electro-swelled giant UVs (GUVs) (section S3). The orientation of the membrane-associated pcNRs was probed by polarization microscopy (45), capitalizing on the fact that the absorption and emission dipoles of NRs are aligned along their long axis (46). To estimate the orientation of pcNRs in the membrane, we imaged the fluorescence of GUVs loaded with pcNRs using linearly polarized laser excitation. Because the absorption and emission dipoles of NRs are aligned along their long axis, polarized excitation could verify the orientation of pcNRs with respect to the cellular membrane curvature (fig. S2). By analyzing the polarization anisotropy of individual pcNRs and applying a simple absorption anisotropy (AA) threshold, we could estimate that $\sim 58\%$ of the pcNRs were inserted with

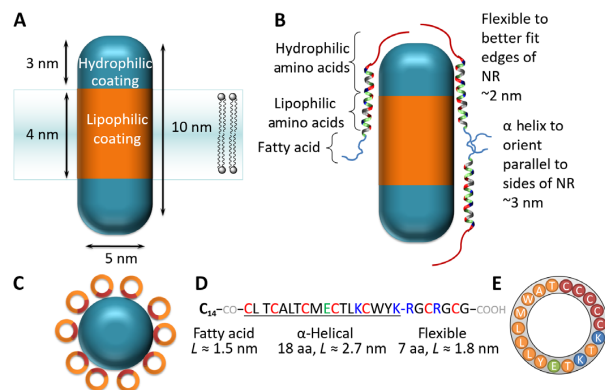


Fig. 1. Surface functionalization. (A) Cartoon describing design principles for rendering NR membrane protein-like properties. This functionalization will favor their stable, spontaneous insertion into the membrane with the correct orientation. (B) Peptide design for implementing (A). (C) Top view of an NR coated with peptides. Brown and orange colors depict Cys-rich and lipophilic faces of the α -helical peptide, respectively. (D) Sequence of the designed peptide. $\text{C}_{14}\text{-CO-}$ stands for myristoyl acid residue attached to the N-terminal amino group. (E) Wheel diagram corresponding to the α -helical part of the peptide. Color coding is the same as in (C). aa, amino acid.

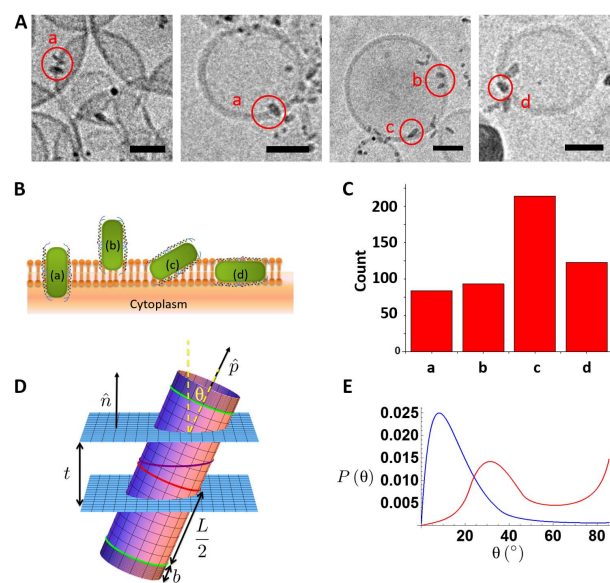


Fig. 2. NR interaction with membrane. (A) CryoEM micrographs of pcNRs inserted into SUVs. Scale bars, 30 nm. (B) Schematics of possible pcNRs association with lipid bilayer: (a) properly inserted, (b) partially inserted, (c) attached to an angle, and (d) horizontally embedded. (C) Histogram of insertion geometries (a) to (d). (D) Schematic of the NR of hydrophobic length L with two hydrophilic ends of length b and radius a . The total length of the rod is then $L + 2b$. It is shown in a piece of membrane of thickness t . The red curve denotes the center of the nanostructure, whereas the purple curve shows the intersection of the rod with the mid-plane of the membrane. (E) Model calculations (see section S7) of canting angles (θ) probability distribution for a membrane-inserted NR. Calculations for no hydrophobic mismatch ($L = t = 4$ nm, blue) and for significant hydrophobic mismatch ($L = 6$ nm, $t = 4$ nm; red) are shown. In both cases, the rods are terminated at both ends by hydrophilic cylinders with a length of 2 nm (details of the model are discussed in section S7).

an orientation that is more perpendicular (threshold, >0), than parallel, to the membrane plane (section S3). In contrast to cryoEM snapshots, AA spectroscopy on the single-particle level could follow NR reorientation dynamics in real time. Moreover, it could help disentangle the blinking dynamics from reorientation dynamics if both horizontally and vertically polarized photons are measured simultaneously. We note that, despite the fact that we have tested thus far only one rationally designed α -helical peptide sequence, a sizeable fraction of pcNRs showed vertical membrane orientation ($\sim 58\%$), and 16% of NRs were properly inserted, supporting the feasibility of this functionalization approach. A control cryoEM experiment showed that as-synthesized (native ligand-coated) NRs do not insert into vesicles' membranes (section S6).

Because the polarization anisotropy of pcNRs in the vesicle fluctuates, we expect that pcNRs in the membrane are not rigid. Considering a simple estimate based on the NR diffusing in a solvent with a viscosity of 1 kg/m-s (a thousand times the viscosity of water), we obtain a rotational diffusion constant on the order of 10 kHz. This would suggest that the azimuthal angle should be rotationally averaged out on the time scale of the measurement. The observation of slower rotational fluctuations might be due to coupling to translational motion or to fluctuation in the level of insertion (that is, the NR moves in and out of the membrane). To assess the cryoEM results, we studied the equilibrium partitioning

between the membrane and the solution of the NRs, as well as their orientational fluctuations within the membrane using the Boltzmann distribution and a simple model of the interaction energy of the NR with the membrane and solvent (see Fig. 2D and section S7 for details).

We found that, for reasonable hydrophobic/hydrophilic energies and typical NR geometries, NRs strongly partition to the membrane. Once embedded in the membrane, we predict that rods will be canted so that their long axis does not lie along the local normal to the membrane. The mean canting angle (θ) depends on the mismatch of the length of the hydrophobic region of the NR and the thickness of the membrane. Examining that figure, we estimate the fluctuations of the canting angle of rods with no hydrophobic mismatch (blue curve) to be in the range of 10° and thus comparable to the mean. Both the mean and the fluctuations are larger for cases of large hydrophobic mismatch (red). We expect larger fluctuations for significantly larger angles based on the large tail of the angle probability distribution. This model predicts that with hydrophobic surfaces covering a length of the pcNRs comparable to the membrane thickness, the fraction of rods inserted into the membrane approaches unity in thermal equilibrium. To stabilize the orientation of rods in the membrane to be close to the membrane's normal, it is advantageous to include hydrophilic ends on the pcNR tips. For reasonable lengths of these ends, they do not significantly change the partitioning of rods between the membrane and the solvent. Moreover, the model predicts a canting angle distribution (Fig. 2E) that resembles the histogram in Fig. 2C, suggesting some degree of hydrophobic mismatch (Fig. 2D). However, we note that the statistical nature of ligand exchange with the designed peptide does not necessarily impart precise hydrophobic surfaces and hydrophilic tips. In addition, we emphasize that the cryoEM visualization of NRs in the vesicular membrane is only a proof-of-concept demonstration and does not serve as a proof for correct insertion into cellular membranes. At this point, we cannot rule out possible differences in membrane insertion geometry and/or efficiency between vesicular and cellular membranes. Such a comparison will be the subject of a future work.

pcNRs can be delivered to the cellular membrane by either vesicle fusion (Fig. 3, A to C) or direct drop-casting method (Fig. 3, E and F). Fusogenic lipids are required for vesicle fusion process. Here, we used 1,2-stearoyl-3-trimethylammonium-propane (DOTAP) or $\beta\text{-[N-(N',N'-dimethylamino)ethane]-carbomoyl}[\text{cholesterol hydrochloride (DC-Chol)}$ and a cone-shaped lipid, 1,2-dioleoyl-sn-glycero-3-phosphoethanolamine (DOPE) (27, 47, 48). Once vesicles were formed, pcNRs were loaded, and their instantaneous staining could be observed (Fig. 3A). When pcNR-loaded vesicles were added to HEK293 tissue culture, they could be delivered to the cell membrane via fusion. Bright-field image (Fig. 3B) and its corresponding fluorescence image (Fig. 3C) capture the moment of vesicle fusion. Z-stack images of the same cell are shown in fig. S3, indicating vesicle fusion and subsequent membrane staining. The pcNRs could also be added directly to the growth medium of a tissue culture, as demonstrated in Fig. 3 (E and F) for HEK293 cells. By diluting the concentration of pcNRs, sparse labeling could be achieved such that individual (or small aggregates of) pcNRs could be observed (Fig. 3F). We observed a loss in the diffraction-limited fluorescence emanating from membrane inserted pcNRs within ~ 1 hour after staining, most likely due to endocytosis (fig. S5).

Membrane voltage sensing with pcNRs was first tested using self-spiking HEK293 cells (49). This cell line exhibits self-oscillations (~ 3 to 4 Hz) in membrane potential once cells reach confluency (49). Figure 4 shows optical recordings of these self-spiking HEK293 cells

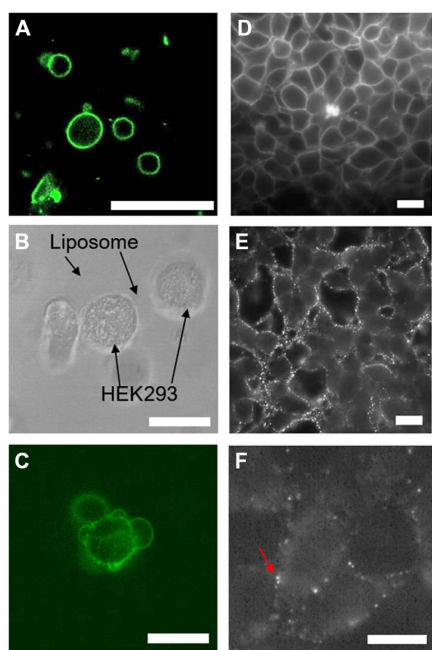


Fig. 3. Delivery of pcNRs to HEK293 cells. (A) Fluorescence of NR-loaded GUVs. (B and C) Bright-field (B) and fluorescence (C) images of pcNR-loaded GUV fused with the cell membrane. (D) Fluorescence image of HEK293 cells stained with ANEPPS (control). (E and F) pcNRs targeted to membranes at high (E) and low (F) concentrations. Scale bars, 10 μm .

with di-8-ANEPPS (ANEPPS) (Fig. 4, A, D, and E, serving as positive control) and pcNRs (Figs. 4, B, C, F, and G). Oscillating membrane potential is resolved by ANEPPS, exhibiting $\sim 10\%$ $\Delta F/F$ on the ensemble level (see Fig. 4D, top, and section S8 for image analysis details). Bottom of Fig. 4D shows four $\Delta F/F$ recordings (from four distinct locations, averaged over 5×5 pixels) marked with open circles of the same color. Figure 4A shows that these recordings are highly correlated with each other and with the ensemble average (black). These recordings were replotted in Fig. 4E by overlaying seven frames around every local maximum in the trajectory (guided with vertical dashed lines in Fig. 4D). The mean $\Delta F/F$'s over 23 cycles are plotted with thicker lines (black, ensemble $\Delta F/F$; blue, red, green, and cyan, local $\Delta F/F$'s in Fig. 4A). This result demonstrates the fidelity of membrane potential recording with ANEPPS.

The same analysis was performed for self-spiking HEK293 cells stained with pcNRs. In contrast to the clear membrane staining of ANEPPS (Fig. 4A), pcNRs are randomly distributed in the membrane and outside of it (cloudy background). In principle, better labeling (and higher contrast images) could be achieved by multiple washes applied to the tissue culture after incubation with pcNRs (as shown in Fig. 3E), but multiple washes abolish self-spiking. To eliminate densely pcNR-labeled regions and diffused background from the analysis of the data represented in Fig. 4B, a 10th-order ($n = 10$) Butterworth-type (high-pass) spatial filter ($\text{HPF}_{\text{pixel}}$) was applied to the image (fig. S7, A and B). The cutoff spatial frequency (ω_c) was 0.244 (pixel^{-1}). This image processing results in improved local contrast and enables the detection/identification of single bright spots (Fig. 4C). In a subsequent step, simple thresholding (threshold = mean + $2 \approx \text{SD}$) was applied to select

only bright, small pcNR-labeled regions (white pixels in fig. S8C) for calculating the ensemble $\Delta F/F$. The spatially averaged (over all white pixels in fig. S8C) temporal fluorescence signal is shown in fig. S8D. Extracting the membrane potential fluctuation from this signal is difficult because of photo-brightening and noise.

Therefore, we implemented an additional temporal bandpass filtering step that is a 5th-order ($M = 5$) Butterworth filter with cutoff frequencies ($f_{\text{high}} = 7$ Hz and $f_{\text{low}} = 2.5$ Hz; fig. S8E). This process further cleans up and highlights these oscillations by removing the slowly varying (low-frequency) photo-brightening and the high frequency shot noise (Fig. 4F, top, black line). The filtered signal in Fig. 4F (top) exhibits ~ 4 -Hz oscillations, similar to the oscillations reported in Fig. 4D. The asymmetric voltage depolarization and repolarization signal (49) is not resolved here because of the long integration time (30 ms). Although the ensemble $\Delta F/F$ is only $\sim 1\%$, it demonstrates that pcNRs can record membrane voltage oscillation. To test whether pcNRs can provide single-particle voltage sensitivity, we analyzed isolated diffraction limited white spots in Fig. 4C (representing either individual pcNRs or very small aggregates of pcNRs). Bandpass-filtered optical recordings from the individual spots marked with colored open circles exhibit up to 5% $\Delta F/F$ voltage oscillations (Fig. 4F, cyan). Figure 4G shows (similar to Fig. 4E) signal time traces of 19 consecutive cycles (seven frames per cycle). The mean value of the signal is also shown with a thicker line. The same analysis was repeated for 129 individual diffraction-limited bright spots. Sixteen percent of all cases exhibited $\Delta F/F > 1\%$.

Additional evidence for voltage sensing by pcNRs was provided by simultaneous patch-clamp and fluorescence measurements. pcNRs were applied directly to wild-type HEK293 cells that were cultured on a coverslip, and fluorescence emission and membrane voltage were recorded simultaneously. Fluorescence movies were recorded in synchrony with the membrane voltage modulation (with a cycle of two movie frames recorded at -150 mV, followed by two movie frames recorded at 0 mV, voltage modulation frequency of 100 Hz, and recording duration of 2000 frames with 400 Hz of frame rate). Figure 5A shows a fluorescence time trajectory recorded from a single (or possibly a small aggregate of) pcNR(s) (as judged by blinking) highlighted by an arrow in Fig. 3F (a link to the movie is provided in section S9.1). The fluorescence trajectory is highly noisy, most likely due to fluorescence intermittency (blinking) and unstable, dynamic fluctuations in membrane insertion (see discussion about membrane insertion stability in section S9). A zoom-in to the trajectory at around 4.6 s (Fig. 5B) shows a zigzag pattern in the fluorescence intensity that is synchronized with the modulated clamped voltage. For each modulation semi-period, we defined a pcNR modulation response $\Delta F/F$ as the difference between voltage-on and voltage-off intensities divided by the mean time-trace intensity. The modulation response ($\Delta F/F$) exhibits a high degree of variations throughout the acquisition time (5 s), with a few spikes of high signal about 100 ms long. We attribute the low reproducibility and low sensitivity of these recordings to the imperfect, unstable insertion of pcNRs into the cellular membrane.

We identified eight individual (or small cluster of) pcNRs in the patched cell's membrane (or its proximity), and for each, we computed the mean modulation response during the entire time trace (excluding the off periods due to the pcNR fluorescence blinking). Of eight pcNRs, only three exhibited a mean absolute modulation that was higher than the mean calculated for pcNRs in membranes of nonpatched cells.

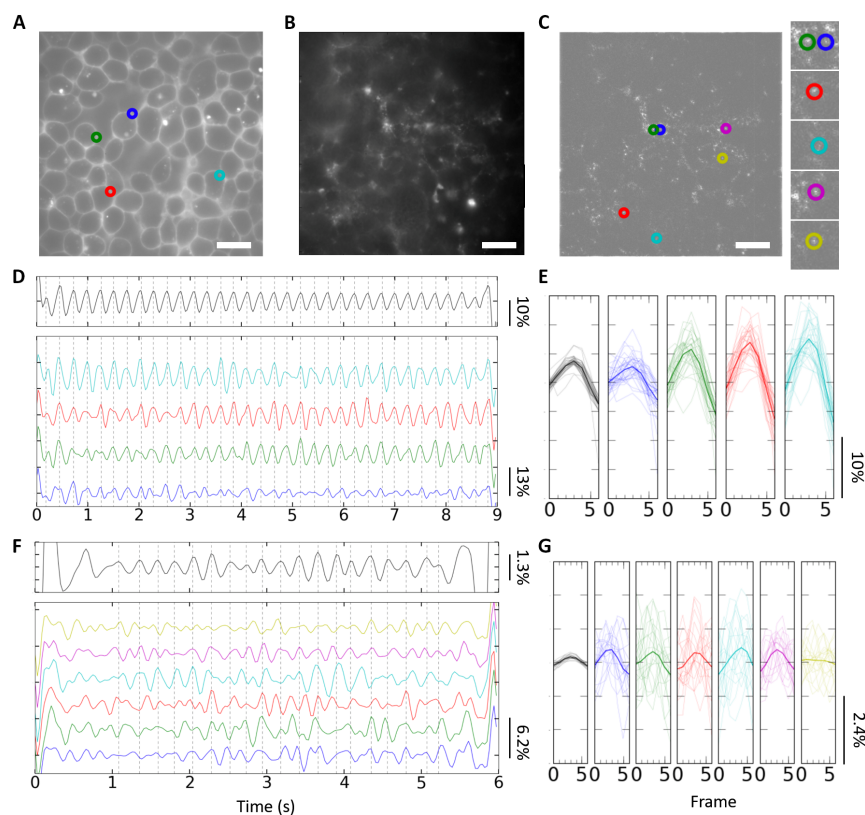


Fig. 4. Membrane voltage sensing of spiking HEK293 cells with pcNRs. (A and B) Fluorescence images of cells stained with ANEPPS (A) and pcNRs (B). (C) Spatially high-pass-filtered image of (B) used to highlight signals from individual pcNRs and remove background signals. (D and F) Temporal bandpass-filtered $\Delta F/F$ time trace of ANEPPS (D, top) and pcNRs (F, top). Each trace (D and F, bottom) shares the same color as the marked open circles in (A) or (C), respectively (see section 5B). (E and G) Overlaid $\Delta F/F$'s of seven frames around the gray dashed lines in (D) and (F). (D) and (F) have 23 and 19 thin lines in each subplot, respectively. Mean traces are shown with thicker line width. The leftmost subplots with black lines are $\Delta F/F$ of ensemble average [generated from top in (D) and (F)]. Scale bars, 10 μm .

However, these three pcNRs all have a negative mean modulation (with a $\pm 1\sigma$ error range that does not include 0), whereas the control group of seven pcNRs in the membrane of nonpatched cells exhibits a mean signal, which is statistically indistinguishable from 0 (fig. S10). Because the modulation response $\Delta F/F$ exhibits spikes or “bursts” of high signal that presumably correspond to brief periods of membrane insertion, we carried out an objective analysis that is focused on these brief bursts. To reduce the effect of noise on the identification of the start and stop of burst regions, we thresholded the running average of the $\Delta F/F$ modulation response. We then computed the integral modulation response in each burst i as $S_i = \frac{1}{P} \sum_i \Delta F_i$ (see Materials and Methods and section S9 for the details on patch-clamp analysis). Figure 5C shows the distribution of integral modulation responses for bursts belonging to pcNRs found in the patched cell membrane (patched in-phase, red) compared to integral modulation responses of controls that should not exhibit any correlated signal. In particular, in the out-of-phase controls, we suppress any intensity fluctuation in-phase with the voltage modulation by averaging frames corresponding to on and off voltage semi-periods (see Materials and Methods). We observe that, although the controls exhibit a symmetric distribution of bursts with positive and negative values for the integral modulation response (consistent with

random fluctuations), bursts of patched pcNRs show a predominance of negative integral modulation response (consistent with fluorescence reduction induced by the applied voltage). However, note that only 18 in-phase bursts were identified and analyzed for the three pcNRs associated with the patched cell membrane (and 20 out-of-phase bursts). For the nonpatched cell control, we identified seven pcNRs (in non-nearest neighbor cells to avoid possible signal leakage) that yield a total of 28 in-phase bursts (and 40 out-of-phase bursts).

DISCUSSION

NRs have many advantages over organic fluorophores, having large voltage sensitivity, large absorption cross section, and reduced photobleaching. However, they are difficult to integrate into biological and neuroscience applications because of their large size and unknown surface properties that lead to nonspecific binding. Furthermore, inserting NRs into membrane bilayers presents additional challenges due to the need for sophisticated facet-selective surface functionalization for control of insertion orientation.

Here, we showed membrane insertion of pcNRs using α -helical peptides as the surface ligand of NRs, as demonstrated by TEM micrograph (Fig. 2A). On the basis of these observations and on a statistical

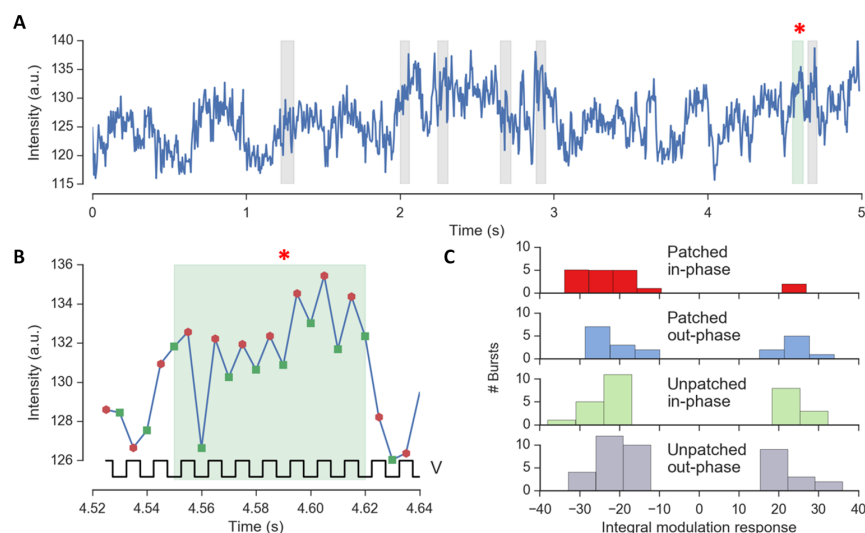


Fig. 5. Voltage response of pcNRs. (A) Intensity trace of a single pcNR with time intervals of large $\Delta F/F$ modulation response (bursts) marked with a shaded area and asterisk (*). (B) Zoom-in of intensity trace during a burst in (A); each marker represents a two-frame average intensity during the voltage-on (green squares) and voltage-off (red dots) semi-period. (C) Histogram of the modulation responses for each aggregating burst from many pcNRs in a video. The first group (red) represents the set of patched pcNRs that exhibit the highest signal. The other three distributions represent control groups for the set of unpatched pcNRs and/or for out-of-phase modulation response. a.u., arbitrary units.

mechanics-based theoretical investigation (Fig. 2E and section S7), we conclude that $>60\%$ of all membrane-associated pcNRs are favorably oriented (long axis parallel to the membrane's normal) but not necessarily fully inserted into the membrane. The polarization microscopy experiment also reveals that the subpopulation of NRs in GUVs is oriented in a favorable orientation (fig. S2). However, for highest voltage sensitivity, pcNRs need to be aligned as parallel to the membrane normal as possible (to guarantee maximal QCSE charge separation), with both tips exposed to the cytoplasm and extracellular matrix, respectively. The small fraction ($\sim 16\%$ of all geometries) of NRs proves the proper insertion in the membrane, showing the feasibility of membrane potential sensing. Fluorescence signals could be recorded from individual membrane-inserted or membrane-associated pcNRs, as is evident from the typical temporal blinking (intermittency) pattern (50) in their emission (movie S1). The high brightness of pcNRs stems from their large absorption cross section and high-emission quantum yield (51). In the patch-clamp experiment, we used a scientific complementary metal-oxide semiconductor (sCMOS) camera and a 488-nm laser (see Material and Methods). With this optical system, we were able to run the camera at a 400-Hz frame rate (2.5-ms integration time per frame) while capturing the modulated signal. We estimate that if an electron-multiplying charge-coupled device (EMCCD) camera is used instead, then, together with a shorter-wavelength laser excitation ($<450\text{nm}$), the emission rate of the higher NR and the higher camera gain will result in a higher S/N ratio. Together, shorter-wavelength laser excitation and EM gain will yield higher S/N ratio, allowing for an acquisition rate of $\sim 1\text{ kHz}$ but at the expense of working with a smaller region of interest through binning (because EMCCD camera acquisition rates are usually slower than those of sCMOS cameras). The absorption cross section of the NR could be further increased by adopting a lower bandgap material. Here, we used NRs consisting of CdSe (seed) and CdS (shell) with an optical bandgap of 600 nm. Using bandgap engineering and a different choice of materials' composition, the bandgap could be lowered toward the near-infrared, whereas excitation could be tuned to the blue/near-ultraviolet region

of the spectrum. In return, this will lead to an even higher single-NR brightness. We believe that by further improving the optical setup and the photon emission rate of the NR, it should be possible to record signals from individual NRs at $>1\text{-kHz}$ rate and, hence, capture individual action potential spikes. Moreover, an increased photon emission rate will allow us to use advanced noise-immune voltage-sensing techniques such as lifetime imaging, spectrally separated ratiometric measurement, or a spectral shift measurement. These approaches are, to a large extent, immune to fluorescence intermittency. On the other hand, the simple intensity-based measurement reported here is highly sensitive to intermittency and therefore required filtering of the raw signals.

Overall, our results demonstrate that individual (or a small aggregate of) pcNR is capable of recording the membrane potential. The voltage sensitivity of an ensemble of membrane-inserted pcNRs in self-spiking HEK293 cells was quite poor (Fig. 4F), with a $\Delta F/F \sim 0.6\%$ (much lower than the sensitivity of ANEPPS, a typical voltage sensitive dye (VSD), exhibiting $\Delta F/F$ of $\sim 10\%$ in Fig. 4D). We attribute this poor performance to imperfect membrane insertion for a large fraction of the NRs. Although larger than 5% signal are captured in Fig. 4 (F and G) intermittently, the averaged $\Delta F/F$ of an individual NR is typically $\sim 1\%$. This is likely due to the blinking feature of the NR and its dynamic movement/orientation fluctuation in the membrane. Because nonblinking nanocrystals are currently introduced, the photoluminescence (PL) fluctuation due to blinking will be improved (52). Because the study of the interaction energy between an NR and its environment (a solvent and a membrane) estimates the orientation of the NR quite accurately (Fig. 2, C to E), the optimized geometry for membrane insertion can be drawn with further theoretical investigation. To achieve stable and robust PL signal, more advanced surface functionalization should be pursued. To exploit the different surface energy between a cylinder wall and the tips of an NR, using face-selective surfactants (hydrophilic surfactants at the tips of the NR) will be one such example. Nonetheless, even with the current generation of NRs and coating, we could find a small fraction ($\sim 16\%$) of individual or small aggregate NRs exhibiting a sizeable $\Delta F/F \sim 5.0\%$.

In a second experiment, a voltage modulation of -150 to 0 mV (somewhat larger than a typical action potential of -70 to 40 mV) was applied to a patched (wild-type) HEK cell. Under this modulation, we were able to observe a higher in-phase modulation response of pcNRs that is statistically significant as compared to unpatched cells, whereas the control experiment (out-of-phase analysis) shows no modulation response, as expected (Fig. 5C). The sensitivity, the noise level, and the temporal resolution of these measurements are as of yet inadequate for electrophysiological recording.

The data presented in Figs. 4 and 5 suggest that with further improvements, pcNRs could be suitable for membrane potential recording. Marshall and Schnitzer (35) estimated 5 and 30% of $\Delta F/F$ during neuronal spiking with type I and type II QDs, respectively. The signal quality could be greatly increased by a series of enhancements. For example, preliminary experiments and calculations suggest that seeded NR heterostructures with type II band offset and large seed position asymmetry could exhibit very high voltage sensitivity (34). Moreover, improved membrane insertion stability will reduce measurement noise and enhance the signal. Last, as previously shown (34), shifts in the spectral peak position are considerably more sensitive than $\Delta F/F$ changes. A simple modification to the optical setup (based on “dual-view” microscopy) (53) could enhance voltage sensitivity even further.

Development of high-sensitivity pcNRs could afford unprecedented ways to study electrical activities in neuronal, neuromuscular, and visual systems on the nanoscale (such as across a single synapse) or the ability to record a large number of signals from a large field of view (high-throughput recording). pcNRs could also find applications in other areas of science and engineering, for example, in inducing action potential (54, 55), characterization of high-density fast integrated circuits, and energy harvesting by membrane-inserted artificial light-harvesting complexes. Last, the ability to impart membrane protein-like properties to inorganic and organic NPs could allow the construction of novel membrane-based hybrid (organic-inorganic) materials with unique exploitable properties.

MATERIALS AND METHODS

Quasi type II NRs synthesis (CdSe seeded in CdS)

Cadmium oxide (CdO; 99.99%), tri-*n*-octylphosphine (TOP; 90%), trioctylphosphine oxide (TOPO; 99%), selenium (Se; 99.999%), and sulfur (S; 99.5%) along with all organic solvents were purchased from Sigma-Aldrich and used without any further purification. Hexylphosphonic acid (HPA) and octadecylphosphonic (ODPA) were purchased from PCI Synthesis. A 50-ml round-bottom flask was loaded with 60 mg (0.5 mmol) of CdO, 280 mg of ODPA, and 3 g of TOPO. After degassing under a vacuum for 1 hour at 120°C , the temperature was raised to 340°C under argon until dissolution of CdO at which point 1.8 ml of TOP was injected and temperature was raised to 370°C . A solution containing 58 mg of Se in 0.5 ml of TOP was swiftly injected, and the heating mantle was removed. The final core size had a diameter of about 2.7 nm. A slight modification of previously reported methods (7) was used for seeded growth of CdS. A 50-ml round-bottom flask was charged with 211 mg (1.6 mmol) of CdO, 1 g of ODPA, 50 mg of HPA, and 3.46 g of TOPO. The reaction flask was degassed for 3 hours at 130°C , and then, temperature was raised to 340°C under argon until dissolution of CdO at which point 1.8 ml of TOP was injected. The CdSe seed solution was separated and purified for reaction by mixing three times with toluene and precipitating with excess methanol. Seeds were then redissolved in 0.6 ml of

TOP. The S:TOP precursor solution was prepared by mixing 51 mg of S (1.6 mmol) in 0.6 ml of TOP. Temperature was raised to 350°C for injection. The amount of dots used was 8×10^{-7} mol. The size distribution of NRs was characterized by EM, yielding 4 ± 0.3 and 10 ± 2.2 nm for the diameter and length of NRs, respectively.

NR functionalization with peptides

The sequence of the two peptides used in this study was myristoyl-CLTCALTCMECTLKCWYKRGCRG-COOH. Peptides were purchased from LifeTein LLC, purified to a level of 70% by high-performance liquid chromatography, characterized by mass spectrometry and circular dichroism (fig. S1). The protocol for NR functionalization with α -helical peptides was similar to that reported by Pinaud *et al.* (39), with the following modifications: As-synthesized NRs were coated with hydrophobic surfactants such as TOPO or ODPA. To exchange these surfactants with the designed peptides, we first stripped the surfactants off the NRs by multiple (five to six times) methanol precipitation steps, followed by redissolution in 450 μl of pyridine. The concentration of the NR was 0.1 μM . Four milligrams of peptides was dissolved in 50 μl of dimethyl sulfoxide (DMSO) and mixed with NRs in DMSO solution. Twelve microliters of tetramethylammonium hydroxide was added to the solution to increase the pH to 10.0, allowing the peptides to bind to the surface of NRs efficiently. The mixture was then centrifuged and redispersed in 150 μl of DMSO in a form ready to be used for cell membrane insertion (staining). For vesicle staining or for cryoEM experiment, NRs in DMSO solution were eluted through a Sephadex G-25 desalting column (Amersham) and equilibrated with phosphate-buffered saline (PBS) buffer. The pcNRs were stored at 4°C . As-synthesized NRs emitted photons of 600 nm. Their initial quantum yield was 15%, which was maintained after the peptide-coating process.

Loading pcNRs into vesicles

1,2-Dimyristoyl-*sn*-glycero-3-phosphocholine (DMPC), DOTAP, and DC-Chol were purchased from Avanti Polar Lipids Inc. Chloroform solutions of DOTAP (25 mM, 6 μl), DMPC (10 mM, 6 μl), and DC-Chol (10 mM, 6 μl) were mixed and dried in a vacuum for 4 hours in a rotary evaporator. The film was then hydrated with 1 ml of 0.1 M sucrose containing PBS buffer (pH 6.24) overnight at 37°C incubator, during which vesicles were spontaneously formed. Vesicles were stored at 4°C , unless used in experiments (they are stable and useable for about 1 week). For the cryoEM experiment, vesicles were extruded through a membrane with 100-nm pore-sized filter. For fluorescence microscopy measurement, 2 μl of pcNRs (eluted through a Sephadex G-25 desalting column) was added to the 10 μl of vesicle solution. pcNRs spontaneously and rapidly (~ 1 min) self-inserted into the vesicles' membranes. For GUVs, the same lipid composition (6 μl of 25 mM DOTAP, 6 μl of 10 mM DMPC, and 6 μl of 10 mM DC-Chol) was diluted with 200 μl of chloroform. Fifty microliters of the lipid in chloroform solution was loaded on the indium tin oxide (ITO)-coated glass. After 30 min of drying, the other ITO-coated glass was faced to the lipid-dried ITO glass. Two glasses are separated by the 3-mm thickness of O-ring, forming the aqueous chamber for electro-swelling. A square-voltage pulse (10 Hz of 1.0 V) was applied to the two ITO glasses for 20 min, followed by GUV preparation for imaging.

CryoEM

For the cryoEM measurement, 10 μl of pcNRs (eluted through a Sephadex G-25 desalting column, producing 0.05 μM) was added to 50 μl of vesicle solution (lipid concentration, 0.27 mM). An aliquot

(3 μl) of sample was placed on holey carbon-coated Quantifoil grid, manually blotted with filter paper, and plunged into liquid ethane to make a cryoEM grid with vesicles embedded in vitreous ice. The grid was transferred to a Gatan 626 cryo-sample holder cooled down by liquid nitrogen and inserted into an FEI TF20 cryo-electron microscope for imaging at 200-kV operating voltage. Images were recorded at several magnifications on a $4\text{k} \times 4\text{k}$ CCD camera (Tietz Video and Image Processing Systems) at $\sim 5\ \mu\text{m}$ under focus, with an accumulated electron dosage of $\sim 20\ \text{e}^{-}/\text{\AA}^2$ on each sample area.

Cell culture and staining

HEK293 cells (American Type Culture Collection) were maintained in 1:1 Dulbecco's modified Eagle medium and nutrient mixture F-12 (Invitrogen) supplemented with 10% fetal bovine serum (Sigma-Aldrich), geneticin (0.6 mg/ml; G418, Life Technologies), and puromycin (5 $\mu\text{g}/\text{ml}$; Life Technologies). Cells were grown on 35-mm glass-bottom dishes until they reached 90% confluency. The same protocol was applied to self-spiking HEK293 cells. For ANEPPS staining, ANEPPS solution in DMSO was added directly to the cells in a 35-mm glass-bottom dish to a final concentration of 0.1 μM . Cells were then incubated at 4°C for 5 min before imaging.

Optical imaging and data acquisition of the fluorescence signal of pcNRs in self-spiking HEK293 cells

The microscope setup was based on an Olympus IX71 inverted microscope equipped with a xenon lamp (75 W; U-LH75XEAP0, Olympus) and excitation filter (BP 470/40, Chroma Technology Corp). The excitation power was 2 mW at the image plane. The emission of the NPs was collected by a $60\times$ objective lens (PlanApo $60\times$, NA = 1.45, oil immersion, Olympus) and passed through a dichroic mirror (505DCXRU, Chroma Technology Corp). Imaging was carried out with an Andor iXon EMCCD camera (Andor iXon). Two microliters of pcNRs in DMSO solution ($\sim 300\ \text{nM}$) were loaded to the glass-bottom dish (Thermo Fisher Scientific) where the self-spiking HEK293 cells were cultured. The pcNRs spontaneously inserted into cell membranes within 1 to 2 min. The pcNR-loading density estimated from the image was $\sim 10^5$ pcNRs per cell. After rapid shaking, the cell medium was changed with Dulbecco's PBS (Life Technologies). The dish was then placed on the microscope. Fluorescence was recorded in a movie format for 9 s with a 30-ms integration per frame.

Simultaneous patch-clamp recording and fluorescence imaging

Two microliters of pcNRs were added directly to the cell culture (in a 35-mm glass-bottom dish with 2 ml of cell culture medium). Cells were then incubated at 37°C for 5 min before patch-clamp recording and imaging. As estimated from images, an average of ~ 10 particles were inserted into each cell. The loading density is approximated to be $\sim 10^{-7}$ pcNRs/ nm^2 . All imaging and electrophysiology were performed in Tyrode's buffer (pH 7.3; containing 125 mM NaCl, 2.5 mM KCl, 3 mM CaCl_2 , 1 mM MgCl_2 , 10 mM Hepes, and 30 mM glucose and adjusted to 305 to 310 mosmol with sucrose). For patch clamp, filamented glass micropipettes (WPI) were pulled to a tip resistance of 5 to 10 megohm and filled with internal solution containing 125 mM potassium gluconate, 8 mM NaCl, 0.6 mM MgCl_2 , 0.1 mM CaCl_2 , 1 mM EGTA, 10 mM Hepes, 4 mM Mg-ATP (adenosine 5'-triphosphate), and 0.4 mM Na-GTP (guanosine 5'-triphosphate) (pH 7.3) and adjusted to 295 mosmol with sucrose. Pipettes were positioned with a Sutter MP-285 manipulator. Whole-cell, voltage, and current-clamp

recordings were acquired using a patch-clamp amplifier (model 2400, A-M Systems), filtered at 5 kHz with the internal filter, and digitized with a National Instruments PCIe-6323 acquisition board at 10 kHz. Simultaneous whole-cell patch-clamp recordings and fluorescence recordings were acquired on a home-built, inverted epifluorescence microscope equipped with a $60\times$ water immersion objective, numerical aperture 1.20 (Olympus UIS2 UPlanSApo $60\times/1.20\ \text{W}$), a long-pass dichroic filter (Chroma zt505-515+650NIR Tpc), and a scientific CMOS camera (Hamamatsu ORCA Flash 4.0). Laser intensity (488 nm; Coherent Obis 488-50) was modulated with an acousto-optic tunable filter (Gooch and Housego 48058-2.5-.55-5W). Imaging of pcNRs was performed at illumination intensities of $\sim 1\ \text{W}\ \text{cm}^{-2}$. For fast data acquisition, a small field of view around the cell of interest was chosen at the center of the camera to achieve a frame rate of 1000 frames/s.

Data analysis of pcNRs' fluorescence during patch-clamp recording

From the video, we manually identified the position of pcNRs on both the patched cell membrane and on nonpatched cells. For each identified pcNRs, the time trace of emission intensity $\{t_k\}$ was obtained by averaging, for each frame k , a circular region of approximately 20 pixels around the pcNR. The time-trace intensity was binned to each of two frames to obtain an intensity $\{\bar{t}_j\}$ for each voltage alternation semi-period, and then, the difference $\{\Delta F_j\}$ was computed as $\{(\bar{t}_1 - \bar{t}_0), -(\bar{t}_2 - \bar{t}_1), (\bar{t}_3 - \bar{t}_2), -(\bar{t}_4 - \bar{t}_3), \dots\}$ (the signal alternates and is "+" and "-" for on-off and off-on transitions, respectively). Finally, these differences were divided by the average time-trace intensity to obtain the signal $\{\Delta F_j/F\}$.

The burst search was performed as follows. The square of the running average of the modulation response $\{\Delta F_j/F\}$ was computed, and the time periods where this squared average was higher than a threshold (set to 60% of the maximum) were identified as bursts. Next, for each burst i , we extracted the total signal (burst score)

$S_i = \frac{1}{F} \sum_j \Delta F_i$. The out-of-phase response was obtained by removing the first video frame and applying the same analysis on the time traces. In this case, the binning step averaged frames between on and off semi-periods, suppressing any signal in-phase with the voltage alternation. See section S9 for detailed description of the patch-clamp data analysis.

SUPPLEMENTARY MATERIALS

Supplementary material for this article is available at <http://advances.sciencemag.org/cgi/content/full/4/1/e1601453/DC1>

- section S1. Design of the peptide sequence for coating NRs
- section S2. Circular dichroism of the designed peptide
- section S3. Fluorescence anisotropy of pcNR-loaded vesicles
- section S4. Cell membrane staining with pcNRs
- section S5. CryoEM control: Ligand-coated NRs do not insert into vesicles' membranes
- section S6. Endocytosis of pcNRs after 1 hour of loading
- section S7. Simulation of the energetics of the NR in the membrane
- section S8. Optical recording of ANEPPS-labeled and pcNR-labeled spiking HEK cells
- section S9. Simultaneous optical and electrical recordings in patch-clamp experiment
- fig. S1. Circular dichroism spectrum of designed peptides dissolved in octanol.
- fig. S2. Orientation-dependent AA of pcNRs in membranes of GV.
- fig. S3. Confocal cross-sections of an HEK293 cell fused with pcNR-loaded vesicles.
- fig. S4. CryoEM images of vesicles after incubation with pcNRs.
- fig. S5. Images of pcNR-loaded HEK293 cells taken 1 hour later.
- fig. S6. Canting angle distribution of NR.
- fig. S7. Image processing of voltage recording with ANEPPS.
- fig. S8. Image processing of voltage recording with pcNR.

fig. S9. Mean of $\{\Delta F/F\}$ for the two sets of patched (left) and unpatched (right) particles.
 fig. S10. Image processing of voltage recording with pcNRs.
 table S1. Absorption anisotropy of NRs in the membrane.
 movie S1. Fluorescence movie of pcNR-stained HEK293 cells.
 Reference (56)

REFERENCES AND NOTES

- C. B. Murray, D. J. Norris, M. G. Bawendi, Synthesis and characterization of nearly monodisperse CdE (E = sulfur, selenium, tellurium) semiconductor nanocrystallites. *J. Am. Chem. Soc.* **115**, 8706–8715 (1993).
- X. Peng, L. Manna, W. Yang, J. Wickham, E. Scher, A. Kadavanich, A. P. Alivisatos, Shape control of CdSe nanocrystals. *Nature* **404**, 59–61 (2000).
- Z. A. Peng, X. Peng, Nearly monodisperse and shape-controlled CdSe nanocrystals via alternative routes: Nucleation and growth. *J. Am. Chem. Soc.* **124**, 3343–3353 (2002).
- L. Manna, E. C. Scher, A. P. Alivisatos, Synthesis of soluble and processable rod-, arrow-, teardrop-, and tetrapod-shaped CdSe nanocrystals. *J. Am. Chem. Soc.* **122**, 12700–12706 (2000).
- D. V. Talapin, J. H. Nelson, E. V. Shevchenko, S. Aloni, B. Sadtler, A. P. Alivisatos, Seeded growth of highly luminescent CdSe/CdS nanoheterostructures with rod and tetrapod morphologies. *Nano Lett.* **7**, 2951–2959 (2007).
- J. Müller, J. M. Lupton, P. G. Lagoudakis, F. Schindler, R. Koeppe, A. L. Rogach, J. Feldmann, D. V. Talapin, H. Weller, Wave function engineering in elongated semiconductor nanocrystals with heterogeneous carrier confinement. *Nano Lett.* **5**, 2044–2049 (2005).
- N. N. Hewa-Kasakarage, M. Kirsanova, A. Nemchinov, N. Schmall, P. Z. El-Khoury, A. N. Tamovsky, M. Zamkov, Radiative recombination of spatially extended excitons in (ZnSe/CdS)/CdS heterostructured nanorods. *J. Am. Chem. Soc.* **131**, 1328–1334 (2009).
- J. Müller, J. M. Lupton, A. L. Rogach, J. Feldmann, D. V. Talapin, H. Weller, Monitoring surface charge migration in the spectral dynamics of single CdSe/CdS nanodot/nanorod heterostructures. *Phys. Rev. B* **72**, 205339 (2005).
- T.-H. Kim, K.-S. Cho, E. K. Lee, S. J. Lee, J. Chae, J. W. Kim, D. H. Kim, J.-Y. Kwon, G. Amaratunga, S. Y. Lee, B. L. Choi, Y. Kuk, J. M. Kim, K. Kim, Full-colour quantum dot displays fabricated by transfer printing. *Nat. Photonics* **5**, 176–182 (2011).
- V. I. Klimov, S. A. Ivanov, J. Nanda, M. Achermann, I. Bezel, J. A. McGuire, A. Piryatinski, Single-exciton optical gain in semiconductor nanocrystals. *Nature* **447**, 441–446 (2007).
- X. Michalet, F. F. Pinaud, L. A. Bentolila, J. M. Tsay, S. Doose, J. J. Li, G. Sundaresan, A. M. Wu, S. S. Gambhir, S. Weiss, Quantum dots for live cells, in vivo imaging, and diagnostics. *Science* **307**, 538–544 (2005).
- S. Li, K. Zhang, J.-M. Yang, L. Lin, H. Yang, Single quantum dots as local temperature markers. *Nano Lett.* **7**, 3102–3105 (2007).
- M. J. Ruedas-Rama, E. A. H. Hall, Azamacrocyclic activated quantum dot for zinc ion detection. *Anal. Chem.* **80**, 8260–8268 (2008).
- H. Aouani, S. Itzhakov, D. Gachet, E. Devaux, T. W. Ebbesen, H. Rigneault, D. Oron, J. Wenger, Colloidal quantum dots as probes of excitation field enhancement in photonic antennas. *ACS Nano* **4**, 4571–4578 (2010).
- H. Zhu, N. Song, H. Lv, C. L. Hill, T. Lian, Near unity quantum yield of light-driven redox mediator reduction and efficient H₂ generation using colloidal nanorod heterostructures. *J. Am. Chem. Soc.* **134**, 11701–11708 (2012).
- I. N. Mora-Seró, J. Bisquert, Breakthroughs in the development of semiconductor-sensitized solar cells. *J. Phys. Chem. Lett.* **1**, 3046–3052 (2010).
- J. B. Delehanty, I. L. Medintz, T. Pons, F. M. Brunel, P. E. Dawson, H. Mattoussi, Self-assembled quantum dot-peptide bioconjugates for selective intracellular delivery. *Bioconjugate Chem.* **17**, 920–927 (2006).
- P. Pandey, S. P. Singh, S. K. Arya, V. Gupta, M. Datta, S. Singh, B. D. Malhotra, Application of thiolated gold nanoparticles for the enhancement of glucose oxidase activity. *Langmuir* **23**, 3333–3337 (2007).
- G. Tikhomirov, S. Hoogland, P. E. Lee, A. Fischer, E. H. Sargent, S. O. Kelley, DNA-based programming of quantum dot valency, self-assembly and luminescence. *Nat. Nanotechnol.* **6**, 485–490 (2011).
- I. L. Medintz, H. T. Uyeda, E. R. Goldman, H. Mattoussi, Quantum dot bioconjugates for imaging, labelling and sensing. *Nat. Mater.* **4**, 435–446 (2005).
- I. L. Medintz, M. H. Stewart, S. A. Trammell, K. Susumu, J. B. Delehanty, B. C. Mei, J. S. Melinger, J. B. Blanco-Canosa, P. E. Dawson, H. Mattoussi, Quantum-dot/dopamine bioconjugates function as redox coupled assemblies for in vitro and intracellular pH sensing. *Nat. Mater.* **9**, 676–684 (2010).
- J. Xu, T. Teslra, T.-H. Wu, P.-Y. Chiou, M. A. Teitell, S. Weiss, Nanoblade delivery and incorporation of quantum dot conjugates into tubulin networks in live cells. *Nano Lett.* **12**, 5669–5672 (2012).
- M. L. Schipper, G. Iyer, A. L. Koh, Z. Cheng, Y. Ebenstein, A. Aharoni, S. Keren, L. A. Bentolila, J. Q. Li, J. Rao, X. Chen, U. Banin, A. M. Wu, R. Sinclair, S. Weiss, S. S. Gambhir, Particle size, surface coating, and PEGylation influence the biodistribution of quantum dots in living mice. *Small* **5**, 126–134 (2009).
- J. B. Blanco-Canosa, M. Wu, K. Susumu, E. Petryayeva, T. L. Jennings, P. E. Dawson, W. R. Algar, I. L. Medintz, Recent progress in the bioconjugation of quantum dots. *Coord. Chem. Rev.* **263–264**, 101–137 (2014).
- W. T. Al-Jamal, K. T. Al-Jamal, B. Tian, L. Lacerda, P. H. Bomans, P. M. Frederik, K. Kostarelos, Lipid-quantum dot bilayer vesicles enhance tumor cell uptake and retention in vitro and in vivo. *ACS Nano* **2**, 408–418 (2008).
- J. A. Kloepper, N. Cohen, J. L. Nadeau, FRET between CdSe quantum dots in lipid vesicles and water- and lipid-soluble dyes. *J. Phys. Chem. B* **108**, 17042–17049 (2004).
- G. Gopalakrishnan, C. Danelon, P. Izewska, M. Prummer, P.-Y. Bolinger, I. Geissbühler, D. Demurtas, J. Dubochet, H. Vogel, Multifunctional lipid/quantum dot hybrid nanocontainers for controlled targeting of live cells. *Angew. Chem. Int. Ed.* **45**, 5478–5483 (2006).
- H. S. Wi, S. J. Kim, K. Lee, S. M. Kim, H. S. Yang, H. K. Pak, Incorporation of quantum dots into the lipid bilayer of giant unilamellar vesicles and its stability. *Colloids Surf. B Biointerfaces* **97**, 37–42 (2012).
- M. Langecker, V. Arnaut, T. G. Martin, J. List, S. Renner, M. Mayer, H. Dietz, F. C. Simmel, Synthetic lipid membrane channels formed by designed DNA nanostructures. *Science* **338**, 932–936 (2012).
- A. Seifert, K. Göpfrich, J. R. Burns, N. Fertig, U. F. Keyser, S. Howorka, Bilayer-spanning DNA nanopores with voltage-switching between open and closed state. *ACS Nano* **9**, 1117–1126 (2015).
- J. Geng, K. Kim, J. Zhang, A. Escalada, R. Tunuguntla, L. R. Comolli, F. I. Allen, A. V. Shnyrova, K. R. Cho, D. Munoz, Y. M. Wang, C. P. Grigoropoulos, C. M. Ajo-Franklin, V. A. Frolov, A. Noy, Stochastic transport through carbon nanotubes in lipid bilayers and live cell membranes. *Nature* **514**, 612–615 (2014).
- K. Becker, J. M. Lupton, J. Müller, A. L. Rogach, D. V. Talapin, H. Weller, J. Feldmann, Electrical control of Förster energy transfer. *Nat. Mater.* **5**, 777–781 (2006).
- R. M. Kraus, P. G. Lagoudakis, A. L. Rogach, D. V. Talapin, H. Weller, J. M. Lupton, J. Feldmann, Room-temperature exciton storage in elongated semiconductor nanocrystals. *Phys. Rev. Lett.* **98**, 017401 (2007).
- K. Park, Z. Deutsch, J. J. Li, D. Oron, S. Weiss, Single molecule quantum-confined Stark effect measurements of semiconductor nanoparticles at room temperature. *ACS Nano* **6**, 10013–10023 (2012).
- J. D. Marshall, M. J. Schnitzer, Optical strategies for sensing neuronal voltage using quantum dots and other semiconductor nanocrystals. *ACS Nano* **7**, 4601–4609 (2013).
- J. M. Kralj, A. D. Douglass, D. R. Hochbaum, D. Maclaurin, A. E. Cohen, Optical recording of action potentials in mammalian neurons using a microbial rhodopsin. *Nat. Methods* **9**, 90–95 (2012).
- E. W. Miller, J. Y. Lin, E. P. Frady, P. A. Steinbach, W. B. Kristan Jr., R. Y. Tsien, Optically monitoring voltage in neurons by photo-induced electron transfer through molecular wires. *Proc. Natl. Acad. Sci. U.S.A.* **109**, 2114–2119 (2012).
- K. Park, S. Weiss, Design rules for membrane-embedded voltage-sensing nanoparticles. *Biophys. J.* **112**, 703–713 (2017).
- F. Pinaud, D. King, H.-P. Moore, S. Weiss, Bioactivation and cell targeting of semiconductor CdSe/ZnS nanocrystals with phytochelatin-related peptides. *J. Am. Chem. Soc.* **126**, 6115–6123 (2004).
- F. Pinaud, X. Michalet, L. A. Bentolila, J. M. Tsay, S. Doose, J. J. Li, G. Iyer, S. Weiss, Advances in fluorescence imaging with quantum dot bio-probes. *Biomaterials* **27**, 1679–1687 (2006).
- J. M. Tsay, S. Doose, F. Pinaud, S. Weiss, Enhancing the photoluminescence of peptide-coated nanocrystals with shell composition and UV irradiation. *J. Phys. Chem. B* **109**, 1669–1674 (2005).
- G. Iyer, F. Pinaud, J. Tsay, S. Weiss, Solubilization of quantum dots with a recombinant peptide from *Escherichia coli*. *Small* **3**, 793–798 (2007).
- G. Iyer, X. Michalet, Y.-P. Chang, F. F. Pinaud, S. E. Matyas, G. Payne, S. Weiss, High affinity scFv-hapten pair as a tool for quantum dot labeling and tracking of single proteins in live cells. *Nano Lett.* **8**, 4618–4623 (2008).
- A. Senes, D. C. Chadi, P. B. Law, R. F. S. Walters, V. Nanda, W. F. DeGrado, E₂, a depth-dependent potential for assessing the energies of insertion of amino acid side-chains into membranes: Derivation and applications to determining the orientation of transmembrane and interfacial helices. *J. Mol. Biol.* **366**, 436–448 (2007).
- I. Wróbel, D. Collins, Fusion of cationic liposomes with mammalian cells occurs after endocytosis. *Biochim. Biophys. Acta* **1235**, 296–304 (1995).
- D. Axelrod, Carbocyanine dye orientation in red cell membrane studied by microscopic fluorescence polarization. *Biophys. J.* **26**, 557–574 (1979).
- J. Xu, P. Ruchala, Y. Ebenstein, J. J. Li, S. Weiss, Stable, compact, bright bifunctional quantum dots with improved peptide coating. *J. Phys. Chem. B* **116**, 11370–11378 (2012).
- C. Lonz, M. F. Lensink, E. Kleiren, J.-M. Vanderwinden, J.-M. Ruyschaert, M. Vandenbranden, Fusogenic activity of cationic lipids and lipid shape distribution. *Cell. Mol. Life Sci.* **67**, 483–494 (2010).

49. J. Park, C. A. Werley, V. Venkatachalam, J. M. Kralj, S. D. Dib-Hajj, S. G. Waxman, A. E. Cohen, Screening fluorescent voltage indicators with spontaneously spiking HEK cells. *PLoS ONE* **8**, e85221 (2013).
50. M. Nirmal, B. O. Dabbousi, M. G. Bawendi, J. J. Macklin, J. K. Trautman, T. D. Harris, L. E. Brus, Fluorescence intermittency in single cadmium selenide nanocrystals. *Nature* **383**, 802–804 (1996).
51. D. V. Talapin, R. Koepppe, S. Götzinger, A. Kornowski, J. M. Lupton, A. L. Rogach, O. Benson, J. Feldmann, H. Weller, Highly emissive colloidal CdSe/CdS heterostructures of mixed dimensionality. *Nano Lett.* **3**, 1677–1681 (2003).
52. J. I. Climente, J. L. Movilla, J. Planelles, Auger recombination suppression in nanocrystals with asymmetric electron–hole confinement. *Small* **8**, 754–759 (2012).
53. K. Kinoshita, H. Itoh, S. Ishiwata, K. Hirano, T. Nishizaka, T. Hayakawa, Dual-view microscopy with a single camera: Real-time imaging of molecular orientations and calcium. *J. Cell Biol.* **115**, 67–73 (1991).
54. E. Molokanova, J. A. Bartel, W. Zhao, I. Naasani, M. J. Ignatius, J. A. Treadway, A. Savtchenko, Quantum dots move beyond fluorescence imaging. *Biophotonics Int.* 26–31 (2008).
55. E. Molokanova, A. Savchenko, Bright future of optical assays for ion channel drug discovery. *Drug Discov. Today* **13**, 14–22 (2008).
56. H. Shen, Interactive notebooks: Sharing the code. *Nature* **515**, 151–152 (2014).

Acknowledgments: We acknowledge the help of A. Cohen for providing the self-spiking HEK cell line and for providing access to the laboratory and the patch-clamp fluorescence setup.

Funding: We also acknowledge the use of instruments at the Electron Imaging Center for NanoMachines supported by the NIH (1S10RR23057 and GM071940 to Z.H.Z.) and the Advanced Light Microscopy/Spectroscopy core, both at the California NanoSystems Institute at the University of California, Los Angeles. We also acknowledge the participation in the USER Program (#1726 and #3244) of the Molecular Foundry at the Lawrence Berkeley National Laboratory, which was supported by the U.S. Department of Energy Office of Science, Office of Basic Energy Sciences under contract no. DE-AC02-05CH11231. S.W. acknowledges the funding

from the United States–Israel Binational Science Foundation (#2010382), the Human Frontier Science Program (#RGP0061/2015), and the Defense Advanced Research Projects Agency/Biological Technologies Office (award no. D14PC00141). This material is based on work supported by the U.S. Department of Energy Office of Science, Office of Biological and Environmental Research program under award no. DE-FC02-02ER63421. A.J.L. acknowledges partial support from NSF-DMR-1309188. S.W. and Z.H.Z. acknowledge partial support from the NSF (DMR-1548924). **Author contributions:** K.P. and Y.K. performed the experiments, data analysis, and wrote the manuscript. V.S. designed the peptides and helped edit the manuscript. A.I. performed the signal analysis for the patch-clamp experiments and wrote the manuscript. X.D. and Z.H.Z. performed the vesicle imaging with cryoEM. L.H. and W.K. performed the experiments. P.Z. performed the patch-clamp experiment. J.L. synthesized the NPs for this study. A.J.L. developed the theory, performed the simulations for membrane insertion, and wrote the manuscript. S.W. conceived and managed the project and wrote the manuscript. All authors discussed the results and contributed to the writing of the manuscript. **Competing interests:** S.W., K.P., Y.K., V.S., and J.L. are inventors on a U.S. Provisional Patent application submitted by the University of California, Los Angeles (application no. 62504307, filed 05 October 2017). All other authors declare that they have no competing interests. **Data and materials availability:** All data needed to evaluate the conclusions in the paper are present in the paper and/or the Supplementary Materials. Additional data related to this paper may be requested from the authors.

Submitted 26 June 2016

Accepted 8 December 2017

Published 12 January 2018

10.1126/sciadv.1601453

Citation: K. Park, Y. Kuo, V. Shvadchak, A. Ingarciola, X. Dai, L. Hsiung, W. Kim, Z. H. Zhou, P. Zou, A. J. Levine, J. Li, S. Weiss, Membrane insertion of—and membrane potential sensing by—semiconductor voltage nanosensors: Feasibility demonstration. *Sci. Adv.* **4**, e1601453 (2018).

Supplementary Materials for

Membrane insertion of—and membrane potential sensing by— semiconductor voltage nanosensors: Feasibility demonstration

Kyoungwon Park, Yung Kuo, Volodymyr Shvadchak, Antonino Ingargiola, Xinghong Dai,
Lawrence Hsiung, Wookyeom Kim, Z. Hong Zhou, Peng Zou, Alex J. Levine, Jack Li, Shimon Weiss

Published 12 January 2018, *Sci. Adv.* **4**, e1601453 (2018)

DOI: 10.1126/sciadv.1601453

The PDF file includes:

- section S1. Design of the peptide sequence for coating NRs
- section S2. Circular dichroism of the designed peptide
- section S3. Fluorescence anisotropy of pcNR-loaded vesicles
- section S4. Cell membrane staining with pcNRs
- section S5. CryoEM control: Ligand-coated NRs do not insert into vesicles' membranes
- section S6. Endocytosis of pcNRs after 1 hour of loading
- section S7. Simulation of the energetics of the NR in the membrane
- section S8. Optical recording of ANEPPS-labeled and pcNR-labeled spiking HEK cells
- section S9. Simultaneous optical and electrical recordings in patch-clamp experiment
- fig. S1. Circular dichroism spectrum of designed peptides dissolved in octanol.
- fig. S2. Orientation-dependent AA of pcNRs in membranes of GV.
- fig. S3. Confocal cross-sections of an HEK293 cell fused with pcNR-loaded vesicles.
- fig. S4. CryoEM images of vesicles after incubation with pcNRs.
- fig. S5. Images of pcNR-loaded HEK293 cells taken 1 hour later.
- fig. S6. Canting angle distribution of NR.
- fig. S7. Image processing of voltage recording with ANEPPS.
- fig. S8. Image processing of voltage recording with pcNR.
- fig. S9. Mean of $\{\Delta F_i/F\}$ for the two sets of patched (left) and unpatched (right) particles.
- fig. S10. Image processing of voltage recording with pcNRs.

- table S1. Absorption anisotropy of NRs in the membrane.
- Reference (56)

Other Supplementary Material for this manuscript includes the following:
(available at advances.sciencemag.org/cgi/content/full/4/1/e1601453/DC1)

- movie S1 (.avi format). Fluorescence movie of pcNR-stained HEK293 cells.

section S1. Design of the peptide sequence for coating NRs

Selective insertion of peptide-coated nanorods (pcNRs) into membrane in a vertical orientation could be achieved by lipophilic coating of the central part of pcNRs and hydrophilic coating of the edges (Fig. 1). Edges and sides of pcNRs have the same chemical properties but different curvature of the surface. To selectively modified them, we decided to use a peptide containing α -helical and unstructured domains. Relatively rigid α -helical domain can bind cylindrical sides of NR but its binding to bended edges is less efficient, meanwhile the flexible part can efficiently fit curved surface of NR edges. The average size of NR is approximately $5 \text{ nm} \times 10 \text{ nm}$. We decided to construct a $\sim 5 \text{ nm}$ long peptide (half of the NR height) with strong gradient of polarity from the N- to C-terminus (Fig. 1B). Flexible polar C-terminal part is expected to bind edge of NR and determine peptide orientation. Lipophilicity of amino-acids gradually increases towards the N-terminus that is additionally modified by highly lipophilic myristoyl fatty acid residue that is expected to be located approximately at the center of NR. Affinity of the peptide to NR was achieved by introducing cysteines approximately at every third or fourth residue (Fig. 1D). In α -helical domain cysteines were located on one face of the helix (Fig. 1E). We also introduced two charged residues in the helical domain to avoid peptide aggregation and two residues having preferential positioning on membrane-water interface between α -helical and flexible parts of peptide to improve membrane localization.

section S2. Circular dichroism of the designed peptide

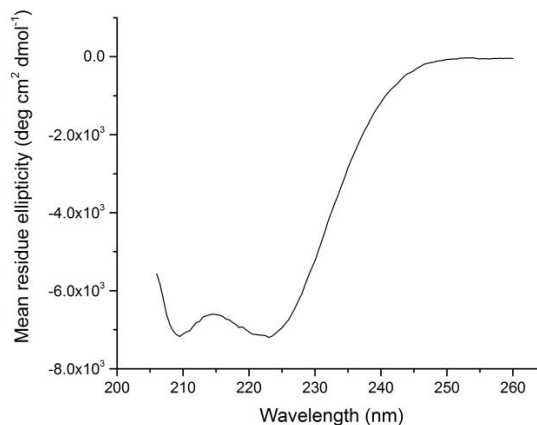


fig. S1. Circular dichroism spectrum of designed peptides dissolved in octanol.

The secondary structure of the designed peptides is determined by circular dichroism (CD). The peptides were dissolved in octanol, which mimics the nonpolar interior of the cell membrane. 4 mg of the peptides were dissolved in 1 ml of octanol and the excess solid peptides were filtered out to yield a saturated peptide solution. The concentration of the saturated peptide solution was determined to be $\sim 17 \mu\text{M}$ ($\sim 0.05 \text{ mg/ml}$), by the absorbance of tryptophan at 280 nm using UV-Vis spectrometer. The CD spectrum was acquired at 25°C under N_2 purge, using a quartz cuvette with 1 cm path length. The large, 1 cm path length was selected, due to the low solubility of the peptide in octanol and hence low absorbance of the solution when using a cuvette with 1 mm path length. The CD spectrum above 205 nm showed a characteristic alpha-helical structure, while the spectrum below 205 nm was oversaturated due to the solvent. (fig. S1).

section S3. Fluorescence anisotropy of pcNR-loaded vesicles

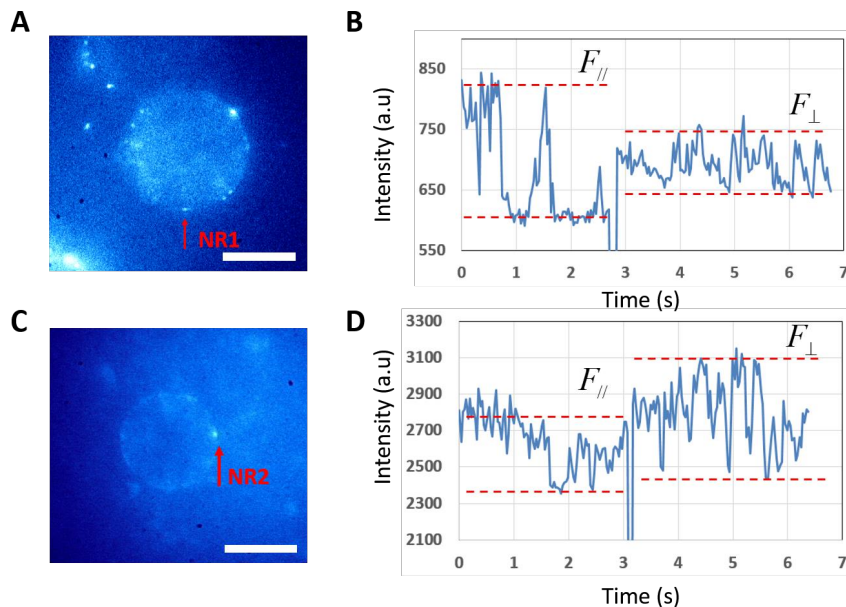


fig. S2. Orientation-dependent AA of pcNRs in membranes of GV. (A, C) fluorescence images of pcNR-loaded vesicles. NR1's (B) and NR2's (D) fluorescence trajectories, marked with red arrows in (A) and (C). During the measurement, the half-wave plate was removed, leading to excitation polarization change from vertical ($F_{//}$) to horizontal (F_{\perp}). Scale bar is 20 μm . An integration time is 32 ms.

To estimate pcNRs' orientation in membranes, we first made and attached vesicles to the microscopy cover glass. 8 μl (25 mM in chloroform) of 1,2-stearoyl-3-trimethylammonium-propane (DOTAP) and 1 μl (25 mM in chloroform) of 1,2-dioleoyl-*sn*-glycero-3-phosphoethanolamine (DOPE) were mixed and dried under ambient condition. 100 μl of 100 mM NaCl with 1 volume percent of glycerol of distilled H_2O (dH_2O) were then added to the dried lipids, and stored in a 4°C refrigerator for 24 hrs, followed by one minute of sonication. 5 μl of the vesicle solution was then loaded to the cover glass. To immobilize the vesicles, 500 μl of 100 mM NaCl in dH_2O (no glycerol) were added to the vesicle solution. After 10 minutes, immobilized giant vesicles (GV) could be observed. Finally, pcNRs were added to the vesicle-containing water droplet. Figure S2A and C show fluorescence images of pcNRs loaded vesicles, excited with

vertically polarized light. 200 frames movies were acquired and time trajectories from individual pcNRs were analyzed. During the movie acquisition, the excitation polarization was rotated by 90° by removing a half-wave plate in the excitation path.

pcNRs at 0°, 90°, 180°, 270° of the vesicles' cross-section (at horizontal or vertical plane) are selected and analyzed. The representative intensity trajectories from membrane inserted pcNRs during polarization modulation are shown in fig. S2A and B. From such trajectories, absorption

anisotropy ($AA = \frac{FP_{\parallel} - FP_{\perp}}{FP_{\parallel} + FP_{\perp}}$) could be obtained by measuring fluorescence signal. 26 pcNRs

were analyzed and 15 out of them show AA corresponding to vertical orientation in membrane (AA > 0 for pcNRs in the vertical plane of GUV) indicating a preference towards vertical insertion, consistent with cryoEM results.

table S1. Absorption anisotropy of NRs in the membrane.

| | Vertical plane | Horizontal plane |
|--|----------------|------------------|
| AA expected for transmembrane NR insertion ^{a)} | 0.63 | -0.5 |
| AA expected for NR oriented parallel to membrane surface | -0.5 | 0.63 |
| Average observed AA ±SD | 0.12±0.30 | -0.10±0.31 |
| Number of pcNRs with transmembrane orientation ^{b)} | 5 | 1 |
| Number of analyzed pcNRs | 17 | 9 |

^{a)} Calculated based on the highest and lowest AA observed for all imaged pcNRs. The difference from 1 is because NR can be excited with light that is not in the plane of the main axis. The difference of the modules of values for vertical and horizontal plane are due to different intensity of the parallel and perpendicular light excitation.

^{b)} including those with tilt less than 30° (the difference of AA from expected values was less than (1-cos30°)×100%)

section S4. Cell membrane staining with pcNRs

Fusogenic vesicles loaded with pcNRs was prepared as explained in Methods. They were added to cultured wild type HEK293 cells in PBS buffer. After incubating for 10 minutes, a series of confocal cross-sections was taken by Leica SP-2 microscopy. Figure S3 shows that the cell membranes are stained with pcNRs and pcQDs, respectively.

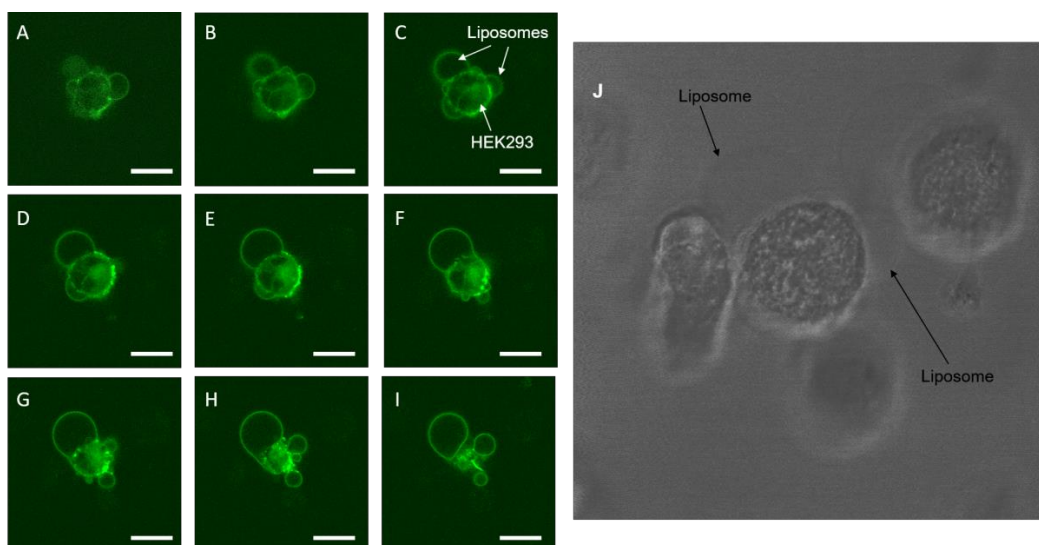


fig. S3. (A~I) Confocal cross-sections of an HEK293 cell fused with pcNR-loaded vesicles. Scale bar 10 μm . z-step is 0.5 μm . (J) A bright field image of (c) for clarifying the liposomes.

section S5. CryoEM control: Ligand-coated NRs do not insert into vesicles' membranes

As synthesized NRs were dissolved in toluene or hexane and precipitated by adding methanol multiple times to remove excess ligands. The NRs were then dissolved in DMSO and sonicated for 10 mins to minimize aggregation before adding to the vesicle solution (see Methods). 250 μl of the vesicle solution

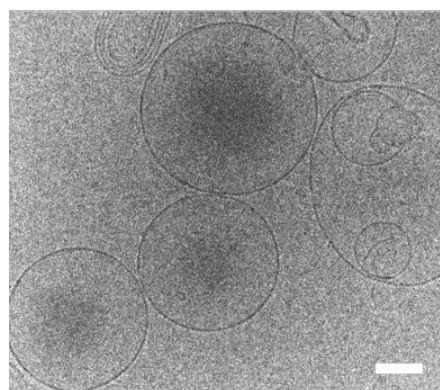


fig. S4. CryoEM images of vesicles after incubation with pcNRs. No NRs were observed to insert into the membrane. Scale bar 100nm.

was extruded through a membrane with 100 nm pore size to facilitate formation of 100 nm SUVs, and 2 μ l of the NR solution in DMSO was mixed with the extruded vesicle solution. The mix solution was then deposited on TEM grids and frozen according to the methods described in Methods. As shown in fig. S4, the vesicles were not loaded with any NRs, indicating these NRs did not insert into the membrane of the vesicles.

section S6. Endocytosis of pcNRs after 1 hour of loading

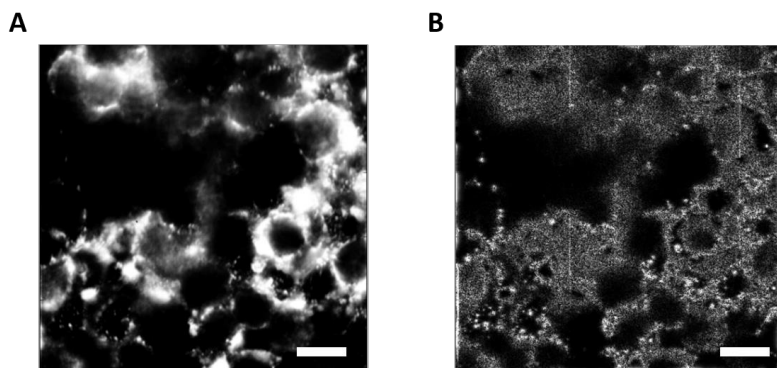


fig. S5. Images of pcNR-loaded HEK293 cells taken 1 hour later. (A) Fluorescence image of HEK293 cells after 1 hour of pcNRs' loading. (B) HPF filtered image. The same spatial filter in fig. S8 is used. Scale bar 10 μ m.

section S7. Simulation of the energetics of the NR in the membrane

Since the energy of any nanorod configuration in the membrane is determined by the areas of hydrophobic and hydrophilic surfaces in contact with the interior of the membrane and (aqueous) solvent, the energy calculation becomes a straightforward exercise in geometry. In this section we outline calculation of the various areas involved in determining the nanorod insertion energy. We use these calculations to address two points. First, we examine the orientational stability of rods in the membrane by computing their mean tilt (or canting) angle with respect to the membrane local normal. We also consider the thermal fluctuations

of that tilting angle. Secondly, we consider the equilibrium partitioning of the nanorods between the solvent and the membranes, and find that for almost all hydrophobic (hydrophilic) energy scales and nanorod dimensions, the rods will strongly partition to the membrane.

SI-7.1 Geometry of the nanorod in the membrane

In the frame of the rod or radius a and length L , the points on the surface of the rod are given by

$$\tilde{\mathbf{r}} = a \cos \phi \hat{x}' + a \sin \phi \hat{y}' + \rho \hat{z}' \quad (7.1)$$

where $|r| < L/2$ and the azimuthal angle f covers the unit circle, $-\rho \leq f < \rho$.

In the reference frame where the membrane (of thickness t) has unit normal $\hat{n} = \hat{z}$ and occupies the space $|z| < t/2$, the nanorod is oriented so that its symmetry axis lies along \hat{p} , $\hat{p} \cdot \hat{n} = \cos q$ and has its center at height h above the midplane of the membrane – see fig. S6A for a schematic representation of the configuration in terms of these degrees of freedom. Putting the nanorod in the xz -plane (without loss of generality) the surface of the cylinder lies on

$$\mathbf{r} = \hat{x} [r \sin q - a \cos q \cos f] + \hat{y} a \sin f + \hat{z} [h + r \cos q + a \sin q \cos f] \quad (7.2)$$

where ρ and f range over the same intervals as above. We neglect the endcaps of the cylinder for now.

The curve defining the intersection of the cylinder with the upper boundary of the membrane $z = t/2$ is given by

$$r_{top}^{(0)}(f) = \frac{t}{2 \cos q} - \frac{h}{\cos q} - a \tan q \cos f \quad (7.3)$$

Since the ends of the cylinder may be in the interior of membrane, the upper limit of ρ is actually

$$r_{top}(f) = \min \left[\frac{L}{2}, r_{top}^{(0)}(f) \right] \quad (7.4)$$

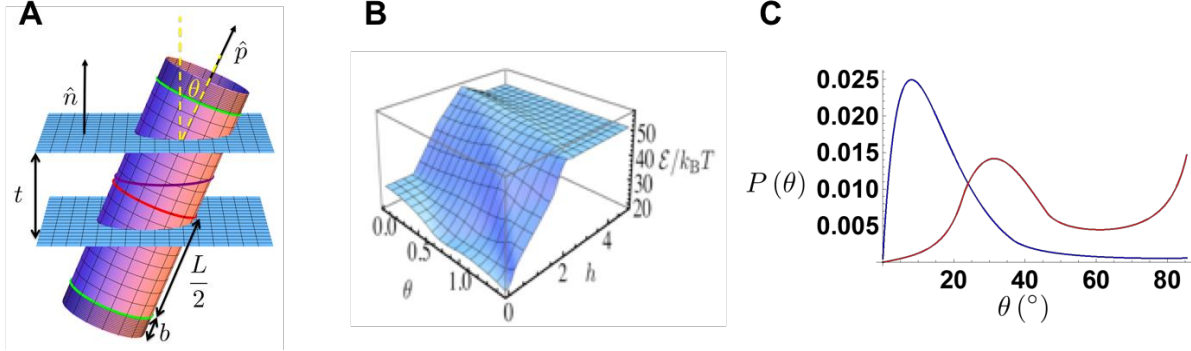


fig. S6. Canting angle distribution of NR. (A) Schematic of the nanorod in a membrane. hydrophobic length L with two hydrophilic ends of length b and radius a . The total length of the rod is then $L + 2b$. It is shown in a piece of membrane of thickness t . The green circles show the ends of the hydrophobic rod. The red circle denotes the center of the nanostructure, while the purple curve shows the intersection of the rod with the midplane of membrane. (B) Energy of the nanorod of radius $a = 2$ nm as a function of its orientation in the membrane, parameterized by θ , h . The hydrophobic length of the rod is $L = 8$ nm, with hydrophilic end cylinders of length 2 nm. The energies (in units of $k_B T/\text{nm}^2$) are $\gamma_c^o = 2.0, \gamma_c^e = 0.1, \gamma_o^o = 0.1, \gamma_o^e = 1.0$. (C) Probability distribution for canting angle θ of a nanorod in the membrane for no hydrophobic mismatch $L = t = 4$ nm (blue) and significant hydrophobic mismatch $L = 6$ nm for the same membrane thickness. In both cases the rods are terminated at both ends by hydrophilic cylinders of length 2 nm.

For certain values of the vertical displacement h and tilt angle θ , the top of the cylinder is buried in the membrane, at least for some azimuthal angles f .

Similar considerations apply to the set of points on the cylinder where it intersects the lower edge of the membrane. These points are defined by

$$r_{bottom}^{(0)}(f) = -\frac{t}{2\cos q} - \frac{h}{\cos q} - a \tan q \cos f \quad (7.5)$$

As discussed with regard to Eq. 7.4, some of these points may be off the lower end of the cylinder when all or part of the bottom of the cylinder is buried in the membrane. To account for this case, we must use a lower limit given by

$$r_{bottom}(f) = \max \left[-\frac{L}{2}, r_{top}^{(0)}(f) \right] \quad (7.6)$$

To compute the surface area of the rod enclosed in the membrane, we integrate over the surface using the limits of integration obtained above in Eq. 7.4 and 7.6

$$A = \int_{\rho}^{\rho} a df \int_{r_{bottom}(f)}^{r_{top}(f)} dr Q(r; q, h, f) \quad (7.7)$$

where we include in the integrand Θ , which vanishes if the bottom of the cylinder is above the upper edge of the membrane or if the top of the cylinder is below its lower edge.

The above analysis is designed to account for the central hydrophobic part of the cylinder, which is of length L . It is, however, a simple matter to compute the amount of hydrophilic surface area inside and outside the membrane by redoing the above analysis with different ranges of ρ . Specifically, to account for the upper hydrophilic part of the cylinder of length b , we shift the range of ρ to $(L/2, L/2+b)$. The lower hydrophilic cylinder corresponds to a range of ρ given by $(-b-L/2, -L/2)$. The necessary adjustments to the min/max functions and to the Θ function are straightforward, but not given here.

SI-7.2 Energetics of the nanorod in the membrane

The energy of the nanorod is directly determined by four surface energies. We define $g_c^{w,o}$ to be the surface energies, measured in units of $k_B T / \text{nm}^2$ of central hydrophobic rod in water (w) or in the oily (o) interior of the membrane $g_c^o < g_c^w$. We define two analogous surface energies for the outer hydrophilic parts of the rod, $g_o^{w,o}$, where now $g_o^w < g_o^o$.

Height and orientational fluctuations of rods in the membrane

Because of the various geometrically required inequalities obeyed by the integration variables it is difficult to provide a generic, closed-form solution for the energy of the nanorod in the membrane $\varepsilon(\theta, h)$. Instead, we examine a specific case with $L = 8$ nm, $a = 2$ nm, $b = 2$ nm,

and a membrane of thickness $t = 4$ nm. In units of $k_B T / \text{nm}^2$, we take $\gamma_c^o = 2.0, \gamma_c^e = 0.1, \gamma_o^o = 0.1, \gamma_o^e = 1.0$. The energy surface is shown in fig. S6B.

There are two distinct features of this energy surface, both of which are attributable to the mismatch of the hydrophobic center to the membrane thickness. First, when we consider the potential along the h axis at a fixed canting angle θ , it is initially flat – small vertical displacements of nanorod do not change the energy as the hydrophobic section is longer than the width of the membrane. Once, the vertical displacement is sufficiently large so as to begin to bury the hydrophilic ends of the rod, the potential increases rapidly in a nearly linear fashion until the rod leaves the membrane entirely.

Second, when we consider the energy surface in the tilting (θ) direction near symmetric insertion ($h = 0$), we see that the hydrophobic mismatch between the central part of the rod and the membrane thickness leads to a decrease of energy with increasing angle. As the rod tilts, more hydrophobic surface is buried within the membrane lowering the total energy of the system. When the hydrophilic top or bottom of the rod touches the membrane, however, this energy reduction with increasing angle is arrested as it becomes energetically unfavorable to bury more and more of the hydrophilic ends inside the membrane. A local minimum in the energy appears at an angle which depends on the various surface energies of the two regions. We see then that the orientation of the rod along the local membrane normal is unstable to canting as a result of the hydrophobic mismatch. We will see below that, even in cases of zero hydrophobic mismatch, nonzero canting angles are still favored, now solely due to entropic considerations.

For the special case of zero hydrophobic mismatch, the rod is strongly pinned within the membrane, i.e., with h near zero. The effective potential for rod canting (i.e., angling with respect to the local membrane normal) is effectively linear in the angle $\sim a\theta$, with $a \sim O(10k_B T)$ for typical values for nm scale rod dimensions and surface energies of a few $k_B T/\text{nm}^2$. Thus the mean canting angle of the rod is approximately given by

$$\langle \theta \rangle \approx -\partial_a \log \left[\int_0^\infty e^{-a\theta} \sin \theta \right] = \frac{2a}{1+a^2} \quad (7.8)$$

where, noting the rapid decay of the Boltzmann factor for larger angles, we have extended the upper limit of the integrand to infinity. As the potential is made steeper by, e.g., increasing the hydrophobic energy of the interior segment of the rod, the mean angle goes to zero as $2/a$. This angle represents the competition between the energy cost for canting due to the burial in the membrane of the rod's hydrophilic ends and exposure of its hydrophobic interior to the surrounding solvent with the increased orientational phase space associated with larger canting angles.

The fluctuations about this mean value are given by

$$\langle \theta^2 \rangle - \langle \theta \rangle^2 \approx -\partial_a^2 \log \left[\int_0^\infty e^{-a\theta} \sin \theta \right] \approx \frac{2}{a^2} \quad (7.9)$$

in the region of interest. Thus, nanorods with no hydrophobic mismatch typically lie at small angles with respect to the membrane normal, $\langle \theta \rangle \sim 0.2 \sim 10^\circ$ and exhibit small fluctuations about this angle that are comparable to this angle: $\sqrt{\langle \theta^2 \rangle - \langle \theta \rangle^2} \sim \langle \theta \rangle$. Given the similarity of the geometry of these nanorods to transmembrane proteins and their aggregates, we expect similar equilibrium orientations and fluctuations for them as well.

The key determinant of the canting angle distribution and the propensity for the nanorods to lie in the plane of the membrane $\theta \approx \pi/2$ appears to be the amount of hydrophobic mismatch – the difference in the thickness of the hydrophobic layer on the rod and the thickness of the membrane. In Fig. 2G (main text) we show the probability distribution for rod canting angles in the membrane for two rod geometries. In the first case (blue) the hydrophobic mismatch is zero; the length of hydrophobic section of the rod is equal to the membrane thickness $L = t = 4$ nm. Here we see a maximum in the angle probability distribution at angles comparable to the (small) mean canting angle $\langle \theta \rangle$ as computed from Eq. 7.8. In the second case (red), the hydrophobic section of the rod extends significantly beyond the boundaries of the membrane: $L = 6$ nm, while $t = 4$ nm. One observes that the local maximum in the probability distribution has moved to larger angles, with a maximum at a canting angle of $\theta \approx 0.6$, but there a new local maximum has developed for the case of the rod lying in the plane of the membrane, $\theta \approx \pi/2$. Sufficient hydrophobic mismatch will destabilize the (nearly) normal insertion orientation of the rods making them transmembrane poor voltage sensors. In both cases shown here (red and blue) the hydrophilic ends of the cylinder are 2nm long and all hydrophobic and hydrophilic surface energies are identical.

Partitioning of nanorod between solvent and membrane

To determine the equilibrium partitioning of nanorods between the membrane and surrounding fluid, we compare the partition function associated with a nanorod in aqueous solution of volume V

$$Z_{water} = 4\pi v \exp\left[-(4\pi a b \gamma_o^\omega + 2\pi a L \gamma_c^\omega) / k_B T\right] \quad (7.10)$$

with the partition function associated with the rod being in membrane of surface area A

$$Z_{membrane} = 4\pi A \int_0^{+1} d \cos(\theta) \int_{h_{min}}^{h_{max}} dh e^{-\varepsilon(\theta, h) / k_B T} \quad (7.11)$$

In Eq. 7.10 the prefactor of $4\pi V$ accounts for the orientational and translational degrees of freedom of the rod. These factors are similarly accounted for in Eq. 7.11 by the prefactor of $2 \times 2\pi A$. The first factor of two allows for the insertion of the rod in either of its two (identical) orientations. The remaining integrations in that equation are over the degrees of freedom determining the orientation of the rod in the membrane. The height integral is limited to $h_{\min}(\theta)$ and $h_{\max}(\theta)$ determined so that at least some part of the rod is in contact with the membrane.

We define the partitioning fraction of the nanorods R as the fraction of nanorods in the membrane of spherical vesicles of radius \mathfrak{R} at number density n . From Eqs. 7.10, 7.11, this fraction is given by

$$R = \frac{r}{1+r} \quad (7.12)$$

where r is the ratio of the two partition sums given above: $r = Z_{\text{membrane}}/Z_{\text{water}}$. Taking these partition sums from Eqs. 7.10, 7.11, we find

$$r = 4\pi\mathfrak{R}^2 n \exp\left[\left(4\pi ab\gamma_o^\omega + 2paL\gamma_c^\omega\right)/k_B T\right] \int_0^{\pi/2} d\cos(\theta) \int_{h_{\min}}^{h_{\max}} dh \exp\left[-\varepsilon(\theta, h)/k_B T\right] \quad (7.13)$$

The partitioning of the nanorods between the membrane and the solvent is controlled mainly by the hydrophobicity of the central part of the nanorod and the concentration of vesicles in solution. As long as these hydrophobic energies are significant, i.e., on the order of $k_B T/\text{nm}^2$ and the concentration of vesicles is at least in the nM (nanoMolar) regime, essentially all of the nanorods will be inserted into membranes in thermal equilibrium.

One may see this result from a simple estimate of the r factor defined in Eq. 7.13. To simplify the calculation, we assume that the energy difference between the rod in the membrane and in the (aqueous) solvent is due solely to the exposure of the hydrophobic surface of the nanorod to water

when in solution. Taking the length of the rod to be equal to the membrane thickness t , this Boltzmann weight associated with this energy difference is $\exp[2\pi at\gamma_c^\omega] \sim 10^{20}$. Taking there to be only $N \sim 10^9$ vesicles (of micron radius: $\mathfrak{R} = 1 \mu\text{m}$) per liter, we find the estimate for r to be

$$r \sim \frac{\mathfrak{R}^2 t N e^{2\pi at\gamma_c^\omega / k_B T}}{\nu} = 10^{14} \quad (7.14)$$

This estimate assumes that the excess energy cost of putting 1 nm^2 of hydrophobic surface in contact with water instead of the lipid membrane interior is $1 k_B T$. Because of the exponential dependence of the result on this hydrophobic energy cost, reducing that energy difference to $\sim 0.3 k_B T$ per nm^2 , results in $r \sim O(1)$, implying a roughly equal partitioning of the nanorods between membrane and solvent, at least at this low membrane concentration.

section S8. Optical recording of ANEPPS-labeled and pcNR-labeled spiking HEK cells

ANEPPS stained membrane regions of HEK cells were thresholded (= mean + standard deviation). White pixels in fig. S7B are the area with intensity values that are larger than the threshold. Figure S7C shows a temporal time trajectory for the spatial average of all white pixels in fig. S7B, clearly exhibiting photo-bleaching. To remove this slowly varying contribution to the signal, we apply a 5th ($M=5$) order Butterworth-type high pass filter (HPF) with a cut-off frequency of $f_c = 2.5 \text{ Hz}$

$$HPF_{time}(f) = \sqrt{1 - \left(\frac{1}{\sqrt{(1 + f / f_c)^{2M}}} \right)^2}$$

The blue curve in fig. S7D is the fast Fourier transform (FFT) of the signal shown in fig. S7C and the green curve represents the above mentioned Butterworth HPF. The red curve in fig. S7D

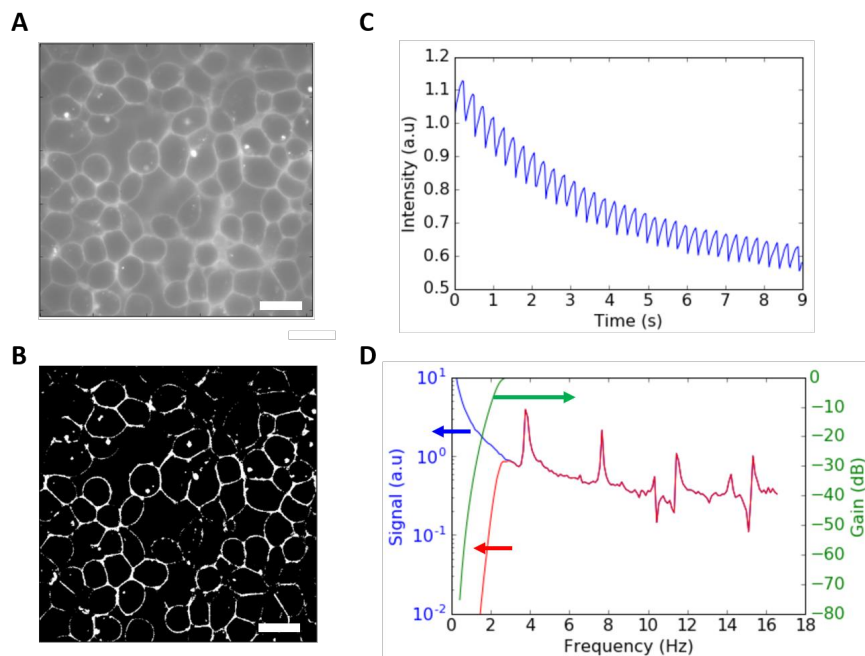


fig. S7. Image processing of voltage recording with ANEPPS. (A) Fluorescence image of ANEPPS stained spiking HEK293 cells (B) The binary image of (A) after thresholding. (C) Intensity time trace of white pixel's average in (B). (D) Blue: FFT of intensity time trace in (C). Green: The Butterworth temporal HPF function. Red: The filtered signal (frequency domain). Scale bar 10 μm .

represents the filtered signal (in the frequency domain). The black curve in Fig. 4D in time domain represents the filtered signal in the time domain.

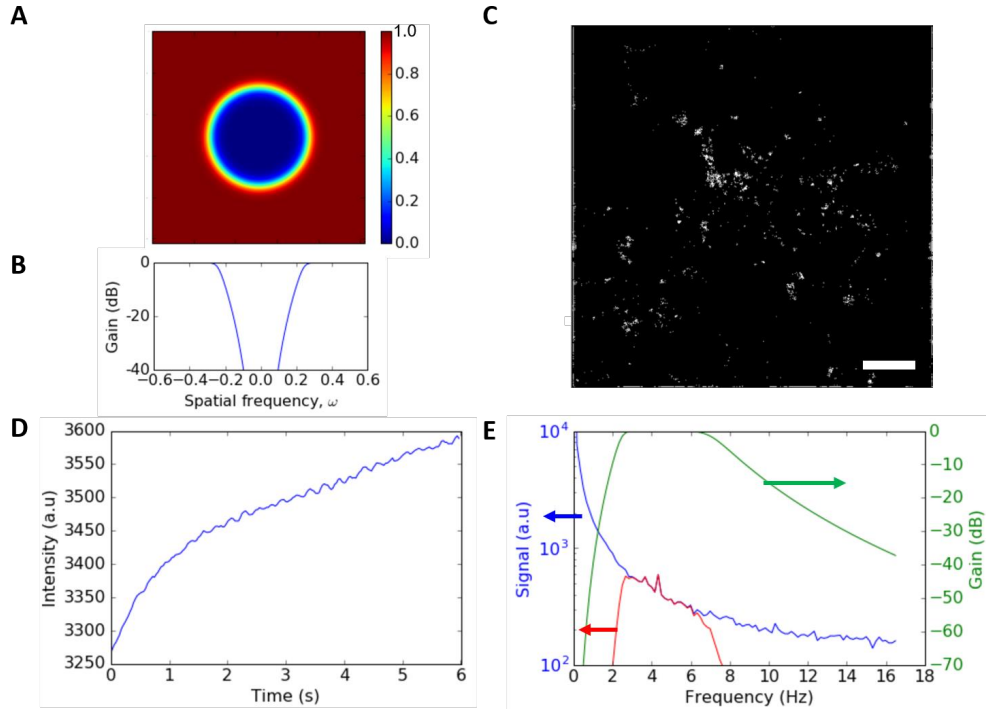


fig. S8. Image processing of voltage recording with pcNR. (A) A Butterworth type spatial HPF (B) The spatial HPF function at $\omega = 0$. (C) The binary image of Fig. 4B after thresholding. (D) Intensity time trace of white pixel's average in (C). (E) Blue: FFT of intensity time trace in (D). Green: The temporal BPF function. Red: The BPF filtered signal. Scale bar 10 μm .

In contrast to the ANEPPS staining, staining with pcNRs is non-uniform, leading to local bright areas with gradients of brightness (The left side of Fig. 4B is brighter than the right side). We applied a 10th order high pass Butterworth filter with 0.244 (pixel^{-1}) as a spatial frequency (ω_c) cut-off. This filter removes the gradient and the cloudy background, increasing the visibility of single (or small aggregates) of pcNRs in Fig. 4C. Next, a simple threshold ($= \text{mean} + 2 \times \text{standard deviation}$) is applied to obtain a binary image (fig. S8C). Using this binary image as a mask, we calculate the intensity time trace averaged over these white pixels (fig. S8D). Unlike the ANEPPS' result, the staining with pcNRs suffers from photo-brightening. To remove this slowly

varying contribution to the signal, and the high-frequency shot-noise, we apply a 5th (M=5) order of Butterworth band pass filter (BPF) with $f_{low} = 2.5$ Hz and $f_{high} = 7$ Hz as cut-off frequencies

$$BPF_{time}(f) = \frac{1}{\sqrt{(1 + f / f_{high})^{2M}}} \sqrt{1 - \left(\frac{1}{\sqrt{(1 + f / f_{low})^{2M}}} \right)^2}$$

The blue curve in fig. S8E is the fast Fourier transform (FFT) of the temporal signal in fig. S8D and the green curve is the BPF function. The red curve in fig. S8E represents the filtered signal (frequency domain). The filtered signal in the time domain is shown in Fig. 4F, black curve.

The spiking cell analysis's data are freely available on figshare:

https://figshare.com/articles/zqd_tif/4229531. The analysis code is published in a public github repository : <https://github.com/pkw0818/spiking-cell-analysis>.

section S9. Simultaneous optical and electrical recordings in patch-clamp experiment

SI-9.1 Data files and software

The data files used in the voltage sensing patch clamp experiment are freely available on figshare: <http://dx.doi.org/10.6084/m9.figshare.1445980>, dataset *122018_take1 100Hz.zip*. The dataset from the patch-clamp experiment consists of a video (272x192 pixels, 2000 frames at 400Hz or 2.5 ms per frame) and a synchronous set of electrical measurements (voltage, current) acquired by a DAQ interface at 10kHz.

Data analysis was performed in python using the Jupyter/IPython Notebook (56) and a few common scientific libraries (numpy, scipy, matplotlib, pandas). The Jupyter notebooks are “live” (i.e. re-executable) documents that contains both a narrative description of the analysis, the code commands and the output (figures, text, links, etc ...). All the software used for data analysis of the patch-clamp experiment are open source and readily available on the internet.

The custom software used for patch-clamp data analysis is published in a public github repository: <https://github.com/tritemio/voltagesensing> where interested readers can find instructions on how to setup and reproduce the entire data analysis workflow. The repository contains a few .py files (python modules) containing low-level functions (data load, timetrace processing, burst search) and a set of Jupyter/IPython Notebooks that perform the full analysis. The notebook used in this paper can be also visualized online (read-only) at the following address: Patch Clamp Analysis - Phase offset-take1. Upon execution, the notebook generates an extensive set of plots of each analysis step and saves, in the *paper figures* folder, all the figures used in this publication (for the patch-clamp experiment). Finally, the raw unprocessed time-traces for each nanoparticle are saved in plain text format in the *results* folder in order to facilitate re-analysis with other tools.

SI-9.2 pcNR identification and ROIs

From the dataset linked above, we manually identified pcNRs positions with sub-pixel accuracy, by analyzing average frames on the raw video and on a temporal high-pass version of the video. The notebook in section 3 ([link](#)) contains figures of the center position of each identified pcNR for particles on the patched cell membrane (in the center of the field of view) and on unpatched cells' membranes. For brevity we will call these groups patched and unpatched pcNR.

A round ROI, centered on the pcNR position, is defined using a pixel radius of 1.8 pixels, resulting in a selection of roughly 20 pixels. Due to the pixel discretization and sub-pixel positioning of the pcNR the exact number of pixels selected for each particle can be slightly different. The notebook shows the exact ROI employed for each patched or unpatched pcNR (cells In [38] and In [39]).

SI-9.3 Time-trace extraction, filtering and blinking removal

For each identified pcNR, we compute the time-trace $\{t_k\}$ by averaging the signal in each ROI for each frame. Each of these raw time-traces is a 2000-element array, each element corresponding to a single video frame (the first 4 frames are discarded on loading since they systematically contain corrupted data due to specificities of the acquisition system). The voltage modulation has a period of 4 frames, of which the first 2 correspond to voltage-on and the last 2 to voltage-off semi-periods. Raw and processed timetraces are shown in the notebook section 4 ([link](#)).

In order to remove the time intervals where the pcNR is not fluorescent (due to blinking), a threshold is usually applied. In the present case, a slow-varying drift in the raw time-traces (1 s time scale) makes it difficult to identify a meaningful threshold. Therefore, we first apply a filter that removes the slow (low frequency) variations in the time-trace. This filter is a high-pass Gaussian filter with sigma of 300 frames (750 ms, see notebook figure [I_n\[42\]](#)). Next, we smooth the time-trace by applying a low-pass filter (Gaussian filter with sigma=10 frames, 25ms) in order to better identify the switch-points related to the particle fluorescence intermittency (blinking). Due to noise, without this smoothing step, we could erroneously detect multiple spurious ON/OFF transitions in correspondence with a single switch-point. Figures of the filtered time-traces overlaid with the smoothed version used to identify the blinking periods are shown in the [notebook section 4](#) (figures [I_n\[44\]](#) and [I_n\[45\]](#)).

Finally, the dark-state periods are removed from each time-trace, making sure that a 4 frames alignment is preserved so that the reduced time-traces are still in phase with the alternation signal. This operation is performed by two python function: the function `get_on_periods_slices()` ([link](#)) performs the quantization to multiple of 4 frames for the start-stop index of each ON blinking

period; `get_on_periods_timetrace()` ([link](#)) performs the stitching of the ON blinking periods in the time-traces.

SI-9.4 Computing the modulated signal

Since each semi-period of the modulating voltage square-wave corresponds to 2 frames in $\{t_k\}$, we reduce the time-traces by averaging the array in blocks of 2 elements (implemented by `block_average()` in *timetraces.py*). The resulting reduced time-trace $\{\bar{t}_j\}$ has 1 element per semi-period (either ON or OFF voltage). Next, the “alternated differences” $\{\Delta F_i\}$ are computed as $\{(\bar{t}_1 - \bar{t}_0), -(\bar{t}_2 - \bar{t}_1), (\bar{t}_3 - \bar{t}_2), \dots\}$ (the sign alternates and is “+” for ON-OFF and “-” OFF-ON transitions). This operation is implemented by `edge_diff_all()` in *timetraces.py*. Please note that one modulation period corresponds to 2 elements in the $\{\Delta F_i\}$ array.

The signal $\{\Delta F_i\}$, the normalized version $\{\Delta F_i/F\}$ (where F is the average time-trace value) and several derived statistics are computed both for particles in the patched cell membrane (*patched set*) and for particle in other position of the field of view (*unpatched set*).

As a control, an out-of-phase version of $\{\Delta F_i\}$ is computed by simply removing the first frame from the raw time-trace prior to the other processing steps. In this case, when computing the 2-element block average to obtain the reduced time-traces, the frame removal results in averaging one ON and one OFF semi-period frame. As a consequence, intensity variations due to the voltage modulations are suppressed. The distribution of out-of-phase $\{\Delta F_i\}$ values has a theoretical mean of zero and a standard deviation that is a characteristic of the background.

Histograms of the in-phase and out-of-phase signal distributions are reported in notebook section 8 ([link](#)). Several statistics for the alternated differences $\{\Delta F_i\}$ are reported in the notebook (i.e.

mean, standard deviation, mean/standard deviation, mean/(mean intensity)). Here, in fig. S9, we show the mean signal for different pcNRs. We note that among the patched pcNRs in positions #0, #1, #3, #4 and #8 exhibit significantly higher signal than the out-of-phase signal and the signals for unpatched particles. However, the pair of positions #0 - #1 (and #3 - #4), have pixels in common (i.e. the ROIs overlap) and show highly correlated time-traces, indicating that the signals are originated from the same particles (or small cluster of particles). In order to avoid treating those pairs as separate particles (and over-representing those positions which exhibit high signal), we discard positions #0 and #3 in the following analysis steps.

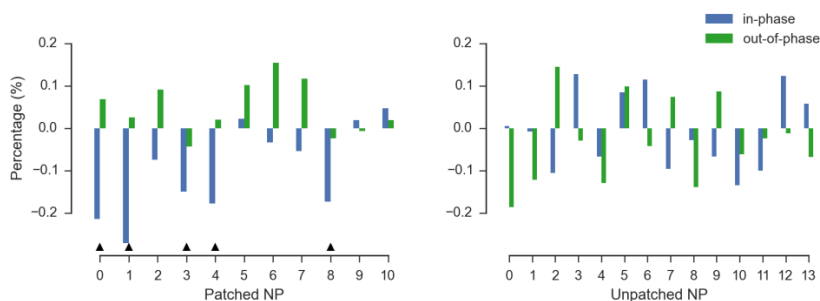


fig. S9. Mean of $\{\Delta F_i/F\}$ for the two sets of patched (left) and unpatched (right) particles.

The patched particles #0, #1, #3, #4, and #8 (black marks) exhibit higher absolute in-phase signal than out-of-phase and unpatched particles.

Figure S10A and S10B show aggregated results for patched and unpatched NPs, both for in-phase and out-of-phase signal. In fig. S10A we show the full distribution for the 4 cases, whereas fig. S10B shows the distribution mean and the $\pm 1\sigma$ error range (computed under assumption of Gaussian distribution). We note that only the in-phase signal for the “patched” set exhibits a statistically significant deviation from 0. The full distribution shows also a larger negative tail for the patched in-phase signal suggesting that there may be a few temporally interspersed “bursts” of negative signal.

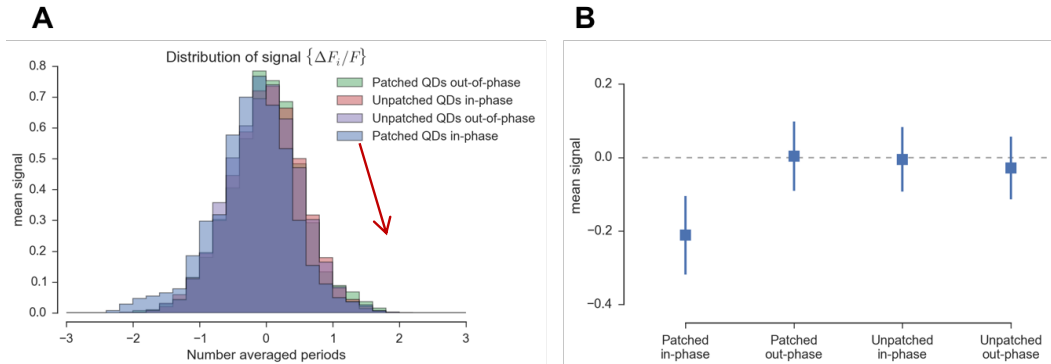


fig. S10. Image processing of voltage recording with pcNRs. (A) Distribution of signal $\{\Delta F_i/F\}$ aggregated from patched (only particles 1, 4 and 8) and unpatched particles, computed either in-phase or out-of-phase. The red arrow highlights the negative tail of the distribution that is more pronounced for the patched set with in-phase signal. (B) Mean signal $\{\Delta F_i/F\}$ aggregated from patched (only particles 1, 4 and 8) and unpatched particles, computed either in-phase or out-of-phase. The error bars correspond to the $\pm 1\sigma$ range. Assuming a Gaussian distribution, σ is computed as $\sigma = \text{std. dev.}(\{\frac{\Delta F_i}{F}\})/\sqrt{N}$, where N is the number of elements in $\{\Delta F_i/F\}$.

SI-9.5 Burst search

The burst search analysis complement the modulated signal analysis by focusing on the brief periods of high signal $\{\Delta F_i/F\}$ in a time-trace, instead of performing averages on the full time-trace. The motivation behind this type of analysis is to better discriminate the small, transient signal from the background under the assumption that pcNRs experience brief periods of transient insertion into/out of the membrane. Signal time-traces are reported in the notebook section 6 ([link](#)). The goal of burst search is detecting the time periods during which the fluorescent signal alternates in phase with the modulating voltage.

We start by computing the square of the running average of the $\{\Delta F_i/F\}$ signal using a block of 12 elements (*squared score*). When the squared score is higher than a threshold, a burst is detected. For each time-trace, the threshold was set to 60% of the maximum of the squared score. Next, for each burst i , we extracted the total signal (*burst score*)

$$S_i = \frac{1}{F} \sum_j \Delta F_j$$

Note that in the previous sum we have a minimum of 12 elements (j) that is the block size for the running average. However, depending on the signal, we can have longer bursts.

The quantity S_i represents the total amount of modulated signal present in each burst. In principle, the burst score can be either positive or negative, depending on whether the fluorescence intensity increases or decreases when the voltage is applied. For the pcNRs employed here, we find that the fluorescence is decreased (see fig. S10A). This is consistent with the observed excess of bursts with negative score for the selected particles on the patched cell membrane (see also main text).